SAPIENZA
UNIVERSITÀ DI ROMA

Experimental and theoretical development of m-scale and high repetition rate plasma sources for plasma-based particle accelerators

Physics Department
PhD School in Accelerator Physics (XXXVII cycle)

Lucio Crincoli
ID number 1993699

Advisors
Prof. Massimo Ferrario
Dr. Angelo Biagioni

Academic Year 2023-2024

A thesis submitted in partial fulfillment of the requirements for the degree of Doctor of Philosophy in Accelerator Physics.

Thesis defended on 30 January 2025.

Experimental and theoretical development of m-scale and high repetition rate plasma sources for plasma-based particle accelerators
PhD thesis. Sapienza University of Rome

This thesis has been typeset by LaTeX and the Sapthesis class.

Author's email: lucio.crincoli@uniroma1.it

Dedicato a mio padre, a cui devo tutto

Abstract

Novel plasma-based particle accelerators allow a drastic reduction in size and cost, compared to conventional RF-based structures, due to strong accelerating and focusing fields established inside plasmas. A key role in the development of plasma-based accelerators is played by plasma sources. Indeed, the design of specific devices able to produce stable and uniform plasma channels is crucial for the efficiency of the plasma acceleration mechanism. The development of plasma sources is particularly focused on the realization of m-scale devices, able to generate stable and long plasma channels for high energy gain acceleration. Furthermore, the longevity of plasma sources is a key aspect for long-term operation at high repetition rate, which is a fundamental requirement for many particle accelerator applications. In this context, this PhD thesis presents the design and development of m-scale and high repetition rate plasma sources for plasma-based particle accelerators. Experimental and theoretical activities are carried out at Plasma_lab laboratory, located at National Laboratory of Frascati (LNF-INFN), and in the framework of EuPRAXIA@SPARC_LAB project, with special focus on plasma discharge capillaries, in which plasma channels are created by means of high voltage pulses. Experimental and numerical studies are performed to investigate the effect of the capillary geometry on the plasma density distribution, aimed at improving the plasma density modulation required for efficient plasma acceleration. Novel schemes are designed and tested for the realization of compact and cost-effective m-scale plasma discharge capillaries, able to provide high energy gain acceleration, staged focusing-acceleration and guiding of charged particle beams. Moreover, high repetition rate tests are performed with innovative ceramic capillaries, assessing the ability of adopted materials to withstand the heat load produced by high voltage plasma discharges. In addition, laser-induced plasma filaments are studied and characterized as an alternative plasma source for high repetition rate applications. In conclusion, a preliminary design and test of a 60 cm-long capillary, conceived for the plasma module of EuPRAXIA@SPARC_LAB project, is presented.

Acknowledgments

Prima di tutto, voglio ringraziare la mia famiglia per essere stata il mio punto di riferimento in questi 30 anni. Ringrazio mio padre e mia madre, che hanno sacrificato tutto per permettermi di inseguire i miei sogni e le mie passioni. Ringrazio i miei fratelli, con cui ho condiviso tutti i momenti più importanti. Grazie a Martina per essere al mio fianco tutti i giorni e per avermi insegnato ad amare.

Ringrazio il prof. Massimo Ferrario per avermi permesso di approcciarmi al mondo della ricerca tramite il progetto SPARC_LAB e per il supporto e gli interessanti spunti di riflessione che mi ha offerto. Grazie ad Angelo Biagioni per la sua guida e gli insegnamenti offerti in questi tre anni e per gli importanti traguardi che abbiamo raggiunto al Plasma_lab.

Voglio ringraziare Stefano Romeo per avermi insegnato che OpenFOAM non si ferma solo a "FOAM FATAL I/O Error". Ringrazio inoltre Valerio Lollo e Donato Pellegrini per il loro prezioso supporto nelle mie attività di ricerca. Grazie a Riccardo Pompili, Mario Galletti, Gemma Costa, Fabio Villa, Maria Pia Anania, Alessio Del Dotto, Livio Verra e tutto il gruppo SPARC per tutto ciò che mi hanno insegnato in questi tre anni di ricerca scientifica. Grazie a Romain Demitra, Cristina Mariani, Michele Opromolla, Federica Stocchi, Gilles Silvi, Daniele Francescone, Gianmarco Parise, Andrea Frazzitta e Marco Pitti per tutte le esperienze fatte dentro e fuori dai laboratori (soprattutto alle conferenze). Voglio inoltre ringraziare Pierre Drobniak per l'aiuto che mi ha offerto con OpenFOAM e per le interessanti discussioni.

Ringrazio Matteo per tutte le sfuriate a Risiko che ci sono state e che ci saranno. Grazie a Lorenzo che rappresenta per me un amico fidato, nonostante sia mezzo francese e mezzo tedesco. Voglio ringraziare Vito, Chiara, Ugo, Ida, Zinja, Jacopo, Luca e tutti i miei amici. Anche se il tempo e la distanza non permettono di sentirci e vederci come prima, mi sento sempre legato a voi.

Finally, I would like to thank Prof. Riccardi and Prof. Zigler, who kindly accepted to referee this thesis and helped me to improve it in every aspect.

Contents

List of Figures

List of Tables

Introduction

Nowadays, particle accelerators are spread all over the world and used in a variety of applications, from research in high energy and particle physics to nuclear medicine, radiotherapy and industrial applications. However, limitations in the size, cost and technology of conventional RF-based accelerators are driving interest towards novel acceleration mechanisms, based on plasma technology.

Plasma-based accelerators rely on the use of laser pulses or particle bunches to drive strong perturbations in plasma channels, resulting in the production of high GV/m accelerating fields and kT/m focusing fields. Such plasma structures provide a drastic reduction in the size and cost of particle accelerators, compared to conventional MV/m-range RF cavities and hundreds T/m-range focusing magnets.

Due to the instability of the acceleration mechanism, plasma-based accelerators do not provide yet the performances of RF-based structures, especially in terms of stability and beam quality. For this reason, the scientific community is putting effort in the development of such technology, with recent achievements that demonstrate the suitability of plasma accelerated beams for practical applications, such as driving FEL radiation. In this regard, a key milestone towards the utilization of plasma accelerators in scientific applications is represented by the EuPRAXIA project (European Plasma Research Accelerator with eXcellence In Applications), which includes the realization of the first plasma-driven FEL user facility (EuPRAXIA@SPARC_LAB project), that will be built at National Laboratory of Frascati (LNF-INFN).

In order to enhance the stability and quality of plasma acceleration, plasma sources play a crucial role. Indeed stable and uniform plasma channels are required to sustain GV/m plasma wakefields in order to accelerate and focus particle beams with high quality (low emittance, low energy spread). For this reason, many different devices are developed and used to create and control plasma channels for plasma-based applications. In particular, plasma discharge capillaries represent a compact and cost-effective plasma source, based on the production of plasma channels by means of high voltage pulses, providing a fine control over the plasma properties, and so on the plasma acceleration mechanism.

Given the GV/m accelerating gradient provided by plasma structures, m-scale plasma channels are required to enhance the energy gain in a single plasma stage to the GeV range. In this sense, R&D on plasma sources is particularly focused on the realization of m-scale devices, able to generate stable and long plasma channels for high energy gain acceleration.

Moreover, another major requirement of many particle accelerator applications, including linear colliders and FEL facilities, is the high repetition rate operation, i.e. from hundreds Hz to the kHz range. In the context of plasma-based acceleration, high

repetition rate operation represents a remarkable challenge, in particular concerning plasma sources constituted by solid structures for the plasma confinement, such as discharge capillaries. Indeed, the heat load produced by high voltage plasma discharges and deposited onto the inner walls of the capillary structure can cause erosion and damage issues and, consequently, the production of plasma discharges at high repetition rate can dramatically affect the longevity of the plasma source. For this reason, the development of plasma sources able to sustain the heat load produced by high voltage plasma discharges at high repetition rate is essential for the realization of plasma-based accelerator facilities for users.

Within this context, the presented PhD thesis project is devoted to the design and development of m-scale and high repetition rate plasma sources for plasma-based particle accelerators. Experimental and theoretical activities, carried out in the framework of EuPRAXIA@SPARC_LAB project, are focused on the development of plasma discharge capillaries, in which the plasma formation is achieved by means of high voltage pulses. Activities related to the PhD thesis project are carried out at Plasma_lab laboratory, within the SPARC_LAB collaboration (LNF-INFN).

Studies on the capillary geometrical design are performed to evaluate the ability to modulate the plasma density according to the required application.

Novel schemes of compact m-scale capillaries are tested and characterized for the development of m-long sources able to produce uniform plasma channels, but also to provide combined configurations for staged focusing and acceleration of particle bunches.

Furthermore, high repetition rate tests are performed to evaluate the longevity of discharge capillaries, specifically made of high temperature resistant ceramics, able to withstand the heat load produced by plasma discharges. In addition, testing and characterization of laser-induced plasma filaments are carried to evaluate the properties of such plasma sources, which represent a suitable option for high repetition rate applications.

0.1 Organization of the thesis

After this introductory discussion, the thesis is organized as follows:

- Chapter 1 presents an overview of particle accelerators, including a detailed description of plasma-based acceleration schemes, their motivation and advantages. In addition, the EuPRAXIA@SPARC_LAB project is introduced, as one of the key milestones in the development of plasma-based accelerators and the main project leading R&D activities on plasma sources in regard of this PhD thesis.

- Chapter 2 provides an overview on plasma sources for plasma-based accelerators, including the different mechanisms adopted for the plasma formation, such as electrical discharges and laser or beam ionization. A particular focus is given to plasma discharge capillaries, widely studied within the thesis project, and their applications, including focusing of charged particle beams (in the so-called Active Plasma Lenses) and guiding of high power laser pulses.

- In chapter 3, the plasma module employed at Plasma_lab laboratory to study and characterize plasma discharge capillaries is presented. Detailed descriptions of the main components of the plasma module are provided, including the design of discharge capillaries, the features of the gas injection and high voltage systems and the diagnostic techniques adopted for the characterization of the plasma.

- Chapter 4 presents a study of the geometrical design of plasma discharge capillaries, performed by means of experimental tests and numerical simulations and aimed at improving the modulation of the plasma density distribution in such plasma sources.

- Chapter 5 includes a series of novel schemes for m-scale plasma discharge capillaries, conceived for the realization of long plasma channels for high energy gain plasma-based acceleration, but also for staged acceleration and focusing within compact plasma sources and for plasma-based bending of charged particle beams.

- Chapter 6 describes the development of high repetition rate plasma sources. First, the longevity issue of plasma discharge capillaries is introduced, discussing the effect of long-term plasma discharge operation. Afterwards, design and testing of high repetition rate plasma discharge capillaries, based on the combined use of machinable and cost-effective ceramic materials, is widely described. Experimental testing of ceramic capillaries and heat transfer simulations are reported, discussing the reliability of such solution for long-term high repetition rate plasma acceleration, in particular concerning the EuPRAXIA@SPARC_LAB project. In addition, Chapter 6 includes the characterization of laser-induced filaments, providing various advantages for high repetition rate operation.

- Chapter 7 presents a preliminary design of a 60 cm-long capillary, targeted for EuPRAXIA@SPARC_LAB project, which includes numerical fluid dynamics simulations and a novel scheme based on a modular capillary structure.

Finally, main results are summarized in the conclusions, with further remarks on future perspectives. Additionally, the Appendix reports the description of distribution functions adopted for the spectroscopic analysis of plasma channels produced by tested capillaries.

Chapter 1

Particle Accelerators and Plasma technology

1.1 Overview on particle accelerators

Particle accelerators are nowadays adopted into a variety of applications, with a total amount of around 40 thousands machines all around the globe. Only a minority of those is devoted to research activities, in the field of high energy physics, particle physics and material science, while the majority is employed in industrial and medical applications [42]. On a general ground, particle accelerators are constituted by the following components:

- **Particle sources**, which produce low energy particle beams, mainly through thermionic or photo-electric emission.
- **Radiofrequency (RF) accelerating structures**, used to accelerate particle beams delivered by the sources.
- **Magnets**, which guide and focus the beams along the accelerator design trajectory.
- **Vaccum systems**, which prevent the interaction between the accelerated beam and the atmospheric gas inside the vacuum pipe travelled by the beam.
- **Cooling systems**. Normal conducting electromagnets and RF systems are usually equipped with water cooling systems, providing heat removal during operation. On the other hand, specific cooling systems based on liquid helium are employed for superconducting magnets and RF structures.
- **Diagnostics systems**. A huge variety of diagnostic tools are employed to monitor the properties of particle beams along the accelerator, such as the beam size (scintillating or OTR screens, wire scanners), beam position inside the vacuum pipe (stripline or cavity beam position monitors), or the beam current (current transformers, Faraday cups).

A schematic representation of a particle accelerator, with mentioned components, is depicted in Fig.1.1.

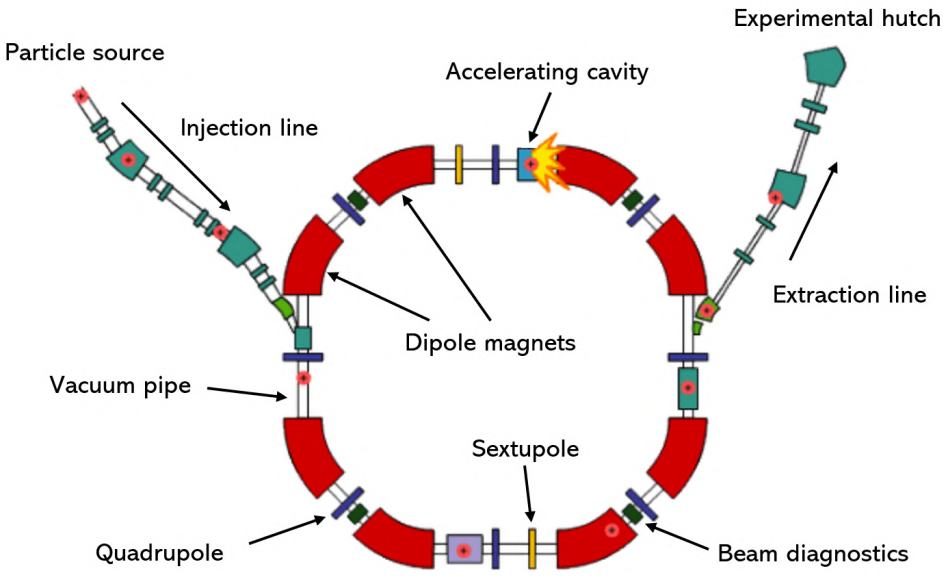

Figure 1.1. Schematic representation of a synchrotron, i.e. a type of circular particle accelerator [74].

1.1.1 Particle sources

According to the specific particle beam, a variety of particle sources are commonly used in particle accelerators. Regarding electron beams, particle sources are divided into two main categories:

- **Thermionic sources**, based on the thermionic effect, are constituted by metal filaments which are heated to few thousands degrees to provide the required kinetic energy to atomic electrons to escape the metal. Usually, a high voltage is applied to facilitate the extraction of electrons and provide an initial acceleration.
- **Photoemission sources**, based on the photoelectric effect, are constituted by a negatively charged electrode, coated with a photosensitive compound. Semiconductors are generally used for such sources, due to their high quantum efficiency, i.e. the ratio between emitted electrons and incident photons. The photocatode is struck by short laser pulses with μm spot size, which induce the emission of electron bunches from a small area of the target within a short time interval. Hence, photoemission sources are able to produce high brightness electron beams, characterized by high peak current, small transverse size and low energy spread, and are commonly used in free electron lasers and for ultrafast electron diffraction.

Furthermore, both types of electron sources can be coupled to an RF cavity, which accelerates the extracted electrons up to the MeV range. The so-called RF

guns allow to mitigate the space charge effect at low energy, thus delivering high peak current beams to the accelerating sections.

1.1.2 Accelerating RF structures

RF structures consist of cylindrical metallic cavities, usually made in copper, which sustain and confine RF accelerating electromagnetic fields. RF cavities are designed such that confined EM waves are characterized by a specific spatial configuration (resonant modes), in particular with a longitudinal component of the electric field. When charged particles travel through an RF cavity, they get accelerated by the Coulomb force associated with the electric field, thus resulting in an increase of their kinetic energy at expenses of the electromagnetic stored energy.

RF waves are produced by high power microwaves generators, called klystrons, and delivered to RF structures by means of waveguides, coaxial cables and couplers.

According to the dynamics of the RF waves, RF structures are subdivided in:

- **Standing Wave (SW) cavities**, in which EM waves oscillate in time without spatial propagation. Such structures are usually composed by multiple cells in π mode operation, meaning that the EM fields in adjacent cells are in phase opposition, such that particle bunches traveling along the cells always experience an accelerating field. Standing wave structures are used for any kind of particle (electrons, protons, ions) but can only work with bunched particle beams.

- **Traveling Wave (TW) cavities**, in which accelerating EM waves co-propagate with the particle beam, with a phase velocity equal to the beam velocity. According to the dispersion curve, the phase velocity of a RF wave, propagating through a cylindrical cavity with constant cross section, is larger than the speed of light c, therefore it cannot be synchronous with a particle beam, having a propagation velocity lower than c. In such case, beam particles would slip along the waveform of the RF wave until they experience a decelerating field, preventing a correct acceleration. To solve this issue, TW structures are designed with a series of metal irises, which allow to reduce the phase velocity to c or below. TW structures are generally used with electrons and positrons, which become ultra-relativistic at low energies (few MeV) and propagate at constant velocity $v \approx c$, allowing an easy synchronization between EM waves and beams. In principle, TW structures could be used also for protons and ions, which are not relativistic below GeV range and so they increase the propagation velocity along the accelerating structure, however the realization of TW cavities with varying phase velocity would be more complex.

Standing wave cavities are characterized by high energy transfer efficiency and compactness and can be used in superconducting structures, however they operate at low frequency (200-800 MHz) and require fine tuning of the structure, leading to high design complexity. Conversely, traveling wave cavities are characterized by lower energy transfer efficiency and longer structures, but operate at higher frequency (>3 GHz) and are easier to design and fabricate. Therefore, SW structures are usually used for proton and ion beams, where efficiency and compactness are required,

whereas TW structures are preferred for electron linear accelerators (linacs) and applications requiring high accelerating gradients at high frequencies, such as medical and research electron linacs.

1.1.3 Magnets

Relying on Lorentz force $\vec{F} = q(\vec{v} \times \vec{B})$, magnets are used to bend and guide particle beams along the designed reference trajectory of a given accelerating machine. Normal conducting electromagnets are made of copper coils wrapped around the poles of iron yokes, generating fields of up to 2 T. Furthermore, superconducting magnets based on NbTi are used for high energy beams, providing maximum fields of up to 8 T. Depending on the magnetic field geometry, different magnets provide different features for the transport of particle beams.

Dipoles

Dipole magnets, characterized by a constant vertical field, apply a transverse force to charged particle beams, bending their trajectory along the accelerating machine (Fig.1.2).

Figure 1.2. (Left) Schematic representation of the magnetic field map in a dipole magnet [93]. (Right) Dipole magnets at SESAME facility [1].

Quadrupoles

Due to electrostatic repulsion between particles of the same beam (so-called space charge force) and intrinsic divergence of the beam due to its initial transverse thermal distribution, particle beams tend to diverge while propagating through the accelerator. For this reason, quadrupole magnets and solenoids are used to focus particle beams, providing a transverse force that focus charged particle beams along the reference trajectory in the center of the vacuum pipe (Fig.1.3).

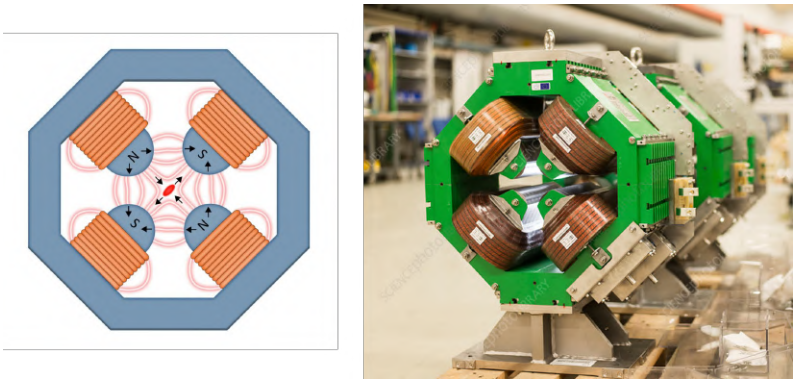

Figure 1.3. (Left) Schematic representation of the magnetic field map in a quadrupole magnet [93]. (Right) Quadrupole magnets at SESAME facility [1].

Sextupoles

When particles with different energies go through a quadrupole, they are focused in different positions. Such phenomenon, analogous to what happens to white light focused by a lens, is the chromatic aberration and it is generally mitigated by higher order magnets, such as sextupoles (Fig.1.4).

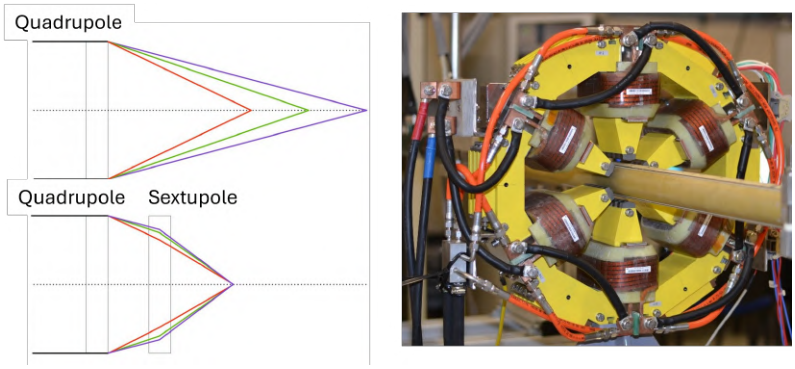

Figure 1.4. (Left) Schematic representation of the chromatic aberration downstream a quadrupole and its mitigation with a sextupole [93]. (Right) Sextupole magnets at SESAME facility [1].

1.1.4 Vacuum systems

In order to avoid any interaction between accelerated particle beams and the atmospheric gas, which would worsen the beam quality (increase in energy spread and divergence, beam losses) and trigger plasma arcs damaging the accelerator components (mainly RF structures), particle beams propagate inside vacuum pipes, in which vacuum levels of up to 10^{-12} mbar are established by specific vacuum pumps. Generally, primary pumps, such as scroll or roots pumps, extract atmospheric gas from the vacuum pipe reducing the pressure from 1 bar to $10^{-2} - 10^{-3}$ mbar, while secondary pumps, such as turbo-molecular pumps, ion pumps or others, provide a further decrease of the residual gas pressure to the required level.

1.2 Motivation of plasma-based accelerators

Since the first RF-based particle accelerator, invented by Ising and Wideroe in 1928 [10], progress in accelerator technology has determined an exponential increase in the highest beam energy that can be achieved. However, technological limitations in bending magnets and RF accelerating structures are leading the maximum achievable energy to saturation, as reported in the Livingston diagram in Fig. 1.5. In the meantime, novel schemes for particle acceleration, based on plasma technology, are experiencing a rapid development in recent decades, approaching the potentiality of conventional RF-based accelerators.

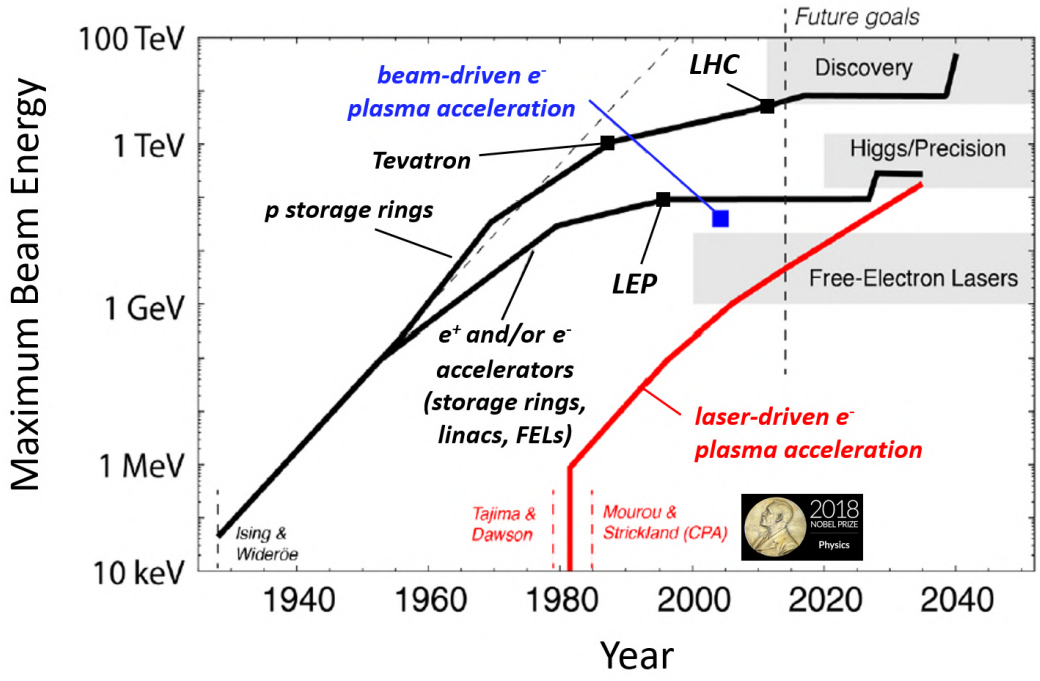

Figure 1.5. Updated Livingston plot for accelerators, showing the maximum reach in beam energy versus time. Grey bands visualize accelerator applications [10].

1.2.1 Limitations of circular accelerators

Hadron beams

Depending on the particle beam, circular accelerators are affected by different limitations. For hadrons, such as proton and ion beams, the highest achievable energy is limited by the size of the accelerator and the magnetic field provided by bending dipoles. In particular, considering the definition of magnetic rigidity, which gives the required magnetic field B to bend a particle beam with charge q and momentum p along the reference trajectory of the accelerator, with curvature radius ρ:

$$\frac{p}{q} = B\rho \tag{1.1}$$

and considering the direct proportionality between the particle energy and momentum, given by:

$$E^2 = p^2c^2 + m_0^2c^4 \tag{1.2}$$

the highest achievable beam energy that can be handled depends on the magnetic field of bending dipoles and the curvature radius, hence the size of the accelerator. Given the highest magnetic fields generated by superconducting dipoles, 8 T for NbTi magnets, used at LHC, and 16 T for Nb_3Sn magnets, currently under development for FCC project, the requirement to increase the energy of accelerated beams beyond the TeV-range can only be meet by increasing the size of the accelerator. For instance, FCC project is studying the construction of a 100 km long proton-antiproton collider with maximum energy of around 100 TeV [72]. Therefore, due to technological limits in magnet dipoles, the cost and the footprint of such accelerator machines is destined to increase.

Lepton beams

Regarding leptons, such as electrons and positrons, the accelerating energy is not limited by magnetic dipoles, since the magnetic rigidity is much lower and a magnetic field of few mT is needed to bend a lepton beam along circular machines. However, lepton circular colliders are affected by another limitation, which is the synchrotron radiation. When relativistic charged particles travel along curved trajectories, they emit electromagnetic radiation in a forward cone, tangential to the particle trajectory, as shown in Fig. 1.6.

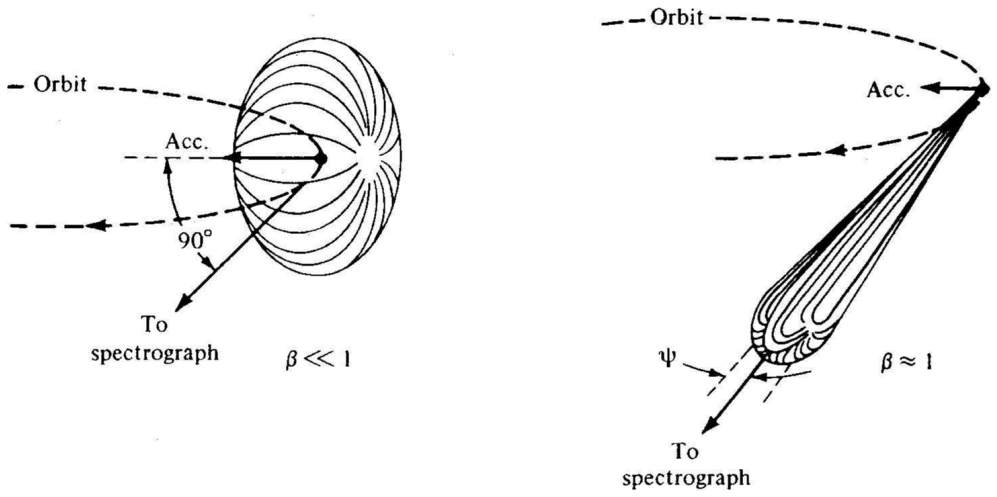

Figure 1.6. Qualitative radiation patterns related to charged particles moving in a circular orbit. The dipole pattern achieved for slow particles (left) ($\beta = v/c << 1$) is distorted into a narrow cone when $\beta \approx 1$ (right) [13].

Such radiation emission results in an energy loss per turn given by:

$$U_0 = \frac{e^2 \beta^4 \gamma^4}{3\epsilon_0 \rho} \tag{1.3}$$

in which $\beta = v/c$ and $\gamma = E/E_0$ are the relativistic velocity and mass Lorentz factors, ϵ_0 is the vacuum permettivity and ρ is the curvature radius of the accelerator. Therefore, the amount of energy emitted by a particle beam per turn increases with the fourth power of the nominal beam energy, related to the Lorentz factor γ. Generally, in circular accelerators, such energy loss is compensated by RF structures, which provide the same amount of energy back to the beam. However, if we consider to increase the beam energy, the energy loss due to synchrotron radiation becomes comparable to the nominal beam energy itself, meaning that the beam loses almost all the energy provided by RF structures. For instance, considering the FCC concept for a 100 km long electron-positron collider, with around 100 GeV maximum energy, so with curvature radius and Lorentz mass factor of 16 km and 2×10^5 respectively, the energy loss per turn would be ≈ 1 GeV. However, in a hypothetical upgrade to 1 TeV, the energy loss per turn would be of ≈ 10 TeV, such that the beams emits through synchrotron radiation all the energy provided by the RF accelerating sections. In conclusion, circular accelerators for leptons do not seem feasible for high energy physics experiments beyond the TeV range.

1.2.2 Limitations of conventional linear accelerators

In order to overcome mentioned limitations of circular machines, linear accelerators (linacs) are coming back into fashion for the next-generation particle colliders. Unlike in circular accelerators, in which particle beams are forced to travel through the same RF sections by means of the bending dipoles, inside linacs particle beams pass through RF structures only once. Therefore, in order to enhance the energy gain E of a particle beam, keeping a reasonable length L of the overall machine, it is necessary to improve the accelerating gradient G of RF structures:

$$E[MeV] = G[MeV/m] \cdot L[m] \tag{1.4}$$

According to the frequency band, typical RF structures are characterized by maximum accelerating fields reported in Tab. 1.1:

Band designation	Frequency	Maximum accelerating field
L-band	1-2 GHz	10 MV/m
S-band	2-4 GHz	20 MV/m
C-band	4-8 GHz	60 MV/m
X-band	8-12 GHz	120 MV/m

Table 1.1. Frequency bands and corresponding maximum accelerating fields.

In particular, recent progress has been achieved in the development of X-band structures with accelerating field of up to 120 MV/m [8], within the framework of CLIC project [79]. Such results have been reached through a wider understanding in the phenomenology of breakdown discharges, which represent the main limitation

in the accelerating field of RF structures. RF breakdown events take place from fractures on the surface of RF structures, caused by electrostatic tensile stress. Neutral molecules in the fractured region are ionized by the strong electric field, resulting in the formation of plasma arcs over the molten area, which in turn causes an intense ion bombardment onto the cavity surface. Plasma discharges cause a significant alteration on the RF structure shape, with crater formations and vacuum breakdown, thus limiting the maximum operating field.

As shown by scaling laws recovered from experimental data [65], the accelerating gradient of an RF structure scales with the breakdown rate (BDR) and the RF pulse length t_p:

$$\frac{G^{30} \cdot t_p^5}{BDR} = const \tag{1.5}$$

Therefore, in order to maximize the achievable accelerating field while limiting the breakdown rate, it is necessary to reduce the RF pulse length, which in turn is limited by the RF peak power. One possibility to reduce the peak power is to decrease the pulse energy required for the same E-field in the structure, by adopting structures operating at higher RF frequency, characterized by a reduced volume to fill with energy. In this way, the stored energy scales with RF frequency as f^{-3}, leading to a considerable reduction of the required input peak power [50].

The design of smaller structures with higher working frequency has led to the achievement of the highest accelerating gradients in RF structures, as for the 300 MeV/m gradient achieved at the Stanford Linear Accelerator Center (SLAC) with a 140 GHz RF structure [41], reported in Fig. 1.7.

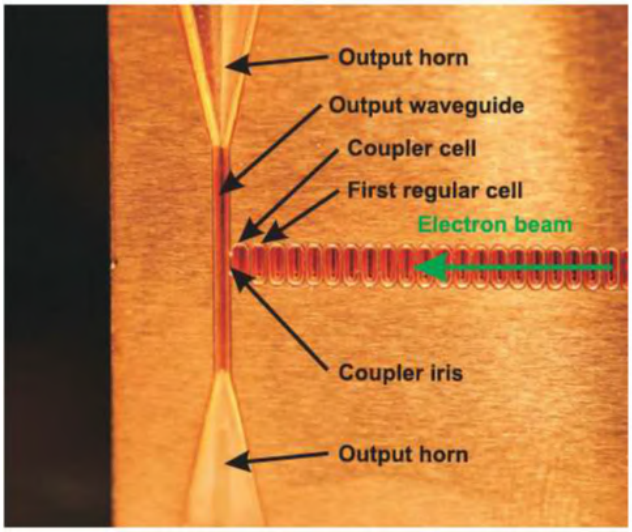

Figure 1.7. mm-range traveling wave accelerating structure with detail of the output part, including coupler and output waveguides [41].

Moreover, a further improvement in high gradient RF copper cavities has been obtained by cooling them to temperatures below 77 K, which results in the reduction of the RF surface resistance, crystal mobility and coefficient of thermal expansion and the increase of the hardness and thermal conductivity, allowing a reduction in

the breakdown rate. Indeed, recent studies show that an X-band structure can be conditioned up to an accelerating gradient of 250 MV/m at 45 K and a breakdown rate of $2{\cdot}10^{-4}$/pulse/m.

On the other hand, such smaller structures are limited by fabrication tolerances and beam instabilities due to wakefields, which are inversely proportional to the third power of the structure aperture and cause energy spread, off-axis deflection and eventually beam losses. Therefore, despite the outstanding upgrades achieved by high gradient RF structures, it is unlike to expect high frequency metallic structures achieving gradients in the range of GV/m [50].

In order to overcome limitations of RF-based accelerators, novel particle acceleration mechanisms, based on plasma technology, are driving interest in the scientific community. In such innovative particle accelerators, metallic structures are replaced by an ionized gas, or plasma, thus solving the breakdown issue of RF structures. Before going into detail of plasma acceleration, a brief overview of plasma physics is provided.

1.3 Principles of plasma physics

1.3.1 Introduction

Generally, a plasma is defined as a quasi-neutral gas of charged and neutral particles, which exhibit collective behavior [29]. Quasi-neutrality consists in the local equilibrium between negative and positive charges, established by Coulomb interaction, which translates into a local balance between plasma electrons and ions:

$$\rho_e = \rho_i, \quad n_e = Z_i n_i \tag{1.6}$$

with ρ and n representing charge and particle densities. The collective behaviour shown by plasma particles is due to the long-range Coulomb interaction, affecting the dynamics of the entire plasma. Indeed, if a local charge separation takes place due to thermal excitation or external perturbations, the charge imbalance generates an electrostatic field, acting to restore the initial neutrality according to Gauss Law:

$$\nabla \cdot \vec{E} = \frac{\rho}{\epsilon_0}, \quad with \quad \rho = e(Zn_i - n_e) \tag{1.7}$$

Likewise, electrical currents established by moving charged particles, having velocities v_i and v_e, result in a magnetic field, according to Ampere Law:

$$\nabla \times \vec{B} = \mu_0 \vec{J}, \quad with \quad J = e(Zn_i v_i - n_e v_e) \tag{1.8}$$

Generated electric and magnetic fields govern the dynamics of the plasma, including its response to external fields, applied through particle or laser beams, like in the case of plasma-based acceleration schemes [58].

1.3.2 Debye shielding

Considering to insert two charged spheres into a plasma, the electrons and ions will rearrange their distribution by moving towards the spheres with opposite charge, as shown in Fig. 1.8.

The time response of plasma electrons and ions is related to their average thermal velocity $\overline{v_{Te}}$ and $\overline{v_{Ti}}$. By definition, considering ions and electrons with same temperature ($T_i = T_e$):

$$\frac{1}{2} m_e \overline{v_{Te}}^2 = \frac{1}{2} m_i \overline{v_{Ti}}^2 = \frac{3}{2} k_B T_e \tag{1.9}$$

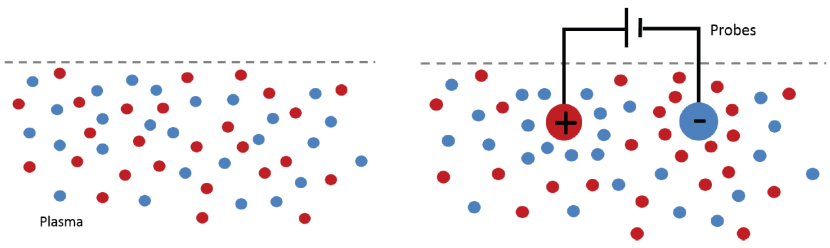

Figure 1.8. Debye shielding of charged spheres in a plasma [58].

and considering a hydrogen plasma ($Z_i = 1$), the ratio between the thermal velocities is:

$$\frac{\overline{v_{Ti}}}{\overline{v_{Te}}} = \sqrt{\frac{m_e}{m_i}} \approx \frac{1}{43} \tag{1.10}$$

Therefore, ions are much slower than electrons and can be considered almost unmovable in the electron motion time scale:

$$n_i = n_0 \tag{1.11}$$

where n_0 is the unperturbed particle density. On the other hand, considering a plasma in thermal equilibrium, electrons follow a Boltzmann distribution:

$$n_e = n_0 e^{e\phi/k_B T_e} \tag{1.12}$$

where ϕ is the electrostatic potential of the external perturbation and k_B is the Boltzmann constant.

By inserting ion and electron densities into Poisson equation, we have:

$$\nabla^2\phi = -\frac{\rho}{\epsilon_0} = -\frac{e}{\epsilon_0}(n_i - n_e) = -\frac{e}{\epsilon_0} n_0 (1 - e^{e\phi/k_B T_e}) \tag{1.13}$$

In the region where $|e\phi/k_B T_e| << 1$, i.e. the potential energy of the external perturbation is much smaller than plasma thermal energy, it is possible to expand the exponential term in the Taylor series:

$$e^{e\phi/k_B T_e} = 1 + \frac{e\phi}{k_B T_e} + \frac{1}{2}\left(\frac{e\phi}{k_B T_e}\right)^2 + \quad ... \tag{1.14}$$

Such approximation is not suitable for the region near the external charged spheres, where $|e\phi/k_B T_e|$ may be large. However, this region does not contribute much to the thickness of the electron and ion sheaths surrounding the charged spheres, because the potential falls very rapidly there [29]. By truncating the Taylor series to the linear term, Poisson equation simplifies to:

$$\nabla^2\phi = \frac{e^2 n_0}{\epsilon_0 k_B T_e}\phi \tag{1.15}$$

As a result, the electrostatic potential of the external perturbation, expressed in spherical coordinates, is:

$$\phi(r) = \frac{1}{4\pi\epsilon_0}\frac{e^{-r/\lambda_D}}{r} \tag{1.16}$$

Comparing ϕ to the 1/r-dependent Coulomb potential of a charged sphere in vacuum, the exponential term describes the damping effect caused by the rearrangement of plasma electrons, which screen off the external perturbation [29]. Such effect is called Debye screening and its characteristic length, the Debye length λ_D, represents the distance over which the external perturbation is shielded by the plasma:

$$\lambda_D = \sqrt{\frac{\epsilon_0 k_B T_e}{e^2 n_e}} \tag{1.17}$$

A general condition that characterizes plasmas is that the Debye length λ_D is much smaller than the dimension of the system L, $\lambda_D << L$, such that whenever local concentrations of charge arise or external potentials are introduced into the system, they are shielded out in a distance short compared with L, leaving the bulk of the plasma free of large electric potentials or fields [29].

Plasmas are characterized by a large amount of charged particles per Debye sphere N_D, such that their collective motion is able to screen off external perturbations and establish quasi-neutrality [59]:

$$N_D \equiv n_e \frac{4}{3}\pi\lambda_D^3 >> 1 \tag{1.18}$$

Alternatively, such ideal behaviour of plasmas is expressed by the so-called *plasma parameter* [29]:

$$g \equiv \frac{1}{n_e\lambda_D^3} << 1 \tag{1.19}$$

Furthermore, the *plasma parameter* describes the relation between long-range collective effects and short-range collisions between charged particles, as described in the following.

1.3.3 Plasma oscillations

To evaluate further the response of the plasma to external perturbations, we consider a quasi-neutral plasma slab in which an electron layer is displaced from its initial position by a distance x. Such displacement results in a charge separation between ions and electrons, which in turn determines the onset of an electric field, analogous to that between two capacitor plates with surface charge $\sigma = \pm en_e x$ [58]:

$$E = \frac{\sigma}{\epsilon_0} = \frac{en_e x}{\epsilon_0} \tag{1.20}$$

Thus, according to Newton Law for plasma electrons:

$$m_e \frac{d^2x}{dt^2} = -eE = -e^2\frac{n_e x}{\epsilon_0} \tag{1.21}$$

$$\frac{d^2x}{dt^2} + \omega_{pe}^2 x = 0 \tag{1.22}$$

in which ω_{pe} is the electron plasma frequency, defined as:

$$\omega_{pe} = \sqrt{\frac{e^2 n_e}{m_e\epsilon_0}} \tag{1.23}$$

Therefore, the electric field produced by the charge separation, generates a restoring force that guides electrons towards their initial positions, setting up plasma oscillations with frequency ω_{pe}. Such oscillations result in electron plasma waves, propagating with phase velocity v_p and characterized by a plasma wavelength given by:

$$\lambda_p = \frac{2\pi v_p}{\omega_p} \tag{1.24}$$

The characteristic time of such plasma oscillations (and in general for long-range collective effects in plasmas) can be considered as the inverse of the plasma frequency, hence it scales as:

$$t_p \propto \frac{m_e^{1/2}}{e n_e^{1/2}} \tag{1.25}$$

The same behaviour concerns plasma ions on a longer time scale, and an analogous ion plasma frequency ω_{pi} can be defined.

In case of a laser pulse or a particle bunch entering a plasma, the plasma response depends on the frequencies of the plasma and the external electromagnetic wave:

$$\frac{\omega_p^2}{\omega^2} = \frac{e^2 n_e}{m_e \epsilon_0} \cdot \frac{\lambda^2}{4\pi^2 c^2} \tag{1.26}$$

The condition $\omega_p^2 = \omega^2$ determines the so-called *critical density*, defined as [58]:

$$n_{cr} = \frac{4\pi^2 \epsilon_0 m_e c^2}{e^2 \lambda^2} \simeq 10^{21} \lambda^{-2} cm^{-3} \tag{1.27}$$

in which λ is the wavelength of the external EM wave, expressed in μm. Therefore, given the external EM wave of a laser pulse, if the plasma density is lower than the critical density, i.e. the external EM wave frequency is higher than the plasma frequency, plasma electrons do not rearrange in time to screen off the external radiation, which propagates through the so-called *under-dense plasma*. Vice versa, if the plasma frequency is higher than the laser pulse frequency, plasma electrons shield the external field and the laser pulse is reflected back. In this case the plasma is *over-dense*.

For typical Ti:Sapphire or Nd:YAG lasers, having 800 nm and 1 μm wavelength respectively, the critical density is around $n_{cr} \simeq 10^{21}$ cm^{-3}, therefore a plasma produced by the ionization of a gas column at atmospheric pressure (around 1 bar), having density of $10^{18} - 10^{19}$ cm^{-3}, will result as an under-dense plasma, allowing the propagation of laser pulses in such wavelength range. In this case, the laser pulse propagates with group and phase velocities depending on the plasma refractive index η [58]:

$$v_\phi \simeq \frac{\omega_L}{k_L} = \frac{c}{\eta} \qquad v_g \simeq \frac{\partial \omega_L}{\partial k_L} = c\eta \qquad \eta = \sqrt{1 - \frac{\omega_p^2}{\omega_L^2}} \tag{1.28}$$

with k_L the laser wavenumber, defined as $k_L = 2\pi/\lambda_L$. The electron plasma wave, excited by the laser pulse, propagates at a phase velocity corresponding to the laser group velocity.

When a laser pulse or an electron bunch propagates through an under-dense plasma, the plasma collective behaviour manifests if $\omega_p \tau_p \geq 1$, with τ_p the duration of the laser pulse or particle bunch. For instance, given a pulse duration of 200 fs, a plasma frequency of $\omega_p = 5$ THz, corresponding to a plasma density of $n_e \sim 10^{16}$ cm^{-3}, is required for an appropriate plasma response to the external perturbation.

This condition is crucial to have a significant plasma response in the laser-plasma or beam-plasma interaction timescale, which is required in many applications, such as short-wavelength radiation, nonlinear refractive properties and plasma acceleration [58].

1.3.4 Collisions in plasmas

Binary collisions in plasmas are divided into Coulomb collisions between charged particles and collisions between charged particles and neutral atoms. In the first case, considering an electron traveling in the vicinity of a positive ion, the long-range Coulomb field generated by the ion determines a deflection of the electron trajectory. The cumulative effect of multiple collisions with ions determine an average variation in the electron velocity given by [59]:

$$\frac{d\left\langle \Delta v_{||} \right\rangle}{dt} = -\nu_{ei} v \tag{1.29}$$

in which $v_{||}$ is the component of the electron velocity in the initial propagation direction and ν_{ei} is the electron-ion collision rate (or frequency), defined as [59]:

$$\nu_{ei} = \frac{n_i Z^2 e^4 ln\lambda_{ei}}{4\pi\epsilon_0^2 m_e^2 v^3} \tag{1.30}$$

where n_i and Z are the ion density and charge, m_e and v are the electron mass and velocity and $ln\lambda_{ei}$ is the Coulomb logarithm, a slowly varying term, usually in the range of 5-20, given by [68]:

$$\ln \lambda_{ei} = \ln \left[\frac{3}{2\sqrt{2\pi}} \frac{(4\pi\epsilon_0)^{3/2} (k_B T_e)^{3/2}}{e^3 n_e^{1/2}} \right] \tag{1.31}$$

The electron-ion collision frequency scales inversely with the cubic electron velocity and, considering that in thermal equilibrium plasma electrons follow a Maxwellian distribution , the average collision frequency between electrons and ions can be derived as [59, 68]:

$$< \nu_{ei} >= \frac{4}{3} \sqrt{\frac{2\pi}{m_e}} \frac{e^4 n_e \ln \lambda_{ei}}{(4\pi\epsilon_0)^2 (k_B T_e)^{3/2}} \tag{1.32}$$

Electron-ion collisions play a key role in presence of an external electric field. When an electric field E is applied to a fully ionized plasma, electrons and ions are accelerated in opposite directions and the increasing relative motion between them produces an increasing electrical current j in the direction of E (mainly due to electron motion, due to higher inertia of ions) [59]. However, Coulomb collisions between electrons and ions impede this relative motion, and after a few electron-ion collision times, a steady state equilibrium is reached, with a relation between the electric field and the current density given by:

$$\vec{E} = \rho_{ei} \vec{j} \tag{1.33}$$

in which the proportionality constant ρ_{ei} is introduced as the plasma resistivity. By means of the equation of motion for electrons, it is possible to directly relate the

plasma resistivity to electron-ion collisions. Indeed, for a uniform plasma, with no pressure gradients and external magnetic fields [59]:

$$m_e n_e \frac{d\vec{u_e}}{dt} = -e n_e \vec{E} + \vec{R_{ei}} \tag{1.34}$$

where m_e, n_e and u_e are the electron mass, density and fluid velocity and $\vec{R_{ei}}$ is the momentum variation of electrons due to collisions with ions, defined as:

$$\vec{R_{ei}} = -m_e n_e < \nu_{ei} > (\vec{u_e} - \vec{u_i}) \tag{1.35}$$

with $< \nu_{ei} >$ the average electron-ion collision frequency and $\vec{u_i}$ the ion fluid velocity. In steady state ($d\vec{u_e}/dt = 0$), combining Eq.1.34, Eq.1.33 and Eq.1.35 and expressing the current density as $\vec{j} = -e n_e(\vec{u_e} - \vec{u_i})$, the plasma resistivity results to be:

$$\rho_{ei} = \frac{m_e}{n_e e^2} < \nu_{ei} > \tag{1.36}$$

Electron-electron collisions are characterized by a repulsive Coulomb force, but with same magnitude compared to electron-ion collisions. Therefore, to within factors of order unity, the related collision frequency is given by [59]:

$$\nu_{ee} \approx \frac{\nu_{ei}}{n_i Z^2 / n_e} \tag{1.37}$$

and in a hydrogen plasma (Z = l) we have $\nu_{ee} \approx \nu_{ei}$, meaning that electrons collide with other electrons as frequently as they collide with ions.

Moreover ion-ion collisions are characterized by a similar frequency as in Eq.1.32, but with a dependence on the ion mass m_i, charge Z and temperature T_i. Thus, for a hydrogen plasma (Z=1) in local thermal equilibrium (with $T_i \sim T_e$) [59]:

$$\nu_{ei}/\nu_{ii} \sim \sqrt{m_i/m_e} \simeq 43 \tag{1.38}$$

As a result, electrons scatter about 43 times faster than ions in a hydrogen plasma.

Electron collisions with neutral atoms are generally the predominant mechanism in weakly ionized plasmas, in which the electron and ion density is many orders of magnitude lower than the density of neutral atoms. According to kinetic theory, the mean free path for electrons in partially ionized plasmas, i.e. the distance traveled by electrons between two subsequent collisions with atoms, can be expressed as [87]:

$$\lambda_{mfp} = \frac{k_B T_e}{\pi r_0^2 p} \tag{1.39}$$

in which T_e is the electron temperature, p the neutral gas pressure and r_0 the Bohr radius. The mean time between collisions can be considered as:

$$\tau = \lambda_{mfp}/v_e \tag{1.40}$$

with v_e the electron velocity, and the electron-atom collision frequency is then:

$$\nu_{ea} = \tau^{-1} = v_e/\lambda_{mfp} = v_e \frac{\pi r_0^2 p}{k_B T_e} \tag{1.41}$$

By averaging electron velocities in a Maxwellian distribution and introducing the electron thermal velocity $v_{Te} = \sqrt{k_B T_e/m_e}$, we obtain the average electron-atom collision frequency [29, 7]:

$$< \nu_{ea} >= \frac{\pi r_0^2 p}{\sqrt{m_e k_B T_e}} \tag{1.42}$$

In case electron-ion and electron-atom collision frequencies are comparable, it is possible to define an overall plasma resistivity, including the contributions from both collisional terms [7]:

$$\rho_{tot} = \rho_{ei} + \rho_{ea} = \frac{m_e}{n_e e^2}(< \nu_{ei} > + < \nu_{ea} >) \tag{1.43}$$

In partially ionized plasmas, considering electron densities and temperatures in the range of 10^{15-19} cm^{-3} and 1-10 eV and gas pressures from tens mbar to few bars, which are typical values in the context of plasma-based acceleration, Coulomb collisions between charged particles (electrons and ions) dominate over collisions with neutral atoms [29].

From dimensional analysis, the characteristic time of short-range binary interactions, considered as the time interval between two subsequent collisions, i.e. in our case the inverse of electron-ion collision frequency, scales as:

$$t_r \propto \frac{m_e^{1/2} T_e^{3/2}}{e^4 n_e} \tag{1.44}$$

1.3.5 Plasma classification

Together with $\lambda_D << L$, another condition that an ionized gas must fulfill to be considered a plasma is that collective electrostatic effects dominate over collisions with neutral atoms. Such condition is described by the relation [29]:

$$\omega_p \tau >> 1 \tag{1.45}$$

in which ω_p is the plasma frequency and τ is the average time between subsequent collisions. If a weakly ionized gas does not fulfill Eq.1.45, its charged particles collide so frequently with neutral atoms that their motion is controlled by ordinary hydrodynamic forces rather than by electromagnetic forces [29].

By comparing the characteristic times of collective electrostatic effects and Coulomb binary interactions, it is possible to define an ideal condition for plasmas, which can be expressed in terms of the plasma parameter [53]. Indeed, by combining Eq.1.25 and Eq.1.44:

$$\frac{t_p}{t_r} = \frac{e^3 n_e^{1/2}}{T_e^{3/2}} = g \tag{1.46}$$

Therefore, if:

- $g << 1$, the plasma is in collective regime, with collective electrostatic interactions dominating over binary collisions. This is considered an ideal condition, which characterizes the majority of natural and artificial plasmas.
- $g >> 1$, the plasma is in collisional regime, in which Coulomb collisions overcome collective interactions. This regime characterizes the dynamics of non-ideal strongly coupled plasmas [53].

Moreover, a second dimensionless parameter is defined to address the quantum behaviour of plasmas:

$$\Sigma = \frac{\hbar^2}{2m_e} \frac{\sqrt{3\pi^2 n_e^{2/3}}}{T_e} = \frac{T_F}{T_e} \tag{1.47}$$

in which T_F is the Fermi temperature [76], $\hbar$ and m_e are the reduced Planck constant and the rest mass of the electron. By definition, if:

- $\Sigma << 1$, i.e. the plasma temperature is much larger than the Fermi temperature, plasma dynamics is well suited with a classical description.
- $\Sigma > 1$, a quantum approach is required.

With defined dimensionless parameters, it is possible to visualize the classification of natural and artificial plasmas in a temperature-density chart, reported in Fig. 1.9.

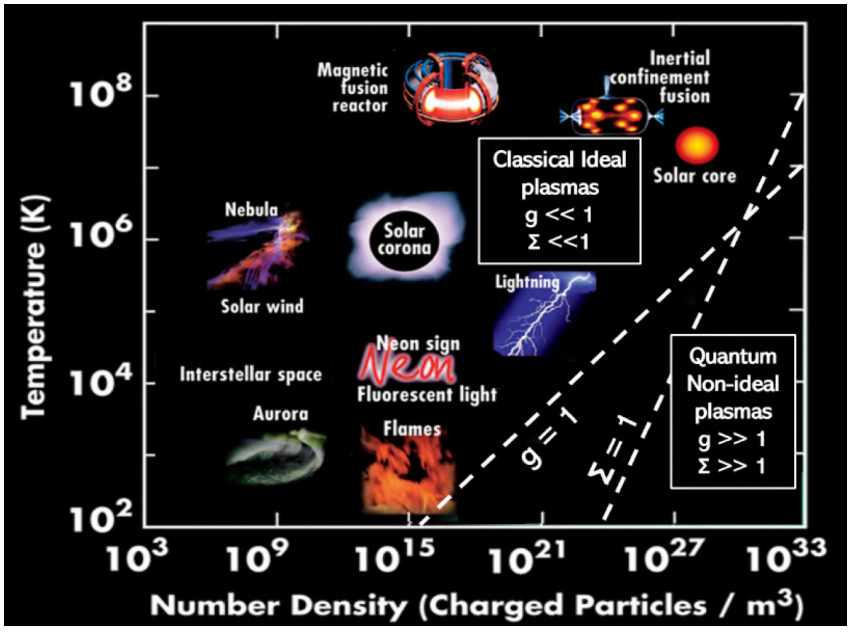

Figure 1.9. Types of plasmas and their position in the temperature-density chart [62].

In the context of plasma-based particle acceleration, as previously mentioned, typical plasmas are characterized by electron densities and temperatures in the range of 10^{15-19} cm^{-3} (10^{21-25} m^{-3}) and 1-10 eV (10^{4-5} K), hence they share the same properties with natural lightning.

1.4 Plasma-based particle acceleration

1.4.1 Introduction

The principle of plasma acceleration is based on the excitation of relativistic plasma waves inside a plasma channel, by means of a so-called **driver pulse**, which can be a high intensity laser pulse (**Laser-driven Wakefield Acceleration - LWFA**) or a high energy ultra-relativistic particle bunch (**Particle-driven Wakefield Acceleration - PWFA**). While propagating through the plasma, the driver pulse induces a strong plasma density perturbation, resulting in the excitation of rapid plasma oscillations, with frequency ω_p and wavelength λ_p (defined in 1.3), which in turn produce high GV/m longitudinal and transverse wakefields. A ultra-relativistic electron bunch, called **witness** bunch, can be externally positioned in the driver wake (or generated by the plasma itself) to take profit of such strong accelerating and focusing fields, gaining a large amount of energy within a short acceleration length (up to tens of MeV in few millimiters). As a result, the plasma acts as a medium to transfer energy from the driver to the witness pulse.

According to the properties of the driver pulse, two main acceleration regimes characterize the excitation of the plasma wakefield. For low intensity laser pulses or low density particle bunches, the plasma response to the external perturbation is linear with the intensity of the driver field. In the so-called linear regime, sinusoidal longitudinal and transverse wakefields are generated, with accelerating gradients of few GV/m. Conversely, high intensity driver pulses induce strong non-linear plasma wakefields that result in the formation of complex structures in the driver wake. This non-linear regime, also called bubble or blow-out regime, is characterized by accelerating wakefields with linear profile and peak amplitude of up to 100 GV/m. A schematic representation of the bubble regime acceleration mechanism is depicted in Fig. 1.10.

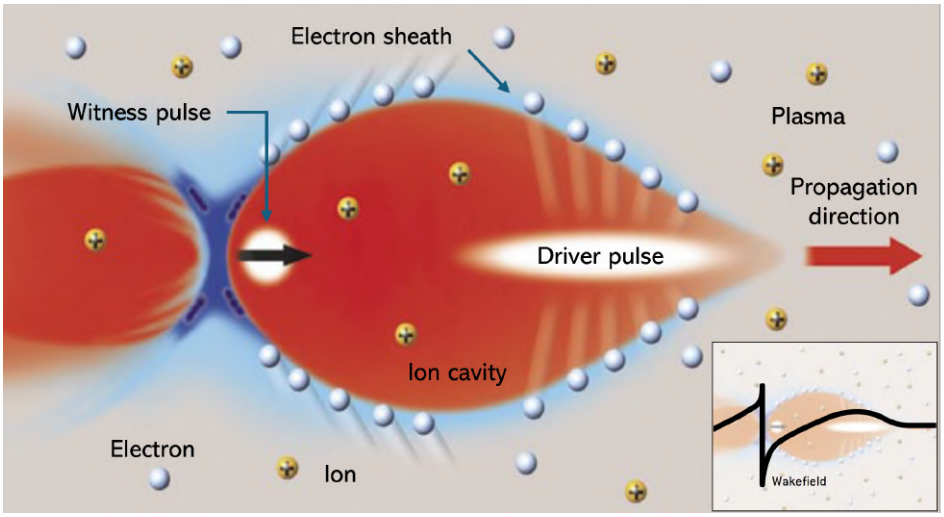

Figure 1.10. Schematic representation of the plasma acceleration mechanism in the bubble regime. In the detailed view, the waveform of the longitudinal wakefield is reported [28].

In the bubble regime, a ultra-short driver pulse propagates through the plasma channel and repels plasma electrons transversely, while leaving on its wake the plasma ions, whose motion is negligible in the timescale of the driver pulse propagation due to their inertia. Behind the driver pulse, positive ions attract plasma electrons back to their initial position, through Coulomb interaction, resulting in the onset of relativistic plasma waves, which in turn determine the formation of ion cavities, or ion bubbles, surrounded by an electron sheath. The electron sheath results from the rearrangement of plasma electrons at the surface of the positively charged ion cavity, whose electrostatic potential is screened off by the electron sheath and does not affect the bulk of the plasma far from the driver propagation axis, according to the Debye shielding mechanism described in Sec.1.3. The charge separation between the outer electron sheath and the inner ion cavity results in strong longitudinal and transverse fields, which can be exploited to accelerate and focus an externally injected witness bunch. Otherwise, if the longitudinal electric field due to the charge unbalance is strong enough (complete blow-out regime), plasma electrons can be injected inside the bubble and accelerated along the driver propagation direction, without the need of external witness beam injection.

A detailed description of the physics of LWFA and PWFA is reported in the following section.

1.4.2 The physics of LWFA and PWFA

In order to give an exhaustive description of the physics of plasma-based acceleration, first we consider the dynamics of a single plasma electron interacting with a intense laser pulse, as for the LWFA mechansim. The motion of a plasma electron is influenced by the EM wave of the laser pulse, as shown by the Lorentz equation:

$$m_e \frac{d^2 \gamma \vec{x}}{dt^2} = e(\vec{E} + \vec{v_e} \times \vec{B}) \tag{1.48}$$

First, considering a Gaussian laser beam with linear polarization, the corresponding electric field is given by:

$$\vec{E}(r, z, t) = Ecos(\omega_L t - k_L z + \phi_L) \tag{1.49}$$

in which ω_L, k_L and ϕ_L are the laser frequency, wavenumber and phase, while the electric field amplitude is given by:

$$E = \frac{E_0}{2} e^{-r^2/w(z)^2} e^{-(t-z/c)^2/\tau_0^2} \tag{1.50}$$

where w and τ_0 represent the spot size and pulse duration, and the two exponential terms describe the transverse and longitudinal envelope of the Gaussian beam. For a non-relativistic case ($v_e << c$ and $\vec{B} = \vec{E}/c$), the equation of motion simplifies to:

$$m_e \frac{d^2 \vec{x}}{dt^2} = -eEcos(\omega_L t - \vec{k_L} \cdot \vec{x} + \phi_L) \tag{1.51}$$

Now, by averaging the electron motion over an optical cycle of the laser, the equation of motion results:

$$m_e \frac{d^2 \langle \vec{x} \rangle}{dt^2} = -\nabla U_p = F_p \tag{1.52}$$

in which U_p and F_p are the ponderomotive potential and force, defined as:

$$U_p \equiv \frac{e^2 E^2}{4 m_e \omega^2} = \frac{e^2 I_0 \lambda^2}{4 m_e}, \quad F_p \equiv -\nabla U_p \propto -\nabla I_0 \tag{1.53}$$

in which I_0 is the laser pulse intensity. As a result, the ponderomotive force, related to transverse and longitudinal gradients in the laser pulse intensity, governs the second-order motion of plasma electrons and is responsible for driving plasma oscillations, as described for LWFA in bubble regime. Another important quantity for describing the electron motion is the laser pulse **normalized vector potential** a_0, defined as:

$$a_0 \equiv \frac{e A_0}{m_e c} \simeq 0.85 \sqrt{I_0 [10^{18} W/cm^2]} \cdot \lambda [\mu m] \tag{1.54}$$

In particular, a_0 provides a useful criterion to distinguish non relativistic ($v_e << c$, $a_0 << 1$) from relativistic plasma electron motion ($v_e \simeq c$, $a_0 \simeq 1$), given the properties of the laser pulse. For example, for a Ti:Sapphire laser (λ =800 μm), the relativistic condition is reached with a laser intensity of around 2×10^{18} W/cm^2.

In order to describe the excitation of relativistic plasma waves by means of the laser ponderomotive force, a fluid dynamic approach is adopted, coupling 1.52 with the continuity equation for plasma electrons and Poisson equation:

$$\frac{\partial n_e}{\partial t} + \nabla (n_e \vec{v}) = 0 \tag{1.55}$$

$$\nabla^2 \Phi = -\frac{\rho}{\epsilon_0} = e \frac{\delta n_e}{\epsilon_0} \tag{1.56}$$

in which $\delta n_e = (n_e - n_0)$ is the plasma density perturbation. As a result, the density perturbation driven by the ponderomotive force is given by [124]:

$$\left(\frac{\partial^2}{\partial t^2} + \omega_p^2 \right) \frac{\delta n_e}{n_0} = \nabla \frac{a_0^2}{2} \tag{1.57}$$

The same phenomenology concerns electron-driven PWFA, in which the space-charge electric field plays the role of the ponderomotive force. In particular, plasma wakefield excitation is described by:

$$\left(\frac{\partial^2}{\partial t^2} + \omega_p^2 \right) \frac{\delta n_e}{n_0} = -\omega_p^2 \alpha \tag{1.58}$$

in which $\alpha = n_b / n_0$ is the ratio between the driver bunch density and the unperturbed plasma density.

Depending on a_0 or α, so on the laser intensity or the electron bunch density, two different regimes characterize the plasma wave excitation, with different features for the density perturbation and electric wakefields.

Linear regime ($a_0, \alpha << 1$)

In case of small laser intensities ($a_0 << 1$), or driver bunch densities ($\alpha << 1$), and weakly perturbed plasmas ($\delta n_e << n_0$), 1.55 and 1.56 yield an analytical solution for the scalar potential:

$$\phi(r, \xi) = -f(r) sin(k_p \xi) \tag{1.59}$$

in which r and $\xi = z - v_g t$ are the radial and longitudinal coordinate in the driver frame, $k_p = 2\pi/\lambda_p$ is the plasma wavenumber, f is a form factor depending on a_0 and $\phi = \frac{e\Phi}{m_e c^2}$ is the normalized scalar potential. From the definition of scalar potential ($\vec{E} = -\nabla\Phi$) and Poisson equation, the normalized density perturbation and the transverse and longitudinal wakefields are given by:

$$\frac{\delta n_e}{n_0} = \frac{1}{k_p^2}\frac{\partial^2 \phi}{\partial \xi^2}, \qquad \frac{E_z}{E_{p,0}} = -\frac{1}{k_p}\frac{\partial \phi}{\partial \xi}, \qquad \frac{E_r}{E_{p,0}} = -\frac{1}{k_p}\frac{\partial \phi}{\partial r} \tag{1.60}$$

in which $E_{p,0}$ is the cold wave-breaking limit, defined in this section. The response of plasma quantities in this non-relativistic regime is shown in Fig. 1.11 for the plasma scalar potential, longitudinal wakefield and density perturbation, driven by a low intensity laser pulse ($a_0 = 0.4$).

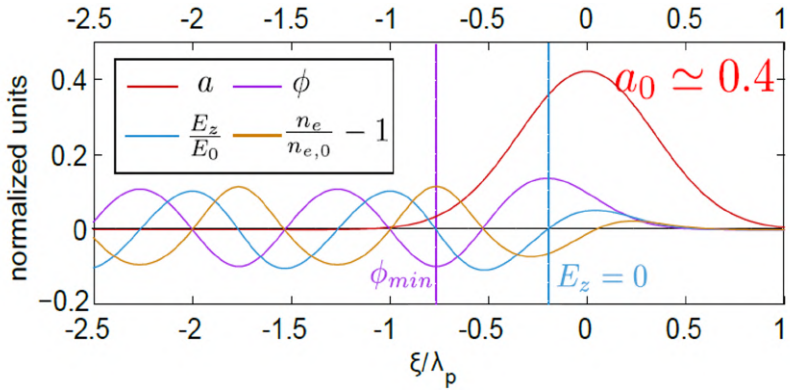

Figure 1.11. Normalized plasma potential ϕ, longitudinal electric field E_z/E_0 and density perturbation $\delta ne/n_0$ on axis (r = 0) in linear regime [128].

A particular aspect of the linear regime is the 90° phase shift between transverse and longitudinal electric fields, determining alternating phase regions of focusing/defocusing and accelerating/decelerating fields, as shown in Fig. 1.12.

Due to this, only a $\lambda_p/4$ phase region allows for an injected witness beam to be both accelerated and focused in the driver pulse wake. Furthermore, the accelerating and focusing fields in this weakly relativistic regime reach gradients of few GeV/m, and further increase is allowed with the laser intensity (or bunch density) until the relativistic regime is reached.

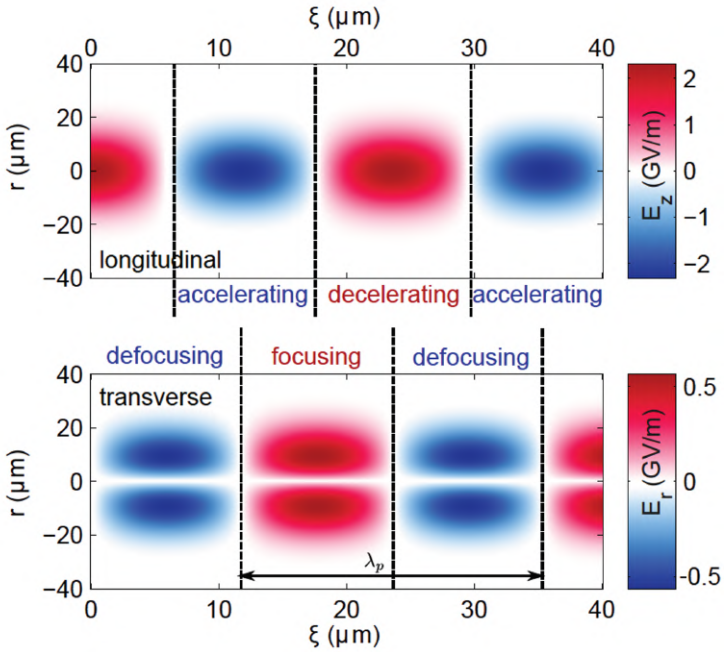

Figure 1.12. Spatial distribution of the (Top) longitudinal $E_z(r,\xi)$ and (Bottom) radial electric field $E_r(r,\xi)$ in the linear regime [128].

Bubble non-linear regime ($a_0, \alpha > 1$)

At high laser intensities ($a_0 > 1$), or driver bunch densities ($\alpha > 1$), the plasma response becomes highly non-linear and has to be treated non-perturbatively. The use of 3D particle in cell (PIC) codes and scaling laws, employed to describe the wakefield excitation driven by highly intense laser pulses, has led to the discovery of the bubble or blow-out regime. In the bubble regime, the driver ponderomotive (LWFA) or space-charge (PWFA) force repels radially plasma electrons, which are then attracted back by plasma ions and cross the driver propagation axis at a distance $\lambda_{p,rel}$, resulting in a density spike, with $\lambda_{p,rel}$ the relativistic plasma wavelength, larger than the non-relativistic one due to electron mass increase in relativistic regime. This determines the formation of a spherical ion cavity, i.e. the ion bubble, with a radius of:

$$r_b = 2\frac{\sqrt{a_0}}{k_p} \tag{1.61}$$

In the bubble regime, the normalized potential and electric fields inside the ion cavity are given by:

$$\phi = \frac{k_p^2}{4}(r^2 - r_b^2), \qquad \frac{E_z}{E_{p,0}} = \frac{k_p}{2}\xi, \qquad \frac{E_r}{E_{p,0}} = \frac{k_p}{4}r \tag{1.62}$$

in which r_b is the bubble radius. The excitation of plasma wakefields is achieved with driver pulses shorter than the plasma period, i.e. with laser pulse length $c\tau_0 \leq \lambda_p/2$ and bunch length $\sigma_z \leq \sqrt{2}/k_p$ (with transverse size $\sigma_r << \sigma_z$ for particle bunches).

For instance, the plasma response driven by a Gaussian laser pulse ($a_0 = 2.1$) is depicted in Fig. 1.13.

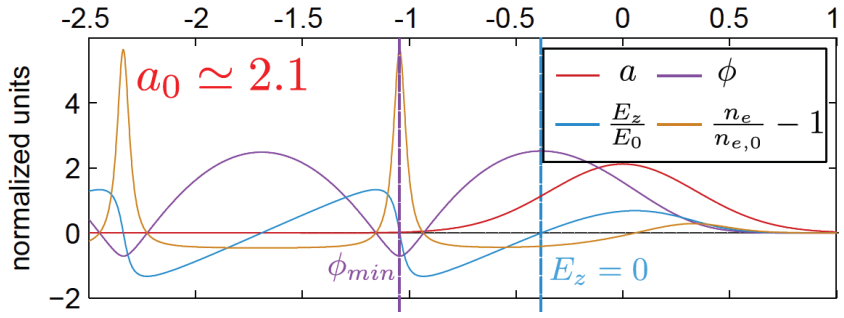

Figure 1.13. Normalized plasma potential ϕ, longitudinal electric field E_z/E_0 and density perturbation $\delta ne/ne_0$ on axis (r = 0) in non-linear regime [128].

While nearly sinusoidal in the linear case, the non-linear density distribution exhibits narrow peaks with a periodicity of $\lambda_{p,rel} > \lambda_p$, separated by low-density regions. The longitudinal electric field has a sawtooth shape and it is linear over most of the period, while the transverse field is focusing all along the period.

Considering to inject a witness electron bunch in the plasma wakefield, in the leading half of the bubble ($0 < \xi < r_b/2$) the longitudinal wakefield would be decelerating, while in the back of the bubble it would accelerate the beam. The accelerating gradient does not depend on the radial position, since the longitudinal field only depends linearly on ξ, as shown in 1.62 and the maximum gradient is reached towards the bubble exit. The transverse focusing region for electrons extends over the whole bubble, while defocusing only occurs around the on-axis density peak, and, in addition, it is an emittance-preserving force, due to the linear dependence of the transverse field on the radial offset.

At high laser intensities or driver bunch density, self-injection into the bubble occurs via transverse wave-breaking at the density spike, at the location of the highest accelerating field. Due to the large initial deflection by the ponderomotive or space-charge force, electrons forming the spike exhibit a large transverse momentum, resulting in a large transverse emittance, with strong transverse oscillations that result in the emission of radiation in the X-ray spectrum (the so-called betatron radiation), analogously to radiation emission in wigglers.

Beam matching, acceleration and extraction

The efficiency of the acceleration process is strongly determined by the plasma channel uniformity. Indeed, as shown in 1.61 and 1.62, both the bubble size and the accelerating and focusing wakefields depend on k_p, which in turn scales as $n_e^{1/2}$. This means that a non-uniformity along the plasma channel would cause the bubble to shrink or expand, thus modifying the wakefields phase regions. Therefore, if the witness bunch is reasonably injected towards the phase of the highest accelerating field, a non-uniformity in the longitudinal plasma density would lead the bunch towards phase regions where the field is zero or even decelerating. For this reason, a longitudinal plasma density plateau is required to provide stability to the overall

accelerating structure along the plasma channel.

Moreover, an optimum condition can be defined for the injection of driver and witness beams in the plasma channel, in order to keep a constant amplitude accelerating wakefield and preserve the accelerated beam quality. For laser pulses, the optimum condition to keep a constant width and intensity is achieved by matching the laser spot size, according to [128]:

$$w_b \simeq r_b = 2\sqrt{a_0}/k_p \tag{1.63}$$

For beam driven wakefields, the beam maintains a constant width, and so drives a constant amplitude wakefield, if the emittance pressure is balanced by the focusing force of the wakefield [49]. The matching condition can be obtained by solving the envelope equation:

$$\sigma_r'' + \frac{k_p^2}{2\gamma}\sigma_r = \frac{\epsilon_n^2}{\gamma^2\sigma_r^3} \tag{1.64}$$

in which σ_r is the transverse beam size, γ is the beam energy and ϵ_n is the normalized emittance. Therefore, given the plasma density, related to the plasma wavenumber k_p, and the beam energy, the matched beam size is given by:

$$\sigma_r = \sqrt{\frac{\epsilon_n}{k_\beta}} \tag{1.65}$$

in which $k_\beta = k_p\sqrt{\gamma/2}$ is the betatron wavenumber. For example, a 150 MeV electron bunch with 1 μm normalized emittance, injected in a plasma channel with around 10^{17} cm^{-3} electron density, should be focused inside the plasma with a 2-5 μm transverse size, producing tens GV/m accelerating gradient. Conventional quadrupoles are not able to fulfill such requirement, therefore it is necessary to relax the matching condition at tens of μm and operate at lower plasma density, even though the accelerating gradient is lower.

To overcome quadrupole limitations, plasma-based focusing devices, called active plasma lenses, represent a promising solution, as described in Sec.2.3.1. Furthermore, another solution can be to use a matching section consisting of a density up-ramp at the entrance of the plasma channel, so to reduce the emittance growth of initially unmatched beams and provide a focusing wakefield that progressively shrinks the beams down to the matched spot size at the beginning of the uniform plasma density plateau. In addition, this concept can be also applied at the exit of the accelerating stage, using a density down-ramp at the end of the plasma channel to catch the witness beam and preserve its emittance towards the exit, which otherwise would rapidly increase in case of free propagation in a drift space.

For these reasons, a fine tailoring of the plasma channel distribution is crucial in plasma-based acceleration, and proper plasma sources are designed and used for this purpose.

Wave-breaking

For very high intensity laser pulses ($a_0 >> 1$), the velocity of background plasma electrons can exceed the phase velocity of the plasma wave, such that electrons are

self-injected inside the accelerating bubble, leading to a breakdown of the wakefield structure, called longitudinal wave-breaking. The corresponding maximum field $E_{p,0}$ can be estimated by assuming that the perturbation involves all the electrons in the plasma wave ($\delta n_e = n_0$), oscillating at ω_p. Therefore, by solving the Gauss Law:

$$\nabla E = -\frac{e}{\epsilon_0} n_0 \tag{1.66}$$

the cold non-relativistic wave-breaking field results:

$$E_{p,0} = \frac{m_e c \omega_p}{e} \qquad E_{p,0}[GV/m] \approx 96\sqrt{n_0[10^{18} cm^{-3}]} \tag{1.67}$$

The self-injection of plasma electrons generally continues once it has started, causing a large energy spread. Therefore, for high beam quality, it is sometimes desired to avoid self-trapping by operating below the wave-breaking threshold, and relying on other injection methods. On the other hand, this approach limits the highest achievable accelerating field and, so, the maximum energy gain for a fixed acceleration length.

Methods for particle injection

Generally, in PWFA experiments, the driver and witness bunches are produced by the same particle source, thus avoiding to create the witness bunch by injecting plasma electrons into the plasma wakefield. On the other hand, in LWFA different injection methods can be adopted for controlling the injection of plasma electrons and so to improve the quality of the accelerated witness bunch, compared to self-injection occurring at the wave-breaking.

- **Injection in a density gradient**. A first method concerns the use of a downward density gradient in a region longer than the plasma wavelength. Inside the density gradient, the plasma wave slows down, reducing the threshold for self-injection and so inducing a controlled wave-breaking in a localized spacial region of the plasma [25]. This mechanism allows to reduce the energy spread of the accelerated beam. However, if the density ramp is too long, the injected beam can be affected by space charge and blow up before reaching relativistic velocities. An alternative way can be to use a sharper density ramp, shorter than the plasma wavelength, which can be obtained through the shock-front created by a knife-edge inserted in a gas jet [107].

- **Injection with colliding laser pulses**. Such method is based on the use of two counter-propagating laser pulses [48]. The first one, the pump pulse, is used to excite the plasma wakefield, while the second one, the injection pulse, is used to heat plasma electrons during the collision with the pump pulse, thus providing them the required energy to be injected in the wakefield. After the collision has occurred, injected electrons are further accelerated in the wakefield. As the overlapping of the lasers is short in time, the electrons are injected over a very short distance and can be accelerated to an almost mono-energetic beam. Moreover, it is possible to tune the energy of the accelerated beam by properly delaying the two pulses and let them collide in a different position of the plasma channel.

- **Ionization injection**. Another scheme for controlled injection includes the use of a high-Z/low-Z gas mixture, e.g. helium with small percentage of nitrogen or argon. When the driver laser pulse propagates through the mixture, the leading edge of the pulse ionizes helium atoms and outer electrons of nitrogen, creating the plasma channel, while the peak of the laser pulse ionizes electrons from the nitrogen K shell, by tunnel ionization, and injects them into the plasma wake [106]. Because of the relativistic self-focusing effect, the laser propagates over many Rayleigh lengths with peak intensity variations that can inject electrons inhomogeneously and on a long distance, thus leading to large energy spread. To improve the accelerated beam quality, ionization injection can be performed with two separate gas cells. The first cell is filled with the gas mixture, so that ionization injection is localized within the first stage and a low energy beam with good quality is created. Downstream, a second long cell is filled with low Z gas (e.g. pure helium), such that no injection takes place and the pre-injected witness bunch gets accelerated over a long distance [95].

Limitations in plasma-based particle acceleration

Regarding LWFA, the main limitations in the achievable energy gain are:

- **Laser diffraction**. As any focused laser pulse, after the beam waist the driving laser pulse tends to diffract, increasing its spot size and thus reducing its intensity. For example, a 1 J, 30 fs FWHM, 800 nm laser pulse focused to a 15 μm spot size to reach $a_0 = 2$, is characterized by a Rayleigh length $z_R = \pi w_0^2/\lambda \approx 1$ mm, i.e. the distance over which the intensity halves due to diffraction. Laser guiding methods are implemented to overcome such limitation and keep a constant radial width along the entire plasma stage, so to excite large and contant amplitude wakefields. The simplest method relies on the relativistic self-guiding, induced by the non-linear plasma refractive index, that for $a_0 << 4$ and $\omega_p << \omega_0$ is given by:

$$\eta \approx 1 - \frac{1}{2}\frac{\omega_p^2}{\omega_0^2}\left(1 + \frac{\delta n_e}{n_{e,0}} - \frac{2\delta\omega}{\omega_0} - \frac{a_0^2}{4}\right) \tag{1.68}$$

  in which ω_0 is the central laser frequency, while n_{e0} and ω_p are the plasma density and frequency. In particular, the $a_0^2/4$ term is due to the relativistic mass increase of plasma electrons in the laser field. Since a Gaussian laser pulse has an on-axis intensity peak, the plasma density and frequency are lowest on axis, leading to a maximum of the refractive index. Therefore, a radially decreasing refractive index, with a maximum on axis, provides a focusing effect to the laser pulse analogous to a lens. As a result, a perfect balance between the laser diffraction and the focusing effect of the plasma lens can be achieved for a laser pulse power above the critical power, defined as [128]:

$$P_c \approx 17\frac{\omega_0^2}{\omega_p^2} \quad GW \tag{1.69}$$

In the bubble regime, the condition for self-guiding is given by [84]:

$$a_0 = \left(\frac{n_{cr}}{n_e}\right)^{1/5} \tag{1.70}$$

in which n_{cr} is the critical frequency. If this condition is fulfilled, the laser pulse propagates with a spot size $w_0 = 2\sqrt{a_0}/k_p r$. Self-guiding has been demonstrated to occur over up to 100 Rayleigh lengths [94] However, pump depletion, taking place during the excitation of plasma wakefields, causes a reduction in the laser energy and after a while the self-guiding condition is no longer fulfilled and the laser diffraction takes place. For this reason and for achieving higher energy gain, laser guiding can be obtained by means of specific waveguides, which provide tailored radial plasma density profiles to focus laser pulses compensating diffraction, as described in Ch2.

- **Dephasing.** During acceleration, the electrons of the witness beam propagate at relativistic velocities ($v_e \approx c$), while the laser group velocity is limited by the plasma refractive index ($v_g = c\eta < c$). Due to this, the witness bunch can catch up the driver beam and dephase, entering the decelerating phase of the wake. The **dephasing length** L_d, defined as the distance travelled by the witness bunch in the lab frame before crossing the zero accelerating field, depends on the plasma wavelength. In particular, in the linear regime L_d corresponds to the distance in which a relativistic electron phase slips by $\lambda_p/4$ with respect to the laser field, exiting the phase region in which the wakefield is simultaneously accelerating and focusing:

$$L_d = \frac{\lambda_p}{2}\frac{\omega_L^2}{\omega_p^2} = \gamma_p^2\frac{\lambda_p}{2} \tag{1.71}$$

in which γ_p is the plasma Lorentz factor. In the non-linear regime, the increase in the plasma wavelength has to be taken into account, resulting in:

$$L_d = \gamma_p^2\lambda_p\frac{a_0}{\pi} \tag{1.72}$$

The dephasing length scales inversely with the electron density ($L_d \propto n_e^{-3/2}$), therefore dephasing can be mitigated by operating at lower densities, albeit at longer acceleration length.

- **Pump depletion**. During propagation, the laser energy is transferred to the plasma wake until it is depleted and acceleration ends. The characteristic length for pump depletion L_{pd} can be estimated by comparing the energy density in the wake, $u_W = \frac{1}{2}\epsilon_0 E_z^2$, contained in the volume $V = \pi w_0 L_{pd}$, and the laser energy density, $u_W = \frac{1}{2}\epsilon_0 E_0^2$, contained in the volume $V = \pi w_L c\tau_L$. The pump depletion length is given by:

$$L_{pd} = \gamma_p^2\lambda_p \times \begin{cases} \frac{1}{a_0^2}(a_0 << 1) \\ \frac{a_0}{\pi}(a_0 >> 1) \end{cases}, \tag{1.73}$$

According to laser parameters, the working point for LWFA is defined through a compromise between the mentioned limitations, aimed at achieving the maximum energy transfer from driver to witness beam.

- **Beam loading**. For highly charged witness bunches, the electric field of the plasma wake is modified by the witness Coulomb field, thus affecting the acceleration process. In a non-linear 1D description, the beam loaded wakefield is evaluated by including the witness bunch density distribution into Poisson equation:

$$\frac{\partial^2 \phi}{\partial \xi^2} = k_p^2 \left(\frac{n_e}{n_{e,0}} - 1 + \frac{n_b}{n_{e,0}} \right) \tag{1.74}$$

Fig.1.14 reports the effect of the beam loading on the plasma wakefield, in case of a driver pulse with $a_0 = 1.5$, considering a Gaussian witness bunch with different bunch densities placed at $\xi = -0.6\lambda_p$.

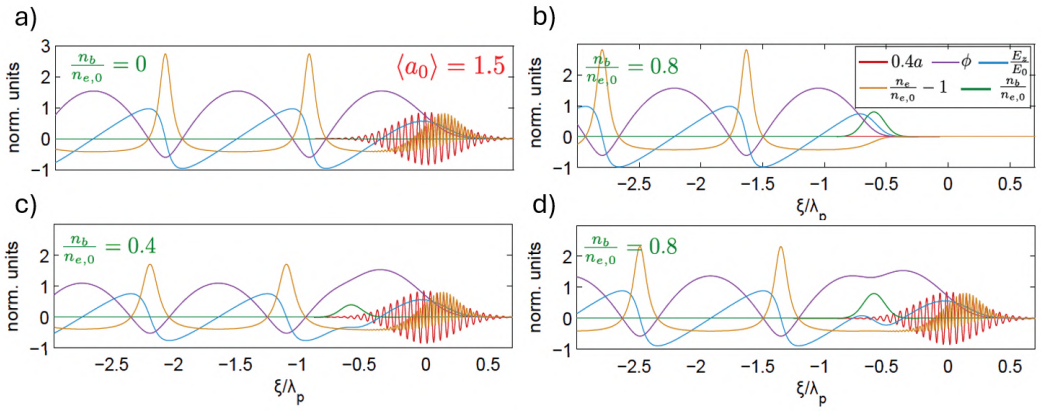

Figure 1.14. Normalized 1D wakefield quantities. (a) Plasma wakefields driven by a linearly polarized 20 fs laser pulse with peak $a_0 = 2.1$. (b) Plasma wakefields driven by a 10 fs Gaussian electron bunch with normalized density $n_b/n_{e,0} = 0.8$. (Bottom) Laser-driven plasma wakefields, beam loaded by the witness bunch at $\xi = -0.6\lambda_p$ with normalized density of 0.4 (c) and 0.8 (d). The bunch charge modifies both the potential and the longitudinal electric field and lengthens the cavity [128].

In the right condition, beam loading can provide benefit to the acceleration mechanism. For example, as shown in Fig.1.14(c) for $n_b/n_{e,0} = 0.4$, the accelerating field (blue line), normally decreasing towards smaller values of ξ, remains constant over the entire duration of the electron bunch. This means that all the bunch electrons experience the same accelerating field, thus reducing the energy spread of the accelerated bunch.

Concerning PWFA, beam loading and pump depletion affect the maximum achievable energy gain as in LWFA, but the dephasing issue is avoided, since the driver bunch propagates at relativistic velocity as well as the witness bunch.

1.4.3 LWFA overview

The first pioneering theoretical work on plasma acceleration, published by Tajima and Dawson [119] in 1979, described how an intense laser pulse can excite a wake of plasma oscillations through the non-linear ponderomotive force associated to the laser pulse. In their proposed scheme, relativistic electrons were externally injected and accelerated in the high GV/m electric field, sustained by relativistic plasma waves.

Since then, many different plasma acceleration regimes have been explored, while the laser technology was pushing towards ultra-short high power laser systems. First evidence of LWFA was obtained with the **laser beatwave** technique, in which the excitation of resonant plasma waves is driven by the beatwave of two long laser pulses of a few tens of picoseconds (i.e. with duration much higher than the plasma period). First results in the excitation of resonant plasma waves and the acceleration of electrons up to 30 MeV were obtained at UCLA [35, 36]. However, accelerated electrons were characterized by a large energy spread, with a Maxwellian energy distribution.

Thanks to the chirped pulse amplification (CPA) technique, invented by Donna Strickland and Gerard Mourou [118] in 1985, the development of powerful laser systems with short pulse duration allowed to discover more efficient acceleration regimes. The **self modulated LWFA** regime, observed with <500 fs long laser pulses, occurs when the laser pulse duration exceeds the plasma period and the laser power exceeds the critical power for self-focusing. The cumulative effects of the self-focusing and the self-modulation of the laser envelope, induced by the initial perturbation of the electron plasma density, generates a train of laser pulses, which become resonant with the plasma wave. As a result, the laser pulse gets modulated at the plasma wavelength during its propagation, as shown in Fig. 1.15 [85].

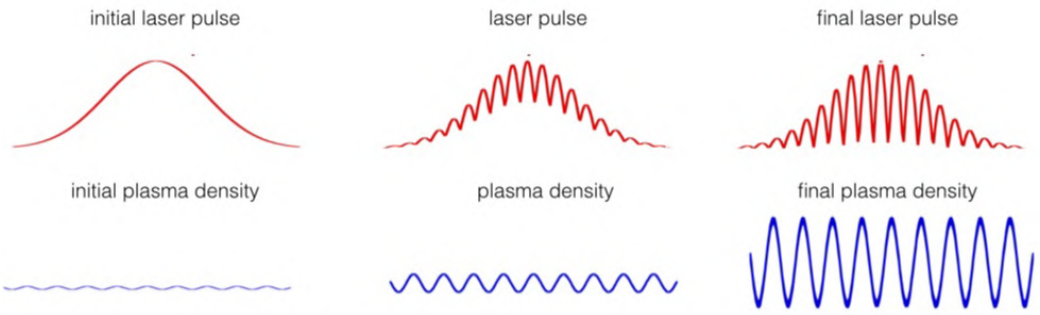

Figure 1.15. Evolution of the laser pulse and plasma density in the self-modulated laser wakefield regime.

Such resonant excitation proceeds until wave-breaking occurs, i.e. oscillating electrons of the plasma wave are self-trapped in the laser wake and get accelerated to high energies. However, because of the heating of the plasma, caused by the interaction with the long laser pulse, the wave-breaking occurs before reaching the theoretical wave-breaking limit (described in the previous Section) thus limiting the highest achievable accelerating field. The self-injection of plasma electrons allows to avoid external injection of electron beams, even though no particular improvement

is obtained concerning the beam quality.

Plasma heating issue is overcome in the **Forced LWFA** regime, achieved by using even shorter laser pusles, with time duration and beam waist approximately equal to the plasma period and wavelength. In this regime, highly non-linear plasma waves can be reached, corresponding to strong accelerating fields of around 100 GV/m. Furthermore, due to a limited interaction between the laser and the accelerated electrons, the quality of the electron beam is also improved [55].

Finally, if the laser pulse duration and spot size are shorter than the plasma wavelength, two efficient accelerating regimes characterize the LWFA mechanism, according to the laser pulse intensity. For relatively low laser intensities ($I < 10^{18}$ W/cm^2), the **linear regime** LWFA characterizes the plasma wave excitation, with sinusoidal longitudinal and transverse wakefields and accelerating gradients of few GeV/m. Conversely, for high laser intensities ($I > 10^{18}$ W/cm^2), the non-linear **bubble regime** is reached [103]. The resulting accelerated bunch is characterized by transverse and longitudinal size smaller than the laser pulse and a quasi-monoenergetic distribution.

Remarkable results of high quality acceleration of monoenergetic electron beams have been obtained at the Berkeley Lab Laser Accelerator (BELLA) [61]. A 20 cm-long discharge capillary was adopted to create plasma channels, heated by laser pulses to generate parabolic radial density profiles, enabling the guiding of petawatt laser pulses at low density ($\approx 3 \times 10^{17}$ cm^{-3}) over ≈ 15 Rayleigh lengths. Laser pulses with peak power up to 850 TW were guided over 20 cm, resulting in the generation of electron beams with hundreds of pC charge and multiple quasimonoenergetic peaks, the highest of which was at 7.8 GeV.

A scheme of BELLA experimental layout is depicted in Fig.1.16, while measured energy and angular spectra of accelerated electron bunches are reported in Fig.1.17.

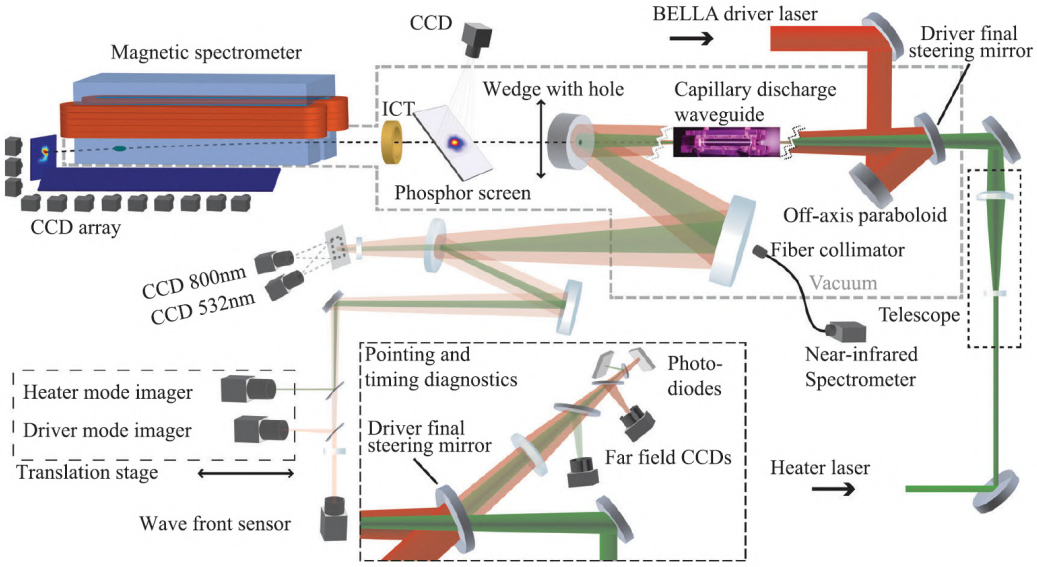

Figure 1.16. BELLA Laser Plasma Accelerator layout, including the main laser and heater laser beamlines, the discharge capillary and the diagnostics setup.

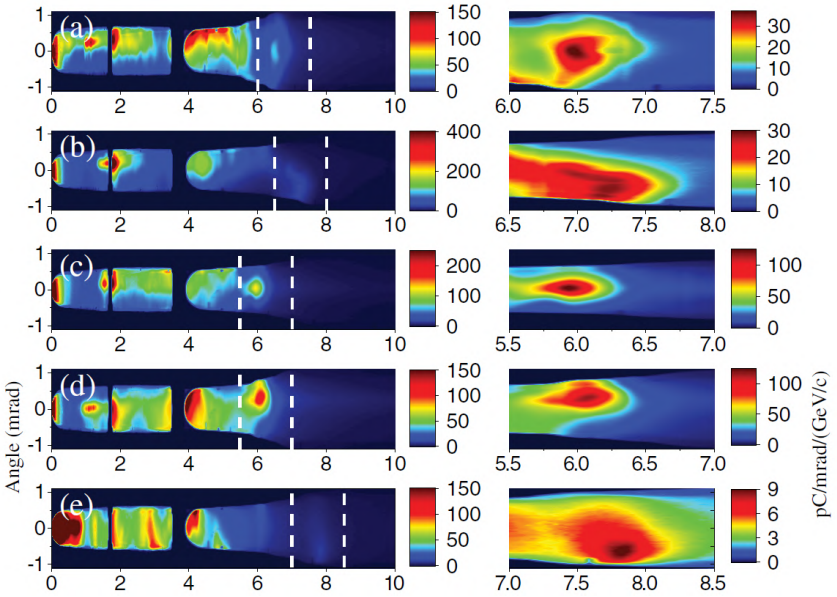

Figure 1.17. Accelerated electron beams angular (left) and energy (right) spectra.

1.4.4 Electron-driven PWFA overview

In 1985, Chen and Dawson [30] proposed to use a bunched electron beam to drive plasma wakes with GV/m accelerating gradients. In the case of electron-driven PWFA, the excitation of plasma waves is driven by the Coulomb repulsion due to the space charge of the electron bunch. Similarly to LWFA, according to the driver bunch intensity, linear and non-linear bubble regimes characterize the wakefield excitation. In the PWFA bubble regime, plasma electrons are blown out radially, but because of the space-charge attraction of the plasma ions, they are attracted back towards the rear of the driver beam, where they overshoot the beam axis and set up a wakefield oscillation. Also in this scheme, a bunch of charged particles can be properly injected in the rear of the driving electron bunch, extracting energy from the wakefield.

The first electron-driven PWFA experiments were achieved in 1988 at the Argonne National Laboratory [104], using low energy electron beam drivers. Since then, important experiments have been carried out at Stanford Linear Accelerator Center (SLAC), using an ultra-relativistic electron beam delivered by the SLAC linac to drive GV/m accelerating fields. As a first experiment, a single 42 GeV long electron bunch was used to drive the accelerating wakefield in a m-scale plasma column [18]. In this configuration, since the electron bunch length is longer than the plasma wavelength, the head of the bunch loses energy to drive the plasma wakefield, while electrons in the tail gain energy from the excited wakefield up to 85 GeV, achieving the doubling of the initial beam energy. On the other hand, since only a small fraction of the beam is actually injected and accelerated, the beam quality is definitely low, with a Maxwellian energy spectrum. In order to enhance the beam quality, a second experiment was performed with two ultra-relativistic electron bunches in the driver-witness configuration [80]. In this case, the witness bunch is properly

distanced from the driver in order to feel the highest accelerating field and extract the highest amount of energy available from the excited plasma. As a result, a 80 pC bunch with 1% energy spread and was obtained with an energy gain of 1.6 GeV and a driver-to-witness energy transfer of 30%, comparable to LWFA results. A schematic representation of the two PWFA experiments is depicted in Fig. 1.18, while Fig. 1.19 reports the corresponding measured energy spectra of the accelerated beams.

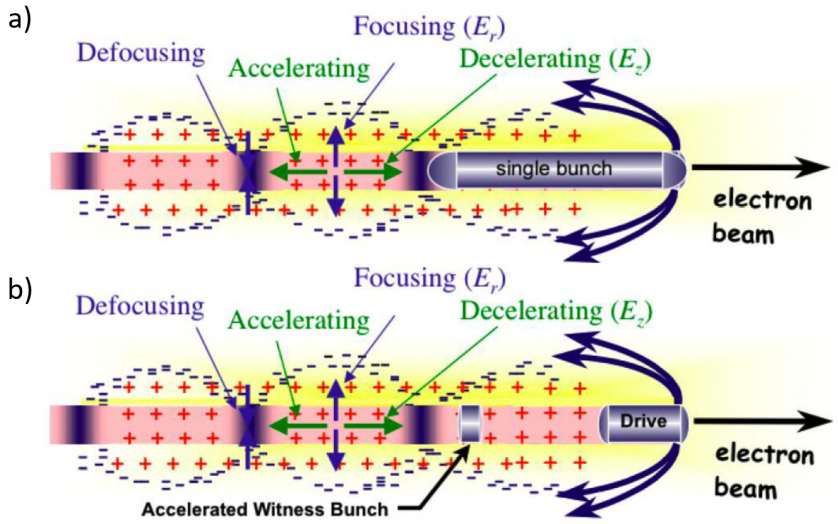

Figure 1.18. PWFA experiments with (a) a single long electron bunch and (b) two bunches in driver-witness configuration [18][80].

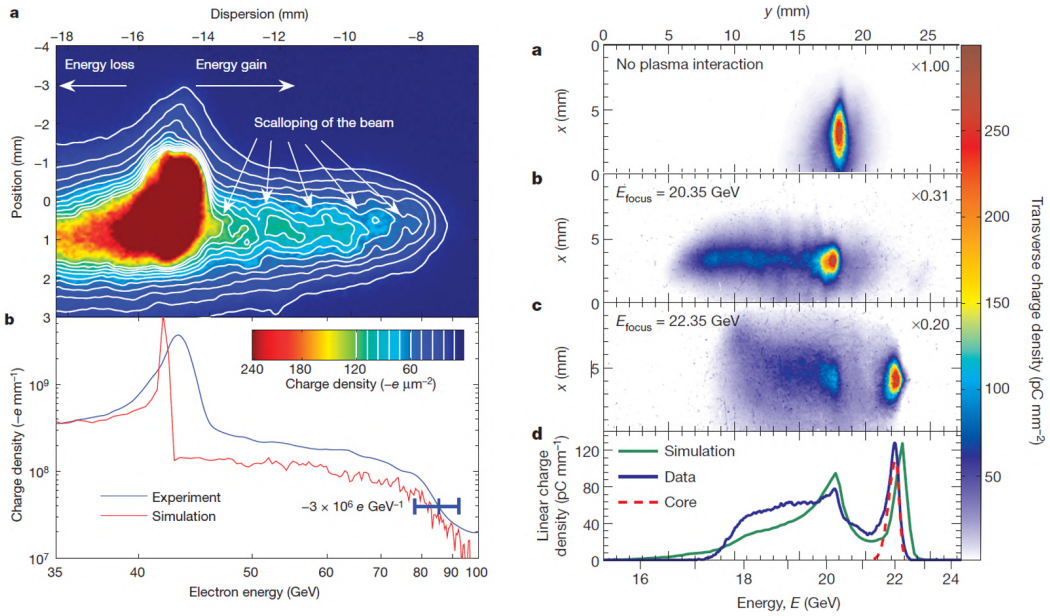

Figure 1.19. Resulting energy spectra of accelerated electron beams in the single bunch (left) and two bunches (right) PWFA experiments [18][80].

1.4.5 Proton-driven PWFA

As previously mentioned, the energy gain in plasma-based acceleration is limited by the energy of the driver beam and its propagation length in the plasma. For linear collider applications, the goal of accelerating nC-range electron bunches up to around 1 TeV would require kJ-range driver beams. To fulfill such requirement, the first idea was to exploit high energy proton beams produced at LHC. The first proposal of proton-driven PWFA was made in 2009, estimating that a proton bunch in resonance with the plasma could accelerate an injected 10 GeV electron bunch to 0.5 TeV in a single 450 m long proton wakefield stage [27]. Due to the lack of such short high-energy proton bunches, the first proton-driven PWFA experiments were proposed and carried out using the CERN SPS 19 kJ, 400 GeV proton beams in the framework of AWAKE project [66]. Since the 10 cm long proton bunch is much longer than the plasma wavelength (1 mm, with plasma density of 10^{14} cm^{-3}, corresponding to a 1 GeV/m gradient), the wakefield excitation is based on the self modulation of the driver bunch, also called self-modulation instability (SMI), schematized in Fig.1.20.

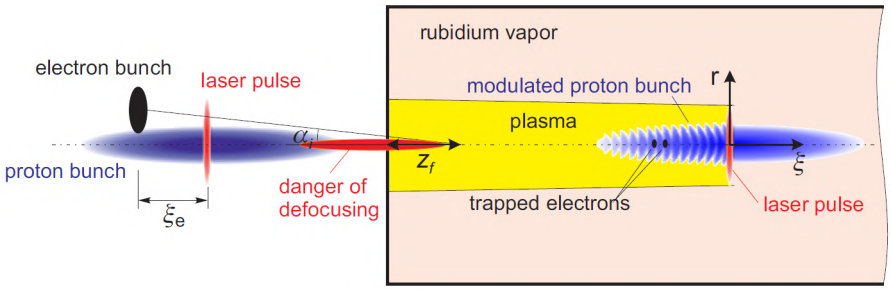

Figure 1.20. Schematic representation of the self-modulation instability (SMI) [67].

During interaction with plasma, the proton bunch is split into a train of micro-bunches that excite resonantly a strong plasma wave. Furthermore, a 100 fs 450 mJ laser pulse, used to ionize a rubidium column and produce a 10 m long plasma channel, additionally provides seeding to the SMI process, thus stabilizing the wakefield and the acceleration mechanism. First results with such scheme have shown the possibility to accelerate 18 MeV electrons, injected at the plasma entrance, up to 2 GeV, even though future upgrades are required to improve the quality of accelerated beams.

1.4.6 Ion acceleration: TNSA

Differently from plasma-based electron acceleration, in which driver and witness beams propagate through a plasma channel originating by the ionization of a neutral gas column, plasma-based proton and ion acceleration relies on the use of high intensity laser pulses impinging on micro-structured solid targets.

Among the various laser-driven ion acceleration regimes, the main one reached by commercial TW-class laser systems is the so-called Target Normal Sheath Acceleration (TNSA) [40]. In TNSA mechanism, schematized in Fig. 1.21, a TW laser pulse

with duration of tens of femtoseconds is focused onto the front side of a μm-thick foil, reaching intensities of around 10^{19} W/cm^2.

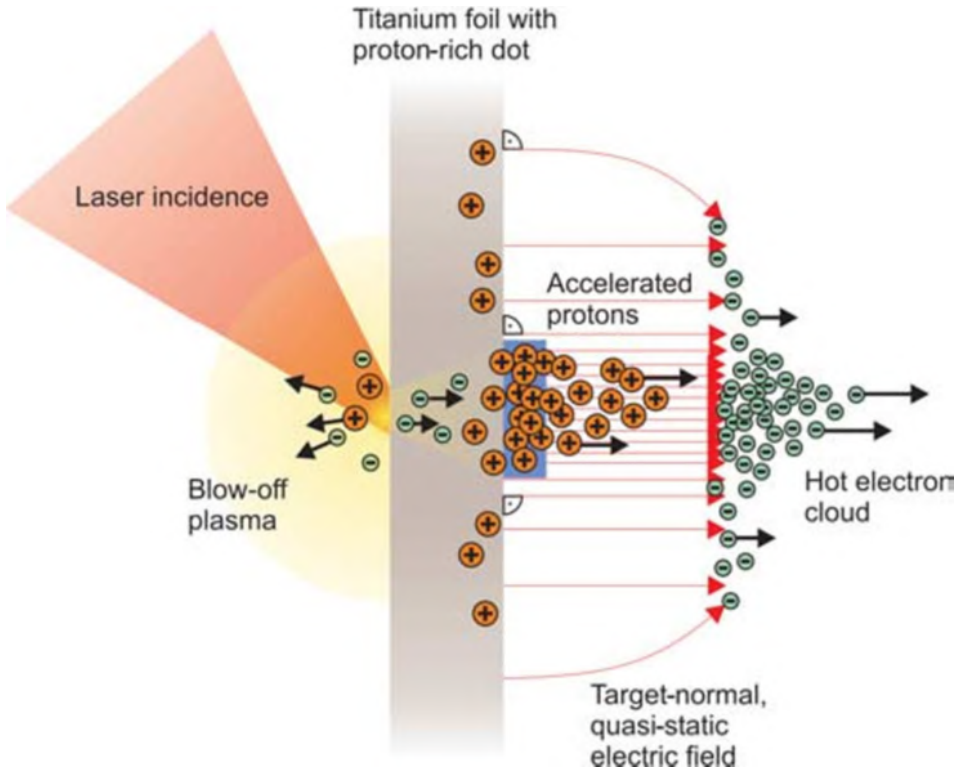

Figure 1.21. Schematic representation of the Target Normal Sheath Acceleration mechanism [109].

When the laser impinges the target, the laser pre-pulse interacts with its front surface, creating a blow-off plasma. The main pulse interacts with the plasma, accelerating plasma electrons mainly in forward direction, through the LWFA mechanism in self-injection regime. Hot electrons propagate inside the target within a 30° emission cone, due to collision with the background material, and they exit its rear surface creating a dense non-homogeneous electron sheath. The resulting charge separation generates an electric field of the order of few TV/m in the rear side of the target, which in turn ionizes atoms in the bulk of the target and rapidly accelerates emitted protons and ions in the forward direction up to energies of 1-10 MeV. Since electron sheath distribution is highly non-homogeneous, protons and ions experience a non-uniform electric field, with a radial decreasing trend, and get accelerated to different energies, depending on their initial position inside the target. This results in the production of ion beams with Maxwellian energy distribution and large angular divergence. On the other hand, thanks to the rapidity of the overall acceleration process, the ion beam is generated within a single bunch with a sub-picosecond time duration and is characterized by low transverse emittance, of 10^{-3} π mm mrad.

Comparing these properties to ion and proton beams produced by conventional RF-based accelerators, which are characterized by complex bunch structures and

lower intensities, proton and ion beams accelerated through TNSA results to be particularly useful for applications that require high time resolution or fast energy deposition in biological targets, such as the FLASH radiotherapy [22]).

In addition to hot electrons and ion and proton beam acceleration, several types of radiations and particles are produced by TNSA. In particular, the relativistic blow-off plasma, created by laser-matter interaction, emits intense electromagnetic waves able to produce secondary particles and radiations, such as neutrons, pions, x-rays, γ-rays and neutrinos and so on, as shown in Fig. 1.22. These particles can be easily separated from protons or ions by applying a dipole magnet, which bends particle trajectories in different directions depending on their charge-to-mass ratio.

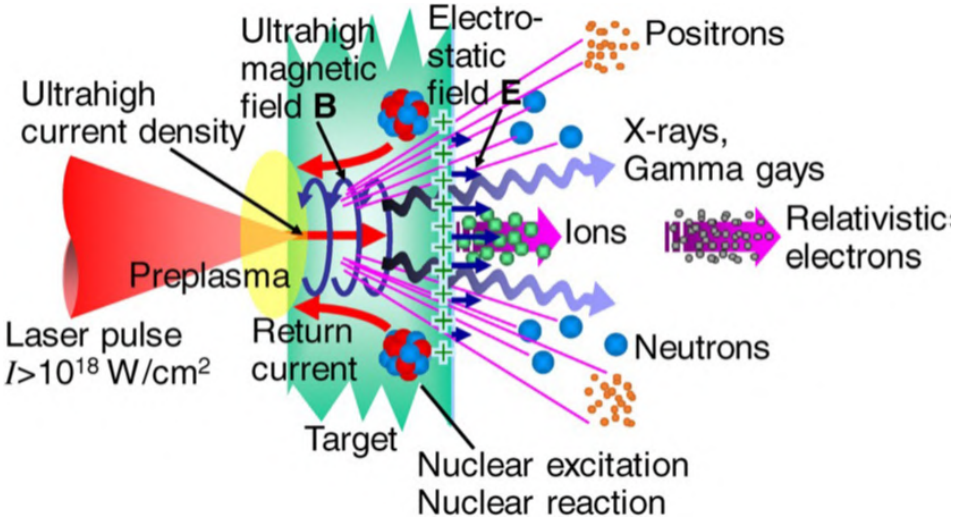

Figure 1.22. Emission of particles and radiation from the laser-ionized blow-out plasma [40].

1.5 EuPRAXIA@SPARC_LAB project

Due to the strong accelerating gradients of up to 100 GV/m, plasma-based acceleration allow a drastic reduction in size and cost of particle accelerators, compared to RF-based structures, leading to a significant impact on various applications such as Free Electrons Lasers (FEL) and beam colliders. In particular, as shown in Fig.1.5, test facilities based on plasma acceleration are approaching the energy range and beam quality required for FEL technology. FEL represent the fourth generation of light sources, characterized by high brilliance and short pulse duration. Due to its excellent properties, FEL technology allows to probe matter at a subatomic scale and in the femtosecond time range, resulting in a powerful tool for material science, biology and other applications.

Nowadays, several X-ray free-electron laser facilities are in operation [2, 44, 71, 5], however, the requirement for large, high-cost, conventional RF accelerators has limited the widespread of FELs. In this context, the advantage of plasma-based particle acceleration in reducing the cost and footprint of accelerators represents a great opportunity for the design of compact cost-effective and sustainable FEL facilities. Moreover, recent pioneering experiments have demonstrated the feasibility of plasma-accelerated electron beams to produce Free Electron Lasing in both SASE and seeded configuration [100, 126, 56, 78].

Achievements in plasma acceleration and the ferment in the scientific community have lead to the creation of EuPRAXIA project (European Plasma Research Accelerator with Excellence In Applications) [11], based on the collaboration of 41 Laboratories within a Horizon 2020 design study, funded by the European Union. EuPRAXIA represents the first European project that develops a dedicated particle accelerator research infrastructure based on novel plasma acceleration concepts and laser technology, aimed at enabling versatile applications in various domains, including compact FELs, compact sources for medical imaging and positron generation, table-top test beams for particle detectors, as well as deeply penetrating X-ray and gamma-ray sources for material testing. EuPRAXIA framework is spread over the European continent and includes the construction of two compact FEL plasma-driven user facilities and the operation of six Excellence Centers, providing scientific and technological support to R&D activities concerning the two FEL sites.

National Laboratory of Frascati (LNF-INFN) has been designated as the first site of the EuPRAXIA framework and will host the so called EuPRAXIA@SPARC_LAB project, which foresees the realization of a FEL user facility, driven by a PWFA particle accelerator [52]. The facility layout, reported in Fig. 1.23, includes the compact accelerator hall, two FEL lines and the corresponding experimental lines in the users hall.

The accelerator is based on a combination of cutting-edge technologies, including a S-band high-brightness photoinjector, a X-band booster and a plasma module for PWFA, schematized in Fig. 1.24:

- The S-band (2.856 GHz) photoinjector is composed by a photocathode 1.6 cells SW RF Gun, one 3m-long and three 2m-long TW S-band structures.
- The X-band (11.994 GHz) booster is composed by 16 0.9m-long TW X-band accelerating structures, with a nominal gradient of 60 MV/m, and 8 X-band

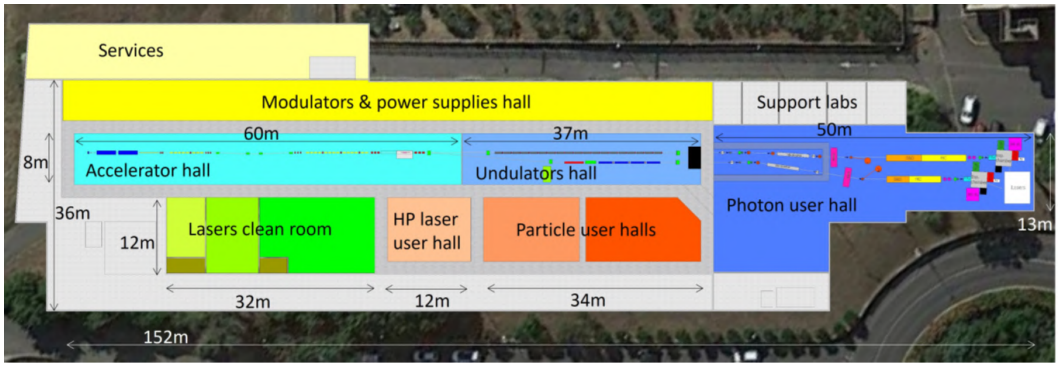

Figure 1.23. EuPRAXIA@SPARC_LAB layout

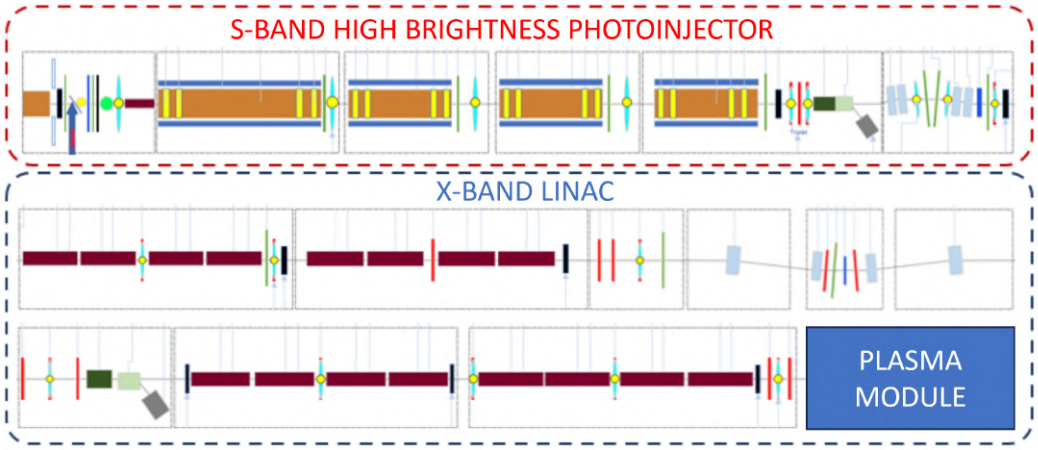

Figure 1.24. EuPRAXIA@SPARC_LAB accelerator

power stations (25 MW, 1.5us, up to 400 Hz).

- The plasma module includes a 60cm-long plasma discharge capillary, installed inside a 3m-long vacuum chamber, used for the PWFA stage.

Two working configurations are considered for electron beams acceleration, as reported in Tab.1.2:

- Two electron bunches are accelerated to 500 MeV by the X-band booster and enter the PWFA stage, in which the first (driver) bunch excite 1 GV/m wakefields along the 60cm-long capillary, accelerating the second (witness) bunch to 1-1.2 GeV.

- A single electron bunch is accelerated to 1 GeV by the X-band booster at full power, without using the PWFA stage.

Comparing the two configurations, the main difference is the lower charge and shorter duration of accelerated beams in the PWFA case, compared to full power X-band. Moreover, the second option does not include a possible future upgrade, since X-band booster design is already at the technological limit. On the other hand,

Parameter	Unit	PWFA	X-band full power
Electron energy	GeV	1-1.2	1
Bunch charge	pC	30-50	200-500
Peak current	kA	1-2	1-2
RMS energy spread	%	0.1	0.1
RMS bunch length	μm	6-3	24-20
RMS normalized emittance	μm	1	1
Slice energy spread	%	≤ 0.05	≤ 0.05
Slice normalized emittance	mm· mrad	≤ 0.8	0.5
Repetition rate	Hz	100-400	100-400

Table 1.2. Expected parameters for the accelerated electron beams at EuPRAXIA@SPARC_LAB

an upgrade of the PWFA stage, with around 3m-long plasma sources and 1.5 GV/m gradient, is foreseen for a future enhancement of the accelerated beam energy to 5 GeV.

Downstream the accelerator hall, high energy ultra-relativistic electrons drive two FEL lines in the Undulators hall. The first one, called AQUA, is a soft X-ray SASE FEL in the water window (2-4 nm), constituted by 10 APPLE-X undulators. The second one, called ARIA, is a VUV seeded FEL in High Gain Harmonic Generation configuration, constituted by a 3 m long modulator, a dispersive section and three radiators. Both the modulator and the radiators are Apple II undulators, which, analogously to Apple X undulators of AQUA, allow to tune the FEL polarization from linear to circular. Moreover, ARIA seeding laser will work in OPA configuration, with 200-400 fs duration, ≥ 20 μJ energy and two possible wavelength ranges (320-400 nm and 600-800 nm), in order to seed FEL radiation in a wide VUV spectrum from 50 to 180 nm.

AQUA FEL radiation will be used to study biological samples (cells, organelles, viruses) through coherent imaging, exploiting the potentiality of the radiation in the water window, i.e. the energy range between carbon (282 eV) and oxygen (533 eV) K-edge, in which the absorption contrast between the carbon of organelles and the water of both cytoplasm and the liquid surrounding the cell is quite high [14]. In addition, X-ray absorption spectroscopy and Raman spectroscopy experiments will be performed to study metals, semiconductors and superconductors. Furthermore, the short pulse duration of plasma-driven FEL radiation will be exploited for time-resolved pump-probe experiments, in order to study fast chemical reactions and processes, such as photo-fragmentation of molecules.

On the other hand, ARIA can provide many different experimental opportunities for investigations with pump–probe techniques in the fields of atomic, molecular and cluster physics, as well as in the study of gas adsorbates at interfaces and liquids [125]. Moreover, the photon energy range of ARIA will give access to the photo-ionization thresholds and to the valence ionic states of atmospheric constituents, while a VUV monochromatic beamline, together with photo-emission techniques, would allow for the study of species of interest in both the physics of the upper atmosphere and in

combustion. In addition, the possibility of changing the polarization of the FEL light from linear to circular allows to obtain important information regarding the chirality and natural dichroism in biotic media.

A set of expected parameters for the FEL radiation produced in the two undulator lines and considered for the mentioned applications is reported in Tab.1.3 and Tab.1.4:

Parameter	Unit	AQUA PWFA	AQUA X-band
Radiation wavelength	nm	3-10	4-10
Radiation energy	eV	415-120	310-120
Photons per pulse	$\times 10^{12}$	0.25-1	0.25-1
Photon bandwidth	%	0.3	0.3
Configuration		SASE	

Table 1.3. Expected parameters for AQUA FEL radiation at EuPRAXIA@SPARC_LAB

Parameter	Unit	ARIA PWFA	ARIA X-band
Radiation wavelength	nm	50-150	50-150
Radiation energy	eV	25-8	25-8
Photons per pulse	$\times 10^{12}$	10-60	12-150
Photon bandwidth	%	0.05	3
Configuration		HGHG seeding	

Table 1.4. Expected parameters for ARIA FEL radiation at EuPRAXIA@SPARC_LAB

1.5.1 SPARC_LAB facility

Towards the realization of EuPRAXIA@SPARC_LAB project, a key role is played by SPARC_LAB accelerator facility. SPARC_LAB [115] is a test-facility operating at the National Laboratory of Frascati (LNF-INFN) devoted to advanced radiation sources and innovative acceleration techniques. Recent activity has been focused on the realization of plasma-based acceleration experiments with the aim to provide large accelerating field, up to several GV/m, for high-quality (small energy spread and normalized emittance) electron beams [99]. These experiments culminated with the first proof of Free-Electron Laser (FEL) lasing from a plasma-accelerated electron beam [100].

SPARC_LAB is based on the combination of the high-brightness ($\approx 10^{15}$ A m^{-2} rad^{-2}) SPARC photo-injector [4] with the high-intensity ($\approx 10^{19}$ W/cm^2) FLAME laser [17]. The joint presence of these two systems allows the investigation of several plasma acceleration schemes, e.g. self and external-injection, laser and beam-driven, and a wide spectrum of interdisciplinary leading-edge research activities based on novel radiation sources such as Free-Electron Laser (FEL), both in Self Amplified Spontaneous Emission (SASE) and seeded schemes, and high peak power THz radiation both in the broadband and narrow-band range [31]. The layout of the facility is shown in Fig. 1.25.

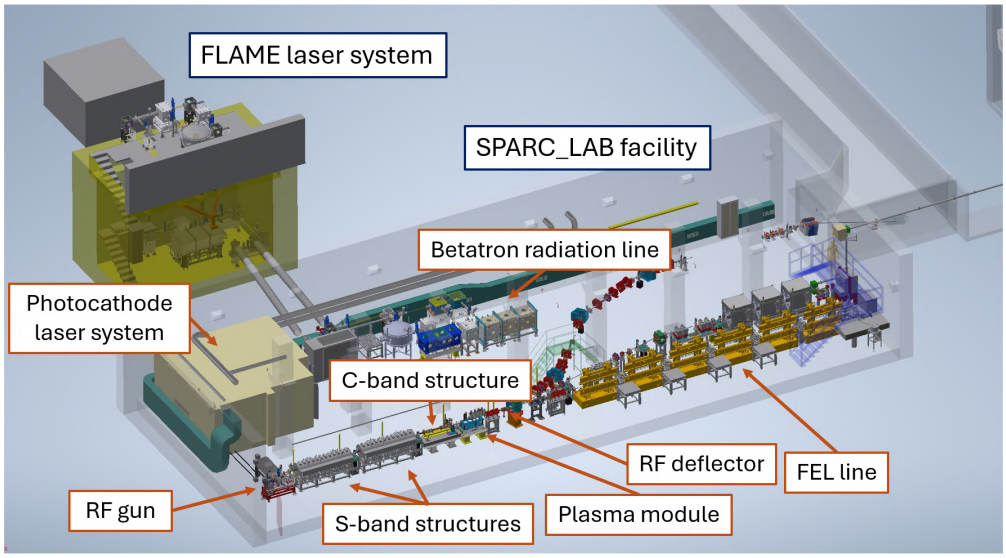

Figure 1.25. SPARC_LAB facility layout

The SPARC photo-injector starts with a S-band ($f_{RF} = 2.856$ GHz) 1.6 cell RF-gun [114], which provides a 120 MV/m accelerating electric field. Electrons are extracted from a copper (Cu) cathode by means of a UV laser ($\lambda_L = 266$ nm), whose shape and duration (0.1-10 ps) can be tailored according to the specific experimental activity. The electrons are accelerated up to 5.6 MeV in the gun and then injected into the linac, consisting of two TW S-band structures and a TW C-band ($f_{RF} = 5.71$ GHz) structure. The maximum achievable beam energy is approximately 180 MeV. The first TW section is also used as RF-compressor by means of velocity-bunching (VB) [111]. Solenoid coils embedding the first two sections can provide additional magnetic focusing during the VB process and control of emittance and envelope oscillations [51]. Downstream the linac, electrons enter the plasma module, in which plasma-based acceleration experiments are performed in PWFA configuration. The plasma module includes a m-long vacuum chamber, in which a 3-20 cm long plasma discharge capillary is installed. The capillary is filled with hydrogen or nitrogen gas and connected to a HV system, which delivers kV-range voltage pulses to ionize the neutral gas and produce the plasma channel for plasma wakefield acceleration. A set of turbo-molecular pumps are connected to the vacuum chamber to preserve a vacuum level of 10^{-8} mbar in the upstream C-band structure. Additionally, the vacuum chamber hosts an electro-optical sampling (EOS) diagnostic, a THz diagnostic and two permanent magnet quadrupole (PMQ) triplets in the Halbach configuration, located before and after the capillary [45]. In particular, the first PMQ triplet is used to match the size of driver and witness bunches to the plasma channel, while the second one catches the accelerated witness bunch after the PWFA stage. A schematic representation of the final part of the photo-injector and the plasma module is reported in Fig. 1.26, while a picture of the plasma module chamber with a 3 cm long capillary is shown in Fig. 1.27.

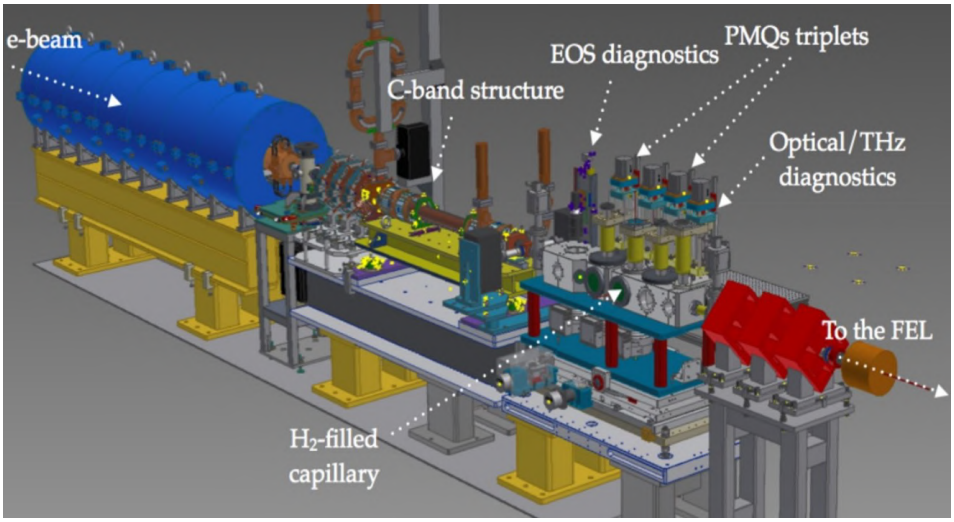

Figure 1.26. Schematic representation of the photo-injector and the plasma module

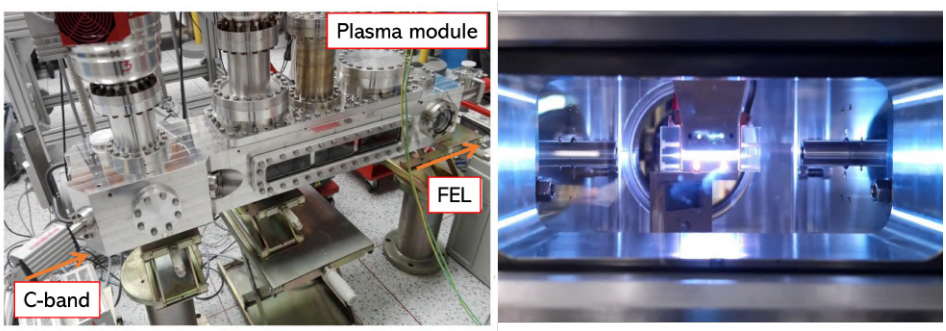

Figure 1.27. (Left) Vacuum chamber of the plasma modoule. (Right) 3cm-long plasma discharge capillary, installed inside the vacuum chamber and used for PWFA experiments.

Downstream the plasma module, a diagnostics transfer line, consisting of a magnetic spectrometer and a RF-deflector (RFD), allows for a complete 6D beam characterization by measuring the beam longitudinal phase space and its projected and slice emittance [33]. The SPARC photo-injector feeds three different beamlines located downstream the main magnetic spectrometer. The first one is dedicated to the Free-Electron Laser (FEL) by means of six magnetic undulators. The second one consists of a dogleg line [97] and hosts two THz undulators devoted to users applications. The third one is currently under development and will be integrated in the EuPRAXIA Advanced Photon Source (EuAPS) project.

The SPARC_LAB framework additionally includes a third experimental laboratory, Plasma_lab, which is devoted to develop and characterize the plasma stages used for acceleration experiments, performed both at SPARC and FLAME. The research activity performed at Plasma_lab concerns theoretical studies and experimental developments of cm-scale devices (few cm up to 60 cm) used to create and confine the plasma. In particular, gas-filled capillary-discharges are employed for particle-driven wakefield acceleration experiments at SPARC_LAB, due to their ability to provide appropriate tailoring of the plasma density distribution, allowing

to optimize the matching with particle beams.

Within Plasma_lab activities and the SPARC_LAB framework, the presented PhD thesis project is focused on the experimental and theoretical design and development of plasma sources, aimed at improving the compactness and cost-effectiveness of plasma-based acceleration and meet the requirements of stability, longevity and reproducibility foreseen for EuPRAXIA@SPARC_LAB project.

Before describing the activities and the achievements related to the thesis project, a description of the main plasma sources, employed in plasma-based particle accelerators, is provided in the following chapter.

Chapter 2

Plasma sources for plasma-based particle accelerators

2.1 Introduction

As described in Ch.1, plasma properties play a key role in the efficiency of plasma-based particle acceleration. In particular, the longitudinal and transverse uniformity of the plasma column is crucial to sustain accelerating and focusing wakefields that remain constant along the acceleration process, allowing to preserve the accelerated beam quality (low emittance and energy spread). On the other hand, a proper tailoring of the longitudinal plasma density distribution can provide direct control over particle injection, thus limiting the energy spread. In addition, tapered density transitions can be used to mitigate the hosing instability [86] and the energy chirp induced by the longitudinal variation of the accelerating wakefield along the witness bunch (in absence of beam loading) [23].

Moreover, plasma channels can be employed for applications other than particle acceleration, including laser guiding, focusing of charged particles and phase space manipulation, as described in the following.

For these reasons, a proper design of the plasma source is crucial for the realization of a plasma-based particle accelerator. In recent years, various plasma sources have been developed and employed in plasma-based experiments, including gas jets [47], gas cells [12], Alkali vapor ovens [18, 66] and discharge capillaries [61, 100]. Such plasma sources rely on different ionization mechanisms for the plasma formation and provide fine tuning of plasma properties for the above mentioned applications.

2.2 Plasma formation mechanisms

Generally, the production of plasma channels is based on the ionization of a neutral gas column, whose distribution is properly controlled by means of a gas injection system. In particular, a plasma source can include one or different gas injection channels (as discussed in Ch.4), with particular configurations that allow to control the pressure distribution of the gas column and hence the density distribution of the plasma channel once the gas is ionized. Eventually the gas injection mechanism can be also studied for gas mixtures, in order to control the distribution of the different

gas components [75]. Gas injection is generally designed to optimize the properties of the plasma channel for the specific application (e.g. density gradients for controlled beam matching, high-Z component localization for ionization injection and so on). The specific mechanisms exploited for the plasma formation are described below.

2.2.1 High voltage electrical discharges

One of the main approaches for producing a plasma is to apply high voltage pulses to a couple of electrodes to ionize an interposed gas column and produce an electrical discharge. Early research on the physics of electrical discharges was historically performed in low pressure devices, whose geometry consists in an evacuated dielectric tube, with two plate electrodes at both ends, connected to a high voltage DC power supply, as schematized in Fig.2.1.

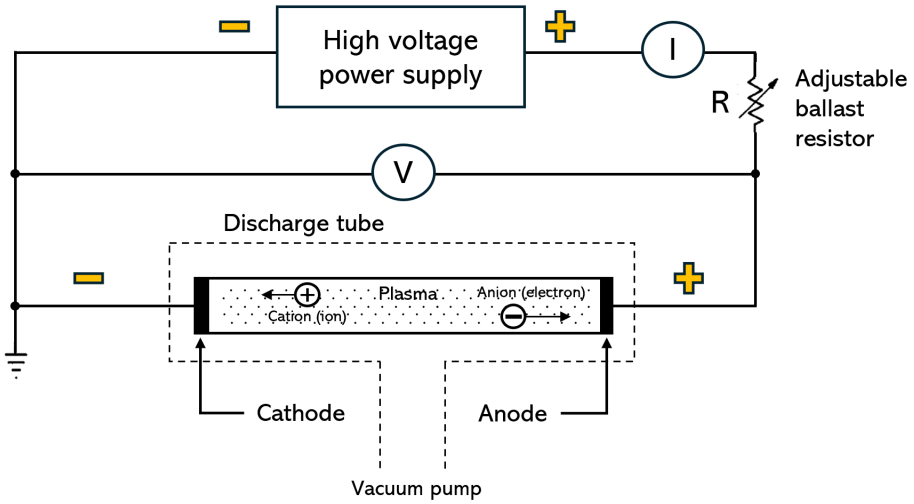

Figure 2.1. Schematic representation of a low pressure electrical discharge tube.

When the voltage is applied and the electrical discharge is triggered, electrons and ions migrate in the formed plasma towards the anode and the cathode respectively, while colliding with the neutral background gas. By adjusting a ballast resistor connected to the electrical circuit, it is possible to raise the voltage and measure the current flowing through the discharge, tracing the non-linear voltage-current characteristic of the discharge tube [105]. As depicted in Fig. 2.2, the V-I characteristic identifies three main regimes for a DC electrical discharge.

Dark discharge

The dark discharge regime occurs in the region A-E of the V-I characteristic. It is characterized by low discharge current (below the μA range) and, except for the corona discharges and the electrical breakdown spark itself, the discharge remains invisible to the eye. Starting from a low voltage in the background ionization regime (A-B in the V-I characteristic), first electrons and ions are created by background radiation originating from cosmic rays, radioactive minerals and leaks from the electrodes surface, but can also include free electrons from previous discharge cycles

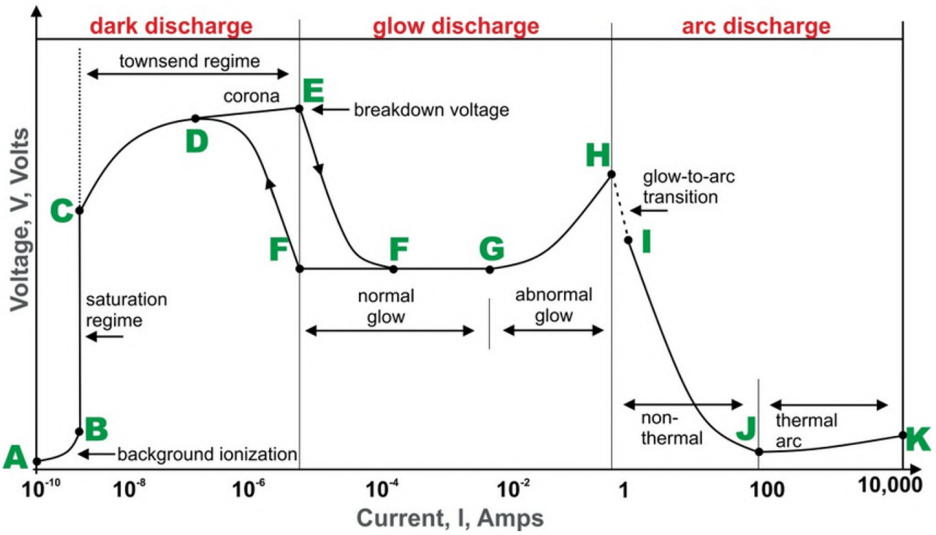

Figure 2.2. Current–voltage characteristic curve of a DC electrical discharge in a low pressure tube. The exact shape of the curve depends on the type of gas, pressure, electrode geometry, electrode temperatures, electrode materials and any magnetic fields present [129].

[105]. Free charges gain energy from the external electric field and collide with orbital electrons of gas atoms and molecules, resulting in the production of other charge carriers [46]. With increasing voltage, the current between the electrodes raises until reaching saturation at few nA. In the saturation regime (B-C in Fig.2.2), all of the ions and electrons produced by background ionization are removed from the discharge volume, and the electrons do not possess enough energy to create new ionization. By increasing the applied voltage, the corresponding electric field gets high enough to accelerate free electrons up to the ionization energy of the gas.

Due to electron impact ionization, other charge carriers are generated, which in turn can accelerate enough to produce further ionization, resulting in a Townsend avalanche, in which the discharge current grows exponentially with the applied voltage (Townsend regime, C-E in Fig.2.2). Given the number of electrons emitted by the cathode n_0, the number of charge carriers produced during the avalanche is given by:

$$\frac{dn_e}{dx} = \alpha n_e \tag{2.1}$$

in which the number of additional free electrons dn_e produced in a distance dx depends on the number of electrons at that point n_e and the Townsend primary ionization coefficient α, i.e. the average number of additional electrons per unit length. As a result, the number of carriers grows exponentially from the cathode to the anode, inside the avalanche [46]:

$$n_e = n_0 e^{\alpha x} \tag{2.2}$$

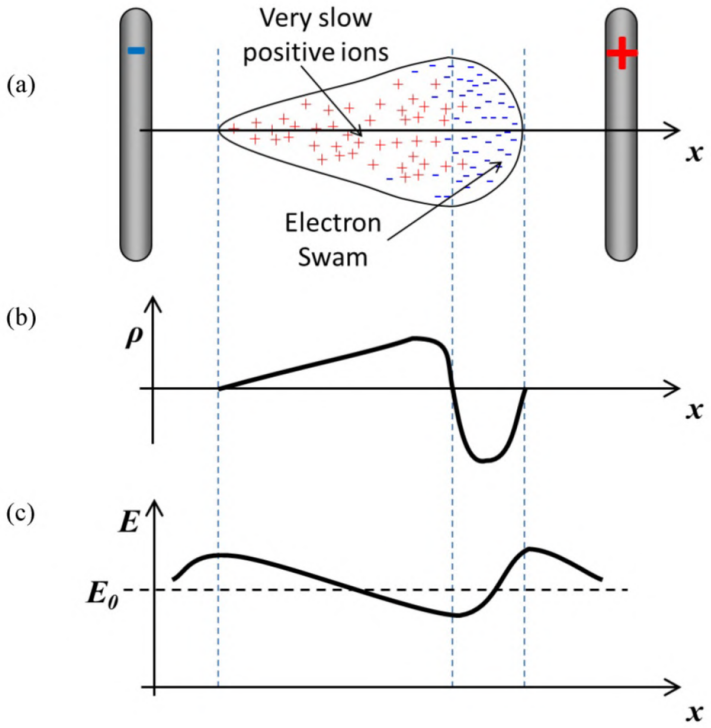

Figure 2.3. (a) Avalanche distribution of charge carriers and corresponding (b) charge density and (c) electric field longitudinal profiles [46].

with $n_e = n_0 e^{\alpha d}$ at the anode, considering d as the distance between the electrodes.

The avalanche is characterized by a negative head, comprising the avalanche of free electrons, and a positive tail, comprising the positive ions left behind after the ionization avalanche has passed. Due to their higher mass, ions take much longer time to accelerate to ionizing energy and they travel a small distance from the ionization point. The difference in mobility of the ions and electrons results in the charge distribution shown in Fig. 2.3, which in turn determines an alteration in the electric field distribution.

Ions, directed towards the negative cathode, would eventually cause ion impact ionization, determining the emission of secondary electrons from the cathode surface. In addition, photons emitted by the primary avalanche contribute to the production of free electrons, which in turn trigger additional avalanches. Secondary emission of electrons from the cathode, due to ion impact on the cathode surface, is taken into account in the secondary ionization coefficient γ, i.e. the average number of electrons emitted from the cathode surface per incident positive ion [81].

The influence of γ on the total discharge current can be deduced as follows. For each electron leaving the cathode, $e^{\alpha d}$ electrons reach the anode and $e^{\alpha d} - 1$ ions are formed in the gap. Ions move towards the cathode, where they impact on the surface and release $\gamma[e^{\alpha d} - 1]$ electrons by secondary ionization. The "second generation" of electrons grows until reaching a total number of $\gamma[e^{\alpha d} - 1]e^{\alpha d}$ electrons at the anode, resulting in $\gamma[e^{\alpha d} - 1]^2$ ions, which in turn produce a "third generation"

of $\gamma^2[e^{\alpha d}-1]^2$ electrons. Therefore, the total amount of electrons emitted by the cathode through primary and secondary ionization is [81]:

$$n_e = n_0\left[1+\gamma(e^{\alpha d}-1)+\gamma^2(e^{\alpha d}-1)^2+\gamma^3(e^{\alpha d}-1)^3+...\right] = n_0\frac{1}{1-\gamma(e^{\alpha d}-1)} \tag{2.3}$$

and the total number of electrons reaching the anode is:

$$n_e = n_0\frac{e^{\alpha d}}{1-\gamma(e^{\alpha d}-1)} \tag{2.4}$$

As a result, the total discharge current collected by the electrode in steady state and produced by primary and secondary ionization is given by [81]:

$$I = \frac{I_0 e^{\alpha d}}{1-\gamma(e^{\alpha d}-1)} \tag{2.5}$$

in which I_0 is the photoelectric current from the cathode.

By increasing the applied voltage to the breakdown condition, the Townsend discharge becomes self-sustained, with a rapid increase of the current expressed by the condition:

$$\gamma(e^{\alpha d}-1) = 1 \tag{2.6}$$

The breakdown voltage of a gas column between two flat electrodes depends on the electron mean free path and the distance between the electrodes. The electron mean free path is the average distance travelled by electrons before colliding with atoms, so it is the key parameter defining the growth of an avalanche discharge. In particular, the electron mean free path is inversely proportional to the gas pressure:

$$\lambda_e = \frac{1}{\sigma n} = \frac{k_B T}{\sigma p} \tag{2.7}$$

where σ is the effective cross-sectional area for collisions, k_B is Boltzmann constant, and the ideal gas relation has been used to relate the gas density to the pressure. At very high gas pressure, the mean free path is too short, so electrons collide without gaining enough energy to ionize atoms and molecules. On the other hand, at very low pressure, the mean free path is longer than the electrodes distance, meaning that electrons accelerate to ionizing energies but they do not significantly interact with neutral atoms. Therefore, in both cases, a very high voltage is required to trigger an electrical breakdown. However, in the intermediate region, there is a minimum of the breakdown voltage, which depends on the gas composition and the electrode material. The dependence of the breakdown voltage on the gas pressure and the distance between the electrodes is expressed by the Paschen curves, reported in Fig. 2.4.

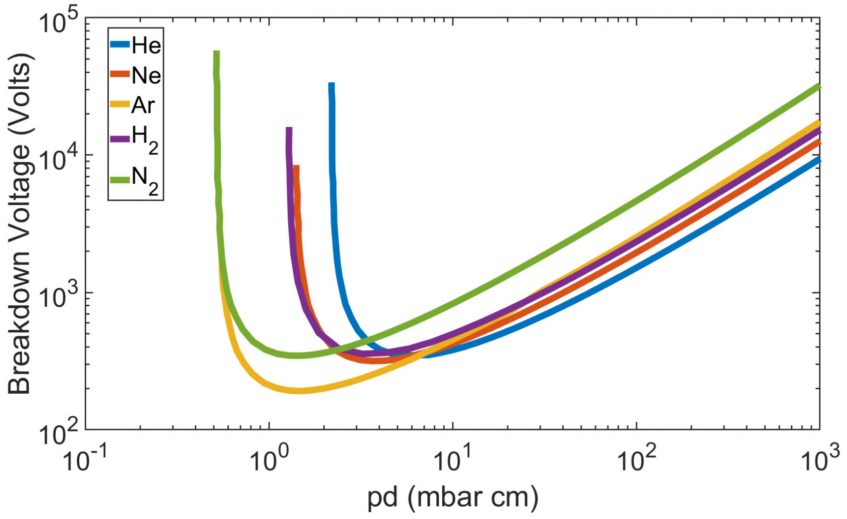

Figure 2.4. Paschen curves for different gases, showing the dependence of the breakdown voltage on the product between gas pressure p and the electrodes distance d [57].

In the region D-E of the V-I characteristic, unipolar corona discharges occur, as the result of local electric field concentrations on the surface of the electrodes at sharp points, sharp edges, or asperities. These strong local electric fields exceed the breakdown strength of the surrounding neutral gas [105].

Glow discharge

When high voltage is applied in low pressure environments, at around 0.1-10 mbar, the avalanche breakdown process can cause a voltage drop to some tens of Volts, indicating that the discharge has entered the glow discharge regime, corresponding to the E-H region of the V-I characteristic in Fig.2.2. The term "glow discharge" is referred to the high luminosity of the plasma, in contrast to the low power dark discharge. After the voltage drop in the region E-F, the discharge enters in the normal glow region, in which the voltage across the discharge is almost independent on the current over few orders of magnitude. The glow discharge is a self-sustained continuous DC discharge, characterized by the emission of secondary electrons through ion impact ionization on the surface of the cold cathode. During a glow discharge, the gas turns into a highly-conductive, cold plasma, with electron temperature and density of 1-3 eV and 10^{9-11} cm^{-3} in the positive column. The pattern of light emission of a glow discharge in a tube is characterized by alternating glow and dark regions [54], as shown in Fig.2.5.

Towards the cathode, electrons are emitted at low energy, not sufficient to excite atoms, resulting in the Aston Dark Space. Downstream the cathode, the electric field accelerates electrons to exciting energy, thus producing the Cathode Glow. Further acceleration of electrons in the Cathode Dark Space leads mostly to ionization, which overcomes electronic excitations of atoms and pertains a reduction in the light emission and a significant increase of electron density. The high electron density at the end of the Cathode Dark Space determines a reduction in the electric field,

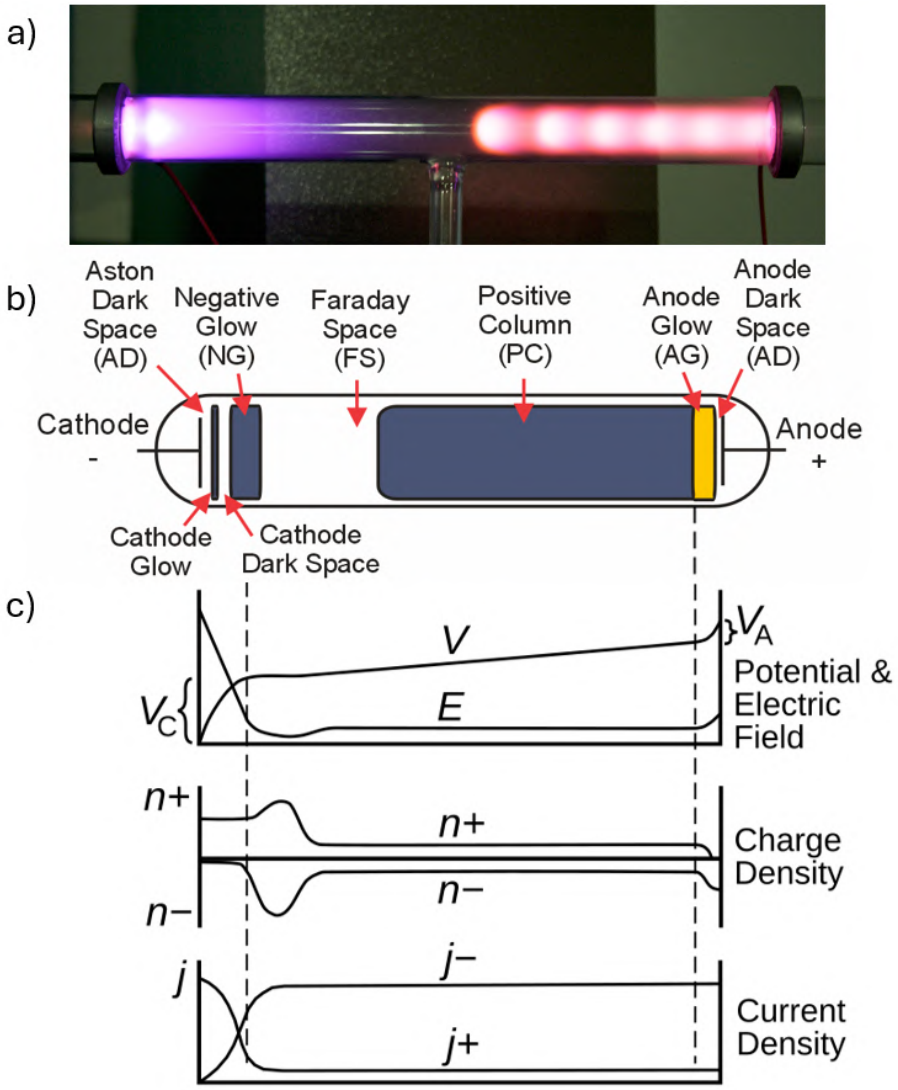

Figure 2.5. (a) Picture of a glow discharge in a low pressure tube [108]. (b) Schematic representation of the light emission pattern [122]. (c) Physical parameters distribution in a glow discharge [83].

which in turn leads to a decrease in the electron energy and hence a lower ionization rate and a higher radiation emission, resulting in the Negative Glow. Further from the cathode, the electron energy decreases until electronic excitation is overcome by vibrational excitation, leading to the dark Faraday Space. Plasma density decreases in the Faraday dark space and the electric field again grows, establishing the Positive Column. The average electron energy in the positive column is about 1–2 eV, which determines emission of light. Finally, towards the anode, positive ions are repelled and electrons are removed from the positive column, creating a negative space charge and leading to an increase of the electric field in the anode layer. The reduction of the charge density and the increase of the electric field result in the Anode Glow and the Anode Dark Space [54].

As mentioned, the current in a normal glow discharge can be increased over few orders of magnitude (from 10 μA to few mA) with very little increase in discharge voltage. During the current increase, the formed plasma distributes around the cathode until its surface is completely covered (point G on Fig.2.2). It is noteworthy that a discharge starting at point G (abnormal glow) with decreasing voltage would experience a form of hysteresis in the V-I characteristic, keeping the normal glow regime until F' and than turning back to Townsend regime.

A further increase in the discharge current from G leads to the abnormal glow (G-H region), in which the voltage raises proportionally with the current. Beyond the point H, the current density on the cathode becomes large enough to heat the cathode to incandescence, thus triggering a discontinuous glow-to-arc transition (H-I region) [105].

Arc discharge

Arcs are self-sustaining DC discharges, with low cathode fall voltage of about 10 V. Due to the electrical breakdown, the large current density produces a massive ion bombardment on the cathode, which rapidly heats up. The cathode heating results in the growth of thermionic emission, which becomes the dominant process in the production of charge carriers and determines the glow-to-arc transition [54]. Thermionic effect consists in the emission of electrons from the hot cathode surface due to thermal energy of electrons located in the metal, which is higher than the metal work function (i.e. the binding energy of the electron in the highest electronic level, also called the Fermi level). Emitted electrons induce an image charge effect that alters the electric potential profile close to the surface [54]:

$$eV(z) = e\Phi - \frac{e^2}{16\pi\epsilon_0 z} \tag{2.8}$$

in which $e\Phi$ is the cathode work function. The negative space charge produced by thermionic emitted electrons prevents further electron emission from the cathode and leads to a saturation current density. An increase in the external electric field results in a reduction of the electrostatic potential towards the cathode, i.e. the Schottky effect, which allows to increase the thermionic emission of electrons and thus the current density. If the external electric field is very high (about 1–3 $\times$ 10^6 V/cm), the effective electrostatic potential turns into a barrier, which can be crossed through quantum-mechanical tunneling. The so-called field emission allows to extract electrons from cold cathodes, without cathode heating. The mechanisms of electron emission from the cathode, governing the arc discharge regime, are summarized in Fig.2.6.

The arc discharge regime is characterized by a hot high-density plasma uniformly distributed in the region between the electrodes. In the non-thermal arc regime (I-J region of the V-I characteristic in Fig.2.2), plasma electrons are hotter than ions and neutral atoms and the voltage drops with increasing current in the range from few to hundreds Amps. As the current in the arc increases to hundreds of Amps, the plasma becomes almost completely ionized and, eventually, the ions accelerate to the same average energy as the electrons, thus reaching local thermal equilibrium. In

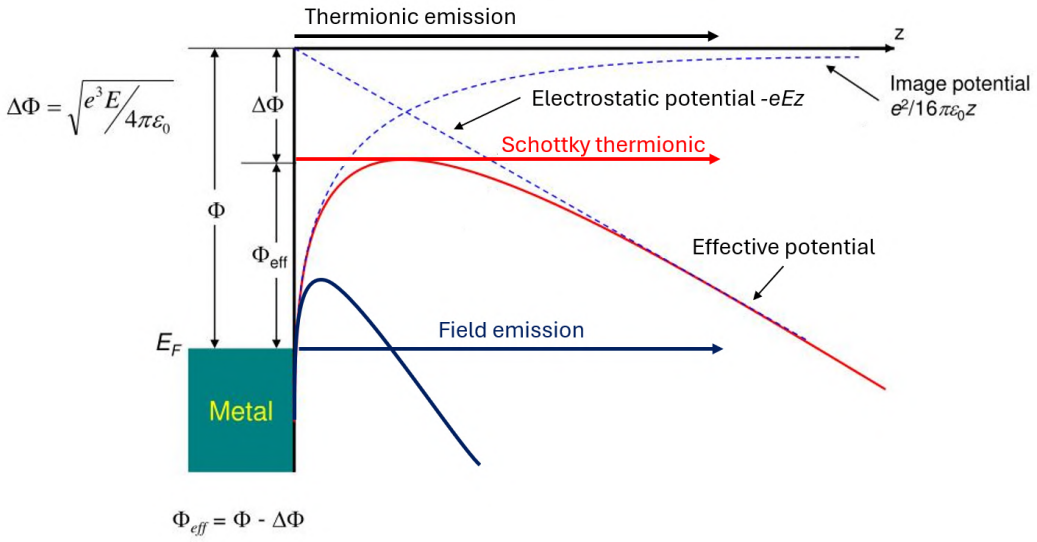

Figure 2.6. Schematic representation of the thermionic, Schottky thermionic and field emission mechanisms from a metal cathode [38].

this case, the discharge enters the thermal arc regime, where the discharge voltage grows as the current increases.

Generally, power supplies can provide high voltage pulses that directly generate thermal arc discharges after the electrical breakdown, resulting in hot high density plasmas. In particular, this is the case for plasma discharge capillaries, used for plasma-based particle accelerators and relying on the use of HV pulses to produce high peak current plasma discharges. An example of arc discharge generated in a 40-cm long capillary at Plasma_lab is reported in Fig.2.7.

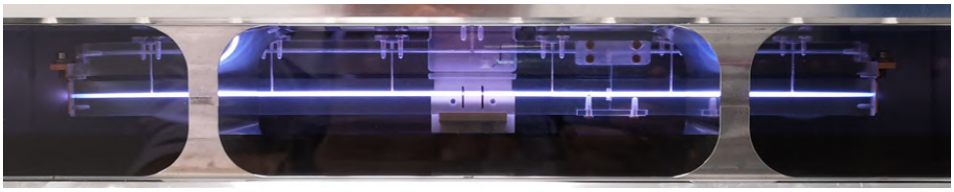

Figure 2.7. Arc discharge in a 40 cm-long capillary, tested at Plasma_lab. The hot plasma distributes uniformly along the capillary channel.

2.2.2 Laser-induced ionization

A convenient method to ionize a gas or solid, arget is by means of laser pulses. Laser-induced ionization relies on the interaction of orbital electrons of the target with laser photons having energy higher than electrons binding potential. Usually, the energy of a single photon from conventional laser systems is not enough to ionize an atom or molecule. For example, Ti:Sapphire lasers are characterized by wavelength of 800 nm, corresponding to 1.55 eV photon energy, while the ionization potential for hydrogen is 13.6 eV. Therefore laser ionization mainly relies on multi-photon ionization, which occurs when the laser intensity is high enough to have a large

number of photons in the atomic volume to simultaneously ionize the atom.

An alternative process governing laser-induced ionization is the barrier suppression ionization, in which the electric field of the laser pulse modifies the electric potential experienced by orbital electrons, bounded to atomic nuclei. In a 1D description, the binding potential affected by the external laser electric field is given by:

$$V(x) = -\frac{Ze^2}{4\pi\epsilon_0 x} - eEx \tag{2.9}$$

where Z is the atomic number minus the electron taken into account for ionization, while E is the laser electric field. By setting the modified potential equal to the ionization potential, it is possible to recover the threshold laser electric field over which suppression ionization occurs:

$$E_t = \frac{\pi\epsilon_0 \Phi_{ion}^2}{Ze^3} \tag{2.10}$$

in which Φ_{ion} is the ionization potential. In practical units, the threshold laser intensity required for ionization is given by:

$$I_t = \frac{\pi^2 \epsilon_0^3 c}{2^6} \frac{\Phi_{ion}^4}{Z^2} \approx 4 \times 10^9 \left(\frac{\Phi_{ion}}{eV}\right)^4 \frac{1}{Z^2} W/cm^2 \tag{2.11}$$

For example, relying on 2.11, the required laser intensity for hydrogen ionization is 1.4×10^{14} W/cm^2, while for complete ionization of helium the required intensity is 8.8×10^{15} W/cm^2. As a consequence, LWFA schemes do not actually require the presence of a pre-formed plasma channel, but they rely on the leading edge of 10^{18} - 10^{19} W/cm^2 driving laser pulses to produce the plasma channel in which to excite strong plasma wakefields.

A further ionization process, tunnel ionization, can take place if the laser electric field is slightly lower than the threshold value. The Keldysh parameter $\gamma = \omega\sqrt{2\Phi_{ion}/I}$ provides a criterion to distinguish the different ionization mechanisms, depending on the laser intensity and frequency, as reported in Fig. 2.8.

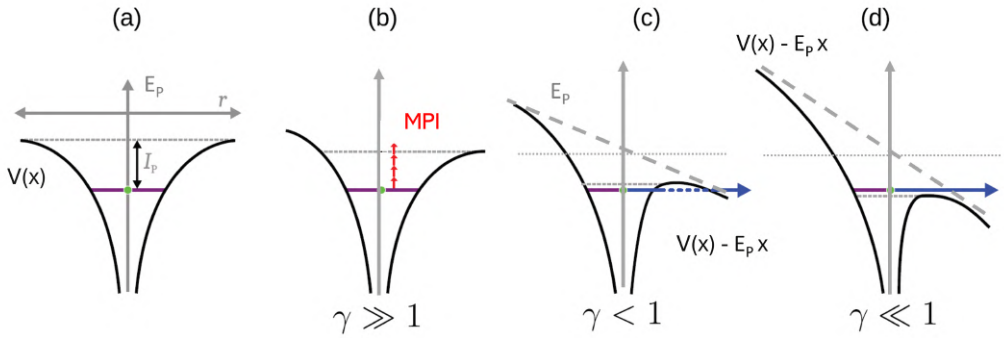

Figure 2.8. The atomic Coulomb potential under the influence of intense laser fields is shown for the (a) unperturbed, (b) multi-photon ionization, (c) tunnel ionization, and (d) barrier suppression ionization cases. I_p and γ are the ionization potential and the Keldysh parameter [6].

2.2.3 Beam-induced ionization

Barrier suppression ionization can also be achieved in PWFA, if the Coulomb field of the driver particle bunch exceeds the threshold defined in 2.10. For example, the electric field of a cylindrical electron bunch is given by:

$$E_{r<r_b} = -\frac{en_b r}{2\epsilon_0} \tag{2.12}$$

$$E_{r>r_b} = -\frac{en_b r_b^2}{2\epsilon_0}\frac{1}{r} \tag{2.13}$$

with maximum field at $r = r_b$, with r_b the bunch radius. The peak field of a cylindrical bunch with $n_b = 10^{18}$ cm^{-3} and $r_b = 5$ μm is 45 GV/m, which is higher than the threshold value of 32 GV/m for hydrogen. On the other hand, in absence of a pre-formed plasma, the driver bunch would be affected by head erosion, due to interaction with the neutral gas. For this reason, the production of pre-formed plasmas by means of suitable plasma sources is preferred for PWFA experiments.

2.3 Gas-filled plasma discharge capillaries

Gas-filled plasma discharge capillaries represent one of the most used plasma sources, thanks to the possibility to easily confine and modulate plasma channels. Such sources are based on the generation of confined plasma channels by means of high voltage (HV) electrical discharges [116]. Capillaries are characterized by a central channel with 1-2 mm diameter, which is filled with low pressure gas, e.g. hydrogen, argon or helium, generally from tens to hundreds mbar. In order to have a uniform gas distribution inside the capillary channel, the capillary design can include a variable number of inlets and particular channel shapes, whose effect on the plasma channel uniformity is discussed in Ch4.

Once the capillary is filled with gas, few tens kV pulses are delivered by a specific HV system to a couple of electrodes attached to the capillary extremities, thus producing the plasma discharge. Electrodes, generally made in copper, steel or other metals, are characterized by a central hole which allows driver and witness beams to pass through. This determines a gas and plasma outflow from the capillary channel to the vacuum in the experimental chamber, thus resulting in the formation of density ramps in the plasma plumes, outside the capillary.

Due to the short μs-range duration of HV pulses, the plasma discharge only lasts for few μs. In particular, during the HV pulse, the plasma density increases along with the gas ionization. Then, after the HV pulse is over, plasma recombines into neutral gas atoms and molecules, with a recombination time depending on the plasma peak density and temperature. It is noteworthy that ultra-relativistic beams travel a 30 cm-long capillary within 1 ns, therefore they do not experience the temporal variation of the plasma density. For this reason, a proper synchronization between the plasma discharge and the injection of driver and witness beams into the plasma channel allows to tune the operating plasma density (10^{15}-10^{18} cm^{-3}) at which plasma acceleration is performed.

Capillaries can be machined or 3D-printed and are generally made in plastic, glass or sapphire. Such transparent materials are used to allow both transverse and longitudinal diagnostics, performed by means of spectroscopic and interferometric techniques, as described in Ch3. Three examples of plasma discharge capillary designs are reported in Fig.2.9.

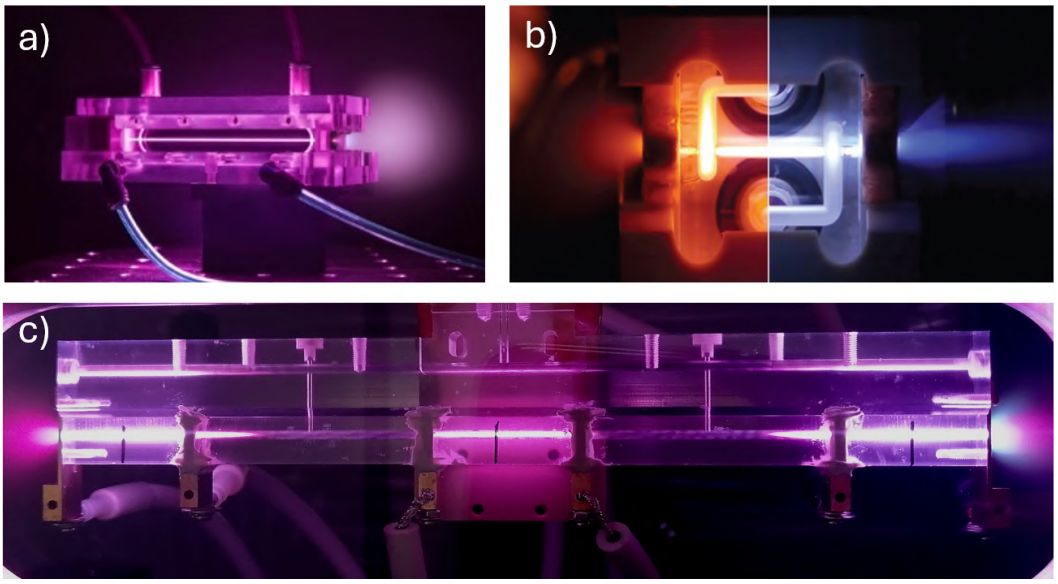

Figure 2.9. Example of discharge capillaries developed at (a) BELLA Berkeley Laboratory, (b) DESY and (c) LNF-INFN.

Due to the stochastic behaviour of plasma discharge formation, shot-to-shot stability can be an important issue for such plasma sources. An easy way to improve the plasma stability is to operate at voltage much higher than the breakdown level, producing almost completely ionized plasma channels. Moreover, shot-to-shot stability can be enhanced by using low power laser pulses, impinging on the anode, to pre-ionize the gas column few μs before HV is applied [16].

Although the advantages of modulability and tunability of the plasma channel density, major issues for discharge capillaries consist in longevity at high repetition rate operation and scalability to m-long sources. In this context, the presented PhD thesis provides novel designs to overcome such limitations, as discussed in Ch.5 and Ch.6.

2.3.1 Active plasma lenses

Apart from plasma acceleration itself, plasma discharge capillaries can be employed as active plasma lenses (APL) for guiding and focusing charged particles. The operation of APLs is based on the magnetic field generated by the electrical current developed during the plasma discharge. According to Ampere Law:

$$\nabla \times \vec{B} = \mu_0 \vec{J} \tag{2.14}$$

in which μ_0 is the vacuum permeability, $\vec{J}$ is the discharge current density and $\vec{B}$ is the associated magnetic field. Assuming cylindrical symmetry and a pure longitudinal discharge current, Ampere Law yields:

$$\frac{1}{r}\frac{\partial}{\partial r}(rB_\phi) = \mu_0 J_z(r) \tag{2.15}$$

$$B_\phi(r) = \frac{\mu_0}{r}\int_0^r J(r')r'\,dr' \tag{2.16}$$

in which r, z and ϕ are the radial, longitudinal and azimuthal coordinates. The focusing strength is then given by:

$$K = \frac{\partial B_\phi(r)}{\partial r}\frac{e_0}{m_0 c\gamma} \tag{2.17}$$

where m_0 and γ are the rest mass and energy of the focused particle. As a result, the plasma discharge current induces an azimuthal magnetic field, which can be exploited to focus charged particle beams in both horizontal and vertical planes. Moreover, plasma discharges with typical peak currents of hundreds of Ampere determine focusing gradients of few kT/m, one order of magnitude higher than conventional quadrupoles, and, in addition, the focusing strength is also easily tunable by changing the discharge current. Thanks to the compactness, tunability and high focusing strength, APLs represent a promising alternative to conventional quadrupoles, which are characterized by maximum focusing strengths of few hundreds T/m and can only focus on one transverse plane at a time. A schematic picture of an active plasma lens is shown in Fig.2.10.

An optimal condition for focusing in an APL is to have a current density perfectly parallel to the capillary axis and with a uniform transverse distribution:

$$J_{ideal} = \frac{I}{\pi R^2} \tag{2.18}$$

where I is the current intensity and R is the radius of the capillary channel. In this case, the magnetic field would be linear with the radial position:

$$B_{ideal} = \frac{\mu_0}{2}J_{ideal}r = \frac{\mu_0 I}{\pi R^2}r \tag{2.19}$$

providing a linear emittance-preserving focusing force, which pushes charged particles towards the capillary axis with intensity proportional to the particle transverse offset. However, according to Ohm Law, the current density is proportional to the plasma conductivity:

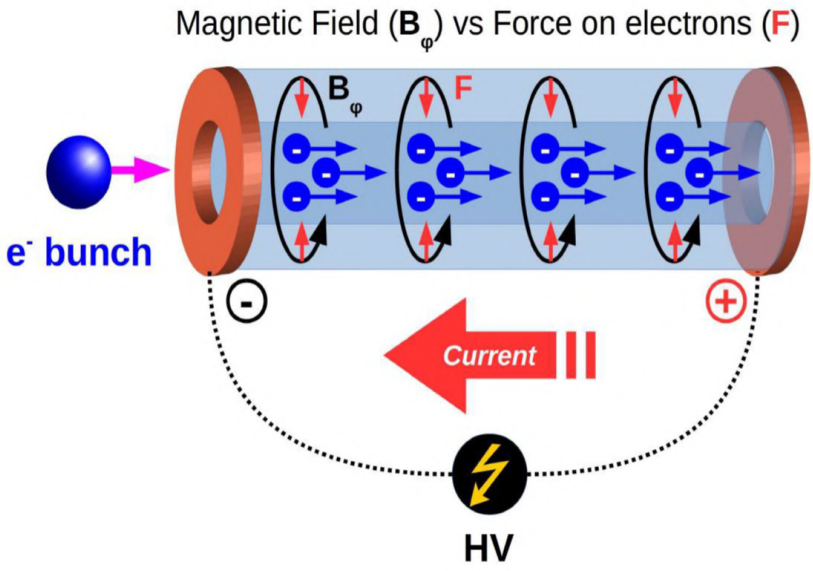

Figure 2.10. Schematic representation of the focusing effect in an active plasma lens [32].

$$J_z(r) = \sigma(r) E_z \tag{2.20}$$

which, in turn, depends strongly on the plasma temperature and weakly on the plasma density [68]:

$$\sigma(r) \propto \frac{T_e^{3/2}}{ln\lambda(n_e, T_e)} \tag{2.21}$$

Due to thermal balance between ohmic heating and heat conduction with the colder capillary walls, the transverse distribution of the plasma temperature is characterized by an on-axis peak and a radial gradient towards the boundary walls. Hence the plasma conductivity is affected by transverse gradients as well, leading to a non-linear magnetic field. In addition, non-linearity can also be caused by partial ionization of the gas column, which forces the current to flow closer to the axis. For example, Fig.2.11 reports the radial profile of the azimuthal magnetic field and the ionization degree for a 130 A peak current H_2 discharge [32], highlighting the non-linear behaviour of the magnetic field towards the capillary walls, where the plasma is weakly ionized [98].

Among the possible applications, APL can play a key role for beam injection and extraction from plasma acceleration stages, since strong focusing fields are required for the beam matching, as discussed in 1.4.2.

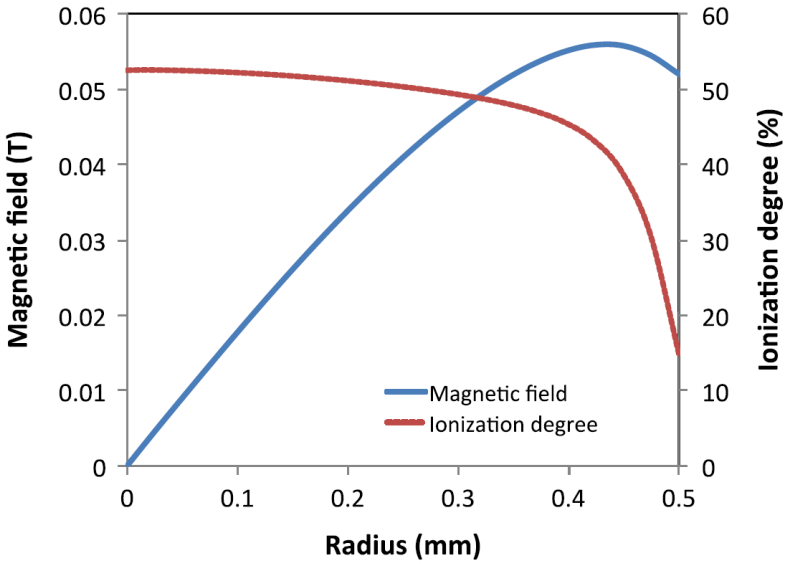

Figure 2.11. Radial profile of the azimuthal magnetic field and the ionization degree for a 130 A peak current H_2 discharge [32].

2.3.2 Capillary discharge waveguides

Another application for plasma discharge capillaries concerns the guiding of high intensity laser pulses. As mentioned in 1.4.2, laser diffraction is a major limitation for LWFA mechanism and it can be mitigated by the focusing effect of plasma channels with radial density gradients, which allow to guide laser pulses over many Rayleigh lengths. In particular, Gaussian laser pulses can be guided by parabolic radial density profiles as:

$$n_e(r) = n_e(0) + \Delta n_e \frac{r^2}{R^2} \tag{2.22}$$

where r is the radial coordinate, R is the plasma channel radius and $n_e(0)$ is the on-axis plasma density. Such density profile, corresponding to a radially decreasing refractive index, is able to guide a laser pulse with matched spot size:

$$w_m = \left(\frac{R^2}{\pi r_e \Delta n_e} \right)^{1/4} \tag{2.23}$$

where r_e is the classical electron radius. Plasma channels with such transverse density modulation can be easily produced by plasma discharge capillaries. As mentioned for APLs, the thermal balance between ohmic heating, related to the electrical discharge, and the heat conduction with the capillary walls determines a radial plasma temperature profile with an on-axis peak and a decreasing gradient towards the boundary walls. The associated pressure gradient causes a re-distribution of the plasma density until the pressure is approximately constant along the capillary radius, with a steady-state parabolic density profile given by [21]:

$$\frac{n_e(r)}{n_e(0)} \approx \left(1 + 0.33\frac{r^2}{R^2} + ...\right) \tag{2.24}$$

with R the channel radius.

For instance, Fig.2.12 reports the hollow radial density profiles measured by [73]. In this work, a Mach-Zehnder interferometer system was adopted to measure the transverse plasma density distribution outside a 2 cm-long glass discharge capillary, characterized by two ends with 300 μm and 500 μm diameter and a monotonic increase of the capillary channel. Plasma density distribution, obtained by means of 8 kV discharge pulses and measured 500 ns after the discharge initiation and 100 μm outside the external electrodes, are characterized by hollow radial profiles, with more than 50% of density decrease from the lateral peaks to the on-axis minimum.

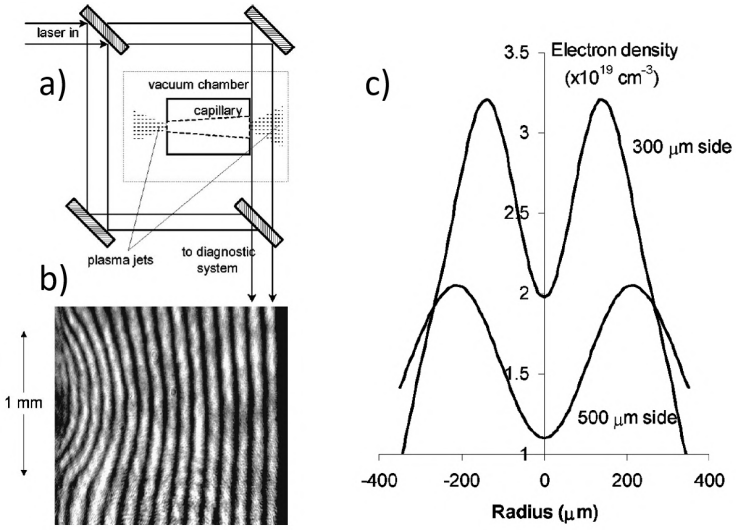

Figure 2.12. (a) Experimental setup for the characterization of the plasma discharge capillary by means of Mach-Zehnder interferometry. (b) Example of interference pattern acquired by a CCD camera. (c) Radial hollow profiles measured at both sides of the capillary, 100 μm outside the external electrodes and at a delay of 500 ns after the discharge initiation [73].

The parabolic density profile produced in plasma discharge capillaries provides laser guiding with a matched spot size:

$$w_m \approx \left(\frac{R^2}{0.33\pi r_e n_e(0)}\right)^{1/4} \tag{2.25}$$

Discharge capillary waveguides have been employed to guide laser pulses with up to 10^{17} W/cm^2 over more than 5 cm distance [26]. Moreover, laser heating can be coupled to the electrical discharge to improve the focusing effect [20]. After the discharge initiation, a long ns-range laser pulse can be used to heat plasma electrons on axis, producing a deeper radial density profile. In addition, by tuning the laser energy, it is possible to control the channel width and depth. This option allows to reduce the on-axis plasma density and increase the matched spot size, which is crucial for guiding high power PW-range laser pulses [61].

2.4 Gas jets

Due to their simplicity, supersonic gas jets represent one of the most common sources used for plasma-based acceleration experiments. The geometry of such devices is based on a convergent-divergent configuration, analogous to de Laval nozzles. High pressure gas (up to 100 bar) is contained in a proper tank and released by a fast valve into the a conical nozzle. After reaching supersonic velocities through the divergent section of the nozzle, the gas enters the interaction region, in which it is ionized by a laser pulse to produce the plasma channel.

The nozzle geometry, in particular the choke and exit diameters and the nozzle height, are designed according to the desired density profile [110]. Flat-top profiles can be obtained with simple geometries, as the one reported in Fig.2.13, whereas more complex geometries are used for a fine control of density ramps. In addition, razor blades can be placed at the exit of gas jets to produce a shock-front in the plasma density profile, triggering controlled electrons injection in a localized region and thus producing high charge, low energy spread beams [24].

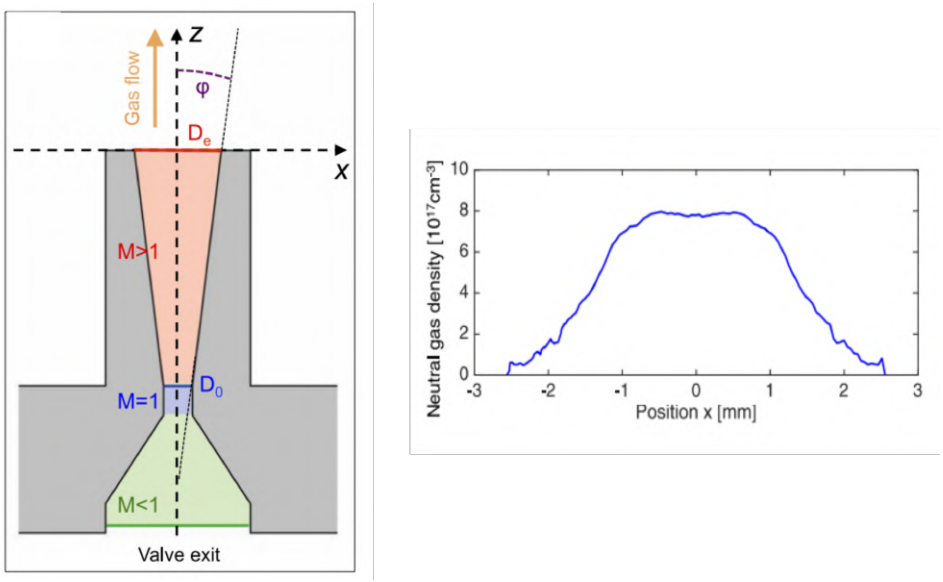

Figure 2.13. (Left) Schematic representation of a supersonic gas jet. The gas flow is tailored by the design of the choke and exit diameters D_0 and D_e and the opening angle ϕ. M is the Mach number in each region of the conical nozzle. (Right) Flat-top density profile achieved by design optimization [110].

A further advantage of the gas jet is the 360° degree access to diagnostics and the easy alignment. On the other hand, the major drawback of gas jets is the large gas volume injected in the experimental chamber, which must be removed by the vacuum system, preventing high repetition rate operation above few Hz. Moreover, the injection of high pressure gas also causes erosion and damage of mechanical components. In addition, imperfections on the nozzle surface can lead to ripples in the gas density profile, causing unwanted self-injection and acceleration of dark current [77].

2.5 Gas cells

Gas cells consist of cylindrical or cubic structures, filled with low pressure gas in the range from few mbar to 1 bar. Two metallic plates with pinholes are placed at the ends of the cell to confine the injected gas and allow the propagation of driver and witness beams [12]. The described geometry allows to create a flat-top plasma density distribution within the two plates and density ramps towards the pinholes, through which the plasma expands entering the experimental chamber. The pinhole diameter and the plate thickness determine the shape of the density ramps, whereas the length of the density flat-top can be tuned by changing the distance between the plates. An example of ELISA (ELectron Injector for compact Staged high energy Accelerator) gas cells, developed at CNRS, is reported in Fig.2.14.

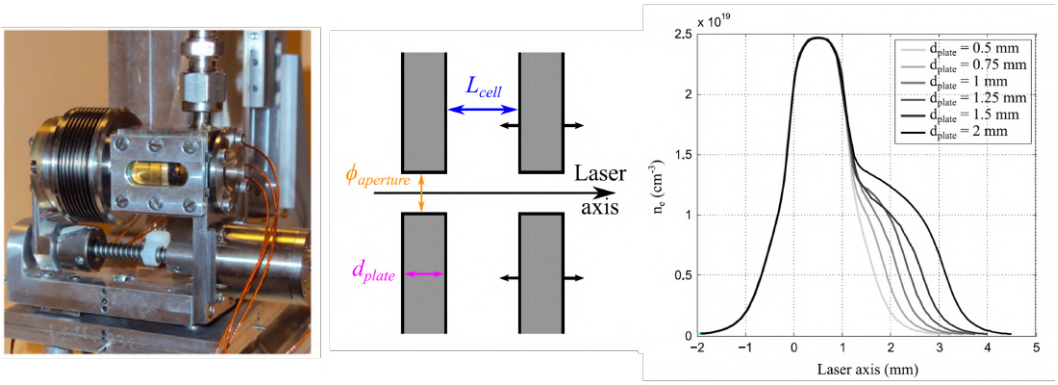

Figure 2.14. (Left) Picture of ELISA gas cell. (Center) Schematic longitudinal cut of the gas cell. (Right) Longitudinal plasma density profiles with different plate widths for the modulation of the exit density ramp [12].

Alternative gas cells have been designed for longitudinal tapering of plasma density distribution, including "sandwich" targets based on the assembly of transparent glass or sapphire layers, as shown in Fig.2.15. In such sources the gas is injected from two independent reservoirs into a main square channel, in which the plasma is produced by an intense laser pulse. The presence of two independent feedlines allows for a fine tuning of the gas distribution, and thus the plasma density profile, and also the possibility to use particular gas mixtures.

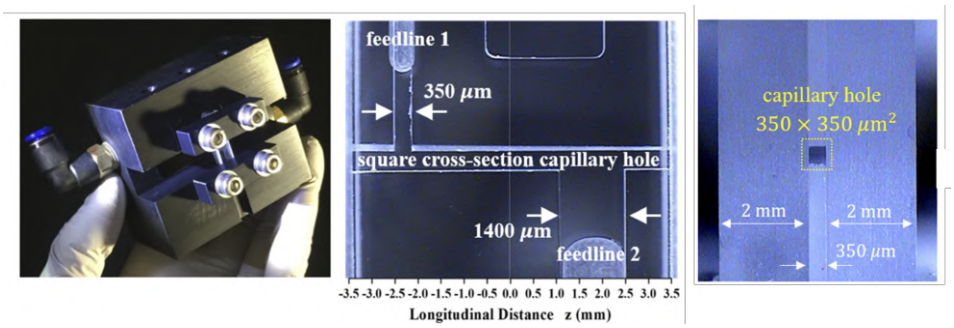

Figure 2.15. (Left) Detailed picture of the gas cell developed by [75]. (Center) Front view and (Right) side view of the assembled cell.

Compared to gas jets, the lower pressure of injected gas allows high repetition rate operation and higher shot-to-shot stability. However, damage of the pinhole, due to the interaction with high intensity laser pulses, can strongly affect the gas cells longevity.

2.6 HOFI channels

Hydrodynamic Optical-Field-Ionized plasma channels represent a novel plasma source for high repetition rate plasma-based applications, including laser guiding and plasma acceleration.

In hydrodynamically formed plasma channels, a cylindrical region of plasma, contained in a gas cell, is formed and heated by one or more laser pulses [112]. Rapid expansion of the plasma column drives a radial shock into the cold, neutral ambient gas to form a transverse electron density profile which increases with radial distance out to the position of the shock front. Such plasma sources are a promising solution for practical plasma accelerators working at kHz-range repetition rate operation, since the plasma channel is free-standing, with no nearby physical structure that could be damaged by the driver pulse.

Initial versions of hydrodynamic expanded plasma channels were based on laser-driven electron-ion collisions. However, since rapid collisional heating requires high plasma densities, it has proved difficult to generate channels with low on-axis densities. For example, plasma channels with typical central densities of around 10^{18} cm^{-3} have been obtained in argon gas [34].

To overcome such limitation, hydrodynamic expansion of plasma columns based on Optical Field Ionization (OFI) allows to generate long and deep plasma channels with low propagation losses. Since OFI operates at the atomic level, the electron heating is independent of the initial density, thus allowing the formation of low density plasma channels. In addition, axicon lenses can be used to focus the ionizing laser pulse over long distance, achieving the production of tens cm-long plasma channels with 10^{17} cm^{-3} plasma density and matched spot sizes of around 40 μm [112]. An example of a HOFI channel, designed at Oxford University, is reported in Fig.2.16.

An improvement in the production of low-density, low-loss, meter-scale plasma channels can be obtained by ionizing the neutral gas collar surrounding the HOFI channel by means of a conditioning laser pulse (CHOFI channels). Such method allows to increase the attenuation length by two orders of magnitude, enhancing the plasma channel length to the m-scale [92].

An example of transverse plasma density profiles obtained with HOFI channels is reported in Fig.2.17, while Fig.2.18 shows the long-term stability of the HOFI channel during operation in the kHz-range [3].

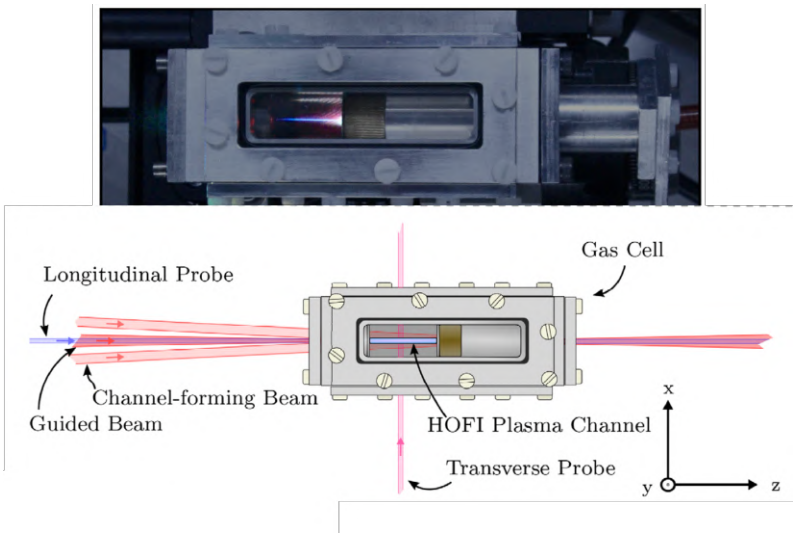

Figure 2.16. (Top) Picture of a 16 mm-long HOFI plasma channel. (Bottom) Schematic representation of the interaction region and the plasma channel formation [113].

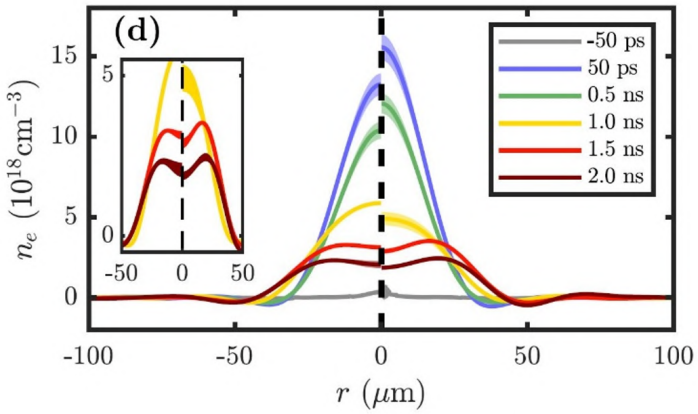

Figure 2.17. Temporal evolution of the transverse electron density profile produced by: (left) a single channel-forming pulse and (right) the second of a pair of channel-forming pulses separated by 1 ms. 1 mJ, 40 fs laser pulses with 5 μm spot size are used to ionize 350 mbar ambient gas [3].

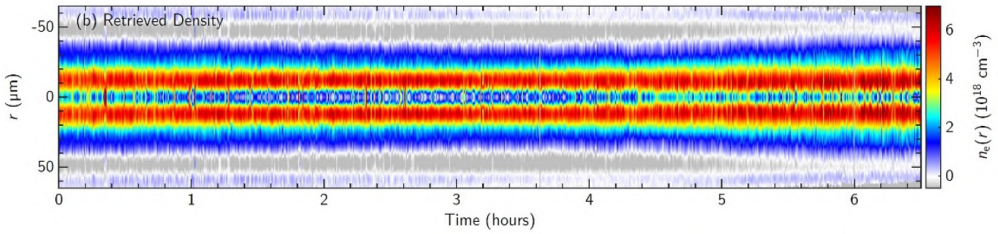

Figure 2.18. Transverse electron density profiles of the HOFI channels formed 1.5 ns after the second of the pair of channel-forming pulses, separated by 1 ms. Measurements are acquired at 200 Hz operation over a period of 6.5 hours [3].

2.7 Alkali metal vapor heat-pipe ovens

In the framework of AWAKE project, m-long plasma sources based on the ionization of alkali metal vapors are used. First versions of such sources, developed at SLAC, consist of heat-pipe ovens, in which few milligrams of lithium are heated to 750°C to produce lithium vapor columns, reaching neutral density of 10^{15}-10^{16} cm^{-3} [89]. The hot Li vapor is confined to the heated central part of the heat-pipe by means of room temperature He buffer gas, located at the ends of the heat-pipe. The Li density is determined by adjusting He pressure, while the length of the Li column is approximately equal to the length of the heated section of the pipe, and can be varied around that value by changing the heating power delivered to the oven [88].

Lithium is adopted for its low ionization potential (5.3 eV) and thus can be ionized over a large volume through a single photon absorption process, using UV laser pulses focused with an axicon lens to ionize the entire vapor column. The low ionization potential of alkali metals allows to produce fully ionized plasma channels, whose uniformity is given by that of the neutral vapor column. Therefore, uniform 10^{14}-10^{16} cm^{-3} plasma channels are obtained by controlling the temperature uniformity inside the oven.

A recent upgraded version of such plasma sources is based on Rubidium, having lower ionization potential (4.18 eV) and requiring lower temperatures for desired density values (150-200°C) [130]. In this version, independently heated liquid reservoirs provide the desired Rb vapor density into a 10 m-long 2 cm-radius pipe, which is heated by another independent circuit. The use of two independent heating systems allows to keep the pipe temperature two degrees above that of the reservoirs, thus preventing Rb condensation inside the pipe. Such operating principle represents a major improvement compared to lithium pipe-ovens, which are based on a dynamic equilibrium, with lithium constantly condensing, evaporating and circulating from the hot region of the device to the cold region, by means of a fine metal structure surrounding the inner surface of the heat-pipe [130]. Fast valves are used to let proton, electron and laser beams pass through the heat-pipe. Schematic representations of the two heat-pipe oven versions are shown in Fig.2.19.

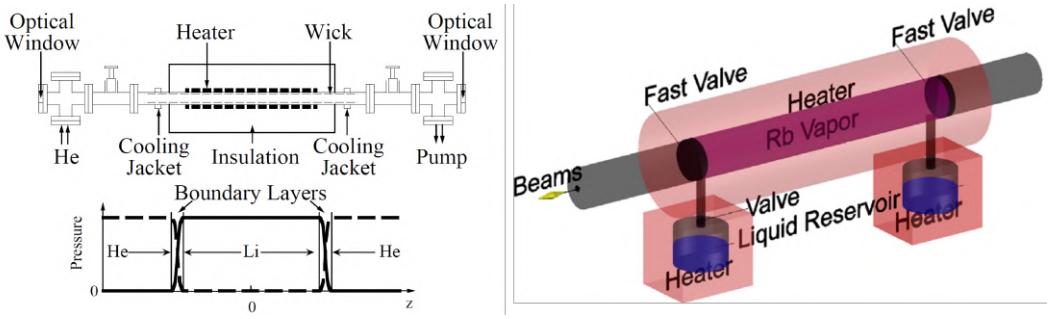

Figure 2.19. Schematic representations of (Left) Lithium and (Right) Rubidium heat-pipe ovens [89][130].

After this general overview on plasma sources, the following chapters are devoted to describe the activities carried out in the context of the presented PhD thesis project. In particular, chapter 3 provides a detailed description of the experimental setup of the plasma module, used at Plasma_lab laboratory to test and characterize plasma discharge capillaries, designed in the framework of EuPRAXIA@SPARC_LAB project.

Chapter 3

Design and characterization of plasma discharge capillaries at Plasma_lab

Plasma sources design and characterization is carried out at Plasma_lab laboratory, located at the National Laboratory of Frascati (LNF-INFN), in the framework of SPARC_LAB collaboration. Experimental and theoretical activities mainly concern the development of plasma discharge capillaries, which are adopted at SPARC_LAB accelerator facility for plasma-based acceleration experiments, as mentioned in Ch.1. Experimental activities include the optimization of the capillary design and the development of the overall plasma module, aimed at improving the stability, reproducibility and uniformity of plasma discharges and enhance the compactness, cost-effectiveness and longevity of tested plasma sources.

3.1 Plasma module setup

The plasma module set up to test and characterize plasma discharge capillaries, is reported in Fig. 3.1. Capillaries are installed inside a vacuum chamber and filled with pure H_2 or different gas mixtures, injected by means of a dedicated gas injection system. A set of vacuum pumps extracts the gas that flows outside the capillary, keeping a vacuum level of 10^{-2}-10^{-3} mbar inside the chamber, suitable to produce and confine plasma discharges.

A high voltage (HV) system delivers kV-range pulses to a couple of electrodes attached to the capillary ends, thus ionizing the gas column inside the capillary channel and producing the plasma discharge. The waveform of the discharge current is acquired by means of an oscilloscope, connected to the HV system. A delay generator synchronizes the HV system with the gas injection system, allowing to deliver high voltage pulses when the capillary channel is filled with neutral gas. In addition, a diagnostic system allows to characterize the plasma discharge by means of the spectroscopic analysis of the plasma-emitted light.

A detailed description of the main components of the plasma module is provided in the following sections.

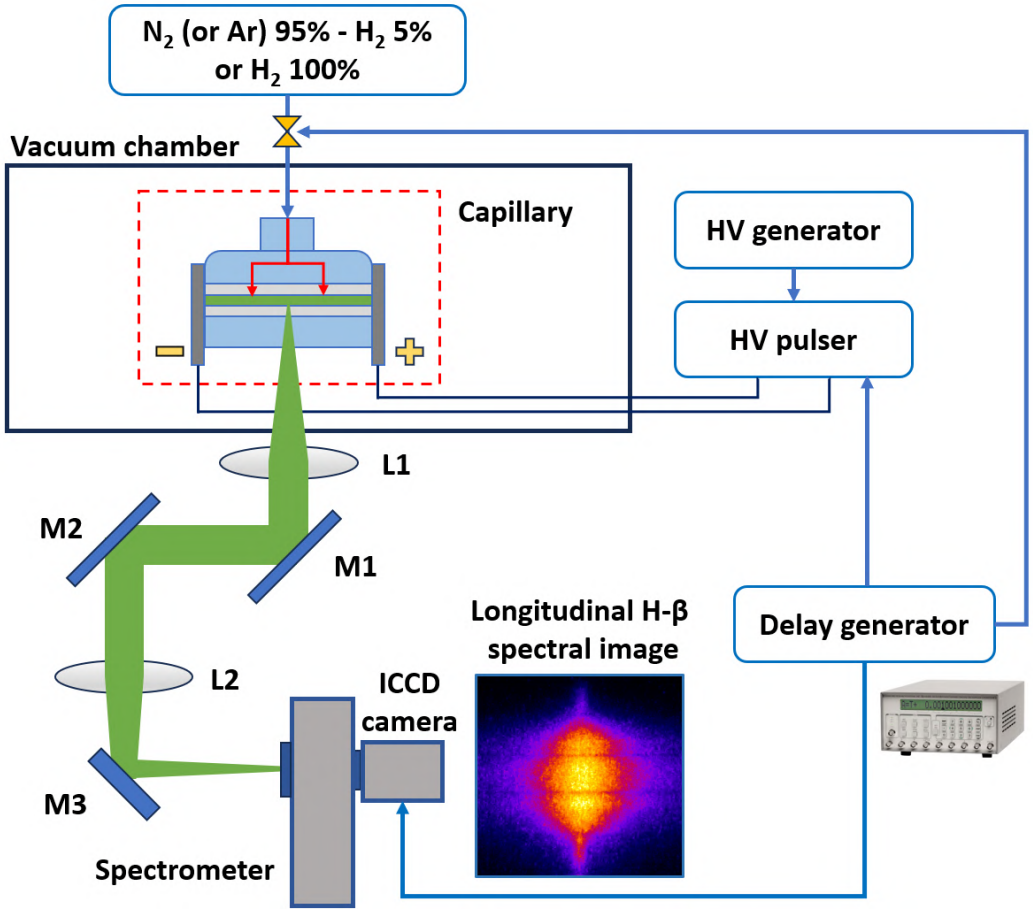

Figure 3.1. Plasma module experimental setup

3.2 Design of plasma discharge capillaries

In the context of the PhD thesis project, a variety of capillaries with different materials and geometrical configurations have been tested, as shown in Fig.3.2. Typical capillary lengths range from 3 cm to tens of centimeters (up to the 60 cm length targeted for EuPRAXIA@SPARC_LAB project), with cylindrical channels having 1-2 mm diameter.

Short capillaries with various number of inlets or particular channel shapes have been tested to determine an optimal configuration for a uniform gas injection into the capillary channel, in order to enhance the plasma density uniformity. For such investigation, tested capillaries are 3D-printed and made in VeroClear, a transparent rigid material that simulates PMMA (polymethyl methacrylate).

On the other hand, longer capillaries are generally produced by mechanical processing of Lexan blocks, which provides a higher precision in the production of thin and long channels.

For high repetition rate studies, plastic materials experience rapid erosion, due to the thermal load delivered by plasma discharges onto the inner capillary walls. For this reason, experimental testing on high melting temperature materials are

performed, including sapphire and ceramics.

Each capillary design includes a series of screw threads, realized on the capillary extremities to attach the electrodes, which in turn are connected to the HV system by means of copper cables. Electrodes are usually made in copper or stainless steel, even though other metals are employed for high repetition rate studies. Cylindrical holes are created into the electrodes, in order to let particle and laser beams pass through the capillary.

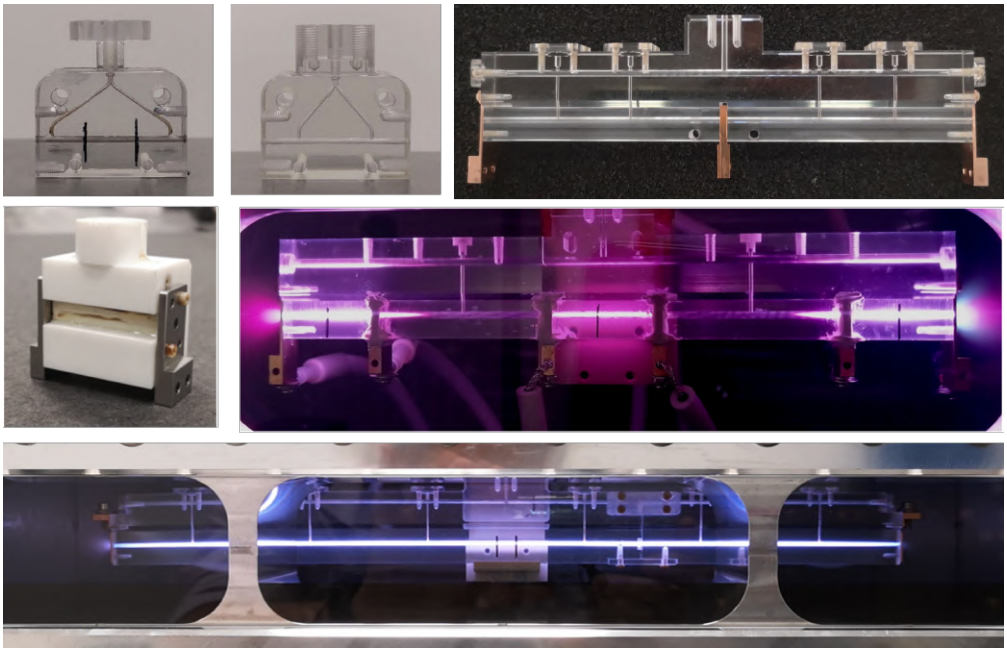

Figure 3.2. Plasma discharge capillaries tested at Plasma_lab

3.3 Gas injection and vacuum systems

The gas injection system includes a NM Plus Hydrogen Generator, which produces pure hydrogen through water electrolysis, and a set of gas tanks, containing mixtures of N_2-H_2 or Ar-H_2 with 5% hydrogen, thus allowing the possibility to use different gas mixtures for the plasma formation. Hydrogen is usually present in gas mixtures, even in small percentage, because it provides a useful method to characterize the plasma discharges, as described in Sec.3.6. A gas distribution network injects the gas into the vacuum chamber, filling the installed capillary. The gas pressure is controlled by means of a mechanical regulator, located outside the chamber, which reduces the injection pressure from 2-5 bar to 100-800 mbar. In addition, an electro-mechanical valve is installed upstream the vacuum chamber to control the repetition rate of the gas injection, with typical frequency of 1-10 Hz and a valve opening time of few milliseconds. Moreover, the valve provides a further decrease of the gas pressure, with a final range of 20-50 mbar inside the capillary.

Once the gas fills the capillary, it flows through the electrodes holes and expands inside the vacuum chamber, in which it is extracted by a set of vacuum pumps. In

particular, two primary scroll pumps and a turbo-molecular pump are used, keeping a vacuum level of 10^{-2}-10^{-3} mbar during the gas injection and 10^{-6} mbar at rest.

3.4 High voltage system for plasma formation

The high voltage system includes a HV generator, feeding in DC operation a HV electrical pulser circuit up to 20-25 kV, which is the operative limit of the circuit. The HV pulser circuit is constituted by a set of resistors and capacitors, which charge and discharge within the μs range, and a SCR switch which delivers kV-range μs pulses to the capillary electrodes through a couple of copper cables, as reported in Fig. 3.3.

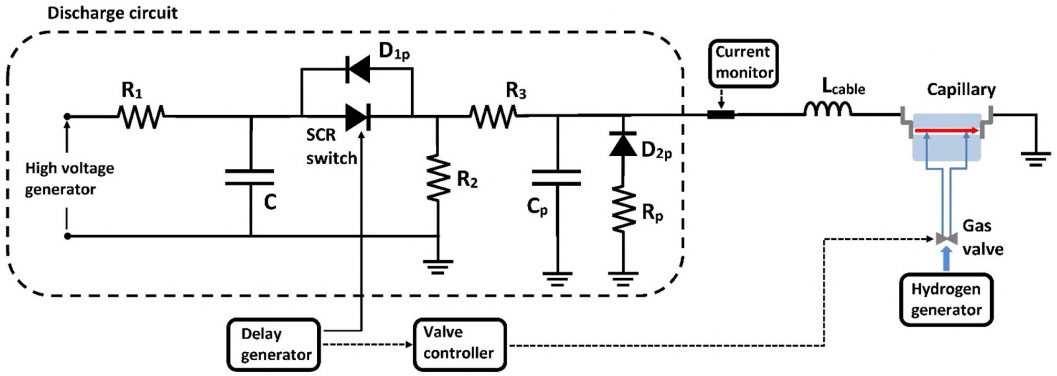

Figure 3.3. Schematic representation of the high voltage system

The circuit branch composed by the protection diode D_{2p} and the resistor R_p prevents any negative overshoot of the current at the end of the current pulse, while the protection diode D_{1p} is used to bypass negative pulses up to 1 kA, that could damage the SCR switch.

As the voltage pulses trigger the electrical breakdown inside the capillary, the resulting discharge current is measured by means of a Pearson 110 probe, which converts the current pulse into a voltage signal with a transfer impedance of 0.1 V/A. The voltage signal is then acquired by a WaveAce 2032 oscilloscope, characterized by a 300 MHz bandwidth, a 1.2 ns rise time, an input range of ± 5 V and a vertical resolution of 8 bits, corresponding to a precision of 10 V/2^8 = 40 mV.The waveform of the discharge current pulse is retrieved by applying the 0.1 V/A factor to the voltage pulse acquired by the oscilloscope.

The typical waveform of a current pulse, produced by a HV capillary discharge, is shown in Fig.3.4a. The reported discharge current waveform is obtained by applying 20 kV pulses to a 3 cm-long 1 mm-diameter capillary, ionizing around 50-100 mbar of hydrogen (breakdown voltage around 5 kV).

In addition, the characteristic current-voltage curve of the pulser circuit is shown in Fig.3.4b for a short circuit configuration and a 3 cm-long capillary, with maximum current of 1200 A and 1100 A respectively. The lower current produced with the capillary is due to the electrical resistance of the plasma channel, which increases with the capillary length.

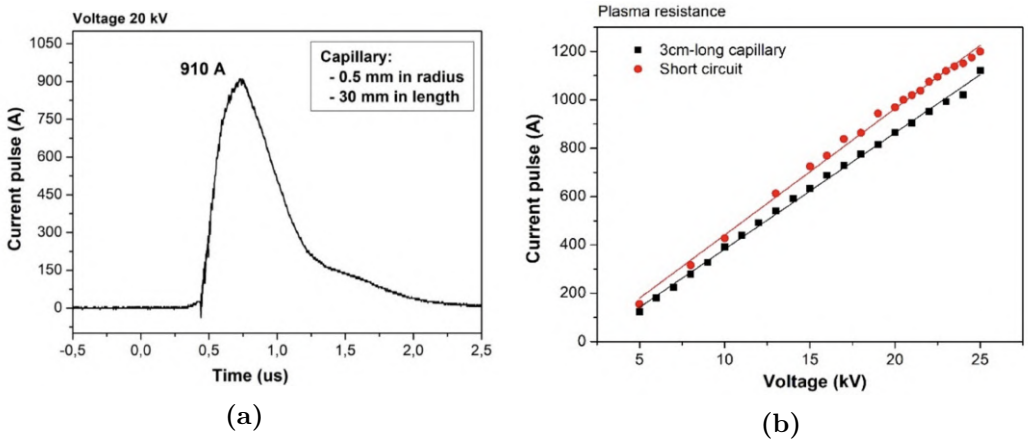

Figure 3.4. (a) Current pulse waveform produced with 20 kV pulses delivered to a 3 cm-long 1 mm-diameter capillary. The FWHM pulse duration is around 600 ns. (b) Peak current as a function of the applied voltage in short circuit configuration (red circles) and with a 3 cm-long capillary (black squares). The lower peak current achieved with the capillary is due to the plasma channel resistance. The pulser circuit characterization is performed in the range 5-25 kV, from around the breakdown condition to the operative limit of the circuit.

The switch activation is synchronized to the electro-mechanical valve by means of a delay generator (Stanford Research DG535), which triggers the ionization of the gas column, and thus the plasma discharge formation, only once the capillary is filled with gas. Typically, the valve opening time is set to 3-5 ms, after which the gas has reached a steady state distribution along the capillary. 5-10 ms after the valve closure, the SCR switch triggers the plasma discharge. Such delay is manually set to optimize the plasma discharge formation.

With capillary lengths of around 3 cm and gas pressure of 50 mbar, the voltage breakdown is around 3 kV, as shown by the Paschen curve for hydrogen gas reported in Fig.3.5.

The highest achievable plasma density depends on the gas pressure. Indeed, according to the Ideal gas Law:

$$p = n_m k_B T \tag{3.1}$$

in which p and T are the gas pressure and temperature, while n_m and k_B are the molecular gas density and the Boltzmann constant. Considering 50 mbar of pure H_2 at room temperature, the molecular density inside the capillary channel is around 1.2×10^{18} cm^{-3}. Since the ionization of a hydrogen molecule produces two free electrons, the highest achievable electron plasma density is around 2.4×10^{18} cm^{-3}, in case of complete gas ionization.

By setting the applied voltage from 5 to 20 kV, it is possible to tune the plasma density by changing the ionization degree inside the plasma channel.

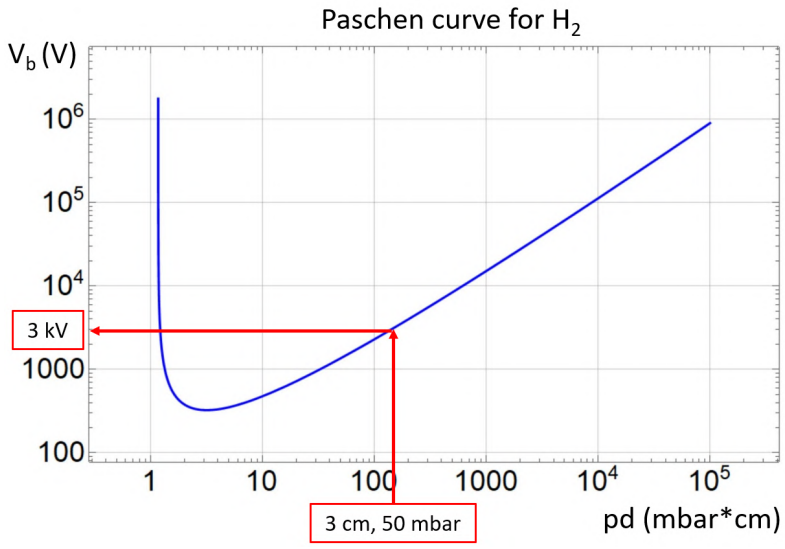

Figure 3.5. Paschen curve for hydrogen, showing the breakdown voltage dependence on the product between pressure and length of the gas column.

3.5 Plasma Diagnostic system

The plasma diagnostics system is based on the spectroscopic analysis of the plasma-emitted light. The light emitted during the plasma discharge exits the capillary, usually made in transparent materials, and is transmitted by a window installed on the vacuum chamber. Outside the chamber, the light is collected through an optical line, made of a series of 3" mirrors and lenses, and is guided into an imaging spectrometer (SpectraPro 275), equipped with an intensified CCD Camera (Andor Istar 320).

3.5.1 Design of the optical line

The optical line, shown in Fig.3.6, is made of a telescopic system (including L_1 and L_2 lenses), which reproduces the image of the plasma discharge at the spectrometer entrance, matching the plasma channel length to the dimension of the spectrometer slit.

Given the vertical dimension of the slit and the portion of the plasma channel light collected by the mirrors, respectively around 6 mm and 5 cm, the required magnification is:

$$M = \frac{6}{50} \approx \frac{1}{8} \tag{3.2}$$

Since the transport line is made of two lenses, the corresponding magnification factors are:

$$M_1 = \frac{1}{4}, \quad M_2 = \frac{1}{2} \tag{3.3}$$

Given the focal lengths of L_1 and L_2, respectively $f_1 = 15$ cm and $f_2 = 8$ cm, the lenses position is determined through the Lens Maker formula and the magnification

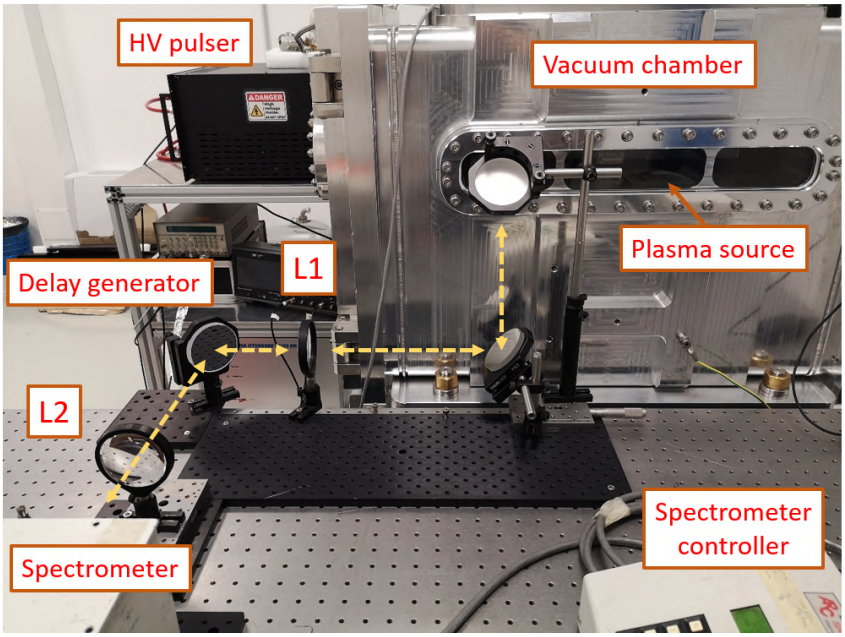

Figure 3.6. Picture of the optical line in the experimental setup

factors:

$$\begin{cases} \frac{1}{p_1} + \frac{1}{q_1} = \frac{1}{f_1} \\ M_1 = \frac{q_1}{p_1} \end{cases} \qquad \begin{cases} \frac{1}{p_2} + \frac{1}{q_2} = \frac{1}{f_2} \\ M_2 = \frac{q_2}{p_2} \end{cases} \tag{3.4}$$

in which p and q represent the object-lens and lens-image distances. As a result, $p_1 = 75$ cm and $q_1 = 18.75$ cm, whereas $p_2 = 24$ cm and $q_2 = 12$ cm. Therefore, L_1 is located 75 cm downstream the capillary, L_2 is placed around 43 cm after L_1 (distance given by $p_2 + q_1$) and the spectrometer is positioned 12 cm after L_2, where the 1/8 de-magnified image of the plasma discharge is located.

The light collected into the spectrometer is decomposed by a 1200 grooves/mm diffraction grating, used to select hydrogen spectral lines which are then guided onto the ICCD camera objective. Spectral images of hydrogen lines are then analyzed to recover the density distribution of the plasma discharge, relying on the Stark broadening method [63], as described in the following section.

3.6 Stark broadening method for plasma density measurements

Generally, the light coming from a plasma discharge is emitted after the plasma recombination into neutral atoms and molecules, occurring when the electrical discharge is over. Once free plasma electrons return to bound atomic states, they perform a sequence of optical transitions from outer to inner energy levels, resulting in the emission of photons. In particular, considering the hydrogen atom, optical transitions from states with principal quantum number $n \geq 3$ to $n = 2$ compose the so-called Balmer series, which is characterized by photon emission in the visible range

of the electromagnetic spectrum. The wavelengths of the Balmer series emission lines can be obtained by the Rydberg formula:

$$\frac{1}{\lambda} = R_H \left(\frac{1}{m^2} - \frac{1}{n^2} \right) \tag{3.5}$$

in which $R_H = 1.097 \times 10^7$ m^{-1} is the Rydberg constant for hydrogen and m and n refer to the final and initial energy levels. In particular, concerning the Balmer series, $m = 2$ and $n \geq 3$. The wavelengths of the emission lines are reported in Table. 3.1 together with the corresponding electronic transitions. Hydrogen emission spectrum in the visible range is reported in Fig. 3.7, together with the other spectral series in the infrared and ultraviolet range.

Name	Transition	Wavelength [nm]
H-α	3→2	656.279
H-β	4→2	486.135
H-γ	5→2	434.0472
H-δ	6→2	410.1734

Table 3.1. Nomenclature, transitions and corresponding wavelengths of hydrogen spectral lines of the Balmer series

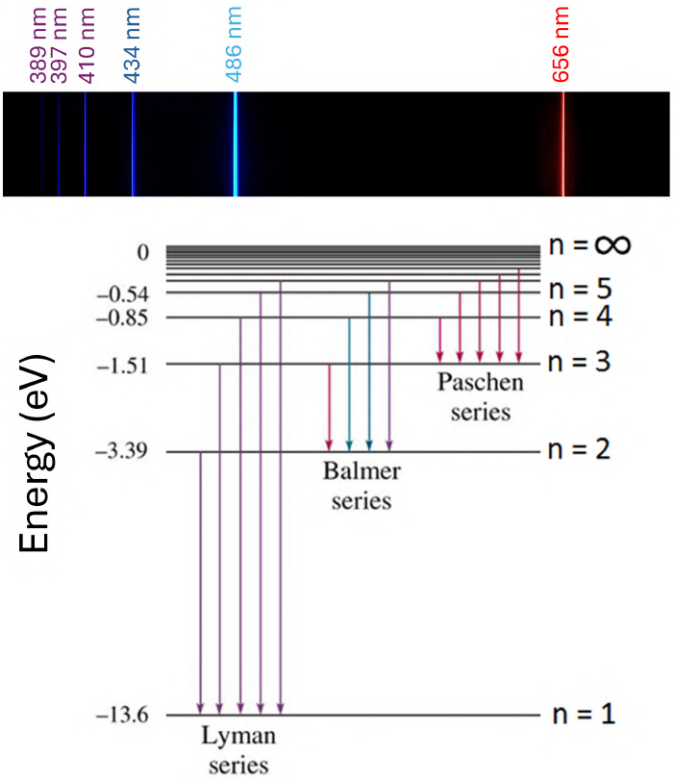

Figure 3.7. (Top) Hydrogen spectral lines of the Balmer series in the visible region. (Bottom) Optical transition series in the UV, visible and IR region (respectively Lyman, Balmer and Paschen series).

In presence of a plasma, in which free charged particles give rise to electromagnetic fields, hydrogen emission lines experience a characteristic broadening that can be related to three main mechanisms.

3.6.1 Natural broadening

According to Heisenberg principle, atomic levels are characterized by an intrinsic energy uncertainty related to their lifetime:

$$\Delta E \Delta t \geq \frac{\hbar}{2} \tag{3.6}$$

Regarding the hydrogen atom, while the ground state ($n = 1$) is stable ($\Delta t = \infty$) and has a determined energy level, the excited states are characterized by energy uncertainty, including the initial and final ones of the Balmer series. Given $E = \hbar\omega$, the energy uncertainty translates into a frequency (or wavelength) uncertainty:

$$\Delta \omega \Delta t \geq \frac{1}{2} \tag{3.7}$$

As a result, the energy uncertainty of the atomic levels of optical transitions determine a "natural" broadening of the corresponding emission lines.

3.6.2 Doppler effect

Due to thermal motion of atoms, photons emitted during optical transitions experience a Doppler shift, which depends on the gas temperature, thus resulting in a characteristic broadening of the corresponding spectral line. Considering a gas in thermodynamic equilibrium, particle velocities are described by the Maxwell-Boltzmann distribution function:

$$f(\vec{v}) = \left[\frac{m}{2\pi k_B T}\right]^{3/2} exp\left(-\frac{mv^2}{2k_B T}\right) \tag{3.8}$$

When a particle emits a photon, while moving towards the observer with velocity $\vec{v}$, the photon emission is characterized by a Doppler shift given by:

$$\frac{\omega - \omega_0}{\omega_0} = \frac{v}{c} \tag{3.9}$$

where ω_0 is the central frequency of the emission line. Therefore, given the relation between the Maxwellian velocity distribution of light emitters and the shape of the corresponding spectral line:

$$L_D(\omega)d\omega = f(\vec{v})d\vec{v} \tag{3.10}$$

and including the Doppler shift 3.9, the spectral line profile due to Doppler effect is given by [64]:

$$L_D(\omega) = \frac{c}{\omega_0} f\left(c\frac{\omega - \omega_0}{\omega_0}\right) \tag{3.11}$$

The obtained Gaussian distribution, describing the so-called Doppler broadening of a spectral line, is characterized by a FWHM linewidth:

$$\Delta\omega = \omega_0 \sqrt{8ln(2)\frac{k_B T}{m_a c^2}} \tag{3.12}$$

or in wavelength units:

$$\Delta\lambda = \lambda_0 \sqrt{8ln(2)\frac{k_B T}{m_a c^2}} \tag{3.13}$$

in which λ_0 is the unshifted wavelength and m_a is the emitter atomic mass. Concerning Doppler broadening in plasmas, 3.13 highlights the dependence on the plasma temperature, while no direct role is played by the particle density.

3.6.3 Stark effect

Regarding spectral emission in plasmas, spectral line broadening can be also related to the plasma pressure. The so-called pressure broadening is generally due to the interaction of emitting atoms with the electric fields established by surrounding charged particles, even though in some cases also the interaction with neutral atoms, through Van der Waals forces, becomes significant. The interaction of neutral atoms with the external electric field produced by plasma electrons determines the Stark effect, consisting in the splitting of energy levels of the emitting atom, as depicted in Fig. 3.8.

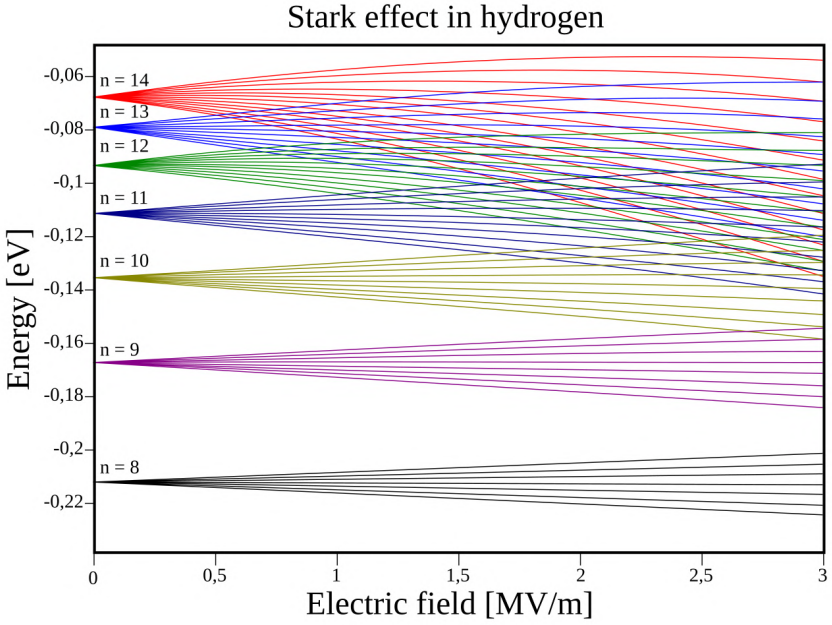

Figure 3.8. Energy level spectrum of hydrogen as a function of the external electric field. Each n level consists of $n-1$ degenerate sub-levels and the application of the external electric field breaks the degeneracy [70].

Due to the energy levels splitting, optical transition photons are emitted in a wider energy range, corresponding to broader spectral lines. For isolated lines, not overlapping with other transitions in the same spectrum range, the line shape given by Stark broadening can be described by a Lorentzian function [64]:

$$L_S(\omega) = \frac{w/\pi}{w^2 + (\omega - \omega_0)^2} \tag{3.14}$$

in which w is the HWHM linewidth and ω_0 the unperturbed transition frequency. For hydrogen spectral lines, Stark broadening theory [64] yields the following relation between the linewidth and the plasma density [9]:

$$N_e = 8.02 \times 10^{12} \left(\frac{\Delta\lambda_{1/2}}{\alpha_{1/2}} \right)^{3/2} \tag{3.15}$$

in which $\Delta\lambda_{1/2}$ is the FWHM linewidth in Å, N_e is the plasma density in cm^{-3} and $\alpha_{1/2}$ is the reduced wavelength tabulated in [63], which depends on the plasma density and temperature. In the context of plasma discharge capillaries, $\alpha_{1/2}$ can be determined assuming the order of magnitude of the plasma density (usually in the range 10^{16}-10^{18} cm^{-3}) and estimating the plasma temperature by means of the quasi-static model of the plasma discharge [19]:

$$T_\mathrm{e} = 5.7 \left[\frac{I[kA]}{r_0[mm]} \right]^{2/5} [eV] \tag{3.16}$$

where I is the discharge current intensity and r_0 is the capillary radius.

As highlighted by 3.15, spectral line broadening depends on the plasma density (which is directly related to the intensity of the external field) and so on its pressure.

Concerning the cold and dense plasmas that are usually employed in particle accelerators, characterized by densities and temperatures of 10^{16}-10^{19} cm^{-3} and 1-6 eV, the predominant contribution to spectral line broadening is given by Stark effect. Indeed Eq.3.15 yields a linewidth ranging from few to hundreds Angstrom, while Doppler effect and natural broadening account for linewidths of 0.1-1 Å. In this way, Stark broadening provides a tool to determine the density of a plasma in presence of hydrogen atoms, by measuring the broadening of hydrogen spectral lines due to the interaction with plasma charged particles.

Such method is adopted for the characterization of plasma discharge capillaries tested at Plasma_lab. As previously mentioned, the plasma-emitted light is collected into a spectrometer, which allows to select hydrogen spectral lines and acquire spectral images of the plasma light with the ICCD camera. The camera objective acquires 1024x255 pixel images with a horizontal resolution of 0.7 Å/pixel given by the 1200 grooves/mm grating of the spectrometer. Acquired light is collected into a Multi Channel Plate for the signal intensification.

For instance, Fig. 3.9a shows the spectral image of a plasma discharge acquired from a 3 cm-long 1 mm-diameter capillary, obtained through the ionization of 10 mbar of pure hydrogen by means of 15 kV pulses. The horizontal axis reports the spectral wavelength, with the line centered at 486 nm (H-β line of the Balmer series), while the vertical axis reports the longitudinal position along the capillary channel. Therefore, by measuring the H-β line broadening at each vertical position of the

image, it is possible to recover the longitudinal profile of the plasma density inside the capillary. The dark horizontal lines correspond to two vertical lines drawn on the capillary, which allow to optimize the image focus and retrieve the vertical resolution. The two spikes at the vertical edges of the spectral image represent the plasma plumes, in which the plasma density drops exponentially due to expansion in vacuum.

Fig. 3.9b shows the fitting procedure performed at a given vertical position of the image (solid green line) to compute the spectral linewidth and recover the plasma density in the center of the capillary channel. A Voigt function, given by the convolution between a Lorentzian and a Gaussian distribution, would properly fit the broadened spectral line. However, since Doppler effect is negligible compared to Stark effect, a simple Lorentzian fitting function, analogous to 3.14, is suitable to appropriately fit the hydrogen spectral line. This is not the case for low density or hot plasmas, for which proper Voigt functions are adopted, as described in A.

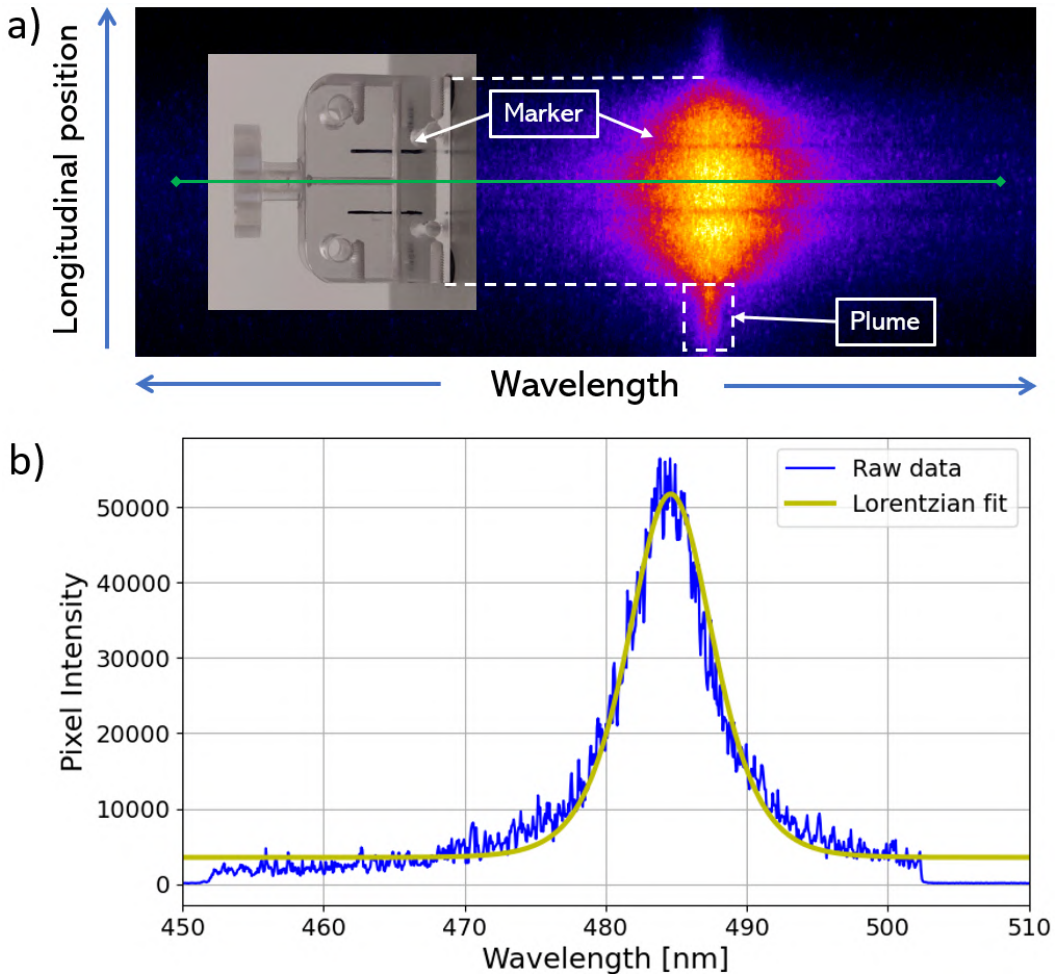

Figure 3.9. (a) Spectral image of a plasma discharge, acquired from a 3 cm long capillary with 1 mm diameter. (b) Lorentzian fitting of the H-β Balmer line at a given vertical position of the spectral image (solid green line from (a)), performed to recover the plasma density in the center of the capillary channel.

The acquisition gate width of the camera is usually set to around 100 ns, so to analyze the plasma density in a short time interval compared to the μs-range duration of the plasma discharge. For lower gate widths the light signal is too low for a reliable measurement. By gating the ICCD camera to the HV system by means of the delay generator, it is possible to acquire spectral images at different delays with respect to the onset of the discharge, thus obtaining a complete temporal-resolved characterization of the plasma source, as described in Ch.4.

The minimum plasma density that can be measured by Stark broadening method is in the range of 10^{15}-10^{16} cm^{-3}, below which H-α and H-β linewidths are below the spectrometer resolution.

3.7 Plasma temperature measurements

Other methods, based on the spectral analysis of plasma-emitted light, allow to retrieve the electron temperature distribution inside plasmas. Such methods are based on the measurement of relative intensities of spectral lines, emitted either by the same atom or ion, or by neighboring ionization stages, or successive iso-electronic ions. In optically thin plasmas of length l along the line of sight, spectrally integrated emission line intensities are given by:

$$I_{nm} = \int i_{nm}(\omega) d\omega \approx \frac{\hbar \omega_{nm}}{4\pi} A_{nm} N_m l \tag{3.17}$$

in which ω_{nm} is the frequency of the transition from the state n to m, A_{nm} is the transition strength and N_m is the ion density in bound state m.

Due to the relatively small differences between excitation energies and theoretical uncertainties, line intensity ratios within a given atom or ion normally do not lead to precise temperature measurements. For this reason, in dense plasmas in local thermodynamic equilibrium (LTE), it is preferable to measure the relative integrated line intensities from ions with subsequent ionization states. In LTE condition, the ratio between the populations of a given ion in two bound states is given by:

$$\frac{N_n}{N_m} = \frac{g_n}{g_m} exp\left(-\frac{E_n - E_m}{kT}\right) \tag{3.18}$$

in which g is the level degeneracy. In addition, the balance between electrons and ions in two subsequent ionization states i and i' is given by Saha equation:

$$\frac{N_e N_{i'}}{N_i} = \frac{2 Z_{i'}(T)}{Z_i(T) a_0^3} \left(\frac{kT}{4\pi E_H}\right)^{3/2} exp\left(-\frac{E_\infty}{kT}\right) \tag{3.19}$$

where a_0 and E_H are the Bohr radius and hydrogen ionization potential, while E_∞ is the ionization energy of the ion at lower ionization state i.

By combining the definition of the integrated line intensity 3.17 with 3.18 and 3.19, the ratio between the spectral line intensities of two ions in subsequent ionization states is given by:

$$R = \frac{I'}{I} = \frac{\omega' A' g'}{\sqrt{\pi} \omega A g} (4\pi a_0^3 N_e)^{-1} \left(\frac{kT}{E_H}\right)^{3/2} exp\left(-\frac{E' - E + E_\infty - \Delta E_\infty}{kT}\right) \tag{3.20}$$

in which N_e is the plasma density, E' and E are the excitation energies of the two ions and ΔE_∞ is the high density correction to E_∞, given by [64]:

$$\Delta E_\infty = 2zE_H \left(\frac{a_0}{\rho_D}\right) \tag{3.21}$$

where ρ_D is the Debye radius and z is the ion charge. Finally, by measuring the integrated intensity of two emission lines, emitted by two ions in subsequent ionization states, it is possible to retrieve the plasma electron temperature from Eq.3.20.

As an example, Fig.3.10a reports the emission spectrum acquired from a plasma channel, produced through laser ionization of a gas mixture composed by N_2 95% and H_2 5%. Emission lines, contained in the acquired spectrum, are identified by means of the NIST Atomic Spectra Database [90] and lines related to subsequent ionization stages of Nitrogen are taken into account. As shown in Fig.3.10b, NI (N) and NII (N^+) lines, centered at 468 nm and 500 nm, are fitted by two Lorentzian

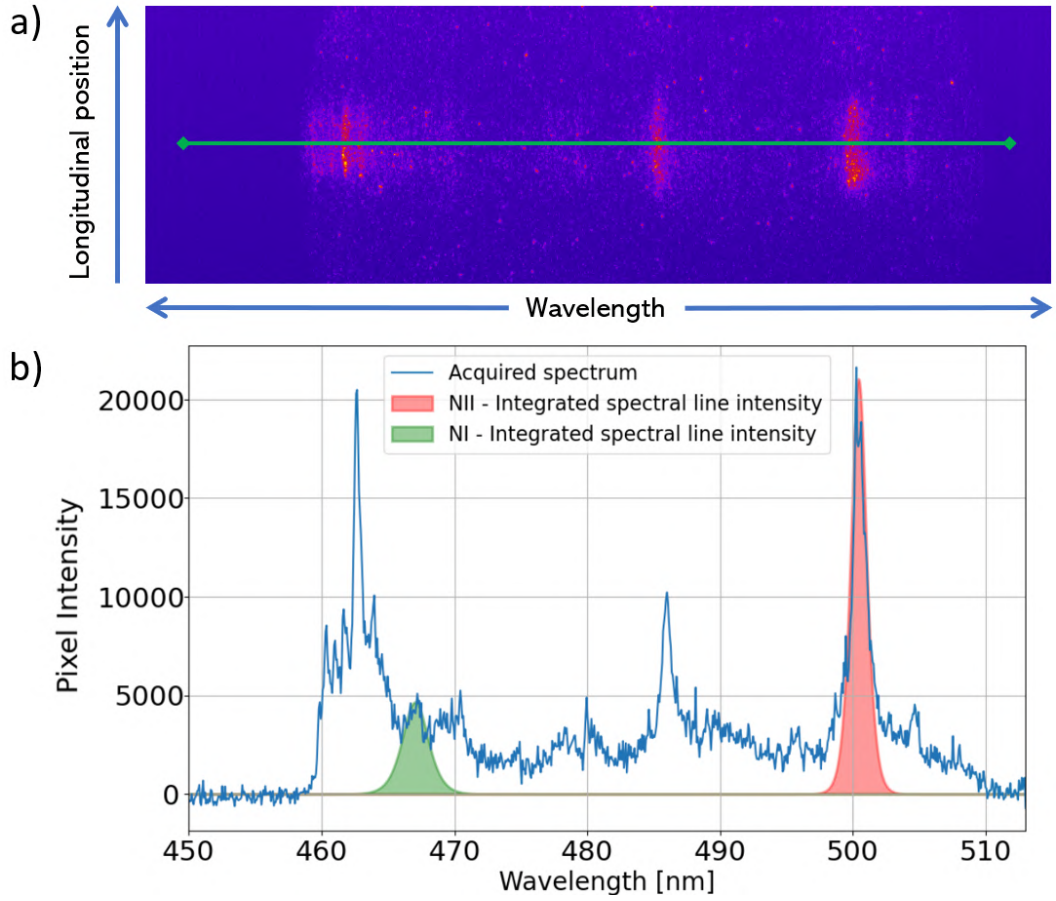

Figure 3.10. (a) Emission spectrum acquired from a plasma channel produced by laser ionization of a N_2 95% - H_2 5% gas mixture. (b) Lorentzian functions are used to fit the emission lines of neutral Nitrogen atoms (NI) and N^+ ions (NII), retrieving the integrated line intensity (green and red areas) at a given position of the plasma channel (solid green line from (a)).

functions to retrieve the integrated line intensity from a given position of the plasma channel. Measured line intensities are then inserted into Eq.3.20, together with the plasma density, previously measured through Stark broadening of the H-β line, and the other parameters of the two emission lines, retrieved by the NIST Atomic Spectra Database as well. Analogously to Stark broadening for plasma density, this method provides a spatial (longitudinal) and temporal characterization of the plasma temperature distribution.

An example of the implementation of such method for the characterization of laser-induced plasma filaments is described in Sec.6.2.

3.8 Laser system for plasma discharge stabilization

As described in Ch2, the electrical discharge between two electrodes is initialized by background ionization, which produces the first free electrons in the gas column. Due to the stochastic behaviour of such phenomenon, the instant of the voltage breakdown is affected by an intrinsic time jittering, resulting in a shot-to-shot variation of the plasma density at arrival time of driver and witness beams. A reliable method to stabilize the plasma formation consists in the use of a laser pulse, impinging onto the negative capillary electrode few tens-hundreds of ns before the high voltage discharge, allowing to control the production of first free electrons [16].

Plasma_lab experimental setup includes a 1064 nm Nd:YAG laser system, which delivers 11 ns laser pulses for the controlled pre-ionization of the gas column. 50-80 mJ pulses are focused onto the negative electrode of the installed capillary with a few mm spot size, resulting in a laser intensity of around 10^9-10^{10} W/cm^2. Such laser intensity is below the ionization threshold for hydrogen, but enough to produce the first free electrons that trigger the arc discharge along the capillary channel.

The laser-induced pre-ionization allows to reduce the time jitter of the discharge current, thus improving the shot-to-shot plasma stability. For example, Fig.3.11 reports the waveforms of the discharge current produced by applying 5 kV pulses to a 3 cm-long capillary, filled with around 10 mbar H_2. Fig.3.11a shows 50 consecutive waveforms acquired by the oscilloscope without the laser stabilization. An amplitude jitter of 10.7 A characterizes the current profile, with peaks varying from 70 to 110 A. In addition, a RMS time jitter of 32 ns is measured. On the other hand, Fig.3.11b shows the current waveforms obtained with gas pre-ionization by means of 80 mJ laser pulses. As a result, amplitude and time jitters of 1 A and 1.7 ns are measured, proving the laser-induced discharge stabilization.

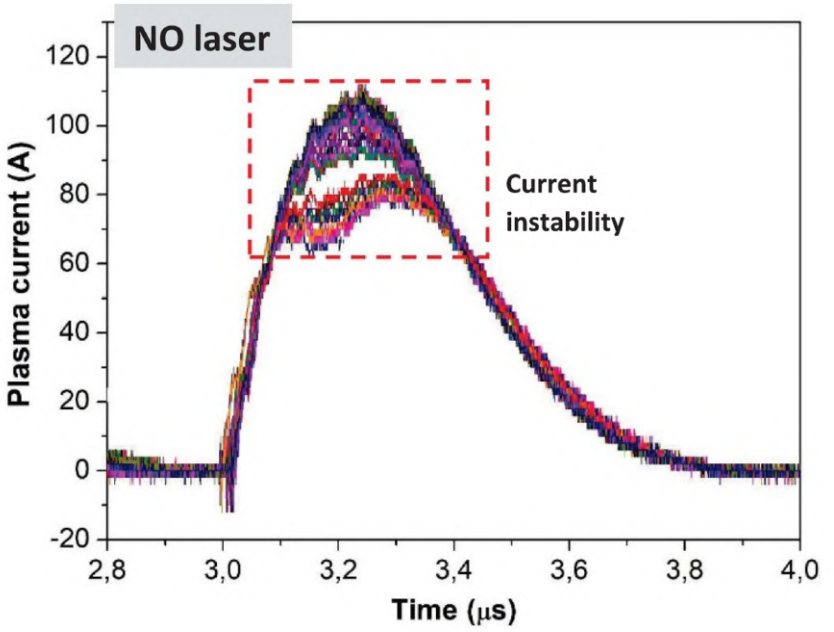

(a)

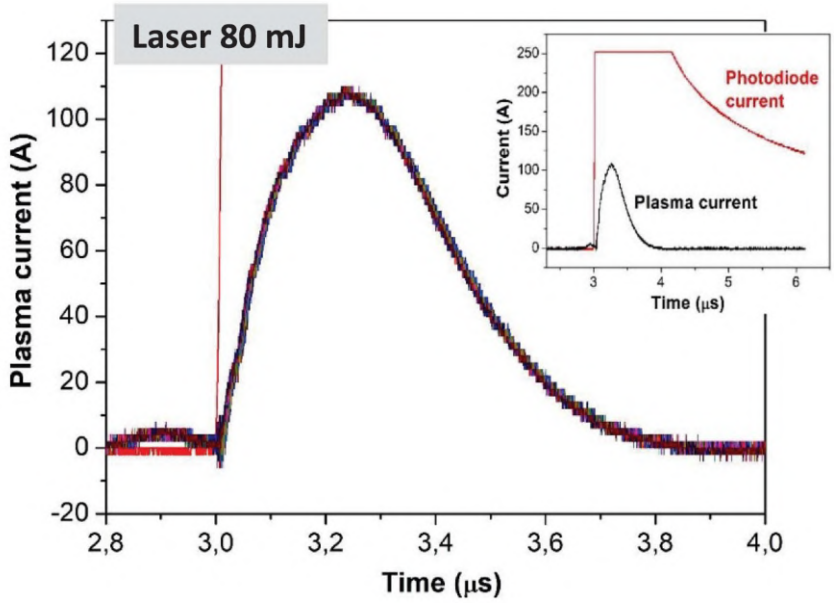

(b)

Figure 3.11. Discharge current waveforms acquired with laser turned off (a) and on with 80 mJ (b) pulse energies. Each plot shows a set of 50 measurements obtained by applying 5 kV between the capillary electrodes. The inset shows the laser pulse signal measured with a photo-diode.

Chapter 4

Geometrical design of plasma discharge capillaries for plasma density modulation

A first study carried out in the context of the PhD thesis concerned the design of the capillary geometry to optimize the modulation of the plasma channel density. As described in Sec.1.4.2, the longitudinal plasma density distribution plays a key role in the plasma acceleration mechanism. A uniform flat-top profile is required to excite constant-amplitude accelerating wakefields along the plasma channel, whereas smooth density ramps can be used to match and extract particle bunches from a plasma accelerating stage.

Therefore, in order to assess the possibility to modulate the plasma density profile with plasma discharge capillaries, different geometrical configurations have been designed and characterized at Plasma_lab laboratory. In particular, 3 cm-long capillaries with 1 mm-diameter, made in 3D-printed VeroClear, were realized and tested, as described in the following Sections.

4.1 Experimental characterization

4.1.1 Inlets arrangement

First, the experimental study was focused on the arrangement of the gas inlets, testing 3 cm-long capillaries with two 0.9 mm-diameter inlets located at different relative distances, respectively 9, 15 and 24 mm, as shown in Fig.4.1.

The characterization of the three capillaries was performed by applying 7 kV pulses at 1 Hz to ionize around 50 mbar of pure hydrogen, producing 380 A peak current plasma discharges. The electro-mechanical valve was set to open for 5 ms, allowing to properly fill the capillaries, while a delay of 7 ms was set between the valve closure and the discharge trigger to optimize the plasma formation.

As described in Ch.3, the plasma-emitted light is collected into the imaging spectrometer, which selects H_2 spectral lines for Stark broadening method. Spetcral images are acquired by the ICCD camera with a gate width of 100 ns and tuning the delay with respect to the HV discharge, so to temporally scan the density distribution

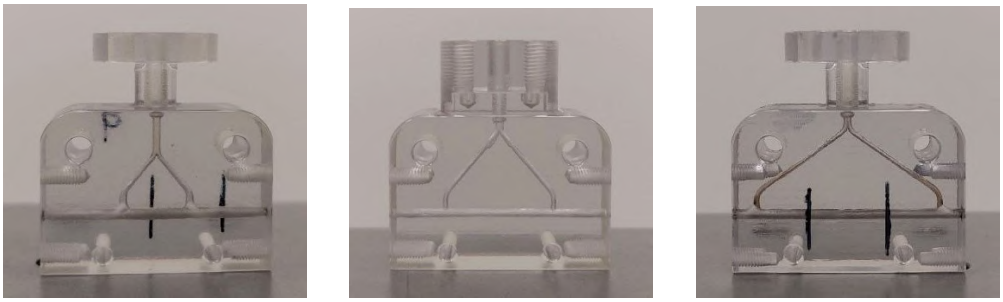

(a) 9 mm spaced inlets **(b)** 15 mm spaced inlets **(c)** 24 mm spaced inlets

Figure 4.1. Tested 3 cm-long 1 mm-diameter capillaries with two inlets located at different distances.

inside the plasma channel.

Fig.4.2 reports longitudinal plasma density profiles measured during the plasma recombination phase, in particular 1100 ns after the discharge trigger.

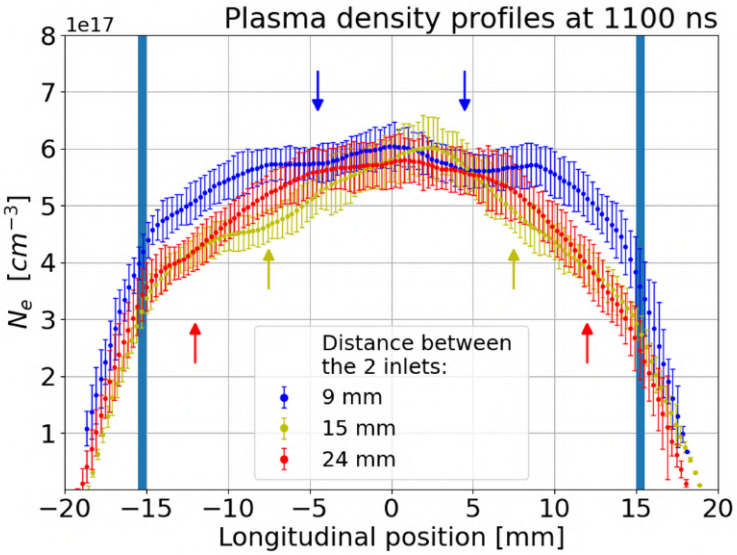

Figure 4.2. Plasma density profiles at a delay of 1100 ns delay for 3 cm-long capillaries with two inlets at different distances. Arrows indicate the inlet positions in the different configurations, while blue rectangles represent the electrodes at the capillaries ends.

Plasma density profiles are peaked at the channel center, with a maximum of 6 $\pm$ 0.3 $\times$ 10^{17} cm^{-3}, and a gradual decrease towards the electrodes, beyond which steep density drops are observed in the plasma plumes. Experimental results show that a higher uniformity in the longitudinal profile is achieved with closer inlets, with a maximum center-to-end uniformity of 75% obtained with 9 mm-spaced inlets. Error bars are computed as the standard deviation of 50 spectral images, acquired for each measurement.

Fig.4.3 shows the temporal evolution of the plasma density, averaged along the longitudinal profile at each delay. No significant difference is observed between the different configurations.

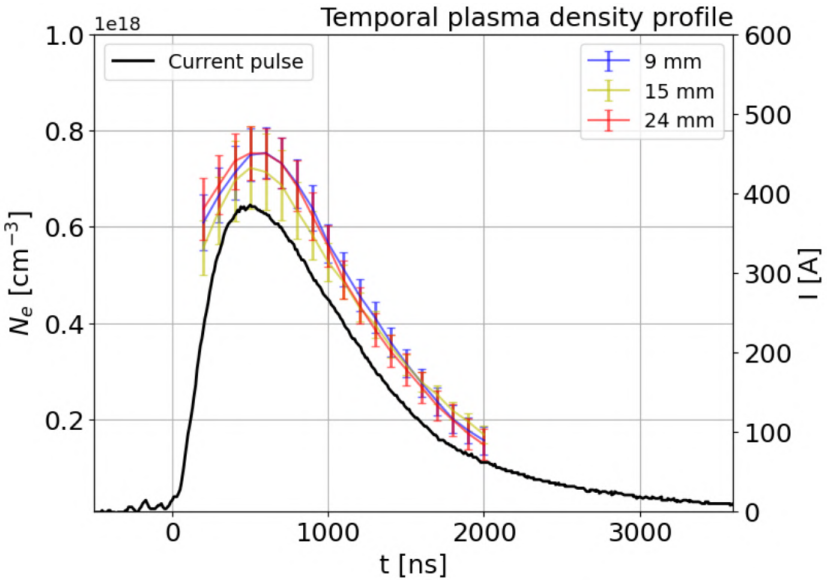

Figure 4.3. Temporal evolution of the average plasma density inside the capillary channel for different configurations. The solid black line represents the discharge current waveform, measured by the oscilloscope.

4.1.2 Channel shaping

A second experimental analysis concerned capillaries with different channel shapes, assessing the possibility to tailor the longitudinal density profile by controlling the gas and plasma expansion within the capillary channel. In particular, the experimental testing was performed with 3 cm-long 1 mm-diameter capillaries with a single 0.9 mm-diameter inlet and three different channel shapes, respectively uniform, cigar (1.3 mm inner and 1 mm outer diameters) and tapered profile with conical ends (1 mm inner and 2 mm outer diameters), as shown in Fig4.4.

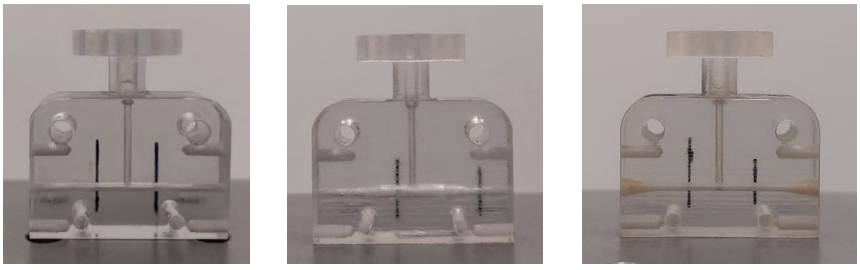

(a) Uniform channel

(b) Cigar-shaped channel

(c) Tapered channel with conical ends

Figure 4.4. Tested 3 cm-long 1 mm-diameter capillaries with different channel shapes.

The experimental characterization was performed in the same experimental conditions, i.e. 7 kV pulses, 50 mbar H_2, 380 A peak current discharges. Longitudinal density profiles measured at 1100 ns are reported in Fig.4.5.

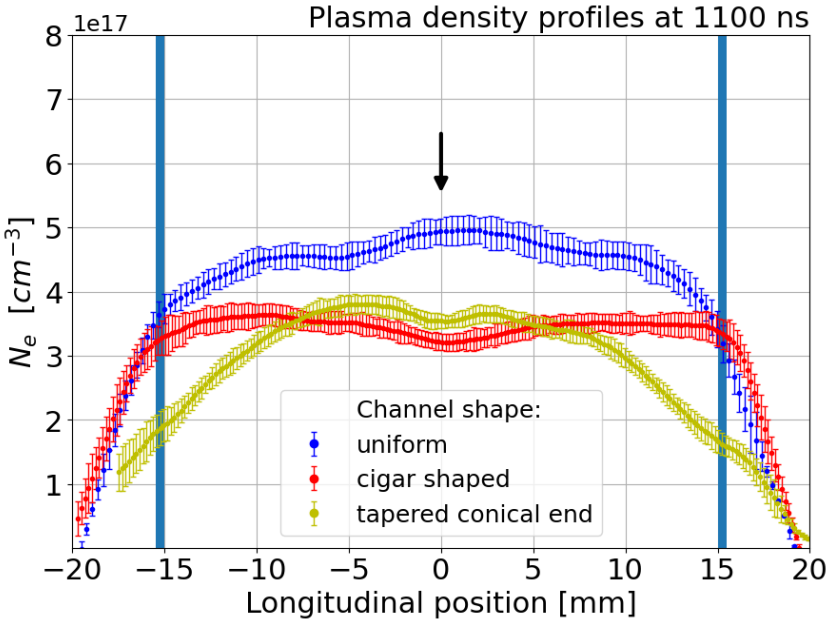

Figure 4.5. Plasma density profiles at 1100 ns delay for 3 cm-long capillaries with one central inlet and different channel shapes. The black arrow indicates the position of the single inlet, while blue rectangles represent the electrodes at the capillaries ends.

Regarding the capillary with uniform channel, a density peak of $5\pm0.2 \times 10^{17}$ cm^{-3} is measured, with a 80% center-to-end density uniformity. The cigar-shaped channel is characterized by a slightly hollow profile, with density peaks of around $3.6\pm0.2 \times 10^{17}$ cm^{-3}. Such lower density is due to the larger cross section in the central part of the channel. However a center-to-end density uniformity of 92% is achieved with such geometry. On the other hand, the tapered channel with conical ends is characterized by smooth density ramps from the channel center towards the channel extremities, with a 50% density drop from the central peak of $3.8\pm0.2 \times 10^{17}$ cm^{-3} to $1.9\pm0.2 \times 10^{17}$ cm^{-3} at the electrodes.

As a result, the cigar shape geometry allows to produce highly uniform plasma channels, whereas tapered ends provide smooth density ramps that can be exploited for beam matching and extraction, as previously mentioned.

The temporal evolution of the average plasma density is depicted in Fig.4.6. Compared to the 1 mm-diameter uniform channel, the other channel shapes are characterized by lower average density, due to the plasma expansion where the cross section diameter is larger.

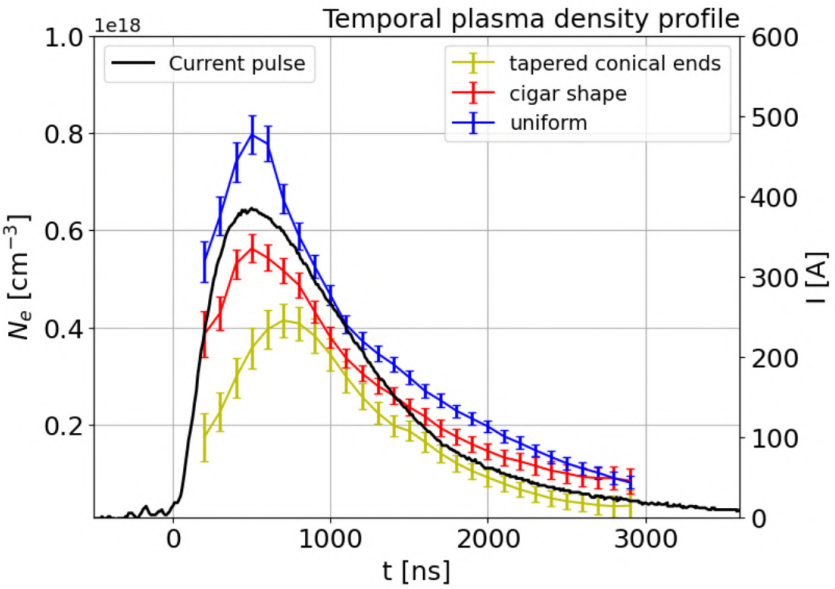

Figure 4.6. Temporal evolution of the average plasma density inside the capillary channel for different shapes. The solid black line represents the discharge current waveform.

4.2 Numerical analysis

In order to provide theoretical support to experimental studies, 3D fluid dynamics simulations were performed with the CFD software OpenFOAM [127], analyzing the H_2 gas dynamics during the filling of tested capillaries. The SonicFoamART solver was employed to simulate the gas in turbulent transient sonic regime. The experimental testing is reproduced in fluid simulations by setting a gas injection pressure of 200 mbar for 5 ms (electro-mechanical valve opening time) and closing the inlet for the following 7 ms (time interval between the valve closure and the electrical discharge trigger), so to have around 50 mbar of H_2 inside the capillary channel at the ionization instant. OpenFOAM is limited to describe only neutral gas dynamics, therefore the electrical discharge formation and the plasma expansion are not included in simulations. However this analysis provides useful information regarding the hydrogen distribution inside the capillary before the plasma formation, and how it relates to the plasma density distribution as well.

Fig.4.7 depicts the pressure distribution in the simulated geometry, specifically for the 3 cm-long 1 mm-diameter capillary with two 15 mm-spaced inlets. An inward pressure of 200 mbar is set at the inlet surface, while two vacuum boxes are connected to the capillary extremities to simulate the gas expansion in the vacuum chamber. The mesh grid is composed by 1 mm-side hexahedral cells, with a refinement level of 2 and 3 respectively at distances of 1 cm and 5 mm from the capillary walls, so to have a better spatial resolution towards the boundary regions.

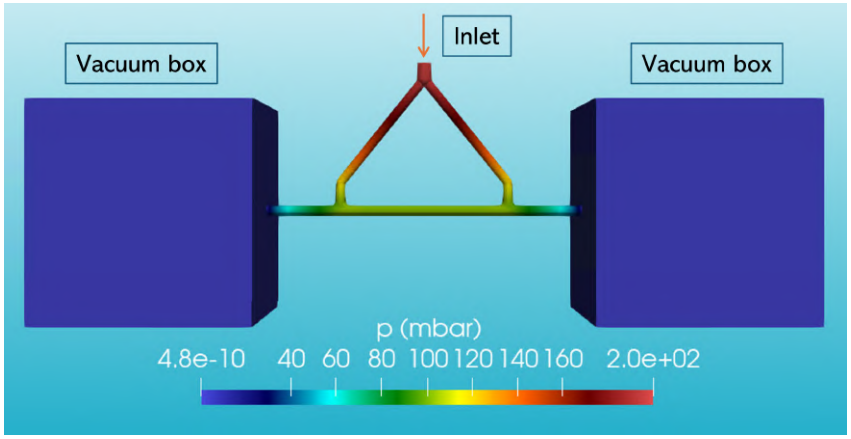

Figure 4.7. 3D view of the pressure distribution inside the simulated geometry

Fig.4.8 shows a longitudinal section view of the H_2 distribution in dynamic equilibrium, which is reached around 2 ms after the valve opening. In particular, a molecular density of around 2×10^{18} cm^{-3} is reached along the capillary channel, corresponding to a maximum achievable plasma density of 4×10^{18} cm^{-3}. Such result is in agreement with the measured plasma density peak of around 7×10^{17} cm^{-3} (Fig.4.3), considering that only a partial ionization of the gas column is achieved.

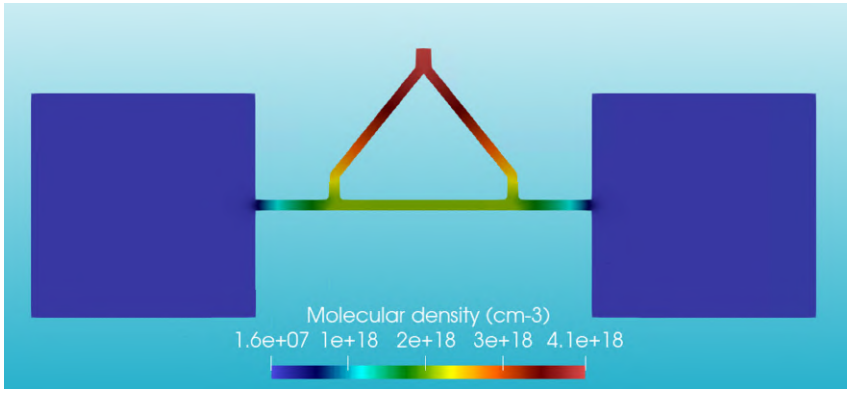

Figure 4.8. 2D hydrogen distribution at fluid dynamic equilibrium, reached 2 ms after the valve activation.

Additionally, equilibrium temperature and velocity distributions are reported in Fig.4.9. Regarding the gas temperature, a uniform room temperature is kept within the entire domain (due to heat exchange with capillary walls), except for the gas plumes towards the electrodes holes, in which a temperature decrease is observed due to the gas expansion in vacuum. Concerning the gas velocity, values around 500 m/s are reached inside the capillary channel, in particular from the inlets to the extremities, thus below hydrogen speed of sound (1300 m/s), whereas supersonic motion is reached in the gas plumes. In the central region between the two inlets, the gas is in stationary condition, which is reached once the region has been filled in the first millisecond of the valve opening time.

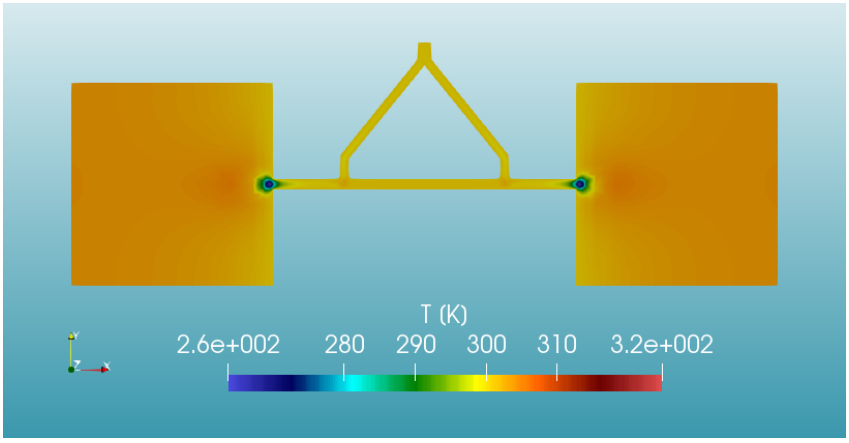

(a) 2D temperature distribution at fluid dynamic equilibrium

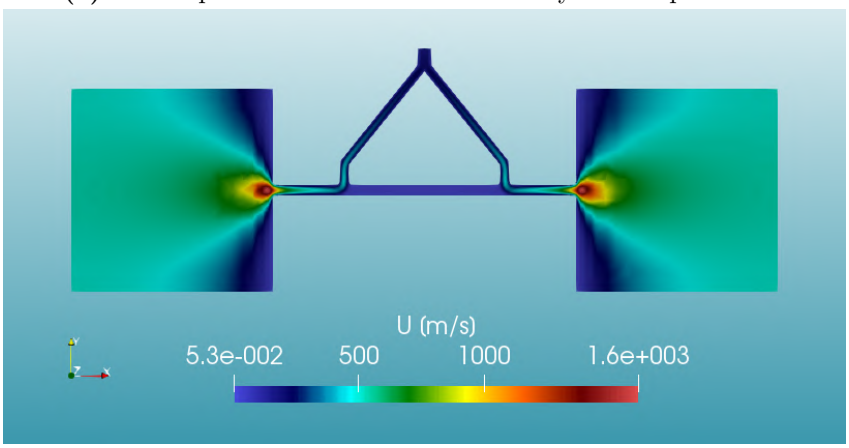

(b) 2D velocity distribution at fluid dynamic equilibrium

Figure 4.9. (a) Equilibrium gas temperature and (b) velocity distributions.

Going back to the comparison between different capillary geometries, Fig.4.10 reports the longitudinal H_2 density profiles, obtained along the channel axis, for the 3 cm-long capillaries with two inlets located at different distances.

In particular, Fig.4.10a shows H_2 density profiles at fluid dynamic equilibrium, reached 2 ms during the valve opening time. Density profiles are characterized by a central plateau in the region between the two inlets, which decreases from 2.6×10^{18} cm^{-3} to 1.4×10^{18} cm^{-3} with larger inlets spacing. In addition, a slightly hollow profile is observed for 24 mm-spaced inlets, probably due to pressure drop taking place within such distance. In addition, steep density drops are observed from the inlets towards the electrodes.

After 5 ms, the inlet is closed and the gas pressure starts to decrease until the gas ionization is triggered, 7 ms after the valve closure. Hydrogen density profiles at the ionization instant are reported in Fig.4.10b.

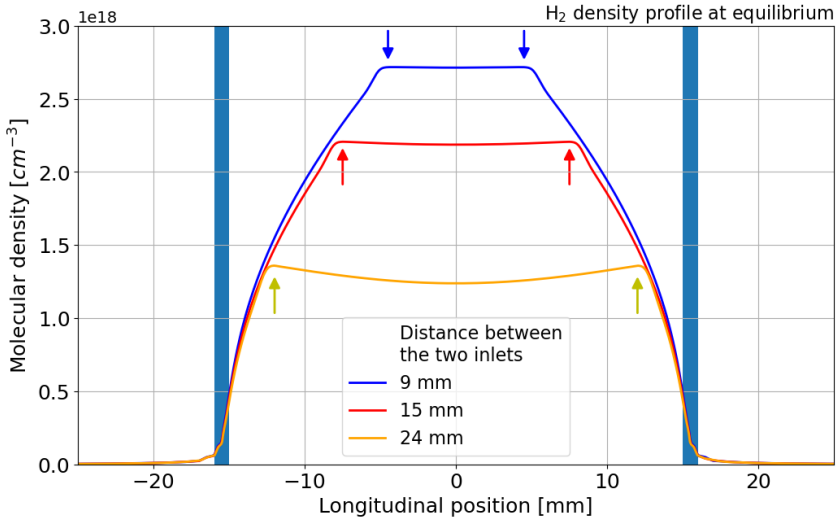

(a) Longitudinal H_2 distribution at equilibrium, during the valve opening.

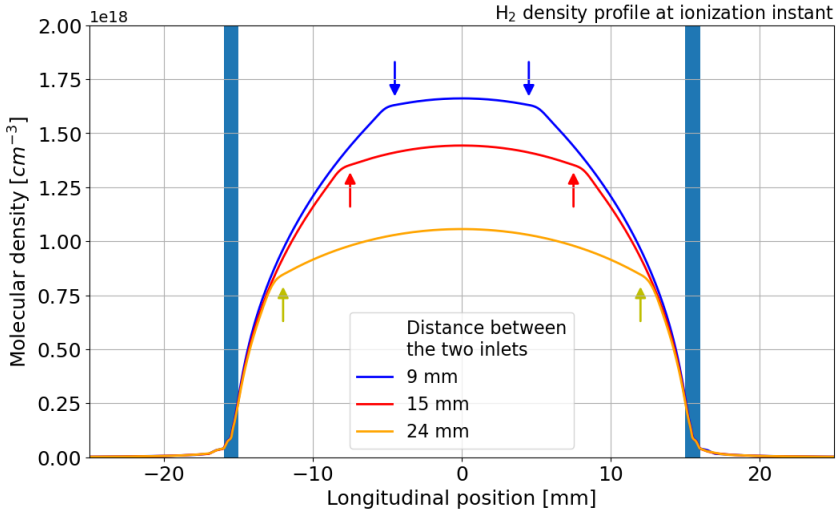

(b) Longitudinal H_2 distribution at the ionization instant, 7 ms after the valve closure.

Figure 4.10. H_2 density profiles at equilibrium (a) and at the ionization instant (b) for 3 cm-long capillaries with different inlet configurations.

Simulation results show that the region between the inlets is characterized by a curved profile, peaked at the center, with a density uniformity that drops from 98% to 76% when increasing the inlets distance from 9 to 24 mm. In addition, steep density drops are observed from the inlets to the capillary ends. A comparison with measured plasma density profiles (Fig.4.2) suggests that the plasma formation and rapid propagation along the capillary significantly alters the density distribution from the simulated neutral gas profiles, especially in the region between the inlets and the electrodes, where the steep gas density drop is turned into a gradual plasma density decrease. However, a correspondence between simulation and experimental results is given by the higher density uniformity observed with closer inlets both for

neutral gas and plasma distributions. Furthermore, CFD simulations also suggest that a higher density uniformity could be achieved by triggering the HV discharge during the valve opening time, in which gas density profiles are characterized by central plateau.

Concerning the effect of the channel shape, Fig.4.11 depicts simulated longitudinal H_2 density profiles both at equilibrium and ionization instant.

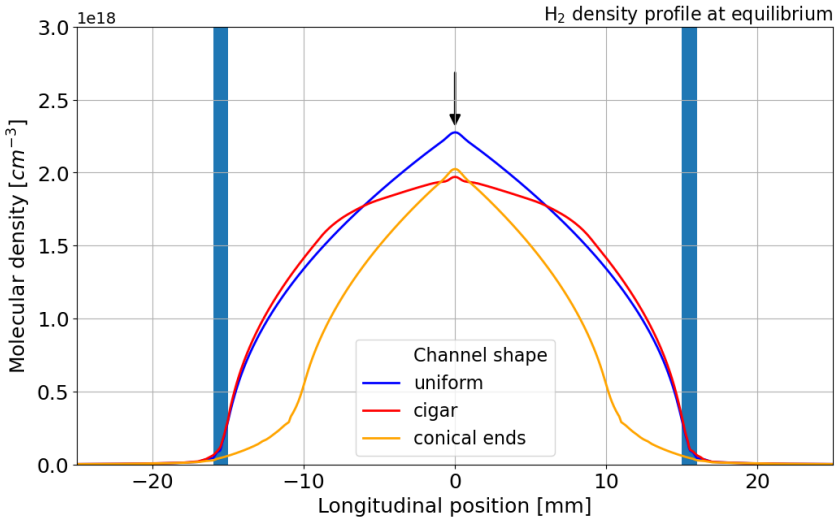

(a) Longitudinal H_2 distribution at equilibrium, reached 2 ms after the valve activation.

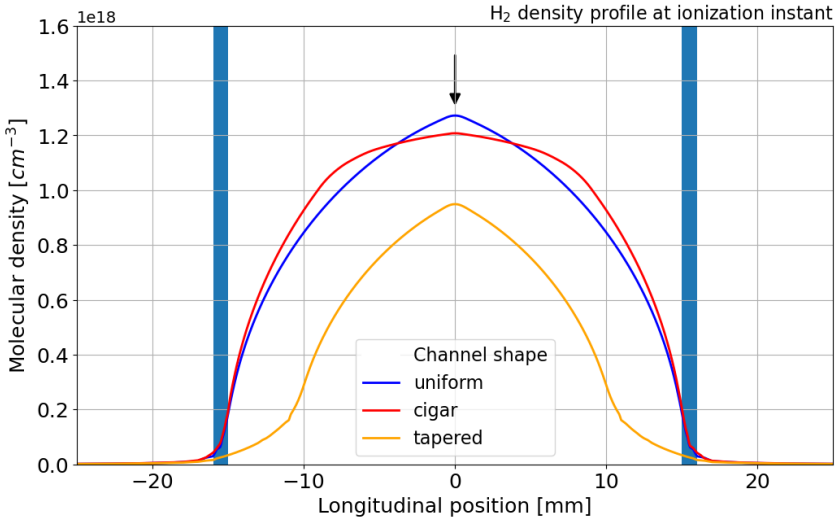

(b) Longitudinal H_2 distribution at the ionization instant, 7 ms after the valve closure.

Figure 4.11. H_2 density profiles at equilibrium (a) and at the ionization instant (b) for 3cm-long capillaries with different channel shapes.

The uniform channel is characterized by a bell-shaped density profile, with sharp density drops from the center to the ends. On the other hand, the cigar-shaped channel geometry partially compensates the density drops towards the capillary

extremities, thus establishing a uniform profile within the central channel region. Obtained results confirm the higher uniformity of the cigar-shaped channel compared to the one with uniform shape. In addition, the tapered channel with conical ends is characterized by smooth density ramps towards the ends, in agreement with experimental results.

In conclusion, experimental and simulation results provided a fundamental insight in the optimization of the capillary geometry to control the gas and plasma density distribution. In particular, the use of inlets at relatively close distance or an enlarged cross section in the central region of the capillary channel can improve the plasma density uniformity, as required for efficient plasma acceleration. On the other hand, a gradual increase in the channel diameter towards the capillary extremities allows to control the plasma density ramps towards the vacuum, which can be exploited for beam matching and extraction in plasma acceleration stages.

Further improvements can be obtained in the future with simulation codes that include the gas ionization and the plasma dynamics, thus providing a direct connection between CFD neutral gas simulations and plasma density measurements. Up to now, due to the lack of reliable codes for the gas ionization, neutral gas dynamics simulations represent a powerful tool to support the design of plasma discharge capillaries.

In addition, studies on the capillary geometry for optimizing the plasma density modulation have been extended to m-scale capillaries, as discussed in the following chapter.

Chapter 5

Novel schemes for compact m-scale capillaries

A key goal in the development of plasma-based particle accelerators concerns the realization of m-scale plasma sources, able to provide stable and efficient plasma acceleration with high energy gain. As described in Sec1.5, EuPRAXIA@SPARC_LAB project includes a PWFA stage based on a 60 cm-long capillary and, in addition, a future energy upgrade is foreseen with a 3 m-long PWFA stage. In this regard, this PhD thesis includes the design and testing of novel schemes for m-scale plasma discharge capillaries. R&D activities, carried out within the thesis project, were not only focused on long plasma sources for high energy gain plasma acceleration, but also on particular devices providing compact plasma-based focusing and guiding for high energy particle beams.

5.1 Segmented capillary

The first scheme, tested in the context of the thesis project, consists in the so-called segmented capillary, based on the production of long plasma channels composed by a series of independent plasma discharges, which are triggered by parallel high voltage circuits. A prototype of the segmented capillary, shown in Fig5.1, consists in a 16 cm-long capillary made in Lexan, constituted by an upper channel for a uniform gas injection, four vertical inlets and a main channel composed by two 8 cm-long segments. The two segments are connected to positive copper electrodes at the edges and a shared grounded electrode in the center of the device. The working principle of the segmented capillary, schematized in Fig5.2, is based on the utilization of two HV generators, feeding in parallel two HV pulser circuits, which in turn apply HV pulses to the capillary segments, triggering two independent plasma discharges.

Such configuration allows to freely modulate the entire 16 cm-long plasma channel by tuning the voltage applied to the segments or by delaying the two discharge triggers by means of a delay generator.

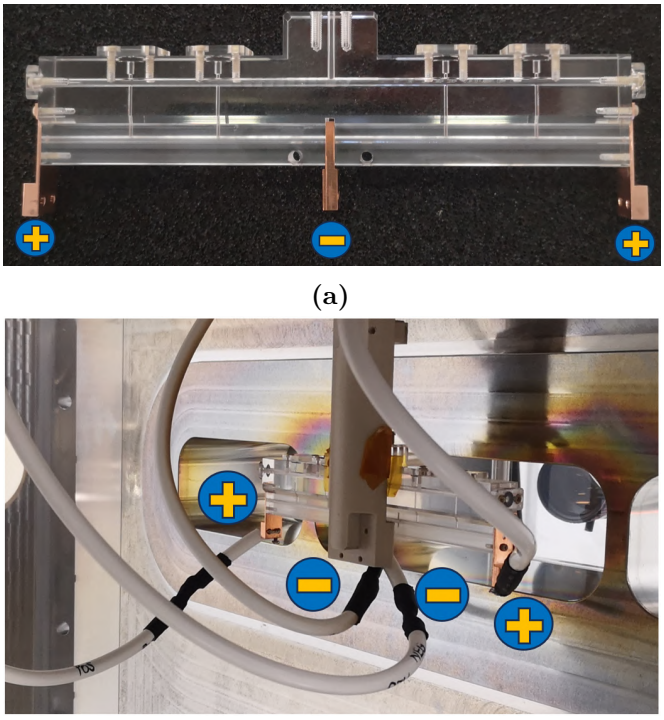

(a)

(b)

Figure 5.1. (a) Picture of the 16cm-long segmented capillary with copper electrodes. (b) Segmented capillary installed inside Plasma_lab experimental chamber. Positive cables are connected to the electrodes at the capillary extremities, while negative (grounded) cables are connected to the central one. Each electrode is made of copper.

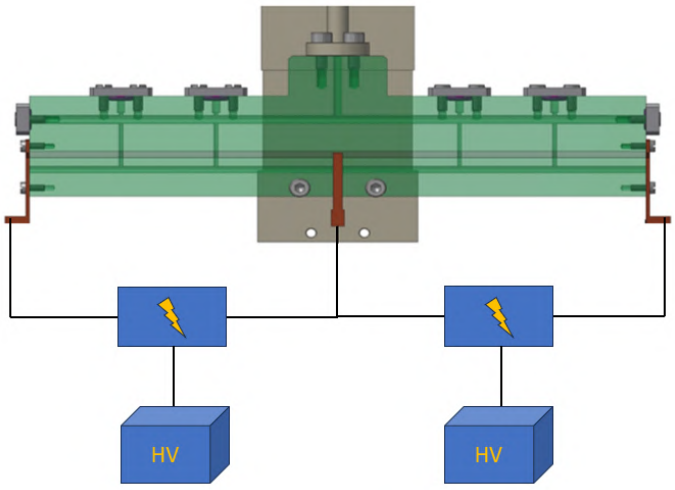

Figure 5.2. Schematic representation of the segmented capillary. Each segment is connected in parallel to an independent HV system, composed by a generator and a pulser circuit, in order to create two independent plasma discharges.

5.1.1 Plasma channel uniformity

A first experimental test with the segmented capillary was performed to demonstrate the production of uniform plasma channels by triggering two synchronized plasma discharges. In the experiment, around 50 mbar of H_2 were injected at 1 Hz into the capillary. 6 kV pulses were delivered at the same time by the two HV systems to the capillary segments, producing synchronized plasma discharges with 280 A peak current. Spectral analysis of the entire plasma channel was performed by shifting the optical line in the longitudinal direction, since the optical line mirrors can only collect 5 cm-long portions of the plasma channel light. Fig.5.3 reports the plasma channel generated during the experiment, with a spectral image of the H-β line acquired from the center of the capillary channel during the plasma formation.

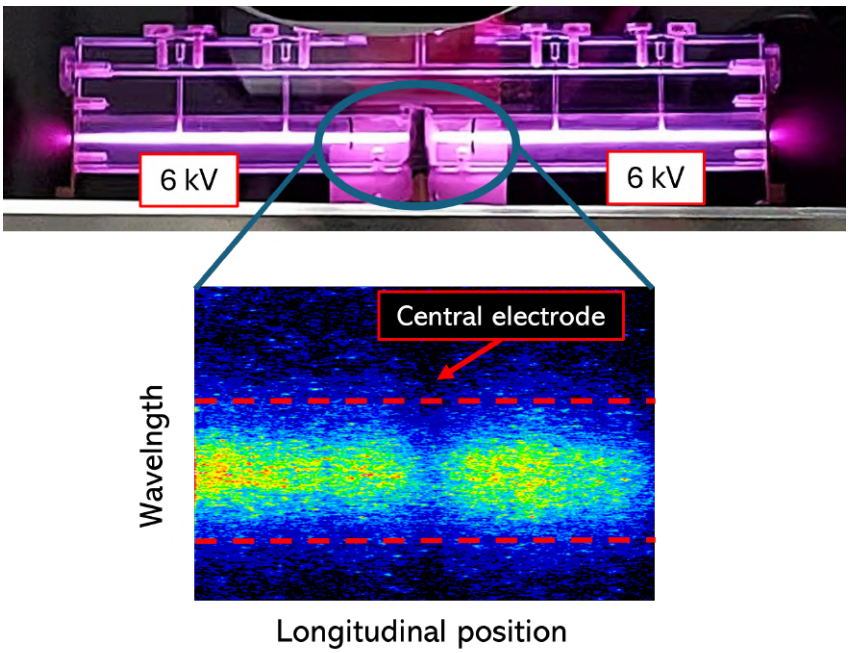

Figure 5.3. (Top) Picture of the plasma channel produced inside the segmented capillary by two synchronized discharges with same current. (Bottom) Spectral image of the the H-β line acquired from the center of the capillary channel 1200 ns after the discharge trigger. The shaded vertical region in the center of the image corresponds to the central electrode. Red dashed lines highlight the identical spectral linewidth in the two segments, corresponding to equal plasma densities.

Plasma density profiles of the entire channel were obtained by stacking longitudinal profiles, measured from three portions of the plasma channel. In addition, plasma density measurements were performed at different delays with respect to the discharge trigger to analyze the temporal evolution of the plasma density in the two segment. Experimental results, reported in Fig.5.4, show that a uniform plasma channel is obtained during the plasma formation (1200 ns), with a density peak of $8 \pm 1 \times 10^{16}$ cm^{-3} and a 80% uniformity along the 16 cm-long channel. On the other hand, an asymmetric plasma distribution is observed in the plasma recombination phase (2800 ns), with density peaks of $1.7 \pm 0.1 \times 10^{17}$ cm^{-3} and 1.1

$\pm$ 0.1 $\times$ 10^{17} cm^{-3} respectively in left and right segments. Error bars are computed as the standard deviation over 50 images acquired for each measurement.

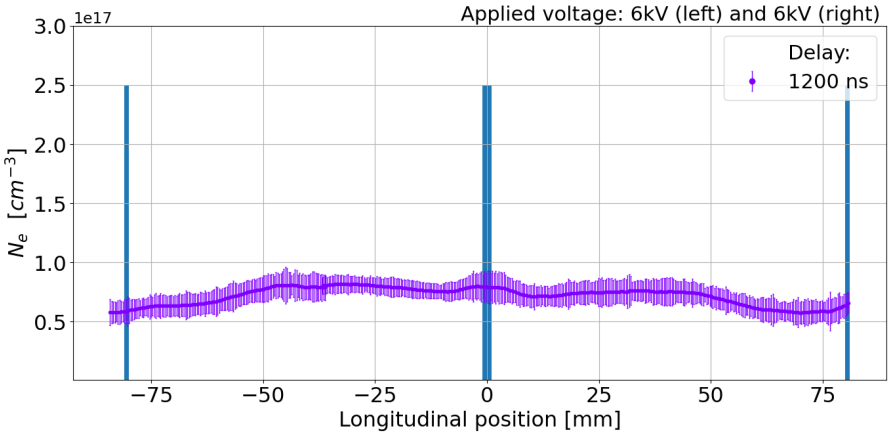

(a) Longitudinal plasma density profile at 1200 ns

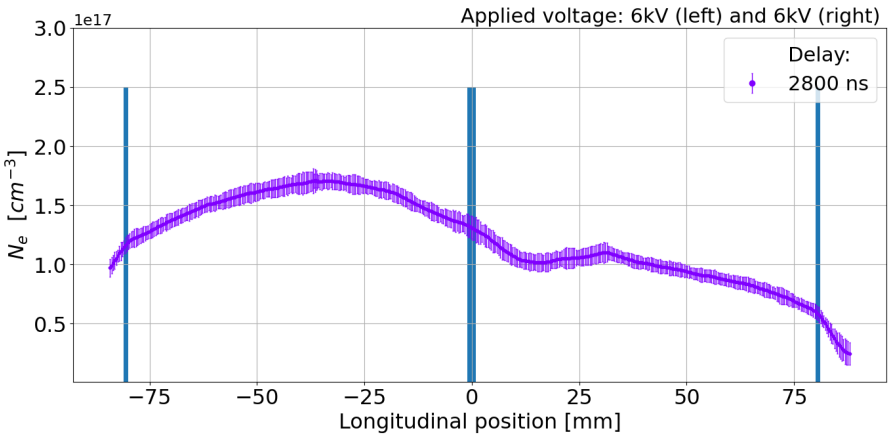

(b) Longitudinal plasma density profile at 2800 ns

Figure 5.4. Longitudinal plasma density profiles measured 1200 ns (a) and 2800 ns (b) after the trigger of the two plasma discharges. Results are obtained by stacking longitudinal profiles measured from three portions of the plasma channel.

This phenomenon can be interpreted by analyzing the temporal evolution of the average plasma density in the two segments, which is reported in Fig.5.5 together with discharge current waveforms measured by the oscilloscope. After the current discharges are triggered, the leading edge of the discharge generated in the left segment is considerably higher than the one in the right segment, leading to a higher gas ionization in the left segment. Due to this, while a uniform plasma channel is produced during the early stage of plasma formation, with equal densities in the two segments, a plasma density unbalance takes place towards the current peak and the recombination phase.

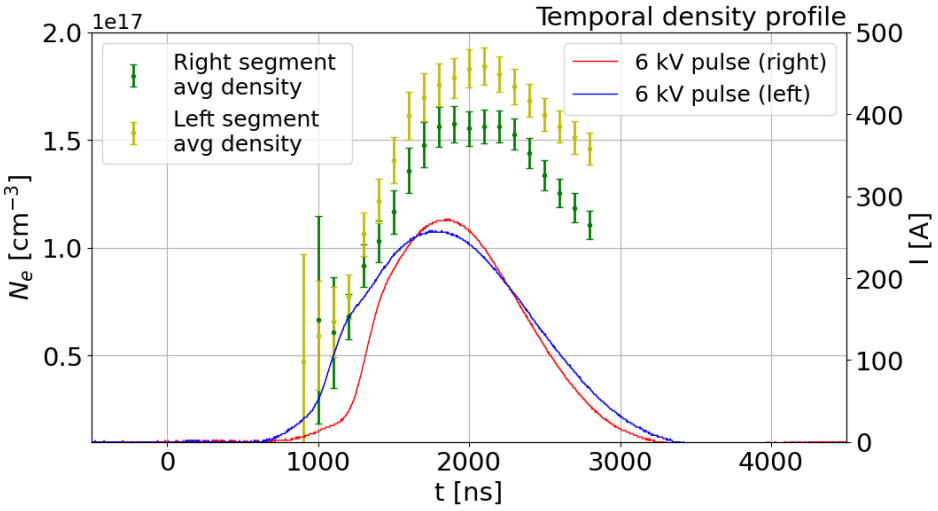

Figure 5.5. Temporal evolution of the plasma density, averaged over the right (green) and left (yellow) segments. Solid line represent the waveform of the two discharge currents produced in the right (red) and left (blue) segments.

In conclusion, this first test proved the possibility to create a uniform plasma channel by properly synchronizing the plasma discharges. However, a precise matching between the two current waveforms is required to keep the plasma uniformity during the entire plasma lifetime.

5.1.2 Plasma density modulation

A second test was carried out to assess the possibility to modulate the density profile of the plasma channel by tuning the voltage applied to the segments. In the experiment, 6 kV and 7.5 kV pulses were delivered at the same time to the left and right segments respectively, producing plasma discharges with 280 A and 360 A peak currents. Fig.5.6 shows the plasma channel produced with such experimental settings, together with a H-β spectral image acquired from the center of the channel at 900 ns, which highlights the larger spectral linewidth in the higher voltage segment, corresponding to a higher plasma density.

Plasma density profiles, measured with the same acquisition procedure as the previous test, are reported in Fig.5.7, specifically at delays of 900 ns and 2300 ns. During the plasma formation, the channel density profile is characterized by a steep density ramp towards the central electrode, interposed between two plateau at 0.8 ± 0.1 and 1.75 ± 0.1 $\times 10^{17}$cm^{-3}, respectively in the left and right segments. On the trailing edge of discharge pulses, corresponding to the plasma recombination phase, the plasma redistributes along the capillary channel, determining a symmetric density profile with a peak of around $1.75\pm0.1 \times 10^{17}$ cm^{-3} and gradual density ramps towards the ends.

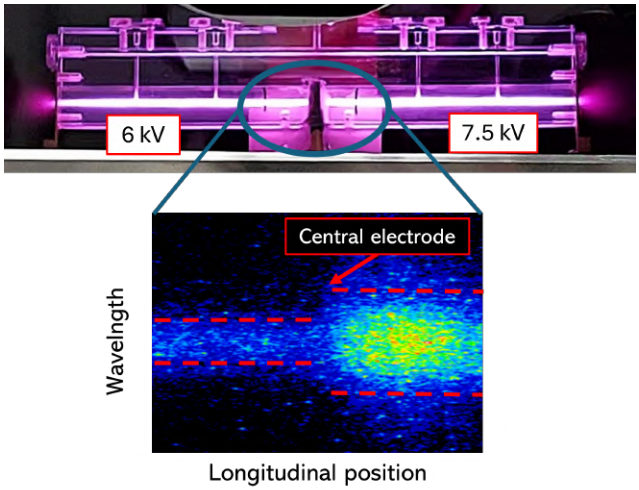

Figure 5.6. (Top) Picture of the plasma channel obtained by applying 6 kV and 7.5 kV pulses to the left and right segments respectively. (Bottom) Spectral image of the the H-β line acquired from the center of the capillary channel at 900 ns. Red dashed lines show that a sharp reduction in the linewidth occurs towards the central electrode, corresponding to a plasma density drop from the right segment to the left one.

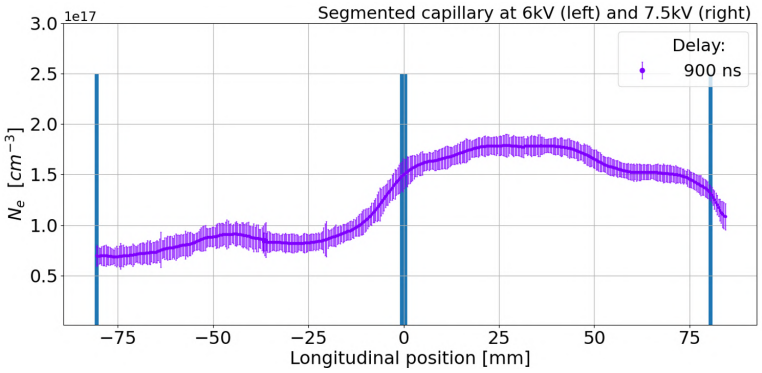

(a) Longitudinal plasma density profile at 900 ns

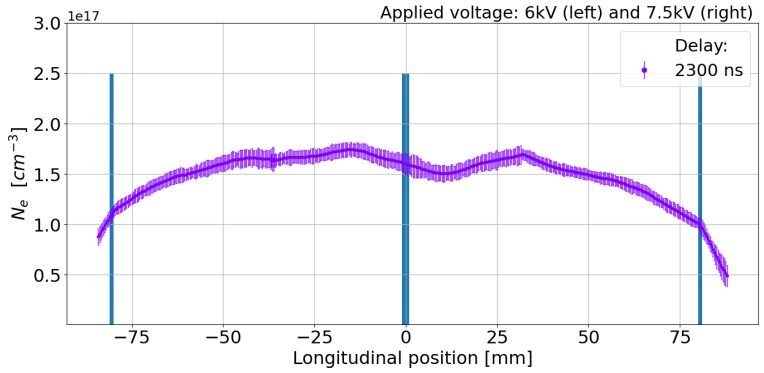

(b) Longitudinal plasma density profile at 2300 ns

Figure 5.7. Longitudinal plasma density profiles measured at 900 ns (a) and 2300 ns (b).

Again, the temporal profiles of the average plasma density in the two segments provide useful information regarding the plasma channel behaviour. As depicted in Fig.5.8, during the plasma formation different plasma density values are reached in the two segments, according to the intensity gap between the two discharge currents. Furthermore, an observed time delay between the leading edges of the discharge current waveforms determines a temporal offset in the density peaks, with the right segment being in advance with respect to the left one. Due to this temporal offset, the right plasma segment starts recombining in advance and its density decreases to the lower values of the left segment, after which the two segments proceed to recombine with the same trend.

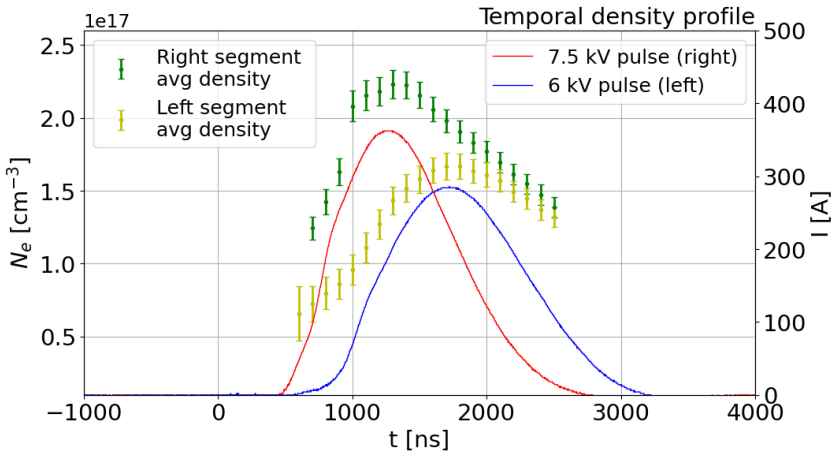

Figure 5.8. Temporal evolution of the plasma density, averaged over the right (green) and left (yellow) segments. Solid line represent the waveform of the two discharge currents produced in right (red) and left (blue) segments.

This second test proved that by tuning the voltage applied independently to the two segments, it is possible to modulate the plasma density profile along the channel. This feature of the segmented capillary is particularly useful for the application of plasma density ramps, including controlled particle injection or beam matching and extraction for plasma accelerating stages. Furthermore, it was also shown that in the recombination phase the plasma redistributes along the channel establishing a symmetric profile with gradual density ramps towards the exits. Therefore, a proper tuning of the plasma discharge pulses in time and voltage allows to freely modulate the plasma density distribution according to the required application.

Another major advantage of such scheme for long plasma discharge capillaries can be visualized on the Paschen curve for hydrogen, reported in Fig.5.9.

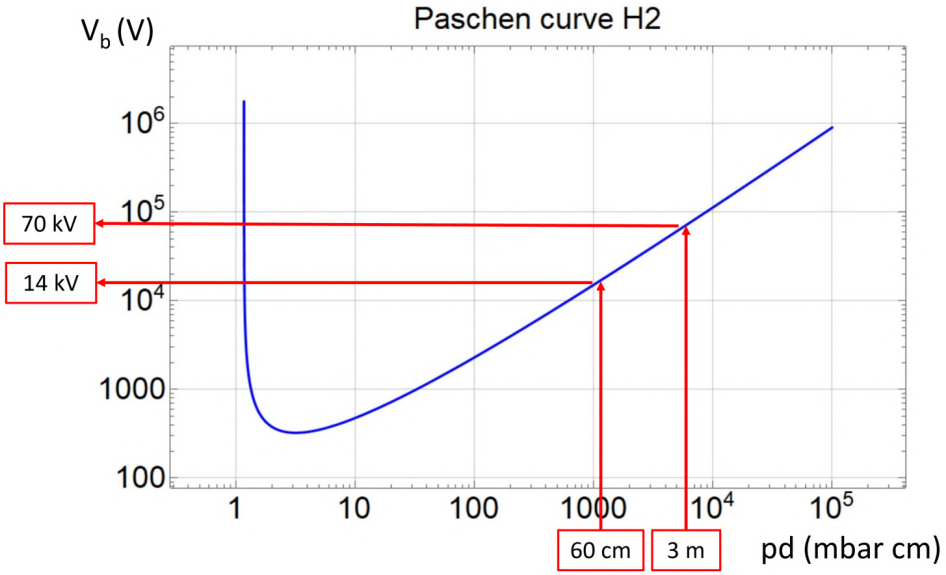

Figure 5.9. Paschen curve for molecular hydrogen, showing the breakdown voltage dependence on the product between pressure and length of the gas column.

Considering to operate a 3 m-long capillary using 10-20 mbar of H_2, the ionization of the entire gas column would require around 70 kV pulses, available only with expensive and cumbersome HV generators. However, a similar device composed by five 50-60 cm-long segments would need only 10-15 kV to produce a 3 m-long plasma channel with independent plasma discharges. In this case, a higher number of HV pulser circuits would be needed, but the total cost and footprint of the overall HV system would be much lower. In addition, the compactness of such HV system could be further improved by feeding the HV circuits with the same HV generator (as it was done for the integrated capillary described in the following Section). In the end, the segmented capillary concept results to be a reliable solution to improve the cost-effectiveness and compactness of the entire plasma module for very long m-scale plasma sources.

5.2 Integrated capillary for staged particle beam acceleration and focusing

An alternative configuration of the segmented capillary was designed to produce three independent plasma discharges, aimed at providing two focusing APL stages and one accelerating PWFA stage, all integrated within a single plasma source. In particular, the first APL matches driver and witness beams at the PWFA stage, while the second one extracts the two bunches, compensating the large divergence at the exit of the accelerating stage. As reported in Fig.5.10, the three stages are independently powered by three parallel HV circuits, which are fed by a single HV generator through a HV mixer.

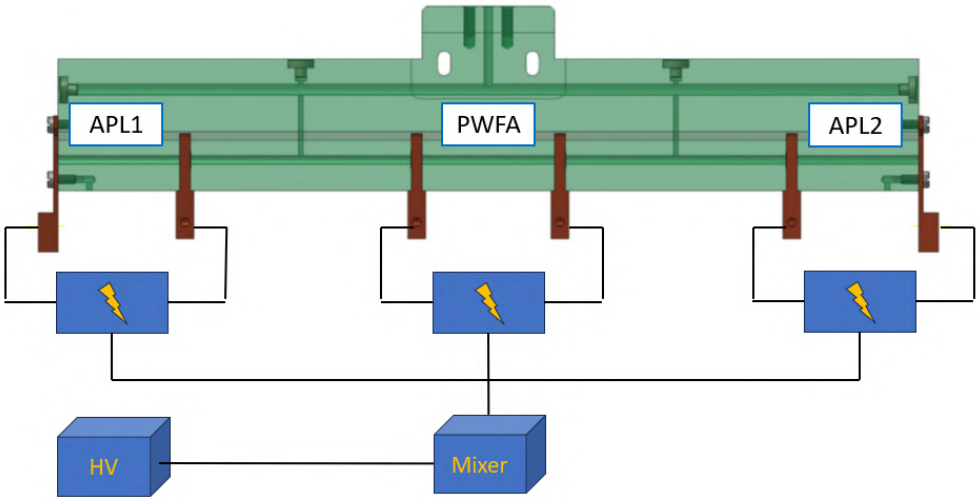

Figure 5.10. Schematic view of the integrated capillary, based on three independent discharge segments powered by parallel HV pulsers, in turn fed by the same HV generator.

A first geometrical configuration of the so-called integrated capillary, depicted in Fig.5.11, consists in a 19 cm-long 2 mm-diameter Lexan capillary, composed by three 3 cm-long segments, separated by two 5 cm-long drifts.

The drift length is given by the expected focal lengths of the APL stages, thus reproducing a FODO-like configuration with alternated beam focusing and

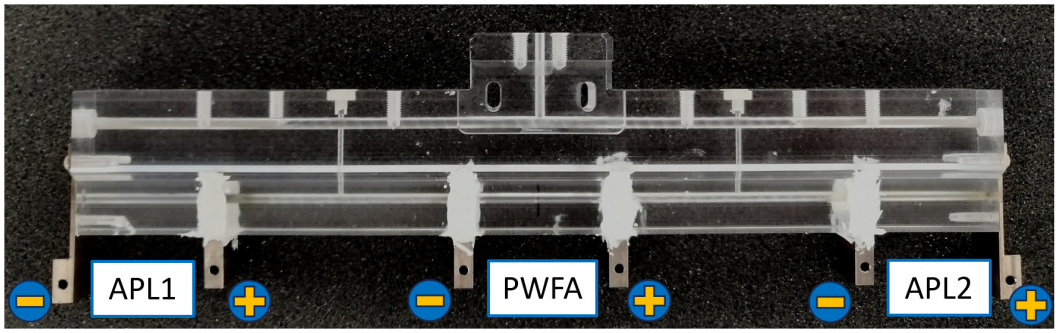

Figure 5.11. Picture of the integrated capillary

acceleration. As for the first segmented capillary, an upper channel distributes uniformly the neutral gas, which is then injected into the two drifts by two 1 mm-diameter inlets, thus filling the entire capillary channel.

Since APL stages are conceived to focus electron beams, the electrode polarization needs to be set such that the discharge current is anti parallel to the beam propagation direction, as shown in Fig.2.10. On the other hand, the electrode polarization is not meaningful in the PWFA stage, if we consider to operate in the plasma recombination phase, in which the current discharge is over and the lower plasma density allows for a simpler beam matching. Therefore, in order to avoid connecting positive electrodes of adjacent stages close to each other, which could cause unwanted discharges propagating from one HV circuit to the other, an alternating polarization was considered for the capillary operation.

A picture of the integrated capillary installed inside the Plasma_lab experimental chamber is reported in Fig.5.12 together with the HV system and the experimental setup.

(a)

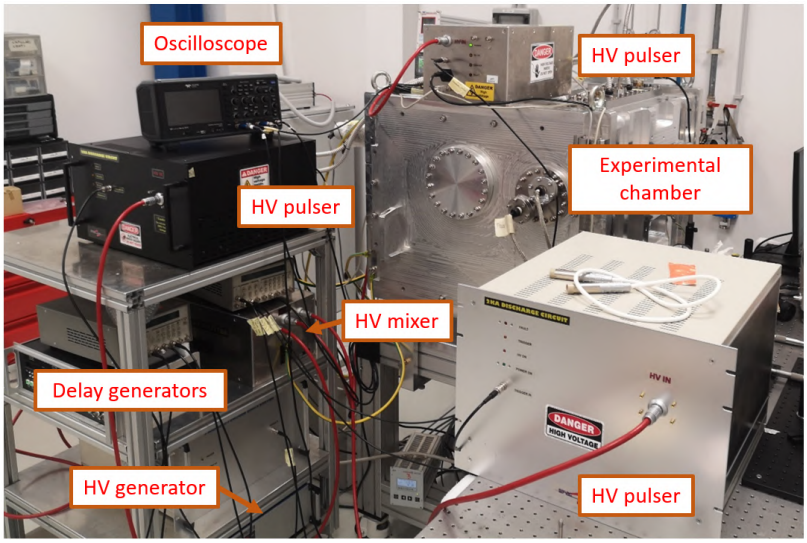

(b)

Figure 5.12. (a) Integrated capillary installed inside the Plasma_lab experimental chamber, with alternating polarization. (b) Experimental setup, including the HV system based on three parallel HV pulser circuits fed by the same generator by means of a HV mixer.

Compared to the previously described segmented capillary, the use of a single HV generator, feeding the independent stages of the plasma source, allows to improve the HV system compactness and cost-effectiveness. Moreover, even though this configuration does not allow to independently tune the voltage in the three stages, the three HV pulsers can still be properly synchronized by a delay generator to freely modulate the plasma density.

5.2.1 Testing and characterization

The working principle of the integrated capillary is based on the synchronization of the three stages with the arrival time of driver and witness beams. As discussed in Sec2.3.1, charged particle beams must pass through the APL stages at the peak of the discharge current, so as to experience the highest focusing field. In addition, as previously mentioned for the PWFA stage, it is preferable to operate in the plasma recombination phase, in which the slowly decreasing trend of the plasma density allows for an easier density tuning and beam matching. For these reasons, the plasma discharge in the central PWFA stage must be triggered few μs earlier than the ones in the APL stages.

In this regard, a first test of the integrated capillary was performed to characterize the operation of the three plasma stages. Around 50 mbar of H_2 were injected at 1 Hz inside the capillary and ionized by 10 kV pulses, delivered by the HV circuits to the corresponding stages, thus producing plasma discharges with peak current of 500 A and 250 A respectively in the APL stages and PWFA stage. Since high current intensity is only required in the APL stages, the HV pulser connected to the PWFA stage was equipped with a lower number of capacitors, hence the lower current intensity measured in the central plasma stage. A delay of 3 μs was set between the central discharge and the other two, so to have a density of around 10^{15} cm^{-3} in the PWFA stage when the plasma discharge is triggered in the APLs.

The characterization of each plasma stage was achieved by shifting the optical line for the acquisition of hydrogen spectral images. Due to the delay between the discharges, the ICCD camera was synchronized to each stage independently to perform plasma density measurements. Fig.5.13 reports the longitudinal plasma density profiles measured through Stark broadening method in the three stages, at a delay of 1500 ns with respect to the discharge trigger of each plasma stage. Regarding the APL stages, it is noteworthy how the plasma propagates through the drifts with smooth density ramps, differently from the steep density drops observed towards the plasma plumes outside the capillary. In the central plasma stage, such smooth ramps were hardly visible due to the lower plasma density (and light intensity).

Fig.5.14 reports the waveforms of the discharge currents in the three stages and the corresponding temporal evolution of the plasma density, averaged over the 3 cm length of each stage. The vertical red line represents the time instant in which driver and witness bunches should be injected to exploit the peak of the magnetic field in the APLs. At the same time, the plasma density in the PWFA stage is around 10^{15} cm^{-3}, below the measureable density range of Stark broadening method.

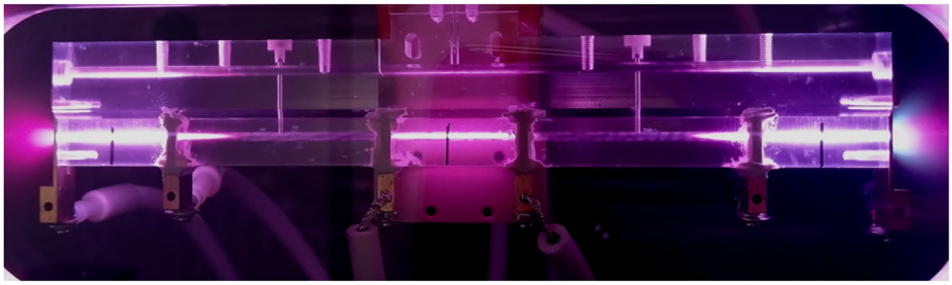

(a)

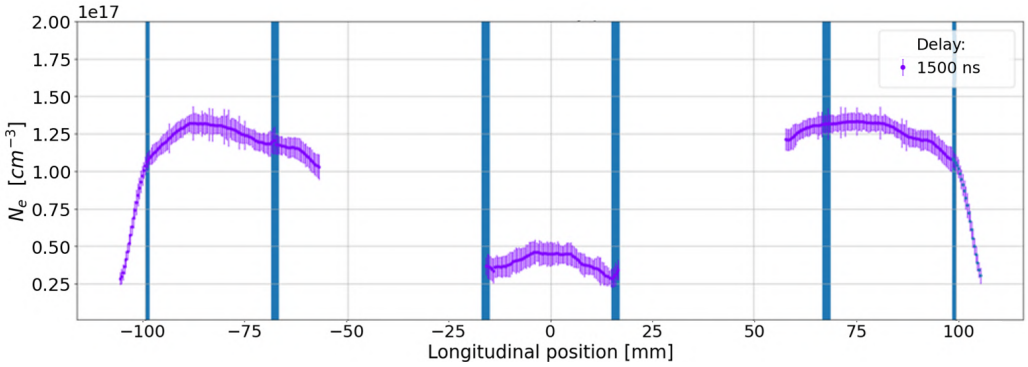

(b)

Figure 5.13. (a) Picture of the integrated capillary during operation. (b) Longitudinal plasma density profiles in the three plasma stages, measured at a delay of 1500 ns with respect to the corresponding discharges, which are triggered with a 3 μs delay between PWFA and APLs stages. It is important to point out that the density profile shown in the central stage is obtained 3 μs before the others, due to the mentioned time delay, whereas a central density of 10^{15} cm^{-3} is reached when the lateral profiles are measured.

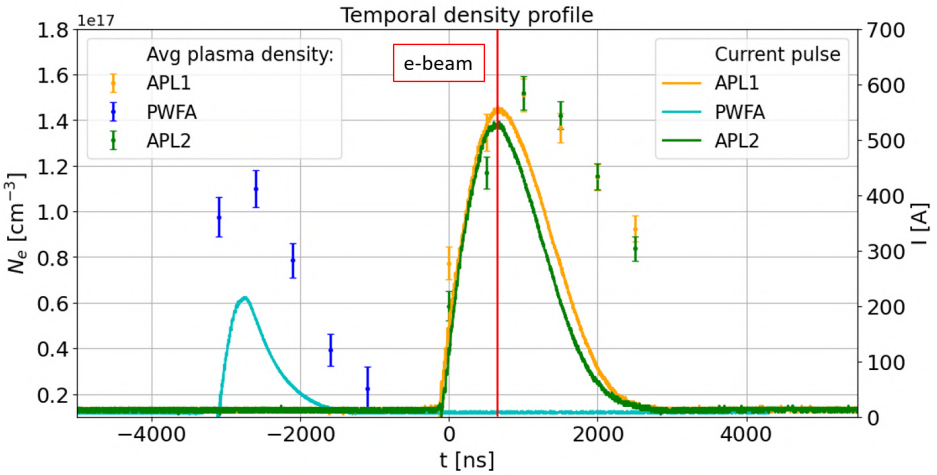

Figure 5.14. Temporal evolution of the plasma density, averaged over the first APL (orange), the PWFA (blue) and the second APL (green) stages. Solid lines represent the three discharge current waveforms produced in the first APL (orange), the PWFA (cyan) and the second APL (green) stages. The red line represents the beam time of arrival.

During the experimental characterization, a remarkable crosstalk was observed between the discharge pulses of the three stages. In particular, the plasma discharge generated 3 μs in advance in the central stage tended to trigger the other two, preventing a correct synchronization between the three stages. Such behaviour was strongly enhanced with the applied voltage and also worsened with heavier gases, such as N_2. Moreover, dust deposition and sputtering were observed towards the negative electrode of the second APL, which was the plasma stage mainly affected by crosstalk.

In order to overcome the crosstalk issue, HV pulser circuits were equipped with an optical insulation to prevent any electronic interference between them. Furthermore, an upgraded version of the integrated capillary, reported in Fig.5.15, was designed and tested. The new configuration is characterized by three inlets in the three stages and two open drifts, such that the injected gas fills the plasma stages and expands in vacuum in the drifts, preventing bridge effects between adjacent electrodes. Moreover, tungsten-copper electrodes were employed, exploiting the higher melting temperature of tungsten (3400°C) to reduce sputtering.

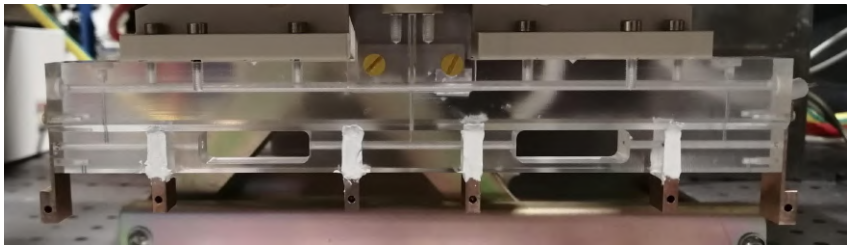

Figure 5.15. Upgraded configuration of the integrated capillary, with two open drifts and three inlets inside the plasma stages.

Fig.5.16 reports the characterization of the first APL stage of the second version of the integrated capillary. As shown by the H-β spectral image and the recovered plasma density profile, measured with a 1200 ns delay, a density drop in the inner region of the drift is obtained similarly to the outer plasma plume, thus reducing crosstalk due to the plasma jet impinging on the adjacent electrode.

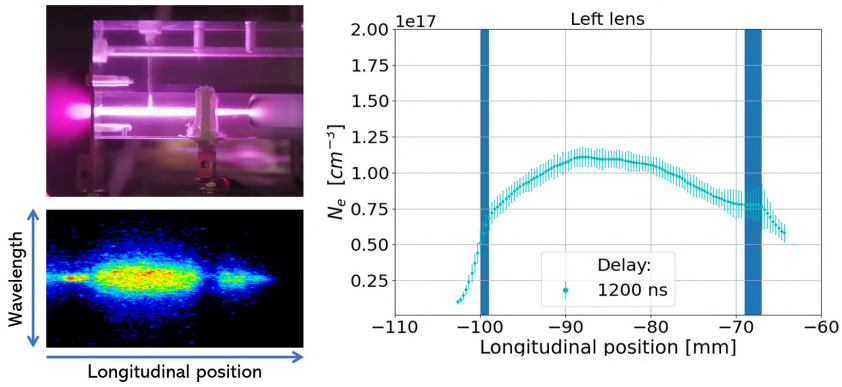

Figure 5.16. Characterization of the first APL stage of the upgraded integrated capillary. Both the H-β spectral image (Bottom left) and the retrieved plasma density profile (right) show that a density drop is obtained in the inner region of the drift.

A final version of the source, depicted in Fig.5.17, was designed to optimize the APL and PWFA stages. The inner drifts are completely removed, except for the portions towards the central stage. In this way, smooth plasma density ramps after the first APL and before the second one are replaced by steep density drops, thus producing a uniform magnetic field localized only inside the plasma stages. On the contrary, smooth density ramps are kept in the central PWFA stage to optimize beam matching and extraction. Moreover, two shields with 2 mm-diameter holes are inserted in each open drift to avoid the plasma jets, emitted by each stage, to reach the adjacent electrodes. In addition, each electrode is shielded by a Lexan coating, as a further countermeasure to crosstalk.

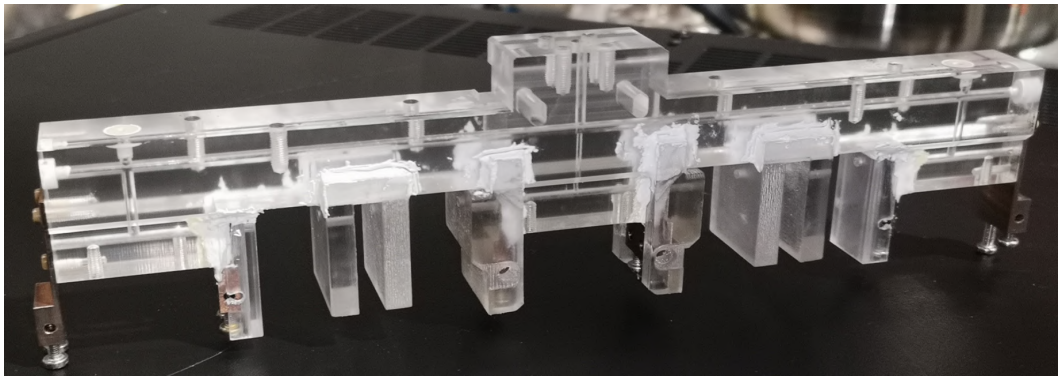

Figure 5.17. Final configuration of the integrated capillary, with Lexan shields and electrode coatings to prevent discharge crosstalk. Drift portions are removed towards the plasma stages, except for the central one.

5.2.2 Staged acceleration and focusing of electron beams at SPARC_LAB

The final version of the integrated capillary was installed in the plasma module of SPARC_LAB accelerator facility, replacing the set of PMQ triplets to demonstrate the possibility to focus, accelerate and remove the large divergence of witness electron bunches within a single plasma source [101]. Such proof of principle experiment was carried out with a 200 pC driver bunch and a 50 pC witness bunch, injected in the capillary with energy of around 72 MeV and properties reported in Tab.5.1.

Parameter	Unit	Driver	Witness
Electron energy	MeV	71.6 ± 0.1	71.9 ± 0.1
RMS energy spread	MeV	0.49 ± 0.03	0.72 ± 0.04
Bunch charge	pC	200	50
RMS bunch duration	fs	185 ± 39	55 ± 32
Driver-witness delay	ps	1.15 ± 0.03	
RMS normalized emittance	μm	6.2 ± 0.7	4.8 ± 0.4

Table 5.1. Beam parameters of driver and witness bunches injected in the integrated capillary for staged focusing and acceleration.

Beam transverse profile measurements were performed with a cerium-doped yttrium aluminum perovskite (Ce:YAP) scintillating screen, located 5 cm downstream the integrated capillary, where extracted bunches are focused by the second APL stage. The magnetic spectrometer downstream the plasma module was then used to characterize the energy profiles of the bunches.

N_2 gas was adopted for the experiment, in order to facilitate the gas extraction from the plasma chamber, keeping 10^{-8} mbar in the upstream C-band structure. A Nd:YAG laser was employed to stabilize the plasma discharge formation in the PWFA stage, reducing its time jitter down to few nanoseconds, as described in Sec.3.8. The laser was installed close to the capillary vacuum chamber and injected into it by means of a metallic mirror. The other stages, characterized by higher current pulses, did not need for external stabilization.

The operative configuration of the plasma source is reported in Fig.5.18.

Plasma stages are powered by means of 10 kV pulses, ionizing around 50 mbar of N_2 gas. A 250 A plasma discharge is triggered in the PWFA stage around 8 μs in advance, so to have a plasma density of around 4×10^{15} cm^{-3} when the electron beams pass through. In particular, this is an optimized condition for the driver-witness configuration described in Tab.5.1 and has also been used in previous experiments at SPARC_LAB [99, 100]. APL stages are syncrhonized such that the electron bunches propagate in correspondence of the discharge current peak, around 600 A, with plasma density of around 2×10^{17} cm^{-3}.

The optimal parameters of the two APLs in terms of discharge current and timing were obtained by measuring the beam size on the Ce:YAP screen with only the second lens turned on, while leaving off the first two stages. In this way, since the distance between the second APL and the screen corresponds to that between the first APL and the PWFA stage, the optimized condition for the second APL to produce a beam waist on the screen was also used in the first APL to focus the beam at the PWFA stage entrance. In addition, a higher discharge current was set

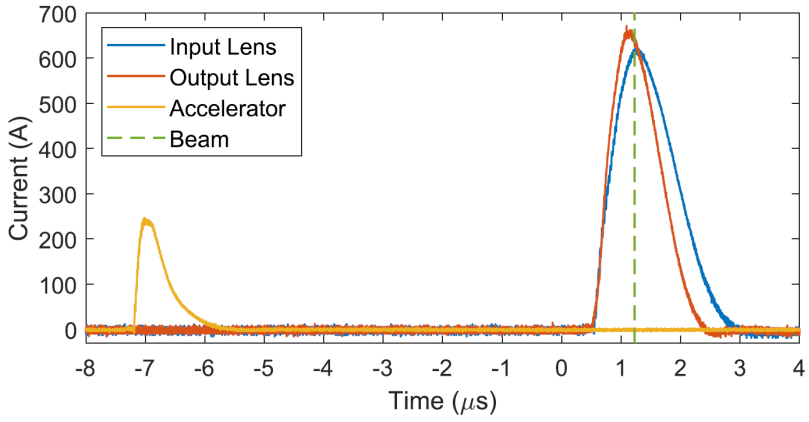

Figure 5.18. Discharge current pulses. The accelerator stage (yellow) is triggered 8 μs before the electron beams arrival time (dashed green line), such that the plasma density reaches the desired value during the recombination. Conversely, the two active-plasma lenses (red and blue lines) are turned on a few hundreds of ns before so that the electron beams experience the strongest focusing in correspondence of the current peak.

in the second APL (670 A) compared to the first one (620 A), to take into account the increase of the witness energy downstream the PWFA stage, which requires a higher focusing field.

Fig.5.19 reports the scan of the beam spot size, performed on the screen by varying the trigger timing of the second APL current discharge with respect to the beam time of arrival. The values are computed from images with both bunches present, thus they represent a convolution of the two transverse profiles, since the dynamics of driver and witness bunches are strongly correlated by the velocity-bunching scheme and cannot be decoupled.

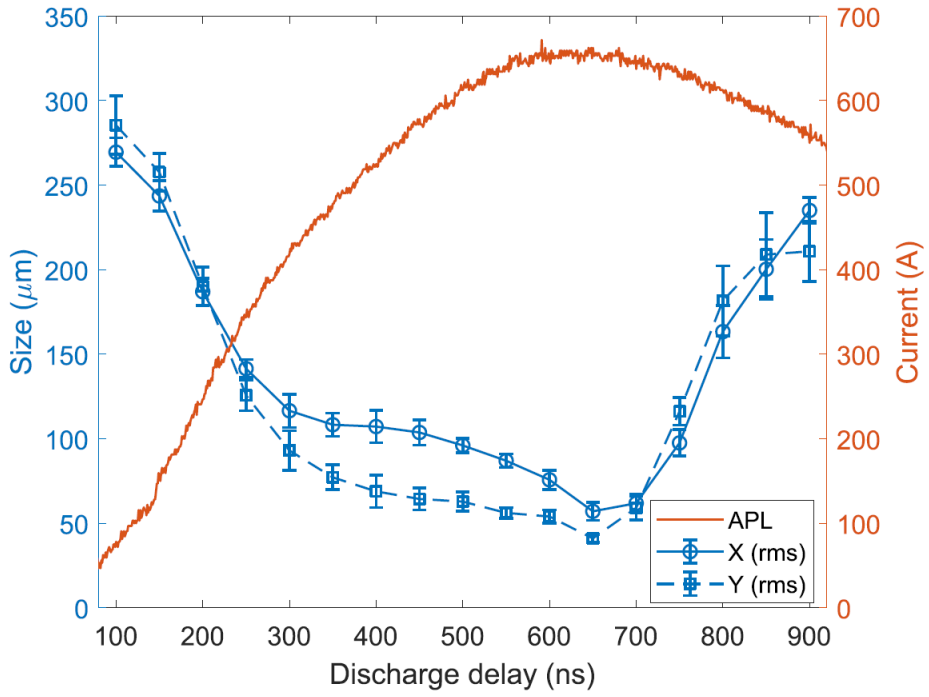

Figure 5.19. APL scan. The data points (blue) show the horizontal (X) and vertical (Y) beam sizes measured on the screen downstream the capillary. The scan is achieved by turning on only the second lens and delaying its discharge current (red line) with respect to the beam time of arrival. The error bars are obtained as the standard deviations of the 50 shots collected for each delay.

With optimized settings for the discharge currents and timings, the PWFA stage was turned on to perform staged focusing-acceleration tests. The witness energy gain was measured on the scintillating screen downstream the magnetic spectrometer. Finally, Fig.5.20 reports 200 consecutive energy spectra of the two beams, acquired with and without the PWFA stage in operation. A final witness beam energy of 76.35 $\pm$ 0.27 MeV was measured, with a resulting energy gain of $\approx$ 4.5 MeV over 3 cm of acceleration length, corresponding to a $\approx$ 150 MeV/m accelerating gradient, and an energy spread of 1.09 $\pm$ 0.12 MeV.

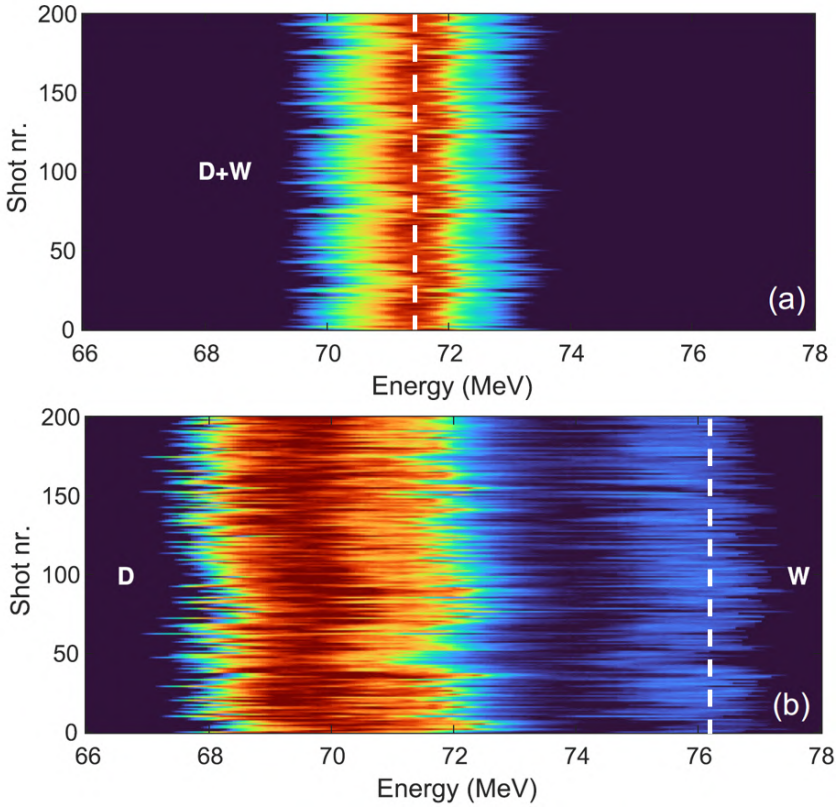

Figure 5.20. Energy spectra with the PWFA stage turned off and on. The plots report the energy spectra of 200 consecutive acquisitions of the driver (D) and witness (W) beams. Each plot is obtained with the APLs turned on and with the accelerator stage turned off (a) and on (b). The spectra are obtained in correspondence of the scintillating screen located downstream the magnetic spectrometer. Vertical white lines highlight the average witness beam energy at the entrance and exit of the PWFA stage, respectively 71.9 and 76.3 MeV, corresponding to a 150 MeV/m accelerating gradient.

The quadrupole scan technique was used to estimate the normalized vertical emittance of the accelerated witness beam, evaluated on the same screen downstream the magnetic spectrometer, where driver and witness bunches are well separated in energy. The scan is obtained by measuring the witness vertical spot size as a function of the current used in the electromagnetic quadrupoles, located between the plasma module and the screen. By performing a numerical fit on the experimental values a normalized emittance of 12.6 ± 1.1 μm is measured for the plasma accelerated witness.

As observed with numerical simulations, the performances of the three staged capillary were limited by a non-optimized matching at the entrance of the APL stages, leading to emittance growth. Future upgrades of the device could be achieved by properly optimizing the bunch spot sizes at the entrance of the APLs, limiting non-linear effects caused by the focusing field.

In conclusion, this proof of principle experiment demonstrated the feasibility of the integrated capillary to provide plasma-based focusing, acceleration and extraction of the witness beam within a single, compact plasma source.

5.3 Curved plasma discharge capillary for compact guiding of charged particle beams

As discussed in Sec.2.3.1, the discharge current produced in plasma discharge capillaries generates strong focusing magnetic fields, which can be exploited to guide and focus charged particle beams. Since the flux of plasma electrons driven by the discharge follows the capillary geometry, such guiding mechanism can be exploited to bend charged particles trajectories along curved plasma channels. This concept is similarly implemented for guiding high intensity laser pulses along curved capillaries [43], relying on the fact that hollow transverse density profiles can be obtained along curved plasma channels for laser guiding.

Curved plasma discharge capillaries for guiding and deflecting charged particle beams, also called Active Bending Plasmas (ABP), can in principle reach greater magnetic fields (and, thus, larger deflection angles) than superconducting dipole magnets and provide a significant reduction in the energy dispersion [96], even though no experimental demonstration of such devices has ever been produced up to now.

5.3.1 Design and characterization

To demonstrate the ABP mechanism and its advantages, a curved capillary was designed, tested and implemented at SPARC_LAB facility for guiding electron bunches on a curved trajectory. The device consists in a 10 cm-long 3D-printed VeroClear capillary, having a 1 mm-diameter central inlet and a 2 mm-diameter channel with vertical curvature. In particular a vertical offset of 3 mm was designed between the channel entrance and exit, such that electron bunches are damped on the capillary walls when the plasma is turned off. In addition, a lower channel was included in the geometrical design, not connected to the gas injection inlet, in order to allow the electron bunches to pass through when the plasma is turned off (after shifting the capillary on the vertical axis). A picture of the curved capillary is shown in Fig.5.21.

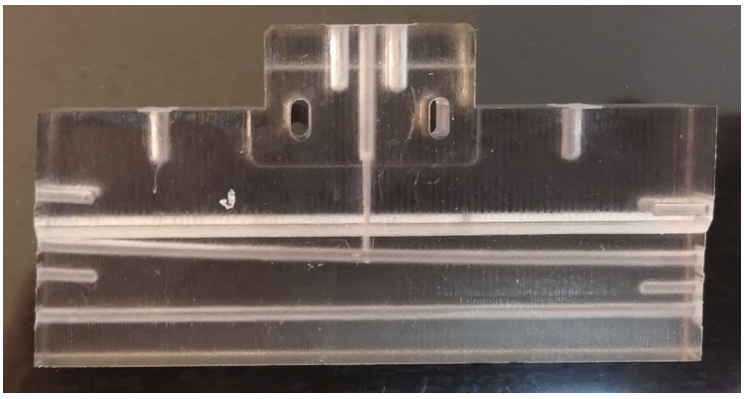

Figure 5.21. Picture of the 10 cm-long curved capillary. A vertically curved channel is designed to provide a 4 degree deflection to electron bunches trajectories, while a lower straight channel allows the beams to pass through without plasma (after moving the capillary in the vertical plane).

The capillary was characterized in the plasma module of the SPARC_LAB accelerator, equipped with systems for gas injection, plasma formation and diagnostics analogous to those of the Plasma_lab setup described in Ch.3. 1 bar of H_2 gas was delivered by a hydrogen generator and injected into the curved capillary by means of an electro-mechanical valve, regulating the gas injection with a pressure of few hundreds mbar and 1 Hz repetition rate. 10 kV pulses were applied to the capillary electrodes by a HV pulser circuit, generating plasma discharges with 730 A peak current and around 1 μs FWHM duration.

Plasma density measurements were performed with Stark broadening method. Since the optical line allows to acquire only 5 cm-long portions of the plasma channel, it was properly shifted to scan longitudinally the capillary. Spectral images were acquired from three different positions and elaborated measurements were stack together to compose the longitudinal plasma density profiles of the entire capillary, measured at different delays with respect to the discharge trigger, as reported in Fig.5.22. Longitudinal profiles are characterized by density flat-tops, with a density peak of $2.6 \pm 0.2 \times 10^{17}$ cm^{-3}, and smooth ramps towards the capillary ends.

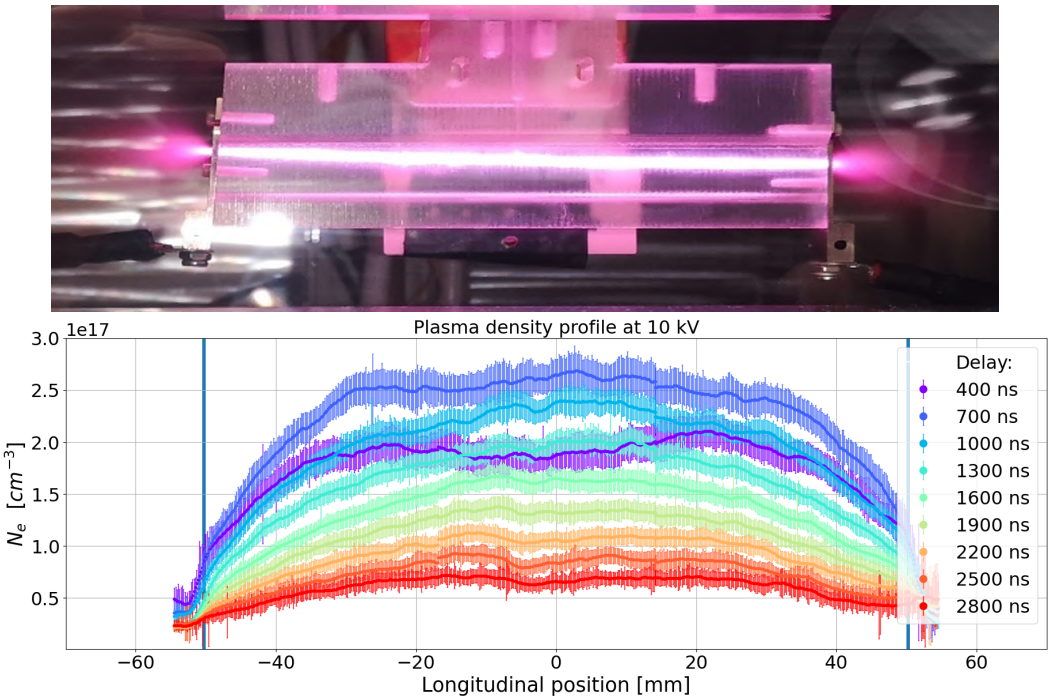

Figure 5.22. Longitudinal plasma density profiles, measured by stacking three portions of the curved plasma channel at different delays with respect to the discharge trigger.

5.3.2 Guiding of electron beams with an active-bending plasma stage

A proof of principle experiment was carried out at SPARC_LAB facility to demonstrate the deflection of relativistic electron beams by means of a curved discharge capillary (ABP) [102]. A schematic representation of the experiment is depicted in Fig.5.23.

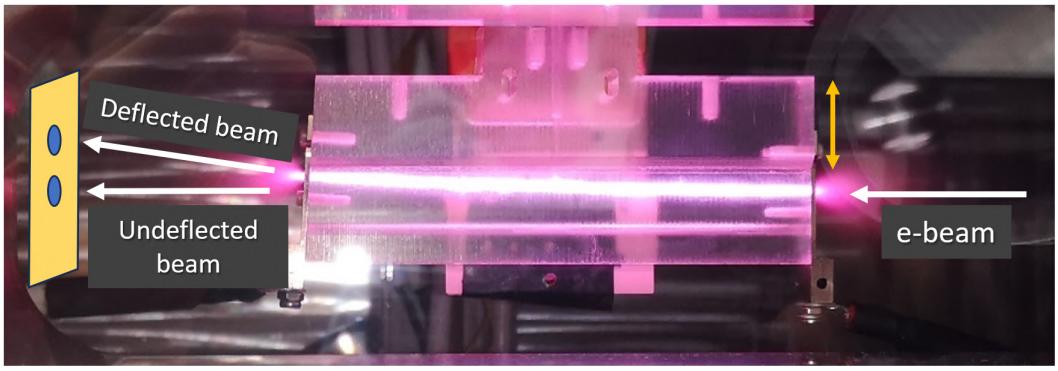

Figure 5.23. Schematic representation of the active bending plasma experiment.

A relativistic electron bunch enters the capillary and is guided along the curved plasma channel by the poloidal magnetic field. The beam trajectory is deflected with a 1.6 m curvature radius, exiting the capillary with a 3 mm offset with respect to the entrance and a deflection angle of 4 degrees. Downstream the capillary, the beam is detected by a scintillating screen. To compare the deflected beam with an undeflected one, the plasma is turned off and the capillary is shifted upwards, allowing the electron bunch to pass through the straight channel in the lower part of the capillary. Additionally, spot size images of the beam were acquired after completely removing the capillary from the beam path, considering that dielectric wakefields in the hollow straight channel, driven by the electron bunch, could affect the beam characterization [123].

The experiment was carried out by using a 50 pC electron beam with 60.2 $\pm$ 0.1 MeV energy, 0.9 $\pm$ 0.1 ps duration, and 0.6 $\pm$ 0.1 μm normalized emittance [102]. The transverse spot size at the capillary entrance is 130 $\pm$ 10 μm (rms) and its time of arrival jitter is $\approx$50 fs. A cerium-doped gadolinium aluminum gallium garnet (GAGG) scintillating screen is installed 10 cm downstream the capillary to measure the spot size of the deflected beam. The light emitted by the screen is collected into a CCD camera with 20.2 μm pixel resolution.

ABP guiding was demonstrated with three beam configurations. The SPARC_LAB RF linac was tuned to produce electron beams with low ($\sigma_E = 17 \pm 1$ keV), medium ($\sigma_E = 0.33 \pm 0.01$ MeV) and large ($\sigma_E = 1.4 \pm 0.2$ MeV) energy spread, while keeping the same energy, in order to prove the absence of chromatic dispersion in the bending mechanism. Energy spectra of such electron beams were measured by the magnetic spectrometer, located downstream the plasma module, as reported in Fig.5.24.

Beam deflection was achieved with a discharge current of 1.5 kA, reached with 20 kV pulses delivered by the HV system. A comparison between deflected and undeflected beams is reported in Fig.5.25, showing that an overall vertical displacement of 9.9 mm $\pm$ 0.1 mm is reached by deflected beams at the screen position. It is noteworthy that no difference is observed between the deflected beams with three different energy spread, proving that the beam chromatic dispersion does not affect significantly the ABP process.

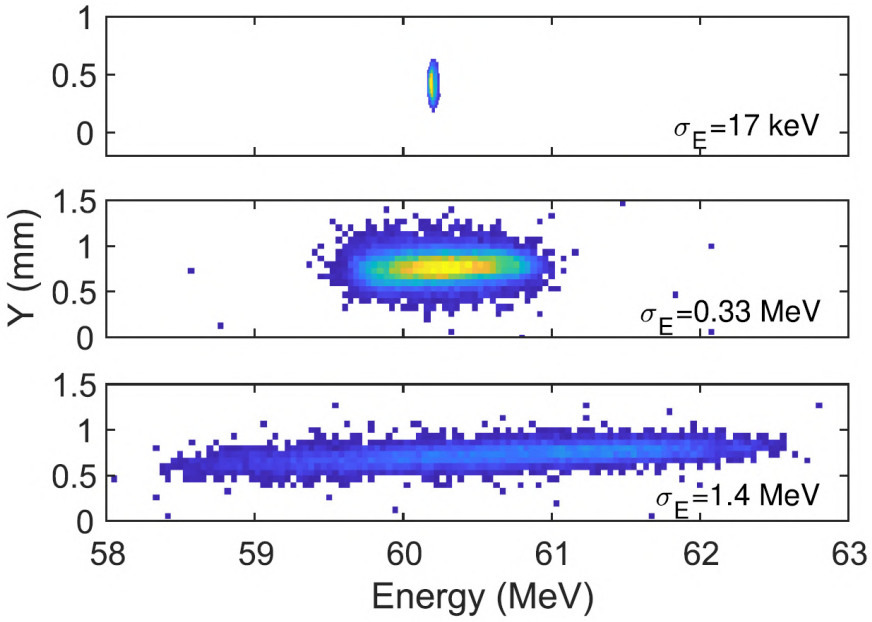

Figure 5.24. Beams energy spectra measured by the magnetic spectrometer for three different working points of the linac. The corresponding energy spreads are indicated in each plot.

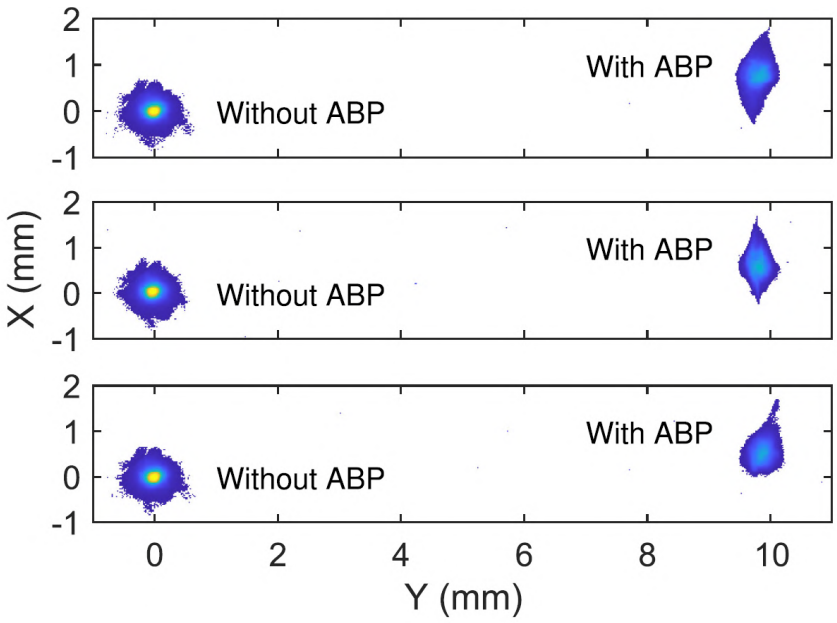

Figure 5.25. Transverse spot sizes of deflected and undeflected beams, measured with a scintillating screen downstream the curved capillary. Each plot is obtained by overlapping a single shot of the undeflected beam (capillary out of the beam path) with a single shot of the deflected one (capillary inserted and discharge current set to 1.57 kA). The beam energy spread in each plot is 17 ± 1 keV, 0.33 ± 0.01 MeV and 1.4 ± 0.2 MeV respectively from top to bottom. A vertical offset of 9.9 mm is observed in each case.

Finally a discharge current scan was performed to evaluate the beam spot size and charge transmission in the three configurations. By tuning the current in the range 1.27±1.57 kA, 100 consecutive single-shot spot size images were acquired and the percentage of transmitted charge was computed as the ratio between the CCD counts with the ABP turned on and the counts when the capillary is removed from the beam path. As shown in Fig.5.26, the beam guiding efficiency increases with the discharge current, up to a 100% charge transmission. Furthermore, no dependence on the energy spread is observed in case of high charge transmission.

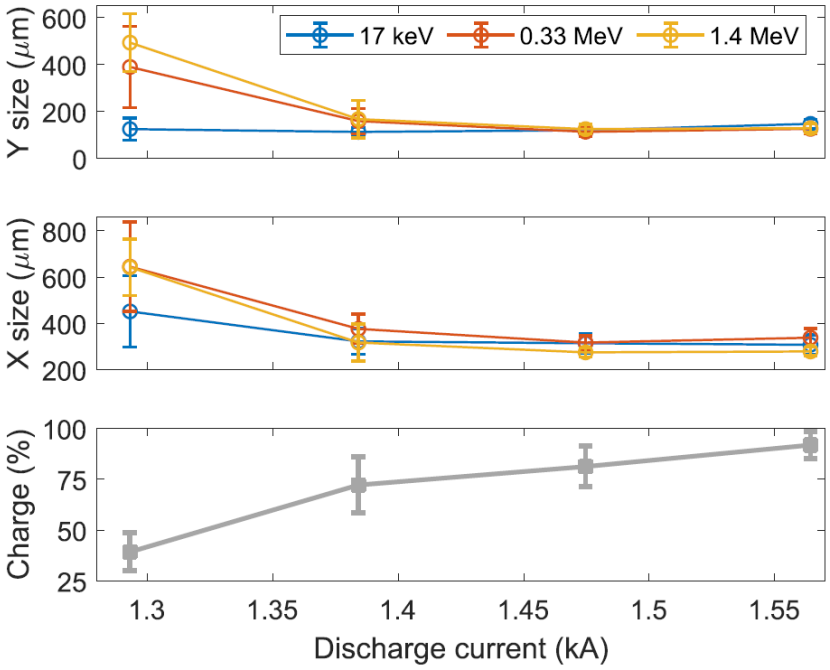

Figure 5.26. The first two plots show the measured vertical and horizontal spot sizes for several discharge currents. Each point is obtained by averaging 100 consecutive single shots, with the error bar computed as the relative standard deviation. The third plot reports the average percentage of transmitted beam charge downstream the capillary with respect to the undeflected one, retrieved by summing the counts of the acquired CCD images.

5.3.3 Capillary erosion and alteration of the plasma properties

At the end of the parametric scan, the curved capillary was characterized again to evaluate possible variations in the plasma (and the source itself), due to long-term operation with high current discharges. After an estimated number of 50000 plasma shots at 1.3÷1.5 kA, a remarkable enlargement of the curved channel was observed, as shown in Fig.5.27. Such increase in the channel diameter is due to plastic erosion, caused by the heat power produced by plasma discharges and delivered onto the capillary walls. Indeed the intense discharge current generated for the ABP guiding, results in considerably high plasma temperature, with $T_e \approx 6.7$ eV for a 1.5 kA peak current, according to Eq.3.16. The increase in the channel transverse cross section resulted in a current density drop, therefore higher currents were required to

continue bending electron beams at the end of the parametric scan, until the erosion was too severe to continue the experiment.

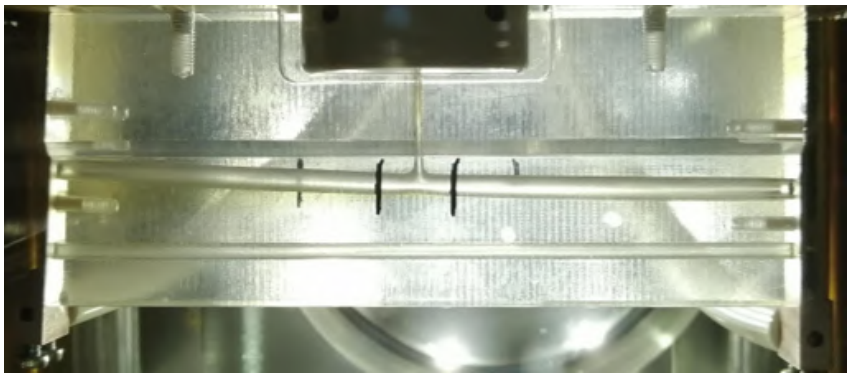

Figure 5.27. Picture of the curved capillary after around 50000 shots with high current discharges. A visible increase in the channel cross section can be noticed.

The same experimental settings were adopted for the plasma characterization, using 10 kV pulses to ionize few hundred mbar of pure H_2 and producing around 720 A plasma discharges at 1 Hz.

Fig.5.28 reports longitudinal plasma density profiles, obtained by stacking density measurements from three portions of the plasma channel, as for the first characterization. Measured density profiles are characterized by a remarkable non-uniformity along the plasma channel and a significant decrease in the overall density compared to results obtained before the ABP experiment (Fig.5.22). The drop in the peak density, from 2.6 $\times$ 10^{17} cm^{-3} to around 1 $\times$ 10^{17} cm^{-3} is due to the capillary erosion, causing an increase in the capillary channel diameter and thus a lower plasma pressure. In addition, the non-uniformity of the density distribution is also due to a non uniform erosion of the channel, which is less evident towards the inlet and the capillary ends, as shown in Fig.5.27.

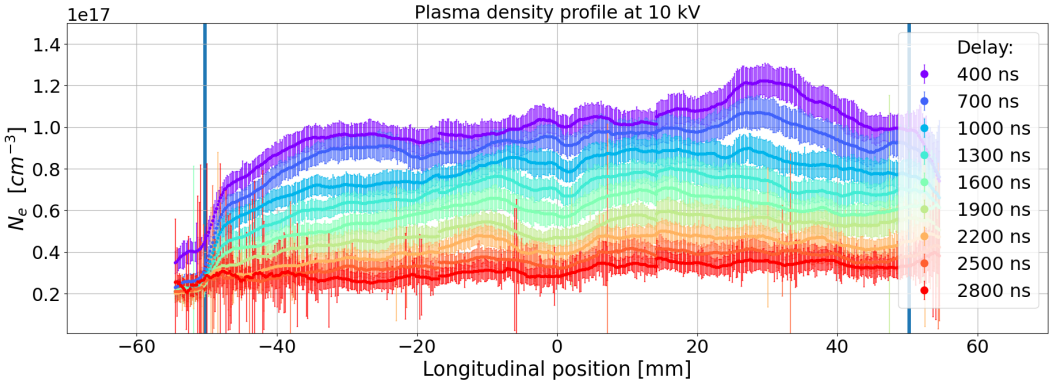

Figure 5.28. Longitudinal plasma density profiles, measured after the ABP experiment. Non-uniformity and an overall decrease of the plasma density can be observed, compared to the preliminary characterization of the curved capillary.

Such density drop can be also visualized by comparing the temporal density profiles before and after the ABP experiment, reported in Fig.5.29. Each point is determined by averaging the plasma density at a given delay along the capillary channel.

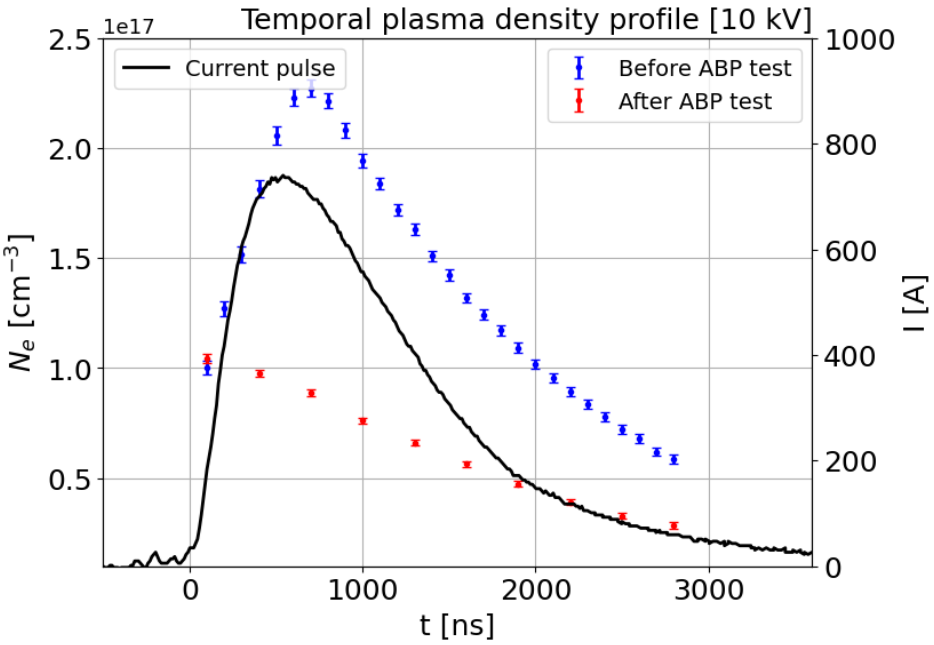

Figure 5.29. Temporal plasma density profiles measured before and after the ABP experiment. Each point is obtained by averaging the plasma density over the longitudinal profile. A dramatic decrease in the plasma density can be observed after long-term high current discharge operation within the ABP experiment.

In conclusion, the novel concept of active bending plasma for guiding and deflecting electron beams represents a promising option for plasma-based transport of particle beams. The experiment carried out at SPARC_LAB have demonstrated for the first time the feasibility of curved plasma discharge capillaries to provide disperionless guiding and deflection of relativistic electron beams within compact devices.

In addition, the characterization of the device used for the experimental campaign has highlighted that erosion issues can affect the longevity of plasma discharge capillaries in long-term operation. For this reason, also considering the requirement of high repetition rate operation for EuPRAXIA@SPARC_LAB project, a specific investigation of high repetition rate plasma sources was included in this PhD thesis project, as discussed in the following Chapter.

Chapter 6

High repetition rate plasma sources

Many applications of particle accelerators, from high energy physics and material science to radiotherapy and industrial applications, require the utilization of accelerated beams delivered with high repetition rate. The number of particle bunches produced and accelerated per second is a key parameter for the luminosity of beam colliders, and, in particular, future linear collider projects as ILC and CLIC foresee operation at 5 Hz [15] and 50 Hz [79] respectively. FEL facilities usually operate at tens-hundreds Hz [2, 44, 71, 5] and, as mentioned in Sec.1.5, EuPRAXIA@SPARC_LAB project foresees operation at 100 Hz, with a future upgrade to 400 Hz.

In the context of plasma-based acceleration, one of the main challenges for high repetition rate operation concerns the availability of plasma sources, able to withstand the heat power deposited by the plasma and the particle bunches into the source. In this regard, a main topic of this PhD thesis concerns the R&D of high repetition rate plasma sources, including the study of suitable materials for plasma discharge capillaries, which can withstand the heat produced by HV electrical discharges. Moreover, laser-induced plasma filaments have been studied and characterized, due to their suitable features for high repetition rate operation.

6.1 Advanced ceramic capillaries for high repetition rate operation

As shown in Sec.5.3, the thermal load produced by high voltage plasma discharges and deposited into the capillary can cause severe erosion and deformation of the capillary channel, affecting the correct operation of the plasma source. This issue is exacerbated by high repetition rate operation, in which the heat flux produced by plasma discharges is enhanced.

Experimental testing carried out on plastic 3 cm-long capillaries, similar to those characterized in Ch.4, have shown that after 10^4-10^5 plasma discharges produced at 1-5 Hz with 300 A peak current (i.e. after few hours of operation), such capillaries experience channel erosion or even a severe damage of the entire structure, as reported in Fig.6.1.

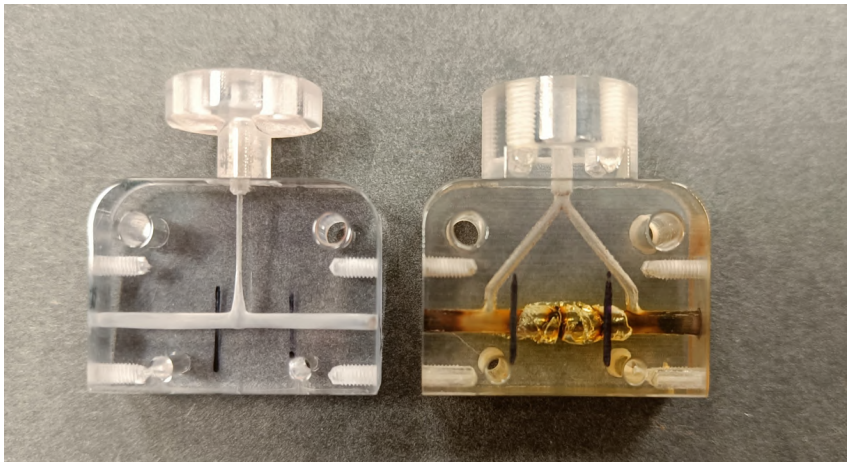

Figure 6.1. Picture of 3 cm-long 2 mm-diameter VeroClear capillaries, tested at 1-5 Hz for 10^4 shots (left) and 10^5 shots (right) respectively. Visible erosion is observed after 10^4 shots, corresponding to few hours operations, while the capillary gets destroyed after 10^5 shots, i.e. few days of testing.

In order to overcome these issues, high melting temperature materials, such as sapphire, have been proposed and widely tested in recent years [60]. However, the significant production cost and poor machinability of such materials for long and complex geometries can dramatically affect the cost-effectiveness of the plasma source.

In this context, this PhD thesis project presents the development of high repetition rate plasma discharge capillaries, based on the combined use of machinable and cost-effective ceramic materials. In particular, the design of such capillaries was based on Shapal Hi M Soft[121] and Macor, which are characterized by high thermal conductivity, high melting temperature and excellent machinability.

An experimental campaign was carried out on a plasma discharge capillary composed by a Shapal core, inserted into a Macor holder, in order to assess the longevity of such materials exposed to high voltage plasma discharges in long-term high repetition rate operation, specifically in the range 10-150 Hz.

Due to Shapal opacity, longitudinal diagnostics were unusable and alternative diagnostic techniques were implemented to characterize the plasma source, such as the transverse Stark broadening method for plasma density measurements. Furthermore, an optical stereomicroscope and a Compact Laser Module were employed to monitor the capillary profile during the experimental campaign, in order to detect any erosion effect.

6.1.1 Ceramic capillary design

As mentioned, the ceramic capillary designed for high repetition rate tests is constituted by an inner core made of Shapal Hi M Soft, which is a hybrid type of machinable Aluminum Nitride (AIN) ceramic, mixed with Boron Nitride (BN). Shapal is characterized by high thermal conductivity (92 W/(m·K) at room temperature, 35 W/(m·K) at 1000°C), more than two times higher than sapphire, and high melting temperature (1900 °C in vacuum). Moreover, its good machinability allows

the realization of long and thin structures, required for the realization of plasma discharge capillaries.

The designed Shapal capillary is characterized by a 3 cm-long channel, with a 2 mm-diameter circular hole, and two inlets with 1 mm-diameter for uniform gas injection. The Shapal core is inserted and glued inside a ceramic holder made of Macor, a machinable glass-ceramic having a thermal conductivity of 1.46 W/(m·K) at room temperature and 1000°C maximum operating temperature. In particular, Macor was adopted for its excellent machinability, cost-effectiveness and availability for large geometries, allowing the design of long capillary holders that can be easily drilled and machined.

Two electrodes, constituted by an inner molybdenum ring and an outer stainless steel plate, are screwed to the extremities of the Macor holder. In such configuration, the higher melting temperature metal (2623°C for molybdenum) is directly exposed to the plasma discharge, while stainless steel is used for the outer plate due to its good machinability, exploited to attach the electrode to the ceramic capillary. Pictures of the ceramic capillary, with Shapal core and Macor holder, and the molybnenum-steel electrodes are reported in Fig. 6.2 .

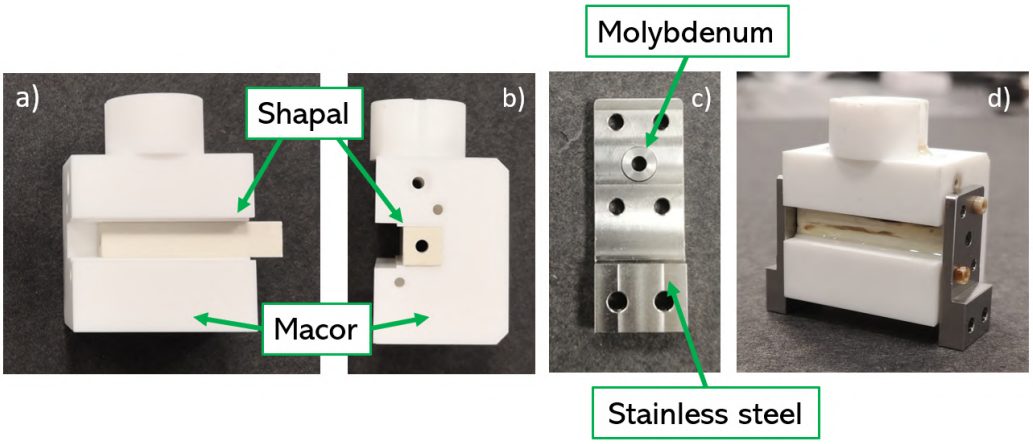

Figure 6.2. (a) Front view and (b) side view of the ceramic capillary, with Shapal core and Macor holder. (c) Molybdenum-stainless steel electrodes. (d) Assembled ceramic capillary.

6.1.2 Experimental setup

The experimental setup, schematized in Fig. 6.3, was slightly modified with respect to the apparatus described in Ch.3, in order to include transverse diagnostics for the ceramic capillary characterization and other variations for high repetition rate plasma discharge operation.

Concerning the gas injection system, the electro-mechanical valve was removed, due to its slow activation preventing operation above 10-15 Hz. As a consequence, gas injection was performed in continuous flow regime, adopting a gas mixture of N_2 (95%) and H_2 (5%) gas, since the H_2 generator does not support continuous flow injection. During the experimental campaign, around 80 mbar of the gas mixture were injected into the capillary by means of a mechanical regulator.

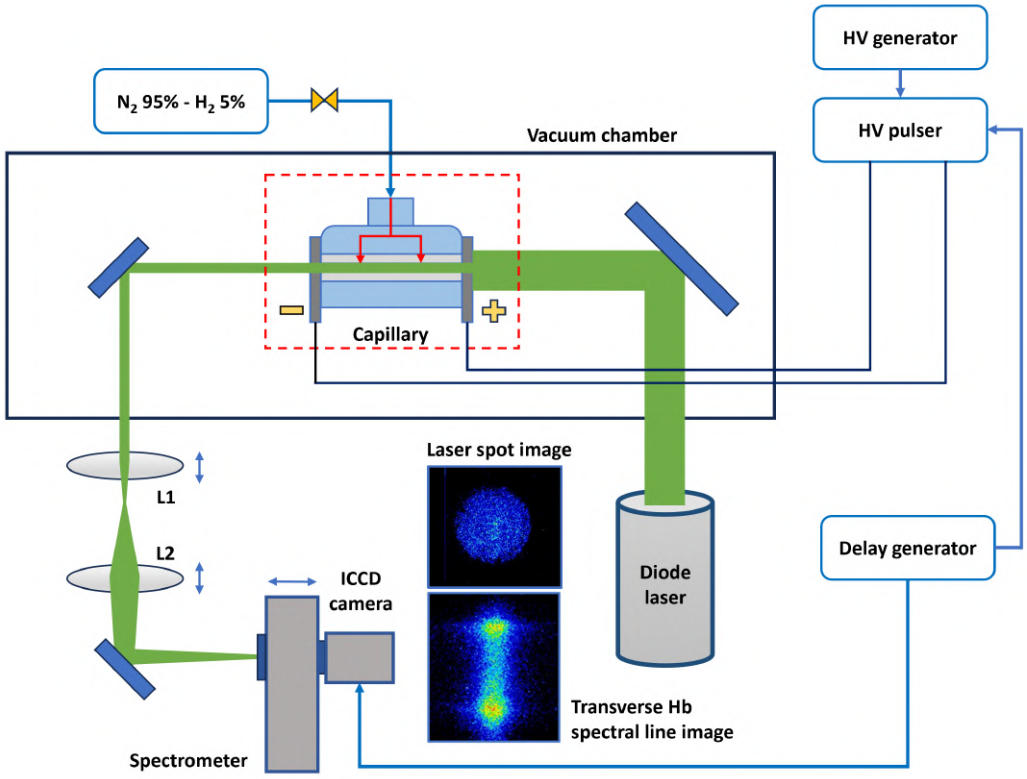

Figure 6.3. Schematic representation of the experimental setup, with transverse diagnostics for the characterization of the ceramic capillary.

Due to continuous flow regime, a higher amount of gas was injected inside the experimental chamber, going to burden on the vacuum system. As a consequence, the turbo-molecular pump was characterized by overheating issues during continuous gas injection, which were properly mitigated by equipping the pump with a water cooling system. As a result, a thermal equilibrium was reached during the experimental campaign, with a pump temperature of around 27° C and a vacuum level of 10^{-2} mbar inside the experimental chamber during gas injection.

Regarding the high voltage system, the production of kV-range pulses at high repetition rate resulted in the overheating of the SCR switch and the resistors of the HV pulser circuit, observed by means of a thermal camera. Also in this case, the overheating issue was mitigated by equipping the circuit with an air cooling system, establishing a thermal steady-state condition below 40° C during the experimental testing. For instance, a thermal image of the HV circuit operating at 50 Hz is depicted in Fig.6.4.

During the experimental campaign, the operating repetition rate was set in the range 10-150 Hz by means of the delay generator. The upper limit was imposed by the maximum current delivered by the HV generator to charge the pulser circuit.

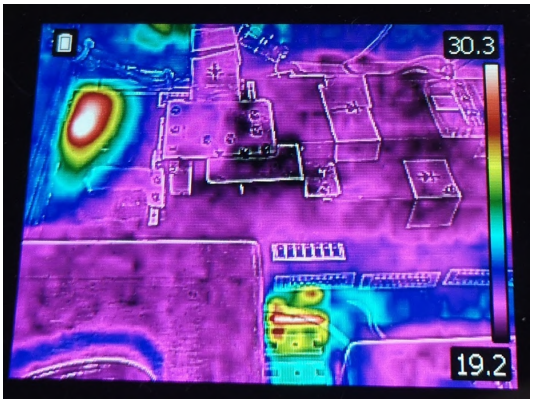

Figure 6.4. Thermal picture of the HV circuit. The SCR switch (top left in the picture) reaches an equilibrium temperature of 30-40° C during operation at 50-150 Hz, thanks to an air cooling system equipped to the circuit.

Transverse diagnostics techniques

Due to Shapal opacity to visible and near-infrared light, longitudinal plasma density distribution was not measurable by means of conventional spectroscopic or interferometric techniques, therefore a transverse spectroscopic analysis was performed to characterize the plasma density. In addition, other transverse diagnostics were adopted to characterize the integrity of the source.

First, a Compact Diode Laser Module (Thorlabs) was employed to monitor any geometrical variation in the capillary channel cross section, eventually caused by Shapal erosion. As shown in Fig. 6.3, the laser beam enters the capillary with a spot size larger than the channel diameter and is guided through a beam transport line, made of a telescopic system analogous to the one described in Ch.3, and collected into the imaging spectrometer. A mirror, implemented inside the spectrometer, guides the laser beam into the ICCD camera. In this way, the shape of the laser spot image, acquired by the camera, is directly related to the channel walls profile and any detected increase of the laser spot would be linked to the widening of the capillary channel, caused by erosion. In addition, the electrodes are characterized by a hole slightly larger than the 2 mm channel diameter, so as to prevent the interference of electrodes erosion in the measurement reliability.

Laser spot imaging resulted particularly useful for online characterization of the source integrity. However, this technique does not allow to detect a channel widening in the inner region of the capillary, eventually caused by erosion, if the edges do not experience the same deformation, therefore a microscopic analysis was performed offline on the ceramic capillary to characterize the entire channel profile with higher precision. In particular, an optical stereomicroscope (Euromex) was employed to measure the cross section diameter along the capillary channel before and after the experimental campaign. Fig.6.5 reports a picture of the stereomicroscope, with a couple of images acquired at the capillary entrance with magnification factors of 1× and 3.5× respectively.

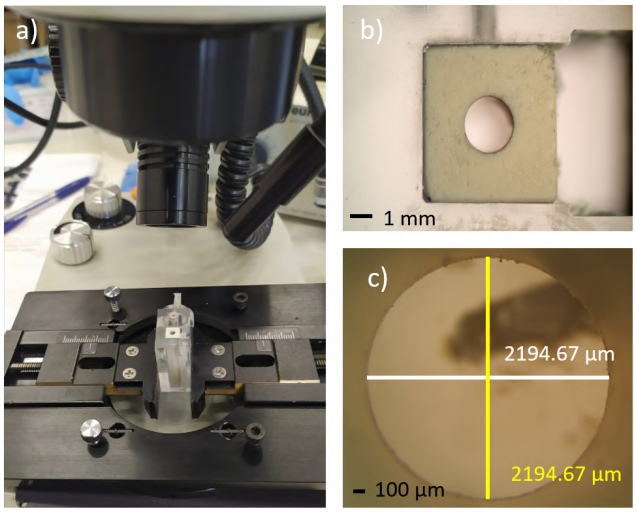

Figure 6.5. (a) Optical stereomicroscope used to analyze the ceramic capillary channel. (b) 1× and (c) 3.5× magnified images of the capillary entrance.

An accurate characterization of the plasma discharge was achieved by means of the transverse Stark broadening method, used to measure the plasma density distribution along the capillary channel. As depicted in Fig.6.6, the light emitted by the plasma channel exits the electrode holes and is guided into the imaging spectrometer by means of the same optical line used for laser spot imaging. Hydrogen spectral lines are selected by the spectrometer diffraction grating (600 grooves/mm) and spectral images are acquired to retrieve the plasma density. In particular, as shown in Fig.6.6, acquired spectral images allow to reconstruct the transverse (vertical) plasma density distribution corresponding to a specific slice of the plasma channel, which is imaged onto the CCD camera detector by the optical line.

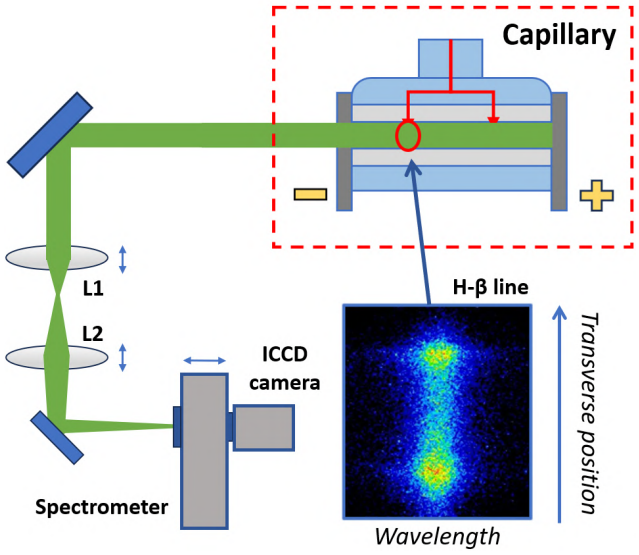

Figure 6.6. Schematic representation of the transverse Stark broadening diagnostics.

By properly shifting the optical line, it is possible to acquire different slices of the plasma channel, performing a longitudinal scan of the plasma density distribution. Moreover, by gating the camera acquisition to the discharge trigger, it is possible to analyze the temporal evolution of the plasma density. As a result, such diagnostic technique allows to perform a complete transverse, longitudinal and temporal characterization of the plasma channel produced inside the ceramic capillary.

Since the Stark broadening method specifically relies on the broadening of hydrogen spectral lines, plasma density measurements were performed with pure H_2 gas, delivered by the hydrogen generator in pulsed injection regime (1 Hz). Therefore, while high repetition rate tests were carried out with the mixture of N_2 (95%) and H_2 (5%) gas, injected in continuous flow, plasma density measurements were performed with pure H_2, injected at 1 Hz by means of an electro-mechanical valve.

6.1.3 Preliminary characterization

Before high repetition rate tests, a preliminary characterization of the ceramic capillary was performed with transverse Strak broadening method. 7.5 kV voltage pulses were applied to the capillary electrodes, ionizing around 50 mbar of pure H_2 and producing plasma discharges at 1 Hz, with 500 A peak current. The telescopic system of the optical transport line was moved by 1 cm to analyze different longitudinal slices of the plasma channel, in particular 1 cm and 5 mm inside the capillary and towards the electrode.

Fig. 6.7 reports the evolution of the transverse plasma density profile, measured 5 mm inside the channel, at different delays with respect to the onset of the HV discharge.

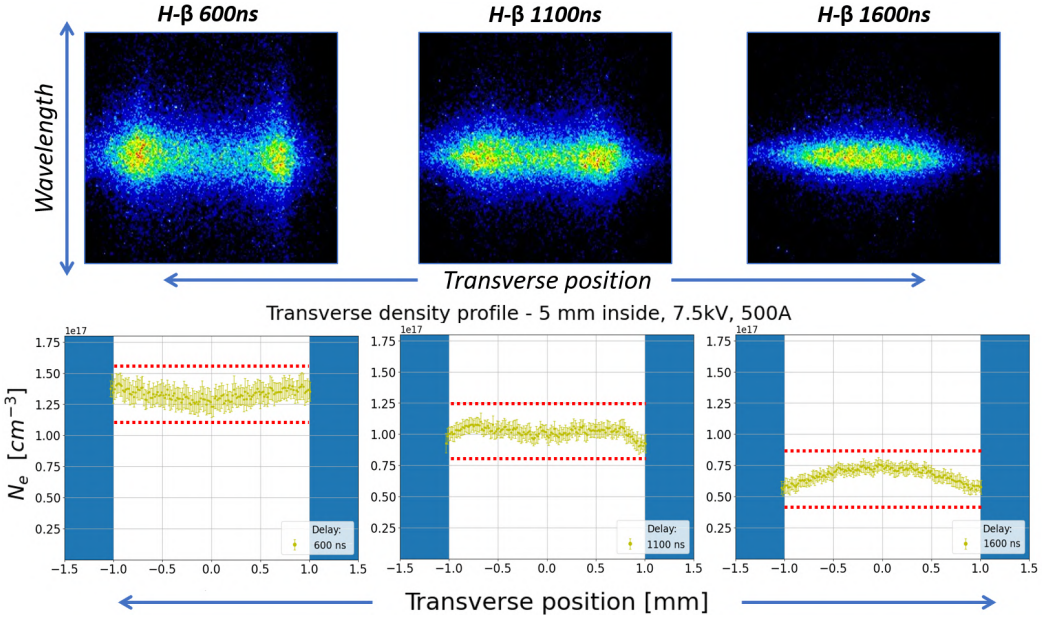

Figure 6.7. H-β spectral images and corresponding transverse plasma density profiles, measured 5 mm inside the capillary channel at different delays with respect to the discharge trigger.

Towards the discharge current peak (600 ns), the plasma density distribution is characterized by a slightly hollow profile, with a on-axis minimum of 1.25±0.08 $\times$ 10^{17} cm^{-3} and a near-wall peak of 1.44±0.08 $\times 10^{17}$, corresponding to a 14% profile depth. In the recombination phase, after the discharge is over (>1500 ns), the transverse distribution turns into a gaussian-shaped profile. Measured error bars represent the standard deviation calculated over 50 acquired images.

The same behaviour is observed in the transverse slice located 1 cm inside the plasma channel, as reported in Fig. 6.8. Hollow profiles are observed during the plasma formation, up to a maximum transverse profile depth of ≈18% at the temporal density peak (600 ns), while a gaussian transverse distribution characterizes the plasma recombination phase.

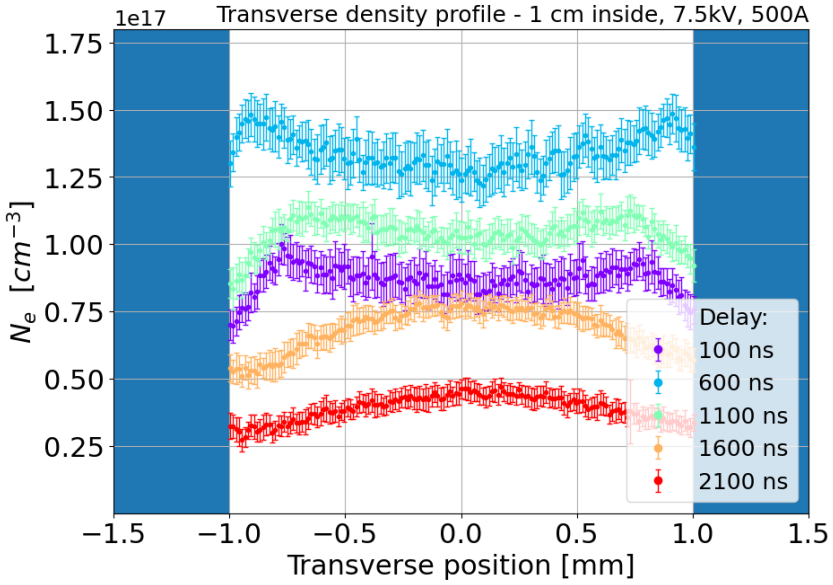

Figure 6.8. Transverse plasma density profiles, measured 1 cm inside the capillary channel at different delays with respect to the discharge trigger.

Observed transverse density profiles are in agreement with theoretical models [19], showing that, due to the thermal balance between ohmic heating and heat conduction with colder capillary walls, the transverse distribution of the plasma temperature is characterized by an on-axis peak and a radial gradient towards the boundary walls, corresponding to a parabolic transverse density distribution, as also discussed in Sec.2.3.2.

Finally, Fig.6.9 reports the temporal evolution of the plasma density in the three channel slices. Each point is obtained at a given delay with respect to the discharge trigger, averaging the plasma density over the transverse profile for each slice. A slight difference is observed between the slices, with a higher density towards the inner part of the channel, consistently with longitudinal density profiles measured in plastic capillaries, as discussed in Ch.4.

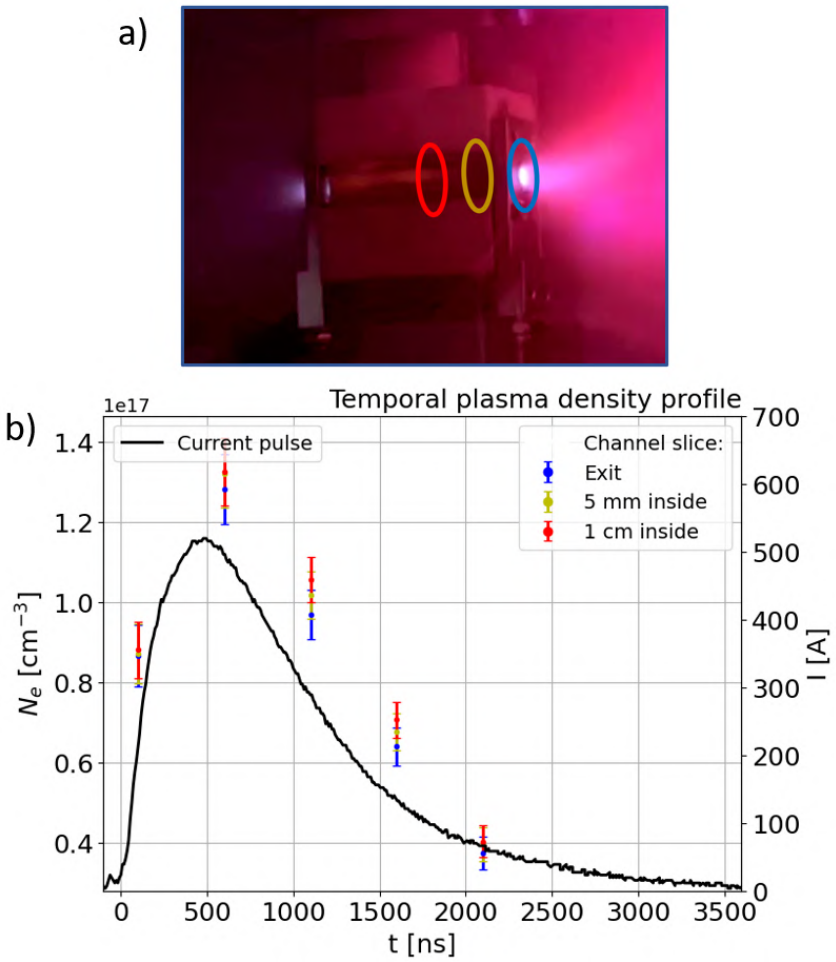

Figure 6.9. (a) Picture of the ceramic capillary discharge during the preliminary characterization. Colored circles represent the three analyzed plasma channel slices. (b) Temporal density profiles measured from three plasma channel slices, specifically 1 cm (red) and 5 mm (yellow) inside the capillary and towards the exit (blue). The 500 A peak current discharge waveform is also reported.

6.1.4 High repetition rate operation

High repetition rate tests were performed in the range 10-150 Hz, using the N_2-H_2 mixture injected at 80-100 mbar in continuous flow inside the ceramic capillary. 5 kV voltage pulses were applied to the electrodes, producing 400 A peak current plasma discharges up to a total amount of 20 million shots, reached after several days of operation.

During the experimental campaign, laser spot imaging and plasma density measurements were performed regularly to monitor any modification both in the capillary walls and the plasma density distribution. In particular, after a given number of shots at high repetition rate, plasma density measurements were acquired by using 7.5 kV pulses to ionize pure hydrogen in pulsed flow regime, as done for the preliminary characterization. Higher voltage pulses were applied, compared to 5 kV

pulses used in high repetition rate tests, in order to maximize the plasma stability and the intensity of the emitted light, thus minimizing the error in density measurements. Results obtained at the end of the experimental campaign are reported in Fig. 6.10, depicting the transverse plasma density profiles acquired 1 cm inside the channel at the density peak (600 ns after the HV discharge trigger).

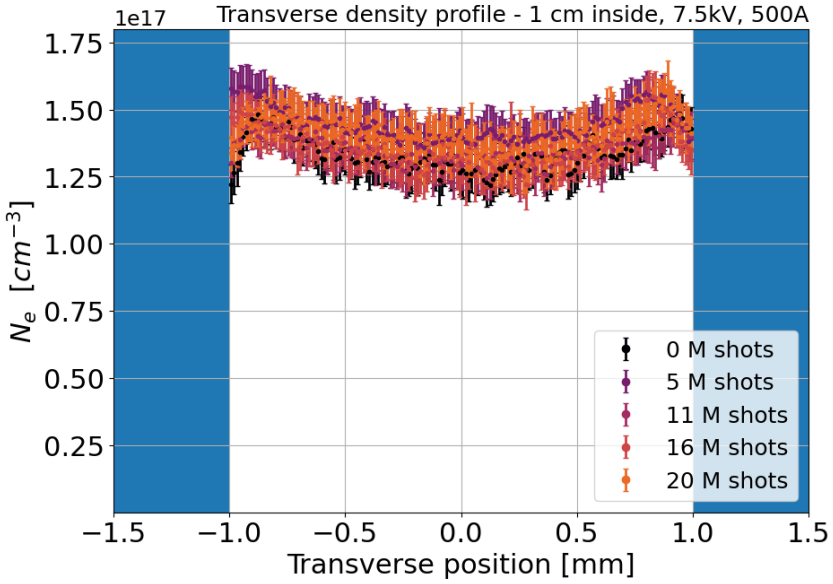

Figure 6.10. Transverse plasma density profiles, measured 1 cm inside the plasma channel at a delay of 600 ns and after different millions of shots.

Transverse density profiles, measured in the same experimental conditions after a different number of plasma discharges, are well overlapped within the error bars, which are computed by acquiring 50 images for each measure.

In addition, Fig. 6.11 reports the evolution of the plasma density after different millions of shots at different repetition rates. Each point represents the plasma density averaged over the transverse profiles shown in Fig. 6.10 and normalized to the average density obtained during the preliminary characterization. Results highlight that the average plasma density remains approximately constant during the entire experimental campaign at 10-150 Hz, thus proving the suitability of the ceramic capillary to preserve the plasma density during long-term high repetition rate operation.

Regarding the capillary channel integrity, Fig. 6.12 reports the analysis of laser spots acquired during the experimental campaign. Horizontal and vertical laser spot lineouts, measured after 10 and 20 millions of shots, are well overlapped to the preliminary results. Error bars were computed by acquiring 50 images for each measurement. In conclusion, no significant increase in the laser spot was observed, meaning that no erosion took place in the capillary during the experimental campaign.

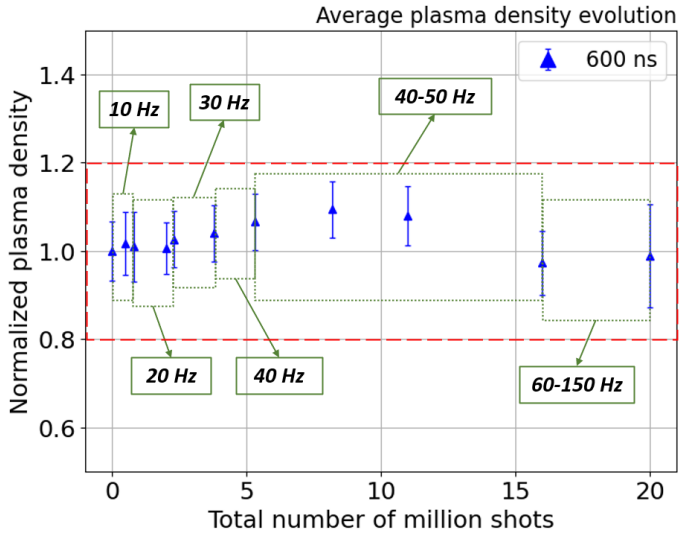

Figure 6.11. Plasma density evolution after different millions of shots at different repetition rates. Each point represents the plasma density averaged over the transverse profiles shown in Fig. 6.10 and normalized to the average density obtained during the preliminary characterization. Results highlight the ability of ceramic capillary to preserve the plasma density during long-term high repetition rate operation.

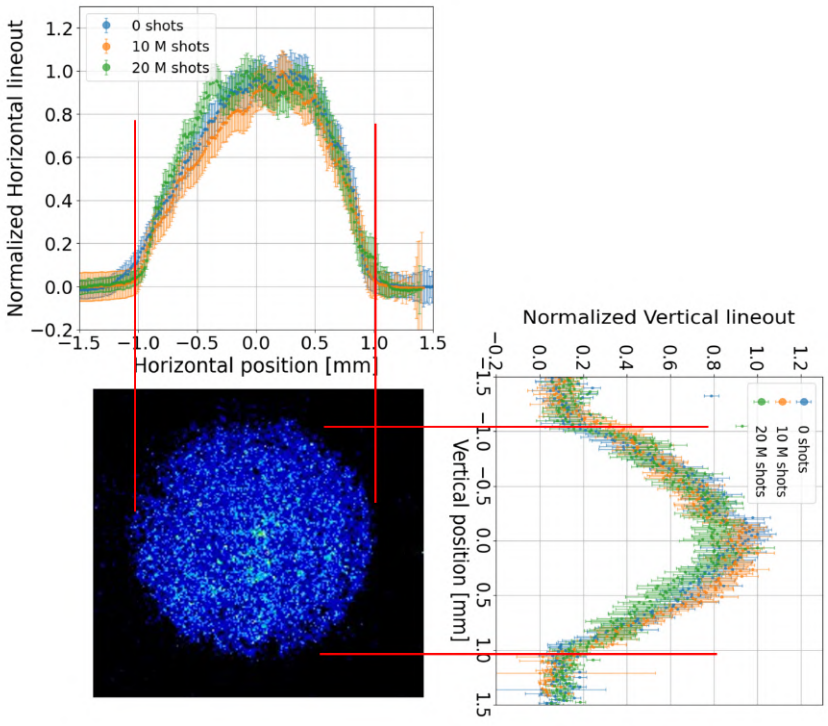

Figure 6.12. Laser spot vertical and horizontal lineouts, measured after 0 (blue), 10 (orange) and 20 (green) million shots at 10-150 Hz. No laser spot increase is observed.

In addition, microscopic analysis was performed at the end of the experimental campaign, scanning the transverse cross section along the capillary channel to assess if any deformation was present due to Shapal erosion. Fig. 6.13 reports the channel diameter measured along the capillary channel, with 2 mm longitudinal steps, after 20 million discharges and normalized to the channel diameter profile measured before the experimental campaign. For each longitudinal position, the reported diameter was obtained by measuring the cross section diameter both in the horizontal and vertical planes and computing the average, in order to take into account possible deformations that would determine a transverse elliptical shape, even though no difference was actually observed in the two measurements. Measured error bars result from 200 acquired images. As shown in Fig. 6.13, the normalized channel diameter is close to unity along the entire longitudinal profile, proving that the capillary channel was well preserved at the end of the experimental campaign.

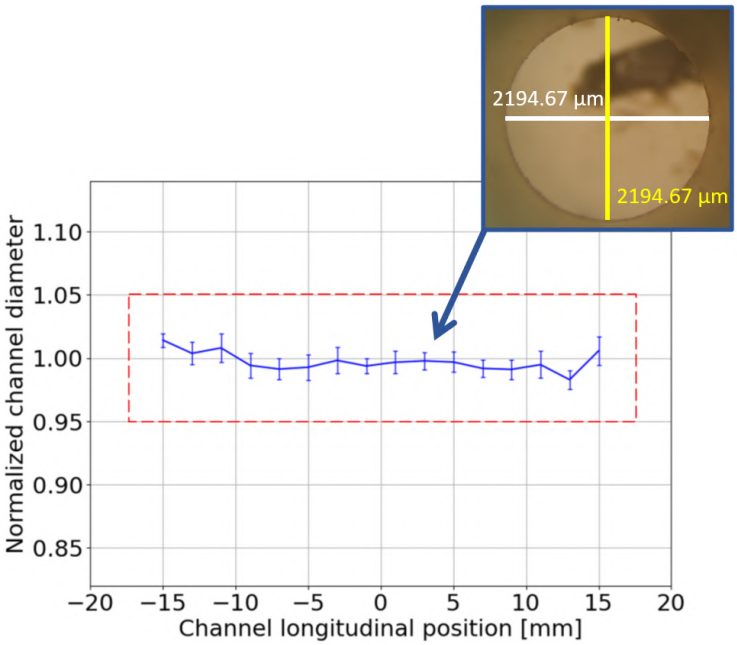

Figure 6.13. Longitudinal profile of the capillary channel diameter, measured after 20 million shots at 10-150 Hz and normalized with respect to the diameter profile measured before the experimental campaign. The insert shows an image acquired from the capillary center, in which the cross section diameter is computed by the average of the horizontal and vertical measurements, supposing an elliptical shape possibly related to erosion.

In conclusion, adopted transverse diagnostics demonstrated the capability of ceramic materials to preserve the plasma properties and the capillary integrity during long-term plasma discharges operation at high repetition rate (up to 150 Hz).

6.1.5 Heat transfer numerical simulations

A numerical analysis was carried out to study the heat transfer inside the whole plasma source during high repetition rate plasma discharge operation, and provide an estimate on the operative limits of ceramic capillaries. Heat transfer inside plasma

discharge capillaries is mainly governed by the heat power produced by plasma discharges through Ohmic heating, which is deposited onto the inner walls of the capillary channel and removed via heat conduction through the other components of the plasma module. First, an analytical method was employed to estimate the heat power produced by a single plasma discharge through Ohmic heating, considering, as a reference, the experimental settings adopted for high repetition rate tests on the ceramic capillary (5 kV pulses, 400 A peak current plasma discharges). According to Joule effect, the Ohmic heating is given by [39]:

$$P(t) = R_p(t) I_p(t)^2 \tag{6.1}$$

in which I_p and R_p are the discharge current intensity and the electrical resistance of the plasma channel. The current discharge I_p was directly measured by the oscilloscope during the experimental campaign, while the resistance of the plasma channel R_p was estimated through Ohm law [117]:

$$R_p(t) = \rho_{tot}(t) \frac{L}{\pi r^2}, \tag{6.2}$$

in which the length L and radius r of the capillary channel are respectively 3 cm and 1 mm, and the plasma resistivity ρ_{tot} is computed according to Eq.1.43:

$$\rho_{tot}(t) = \frac{m_e}{n_e(t) e^2} (< \nu_{ei}(t) > + < \nu_{ea}(t) >) \tag{6.3}$$

Electron-ion and electron-atom collision frequencies are retrieved from Eq.1.32 and Eq.1.42:

$$< \nu_{ei}(t) >= \frac{4}{3} \sqrt{\frac{2\pi}{m_e}} \frac{e^4 n_e(t) \ln \lambda_{ei}}{(4\pi\epsilon_0)^2 (k_B T_e(t))^{3/2}}, \quad < \nu_{ea}(t) >= \frac{\pi r_a^2 P_0}{\sqrt{m_e k_B T_e(t)}} \tag{6.4}$$

in which the Coulomb logarithm $\ln \lambda_{ei}$ is computed through Eq.1.31:

$$\ln \lambda_{ei}(t) = \ln \left[\frac{3}{2\sqrt{2\pi}} \frac{(4\pi\epsilon_0)^{3/2} (k_B T_e(t))^{3/2}}{e^3 n_e(t)^{1/2}} \right] \tag{6.5}$$

The Coulomb logarithm and the collision frequencies were determined by inserting the temporal profiles of the plasma density n_e and temperature T_e, depicted in Fig. 6.14, into Eq.6.3], Eq.6.4 and Eq.6.5. The density temporal profile was obtained by means of plasma density measurements analogous to the one reported in Fig. 6.9, while the temperature temporal profile was computed by inserting the measured discharge current into Eq.3.16. Computed parameters were then included in Eq.6.3 to determine the plasma resistivity and, in turn, retrieve the plasma channel resistance and the heat power from Eq.6.2 and Eq.6.1.

Analytical results for the plasma resistance and the heat power are reported in Fig. 6.15, together with the measured discharge current waveform.

Finally, by integrating the heat power over the plasma discharge duration, an energy per pulse of $\approx$ 100 mJ is obtained. Considering plasma discharge operation from tens of Hz up to the kHz range, the average power deposited onto the capillary walls spans from few Watts (10-50 Hz) to 100 W (1 kHz).

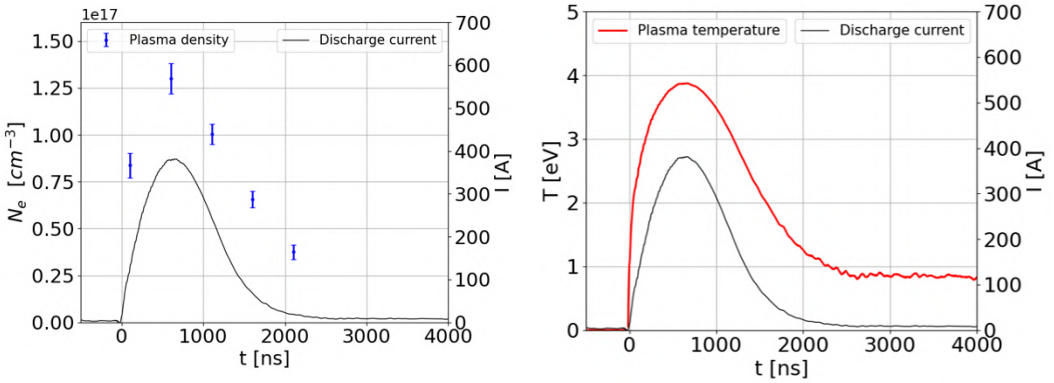

Figure 6.14. Temporal profiles of the plasma density (a) and temperature (b).

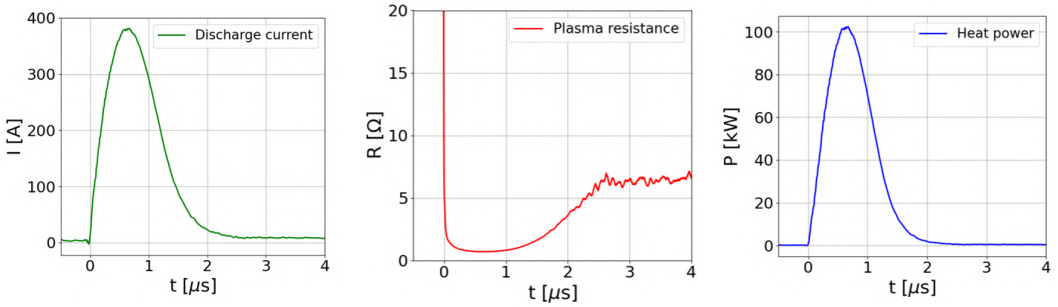

Figure 6.15. (a) Discharge current waveform, acquired during high repetition rate tests. (b) Resistance of the plasma channel. (c) Resulting heat power deposited by a single plasma discharge onto the capillary walls.

Given these reference values, 3D numerical simulations were performed with COMSOL Multiphysics [37] to analyze the capillary overheating and the heat removal inside the plasma source. Relying on Fourier law of heat conduction, the temperature gradient inside the whole source is computed, given the thermal conductivity k of the different components and the heat flux q, estimated through the analytical model previously described:

$$\vec{q} = -k(T)\nabla T \tag{6.6}$$

Heat transfer simulations were performed considering the Shapal-Macor capillary shown in Fig. 6.2, subject to a constant heat transfer rate of 1-100 W flowing through the capillary channel walls, thus reproducing the average power deposited by HV discharges in the range 10 Hz - 1 kHz. As shown in Fig. 6.16, the simulated geometry also includes HV cables and the gas injection pipe, conducting the thermal load from the capillary to the HV pulser and the vacuum chamber, which in turn act as heat sinks. In addition, the external surfaces of all the components are thermally insulated, so as to replicate the experimental conditions inside the vacuum chamber. Due to the heat removal from the source to the heat sink, a thermal steady-state is reached

within the capillary. For instance, Fig. 6.16 displays the equilibrium temperature distribution within the whole plasma source, with a maximum temperature of 840°C inside the capillary, reached after three hours of continuous plasma discharge operation at 300 Hz.

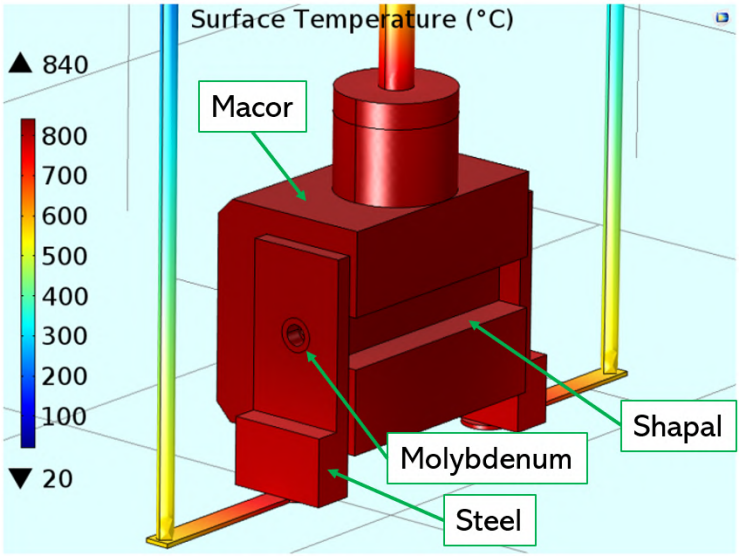

Figure 6.16. 3D view of the steady-state surface temperature distribution during plasma discharge operation at 300 Hz. Thermal equilibrium is reached within around three hours of continuous operation due to heat exchange with external components of the plasma module.

Fig.6.17 reports the temporal evolution of the temperature on the capillary channel walls for different operative frequencies. A thermal steady state is reached within three hours, due to the slow heat exchange and the large distance between the capillary and the heat sink.

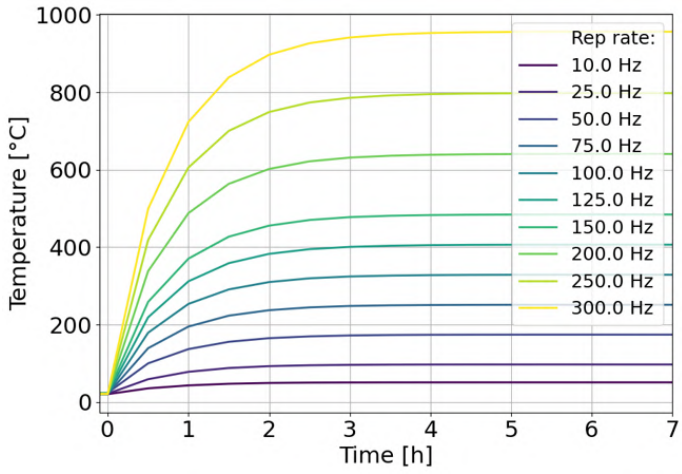

Figure 6.17. Temporal evolution of the temperature on the capillary channel walls for different frequencies. A thermal steady state is reached within three hours of continuous operation.

Moreover, Fig. 6.18 reports the equilibrium temperature on the channel walls, the holder and the electrode, as a function of the repetition rate, showing the operative limits of the capillary according to the adopted materials. Due to the large distance from the heat sink, the whole capillary reaches a uniform temperature, which is equal for the capillary core and holder and the electrodes as well.

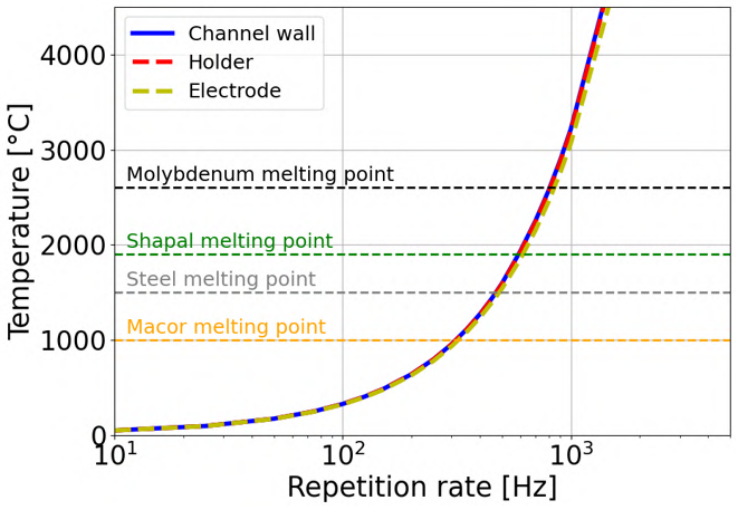

Figure 6.18. Equilibrium temperature reached on the capillary channel inner walls (solid blue curve), the Macor holder (dashed red curve) and the electrodes (dashed yellow curve) as a function of the operating repetition rate. Due to the large distance from the heat sink, the whole capillary reaches a uniform temperature, hence the overlap between the three curves. Horizontal dashed lines indicate the maximum operating temperature for Macor (yellow), steel (grey), Shapal (green) and molybdenum (black).

In the range of 10-150 Hz, assessed during the experimental testing, the equilibrium temperature is kept below the melting temperature of Macor and Shapal, thus preventing any damage in the capillary. For higher repetition rate operation up to the kHz range, the energy per discharge pulse can be reduced by tuning the discharge duration or the current intensity, in order to compensate the repetition rate increase and keep the capillary temperature under control.

In conclusion, a novel ceramic-based plasma discharge capillary was tested at 10-150 Hz to assess the reliability of machinable, cost-effective ceramic materials, such as Shapal and Macor, for long-term high repetition rate operation. Experimental results showed that both the plasma properties and the capillary channel profile are preserved during the experimental campaign, demonstrating the ability of the device to withstand the thermal load produced by high voltage plasma discharges at high repetition rate. Heat conduction simulations confirmed that no excessive overheating takes place during operation up to 150 Hz and the capillary temperature is kept below critical values. In addition, according to the numerical analysis, long-term operation in the kHz range can be achieved by reducing the energy deposited by a single plasma discharge, acting on the discharge duration and current intensity. In this regard, considering the operative range of 100-400 Hz foreseen by the EuPRAXIA@SPARC_LAB project, the proposed design of ceramic plasma discharge capillaries represents a reliable solution in terms of longevity and cost-effectiveness.

6.2 Femtosecond laser-induced plasma filaments

An alternative plasma source was tested and characterized for possible applications in plasma-based acceleration at high repetition rate. Such source consist in plasma filaments induced by laser ionization of low pressure nitrogen columns. Laser pulses propagation inside gas columns can be extended over many Rayleigh lengths, exploiting the balance between relativistic self-guiding and defocusing from low-density plasma induced by multiphoton/tunnel ionization, thus keeping high peak intensity over long distance and produce long plasma channels, also called filaments. The properties of such laser-induced plasma filaments can be controlled for different applications, including plasma-based acceleration, and can provide advantages compared to plasma discharge capillaries, as described in the following.

An investigation on laser-induced plasma filaments was carried out at SPARC_LAB facility. The experimental setup, reported in Fig.6.19, includes a Ti:Sapphire CPA laser system, which delivers 80 mJ laser pulses at 800 nm central wavelength, with a transform-limited duration of 30 fs FWHM and 10 Hz repetition rate. The laser system is split into two beamlines, one seeding the SPARC_LAB linear accelerator and the other one used to create plasma filaments. The filament beamline, after a pulse-shaping stage, delivers pulses with $\approx$ 10 mJ energy, 350 fs (FWHM) duration and $\approx$ 15 mm diameter at $1/e^2$ intensity. A 1 m focal length lens focuses the laser pulse into a 10 cm $\times$ 1 m gas-cell, which is filled with approximately 1 mbar pressure of nitrogen gas with a 5% of hydrogen. The distance between the gas-cell entrance and the lens is about 50 cm.

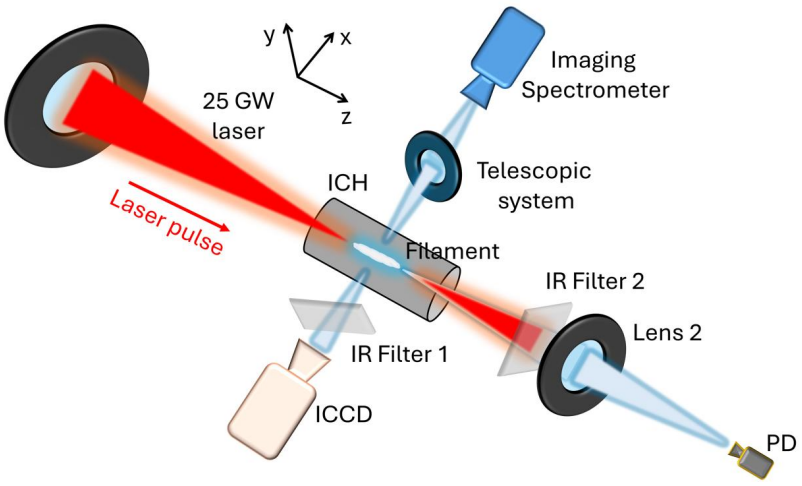

Figure 6.19. Experimental setup for plasma filaments test and characterization. A 25 GW laser pulse is focused onto a 1 mbar N_2 95% - H_2 5% gas column confined in a gas interaction chamber (ICH), producing a cm-scale plasma filament. An ICCD camera acquires side images of the filament light to retrieve its dimensions and decay time, also benchmarked with a photodiode (PD). An imaging spectrometer equipped with an ICCD camera is used to measure the plasma filament density and temperature.

A complete characterization of the plasma filaments was achieved by using a side imaging fluorescence technique to measure the filament size and decay time, also benchmarked with a photodiode, while the spectroscopic analysis of the plasma-

emitted light allowed to retrieve the longitudinal distribution of the plasma density and temperature.

6.2.1 Plasma filament dimensions

The light emitted by the plasma filament was imaged from the side onto a CCD camera, coupled to a Hamamatsu C9547-01 intensifier. The ICCD camera was installed perpendicular to the pulse propagation axis and the plasma emitted light signal was collected and imaged onto the ICCD detector by using a Sigma 180 mm MACRO f 2.8 EX-DG-OS-HSM objective. A band-pass filter coupled with a 0° incident 800 nm dielectric mirror was placed in front of the camera to detect the light emission from the filament, while rejecting the scattered light from the pump laser and all other emissions. The field of view of the ICCD covered an area of about 4×6 cm^2 of the plasma filament. Furthermore, a gate duration of 5 ns was set for the ICCD, with available scanning delay of 0-8 ns with respect to the laser pulse arrival time. By measuring the filament emitted light at different delays, the side imaging technique allowed to determine the temporal evolution of the longitudinal and transverse sizes of the plasma filament. Fig.6.20 reports filament side images acquired at different delays with respect to the laser pulse arrival time.

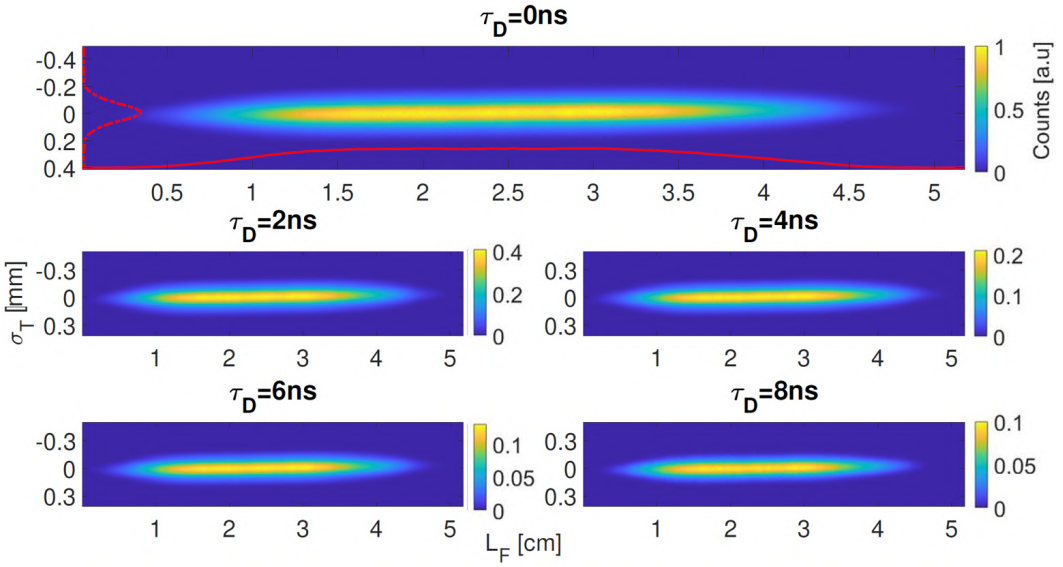

Figure 6.20. Side images of the plasma filament, acquired at different delays with respect to the laser pulse arrival time. The laser pulse propagates from left to right. Additionally, the transverse (red dashed line) and longitudinal (red solid line) projection of the filament are shown.

In addition, Fig.6.21 reports the temporal evolution of the filament length and transverse size, retrieved from side imaging snapshots. Filament length and transverse diameter of 4 cm and $\approx$ 300 μm full width tenth maximum (FWTM) were measured during the observed temporal range of 0-8 ns.

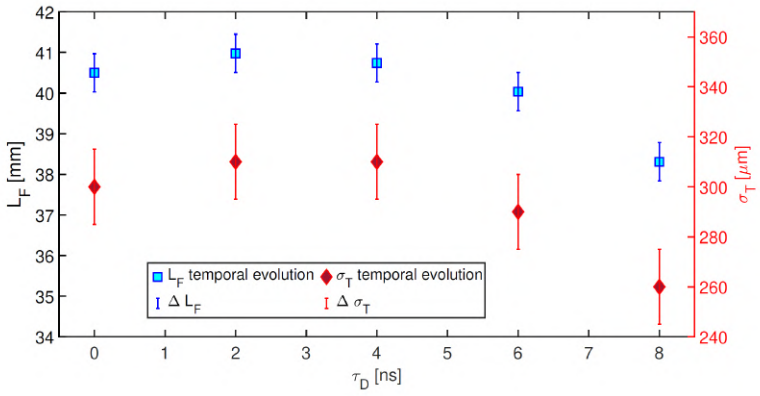

Figure 6.21. Temporal evolution of the filament length (blue) and transverse size (red), retrieved by filament side images.

6.2.2 Plasma density and temperature measurements

Stark broadening method was adopted to measure the plasma density distribution along the filament. Light emitted by the plasma is guided by a telescopic system and collected into an imaging spectrometer equipped with an ICCD camera (the same used at Plasma_lab laboratory). Due to the low amount of H_2, i.e. 5% of 1 mbar gas mixture, the intensity of H-β spectral line was too low for reliable measurements, therefore H-α line was acquired to retrieve the plasma filament density. The ICCD camera acquisition was synchronized with the laser pulse arrival time and, in addition, a gate width of 500 ns was set to maximize the acquired light signal, thus averaging the temporal evolution of the plasma filament.

An improved fitting code was developed to retrieve the plasma density distribution from H-α spectral images, although affected by self-absorption [64]. As shown in Fig.6.22, a Voigt profile coupled with a hyperbolic function, both described in A, were adopted to fit the tails of the H-α line, extrapolating the expected peak (lowered by self-absorption) and the corresponding FWHM to retrieve the plasma density along the plasma filament.

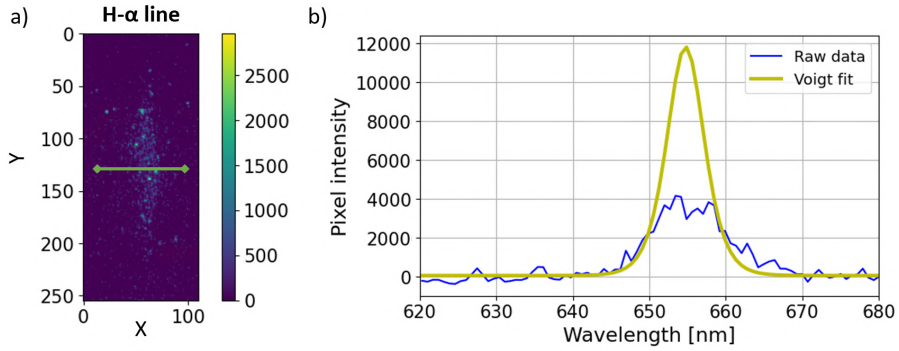

Figure 6.22. (a) H-α spectral image of the plasma filament, acquired at the laser arrival time with a 500 ns gate width. (b) A Voigt function is used to fit the hydrogen line, extrapolate the emission peak and retrieve the plasma density at a given vertical position of the spectral image (solid green line from (a)), corresponding to the filament center.

Concerning the plasma temperature, the spectroscopic method described in Sec.3.7 was adopted to determine the longitudinal temperature distribution of the filament. The emission spectrum of N_2-H_2 mixture was acquired in the range 450-520 nm, as reported in Fig.6.23 and the integrated line intensities of NI and NII ions (corresponding to N and N^+) were measured to retrieve the plasma temperature from Eq.3.20.

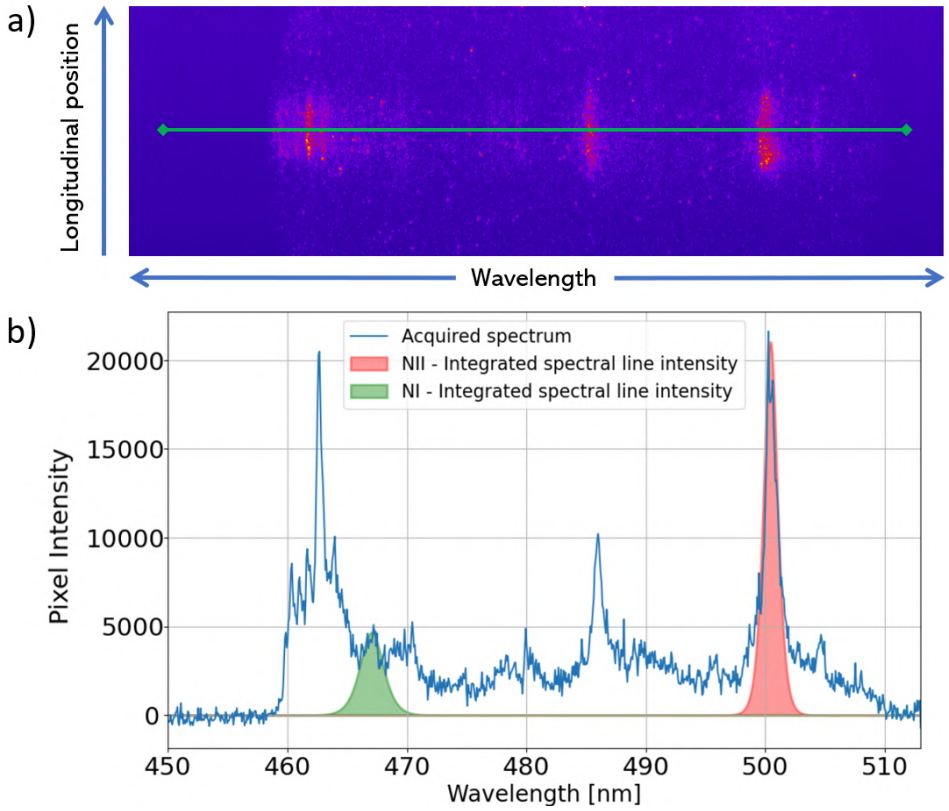

Figure 6.23. (a) Emission spectrum acquired from a plasma channel produced by laser ionization of a N_2 95% - H_2 5% gas mixture. (b) Lorentzian functions are used to fit the emission lines of neutral Nitrogen atoms (NI) and N^+ ions (NII), retrieving the integrated line intensity (green and red areas) at a given position of the plasma channel (solid green line from (a)).

Properties of the two spectral lines, centered at 467.068 nm and 500.515 nm respectively, were obtained by the NIST Atomic Spectra Database [90] and are reported in Tab.6.1, together with other parameters contained in Eq.3.20.

Longitudinal profiles of the plasma filament temperature and density, measured with mentioned methods, are reported in Fig.6.24. Uniform profiles characterize both density and temperature, with plateau at $1.2\pm0.1 \times 10^{16}$ cm^{-3} and 1.3 ± 0.1 eV respectively. In addition, density ramps are observed at the filament extremities. Error bars are computed as the standard deviation over 100 acquired spectral images.

Symbol	Parameter	Unit	Value
λ	NI wavelength	nm	467.068
λ'	NII wavelength	nm	500.515
A	NI transition probability	s^{-1}	3.02×10^5
A'	NII transition probability	s^{-1}	1.14×10^8
g	NI level degeneracy	-	4
g'	NII level degeneracy	-	9
a_0	Bohr radius	m	5.29×10^{-11}
E_H	Hydrogen ionization energy	eV	13.6
E	NI excitation energy	eV	2.654
E'	NII excitation energy	eV	2.476
E_∞	NI ionization energy	eV	14.534
ΔE_∞	Correction factor to E_∞	eV	0.15

Table 6.1. Properties of Nitrogen ions emission lines and additional parameters for plasma temperature measurements.

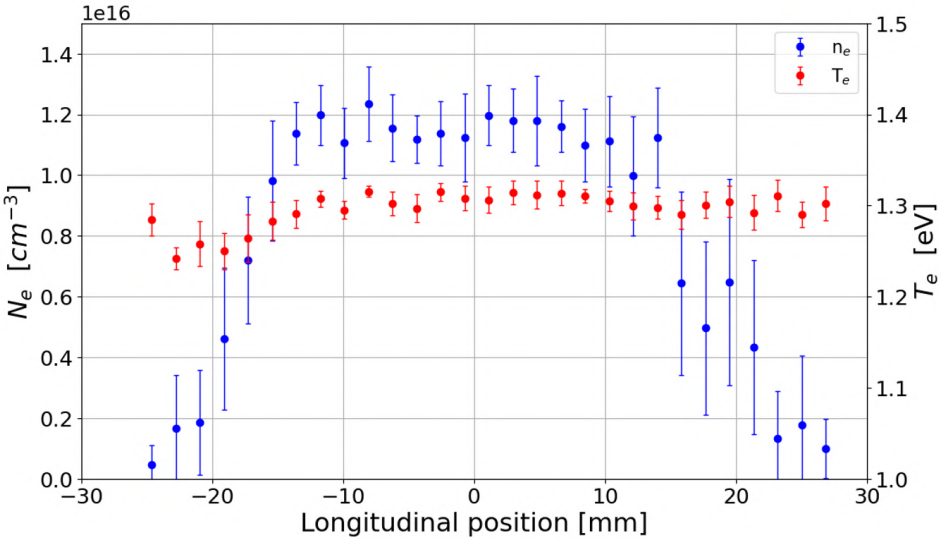

Figure 6.24. Longitudinal profiles of the plasma temperature (red) and density (blue) of the filament, measured at the laser pulse arrival time with a camera gate width of 500 ns.

In addition, plasma density and temperature measurements were benchmarked with NIST LIBS Database spectra [91], tabulated for a N_2-H_2 gas mixture with $n_e = 10^{16}$ cm^{-3} and $T_e = 1.3$ eV. As reported in Fig.6.25, the filament spectrum acquired by the ICCD and integrated over the filament length is well overlapped to the one from the database, thus confirming the reliability of experimental results.

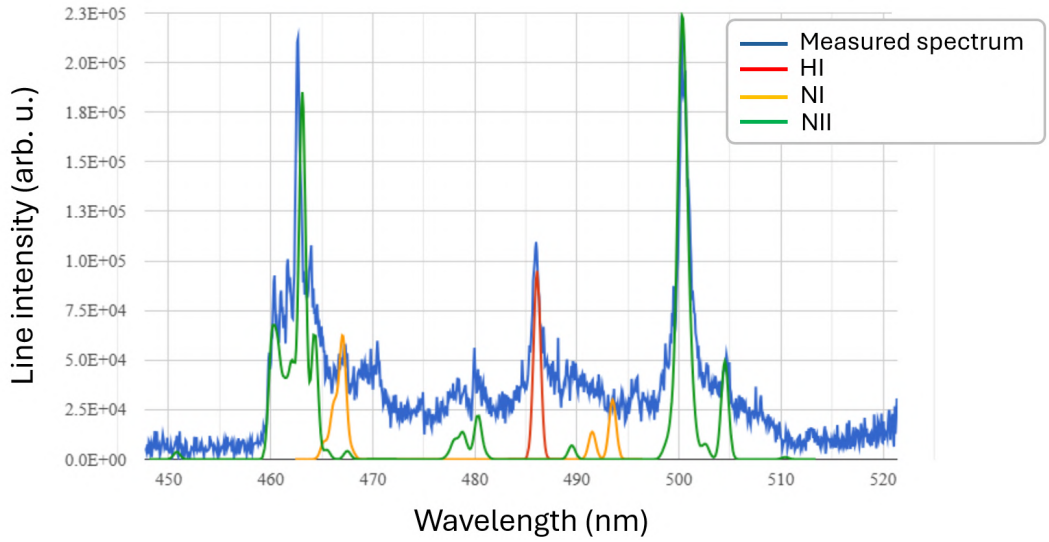

Figure 6.25. Comparison between the acquired filament spectrum, integrated over the filament length, and the NIST Database spectrum, tabulated for a N_2 95% - H_2 5% gas mixture with plasma density and temperature of 10^{16} cm^{-3} and 1.3 eV respectively.

6.2.3 Plasma filament decay time

The temporal evolution of the plasma density was determined by extrapolating the intensity of the plasma emitted light from side images at different delays. The intensity decrease in the observed delay range was calibrated by Stark broadening measurements, retrieving the plasma density temporal profile, reported in Fig.6.26. A decay time of 8 ns was observed, with the plasma density decreasing by one order of magnitude from the peak at 10^{16} cm−3.

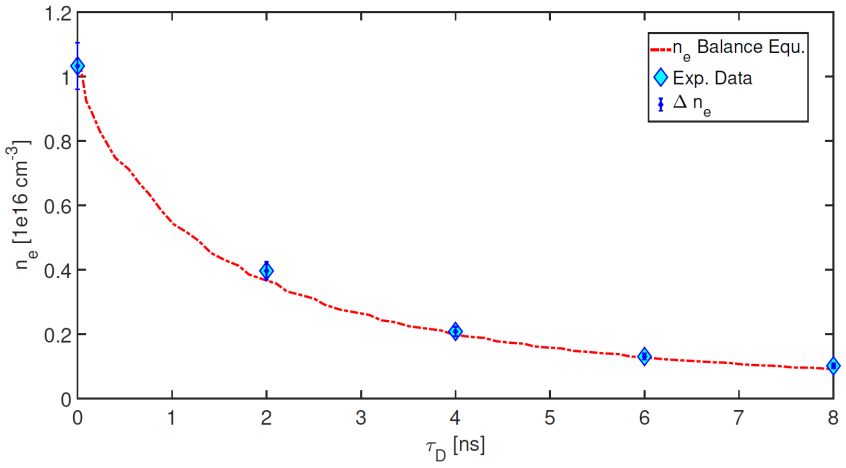

Figure 6.26. Plasma density temporal evolution, retrieved by the side imaging technique.

This result was also benchmarked by measurements with a fast photodiode (1 ns rising time) installed on the laser propagation axis. An in-out band-pass filter coupled with a 0° incident 800 nm dielectric mirror was placed in front of the short

focal length lens to detect the light emission from the filament, while rejecting the scattered light from the pump laser and all other emissions, as for the side images acquisition. Fig.6.27 reports the filament light signal acquired by the photodiode. A decay time of 8 ns is observed.

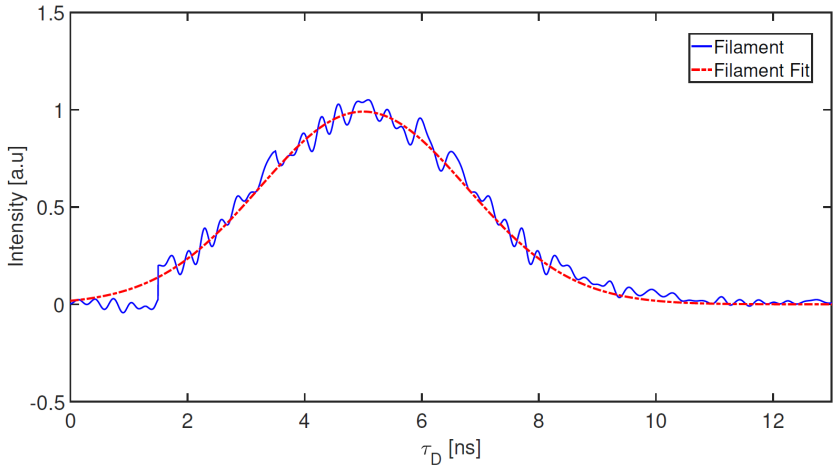

Figure 6.27. Filament light signal measured by the photodiode, with a decay time of 8 ns.

In conclusion, the experimental characterization of laser-induced plasma filaments has demonstrated the possibility to produce uniform plasma channels with suitable density profiles for plasma-based acceleration.

The use of low energy laser pulses to produce plasma filaments provides a significative reduction in the energy deposition onto the walls of the gas cell used to confine the gas column, compared to plasma discharge capillaries. This, together with the lower amount of gas injected in the ICH (1 mbar against 10-100 mbar for plasma discharge capillaries), make plasma filaments a suitable option for high repetition rate plasma acceleration. In addition, plasma filament properties can be easily tuned by acting on the laser pulse energy and spot size. Furthermore, the laser-induced ionization mechanism provides temporal jitter-free operation, since the laser system is also used for the production of electron beams from the photocathode of the particle accelerator, whereas plasma discharge capillaries require laser-stabilization methods to mitigate the intrinsic time jitter of the electrical discharge. These features make laser-induced plasma filaments a promising technology for high energy plasma-based particle acceleration.

Chapter 7

Preliminary design of a 60 cm-long capillary for EuPRAXIA@SPARC_LAB project

In conclusion of this PhD thesis, a preliminary design of the 60 cm-long capillary, targeted for EuPRAXIA@SPARC_LAB project, is presented.

The basic capillary geometry was designed analogously to the segmented and integrated capillaries described in Ch.5, with an upper channel and a series of vertical inlets for a uniform gas distribution inside the main lower channel. In order to maximize the gas uniformity along the capillary, CFD simulations were performed with OpenFOAM to determine an optimized geometrical configuration. In view of the utilization of such device for a PWFA stage operating at 100 Hz, simulations settings were focused on low pressure nitrogen gas. In particular, low pressure allows to keep the breakdown voltage around 10 kV, compensating the remarkable length of the gas column to ionize, and also to preserve the vacuum level required from the upstream RF sections. On the other hand, N_2 is more indicated for continuous gas injection, required for 100 Hz operation, considering the higher impact of hydrogen on the vacuum level and safety procedures.

A first geometrical configuration of the capillary, designed and simulated with OpenFOAM, is characterized by two horizontal 60 cm-long channels and 10 inlets with 1 mm diameter, whose relative distance decreases towards the capillary extremities. This geometry was simulated injecting 40 mbar of N_2 from the main upper inlet and retrieving the molecular density distribution along the main channel at the equilibrium, which is reached around 5 ms after the valve opening. As described in Ch.4, the solver SonicFOAM was adopted for fluid simulations in transient, sonic and turbulent regime. Fig.7.1 reports the 2D equilibrium distribution of N_2 molecular density inside the 60 cm-long capillary.

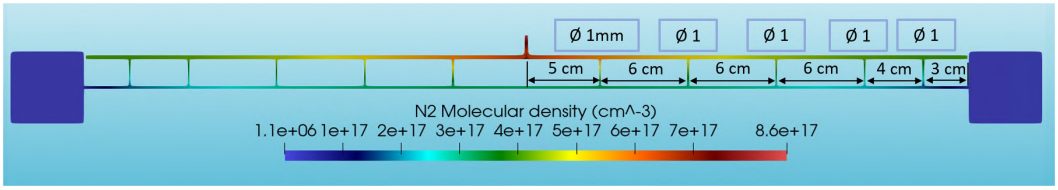

Figure 7.1. 2D N_2 density distribution along the first 60 cm-long capillary design, with 10 inlets having 1 mm-diameter and decreasing relative distance towards the capillary ends.

Different configurations were simulated, modifying the inlets arrangement, number and diameter, and a significant improvement in the uniformity of the gas distribution was achieved. The optimized geometry, reported in Fig.7.2 together with the simulated equilibrium N_2 density distribution, is characterized by 10 inlets with increasing diameter, from 1 mm to 2 mm, from the capillary center towards the extremities.

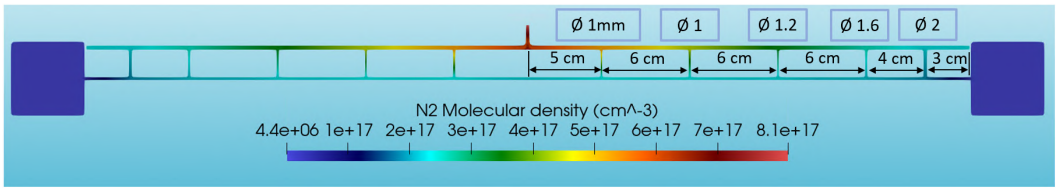

Figure 7.2. 2D N_2 density distribution along the optimized design of the 60 cm-long capillary, with 10 inlets having a progressive increase in the diameter, from 1 mm to 2 mm towards the capillary ends.

Fig.7.3 reports a comparison between the equilibrium longitudinal N_2 density profiles simulated with the first geometry, with constant 1 mm-diameter inlets, and the optimized one, having inlet diameter increasing from 1 mm to 2 mm towards the capillary ends.

As shown in Fig.7.3(a), the first design is characterized by a curved longitudinal profile, with a density peak at 3.2×10^{17} cm^{-3} and smooth density ramps along the entire 60 cm-long channel. On the other hand, by increasing the inlet diameters progressively along the channel, a flat-top profile is established at a lower density peak, around 2.25×10^{17} cm^{-3}. By normalizing the longitudinal profiles with respect to the relative peaks, as shown in Fig.7.3(b), a 80% uniformity is observed from the center to the external inlets in the optimized geometry, compared to a $\approx 58\%$ uniformity in the first configuration. Furthermore, the optimized geometry allows to localize the density ramps in the lateral regions, between the external inlets and the electrodes.

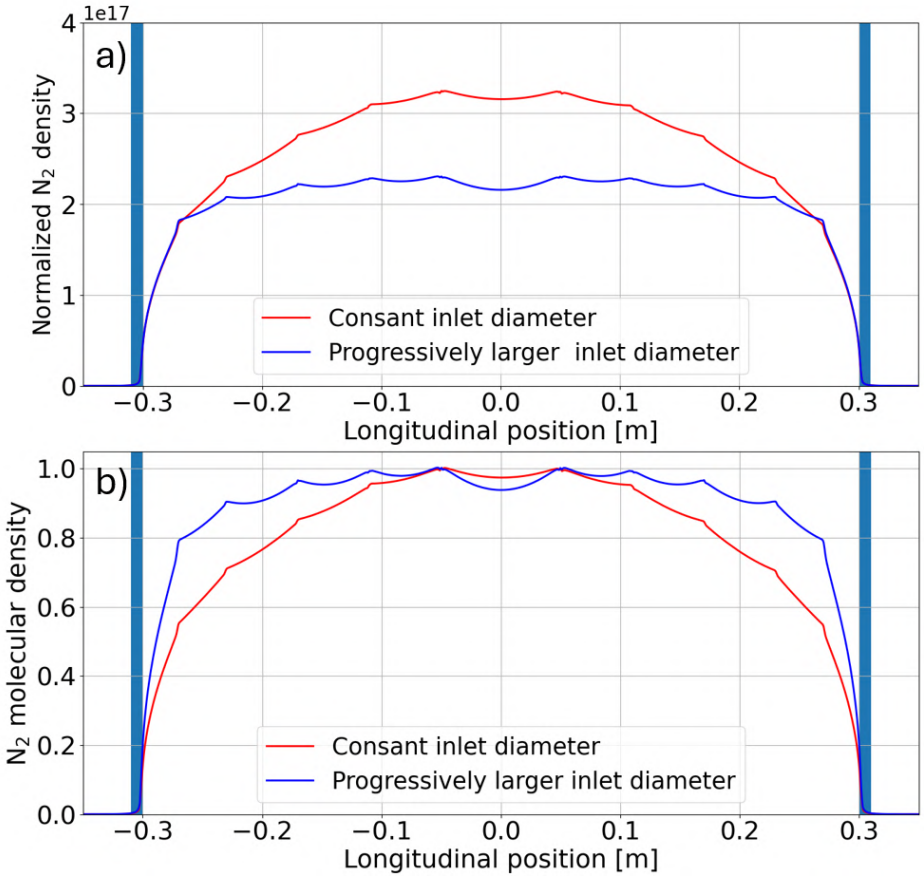

Figure 7.3. (a) Absolute and (b) normalized N_2 density profiles at equilibrium, simulated with the first capillary design with constant inlet diameters (red line) and the optimized geometry with progressively increasing inlet diameters (blue line).

Following the numerical analysis, a first prototype of the 60 cm-long capillary was produced. Due to the difficult realization of tens cm-long holes with sub-mm precision required for the capillary channel, the capillary design was based on a novel approach, characterized by the use of modular blocks properly assembled to compose the entire capillary structure.

A first structure is constituted by a series of rectangular blocks with inner cylindrical holes. Blocks are joined by interlocking connections to create the gas injection network, composed by the two horizontal channels, with 2 mm-diameter holes and the 10 vertical inlets, with different diameters in the range 1-2 mm according to the optimal geometry defined by numerical simulations. In addition, an inner electrode is included in the structure for a segmented capillary configuration, which could improve the capillary operation by reducing the breakdown voltage of the plasma discharge, as discussed in Sec.5.1. The structure is then inserted into a holder matrix and the whole device is held by screwed vertical blocks.

Fig.7.4 reports a prototypical version of the 60 cm-long modular device, realized in Lexan as a proof of concept.

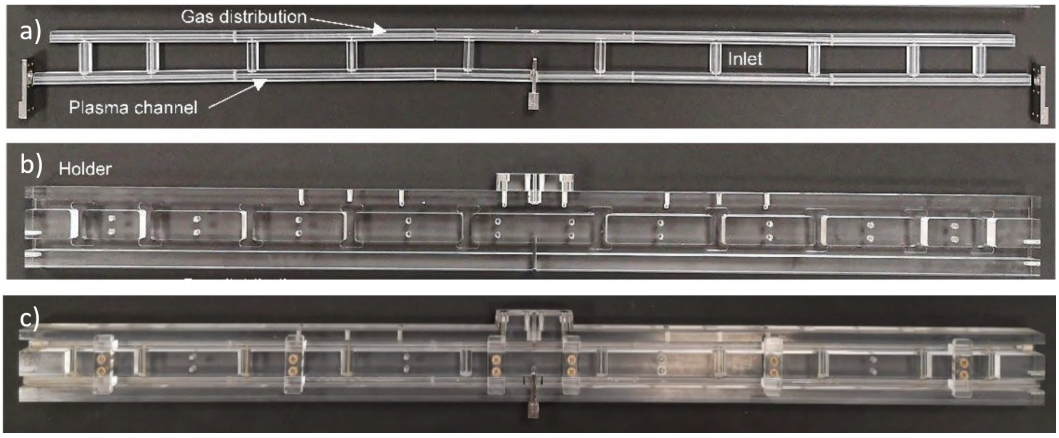

Figure 7.4. (a) Gas injection network, constituted by a series of rectangular blocks joined together to realize the horizontal channels and the vertical inlets. (b) Holder matrix in which the first structure is inserted. (c) Assembly of the 60 cm-long modular capillary.

The device was installed inside the experimental chamber of Plasma_lab laboratory for a preliminary test. The capillary was tested with pure H_2, injected at 1 Hz with 50 mbar pressure and ionized by means of 13 kV pulses, achieving the production of a 60 cm-long plasma discharge without the segmented configuration. A picture of the proof of principle of the modular capillary is reported in Fig.7.5.

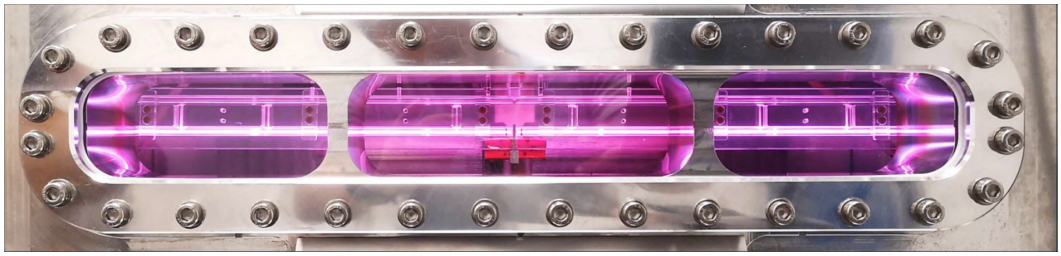

Figure 7.5. 60 cm-long plasma channel produced inside the modular capillary.

In conclusion, a first prototypical version of the 60 cm-long capillary, foreseen for EuPRAXIA@SPARC_LAB project, was designed by means of fluid dynamics numerical simulations and realized with a novel approach, based on the use of modular structures to improve the mechanical processing of the device and also its cost-effectiveness. A preliminary test has proved the feasibility of the modular capillary to produce a single 60 cm-long plasma discharge with 13 kV pulses.

The tested prototype, realized for this proof of principle, was made of Lexan. However, the plasma source that will be designed and implemented in the EuPRAXIA@SPARC_LAB PWFA stage will be made of ceramics, with Shapal and Macor respectively adopted for the inner gas injection structure and the holder matrix. The 60 cm-long ceramic capillary will be equipped with molybdenum or tungsten electrodes for stable long-term operation at 100 Hz, with the possibility of a future upgrade to 400 Hz also by means of a modular capillary entirely made of Shapal.

Conclusions and Future Perspectives

In this PhD thesis, the experimental and theoretical development of plasma sources for plasma-based particle accelerators was presented. Research activities, carried out at Plasma_lab laboratory, located at National Laboratory of Frascati (LNF-INFN), were particularly focused on the design and characterization of plasma discharge capillaries, employed at SPARC_LAB accelerator facility for plasma-based particle acceleration experiments.

An overview on particle accelerators was presented in Ch.1, including a detailed description of plasma-based acceleration schemes, their physical principles, motivation and advantages. In addition, a description of EuPRAXIA@SPARC_LAB project was reported in Sec.1.5, as one of the key milestones in the development of plasma-based accelerators and the main project leading R&D activities on plasma sources in regard of this PhD thesis.

Ch.2 provided an overview on plasma sources, used for plasma-based particle acceleration and other applications, including the different mechanisms adopted for the plasma formation, such as electrical discharges and laser or beam ionization. A detailed description was given about plasma discharge capillaries and their applications, including focusing of charged particle beams (in the so-called Active Plasma Lenses) and guiding of high power laser pulses.

Ch3 presented the plasma module employed at Plasma_lab laboratory to study and characterize plasma discharge capillaries. A detailed description was given about the main components of the plasma module, including the design of discharge capillaries, the features of the gas injection and high voltage systems and the diagnostic techniques adopted for the characterization of the plasma, including the Stark broadening method for plasma density measurements.

The following chapters provided a detailed description of R&D activities carried out in the context of the PhD thesis. Ch.4 presented a study on the geometrical design of plasma discharge capillaries, achieved by means of experimental tests and numerical simulations and aimed at improving the modulation of the plasma density distribution in such plasma sources. Capillaries with different inlet arrangements and channel shapes were tested and characterized, analyzing the plasma density distribution obtained by different geometries. In addition, 3D fluid dynamics simulations were performed with the CFD software OpenFOAM, analyzing the neutral gas dynamics during the filling of tested capillaries. Experimental and simulation results provided a fundamental insight in the optimization of the capillary geometry to control the

gas and plasma density distribution. In particular, the use of inlets at relatively close distance or an enlarged cross section in the central region of the capillary channel can improve the plasma density uniformity, as required for efficient plasma-based acceleration. On the other hand, a gradual increase in the channel diameter towards the capillary extremities allows to control the plasma density ramps, which can be exploited for beam matching and extraction in plasma acceleration stages.

Ch.5 presented a series of novel schemes for m-scale plasma discharge capillaries, conceived for the realization of long plasma channels for high energy gain plasma-based acceleration, but also for staged acceleration and focusing of charged particle beams within compact plasma sources.

Sec.5.1 described the segmented capillary concept, in which long plasma channels are generated by means of independent plasma discharges, produced by parallel high voltage systems. Such scheme is characterized by the possibility to modulate the longitudinal density distribution of the plasma channel by independently tuning the timing and voltage in the different segments. The segmented capillary tested at Plasma_lab was characterized by two segments independently powered by two HV systems to generate a single plasma channel. A first test demonstrated the production of a uniform plasma channel by applying the same voltage to the segments with HV pulses synchronized at the same time. In addition, a second test proved the possibility to modulate the density profile by applying different voltage pulses to the two segments, resulting in the production of localized density ramps that can be exploited for controlled particle beam injection or beam matching and extraction. Moreover, this proof of concept represented an important upgrade towards compact and cost-effective m-scale discharge capillaries, thanks to the possibility to reduce the breakdown voltage of very long gas columns (usually $\sim$50-70 kV) by creating plasma channels composed by multiple independent plasma discharges, each with $\sim$10 kV breakdown voltage.

Sec.5.2 included the design and testing of the integrated capillary, constituted by three independent plasma discharge segments providing two focusing APL stages and one plasma accelerating PWFA stage, all integrated within a single plasma source. In particular, the first APL matches driver and witness beams at the PWFA stage, while the second one extracts the two bunches, compensating the large divergence at the exit of the accelerating stage. Different versions have been tested to overcome crosstalk issues between the three plasma discharges and an optimized design of the integrated capillary was installed at SPARC_LAB facility to focus and accelerate electron beams. The proof of principle experiment demonstrated the ability of the integrated capillary to provide plasma-based focusing, acceleration and extraction of the witness beam within a single, compact plasma source, with an accelerating gradient of $\approx$ 150 MV/m.

Moreover, Sec.5.3 presented the design and testing of a curved capillary for compact guiding and bending of charged particle beams. The capillary was installed at SPARC_LAB facility for a proof of principle experiment, aimed at demonstrating the Active Bending Plasma (ABP) mechanism, consisting in the dispersionless bending of charged particle beams by means of the poloidal magnetic field created by plasma discharges inside curved capillary channels. The experiment demonstrated for the first time the ABP mechanism by deflecting high energy electron beams along the curved trajectory of the capillary channel, with a 4° bending angle and no

significant effects of energy dispersion.

Ch.6 was devoted to high repetition rate plasma sources. Sec.6.1, presented the development of high repetition rate plasma discharge capillaries, based on the combined use of machinable and cost-effective ceramic materials. In particular, the design of such capillaries was based on Shapal Hi M Soft and Macor, which are characterized by high thermal conductivity, high melting temperature and excellent machinability. An experimental campaign was carried out on a plasma discharge capillary composed by a Shapal core, inserted into a Macor holder with molybdenum-stainless steel electrodes, in order to assess the longevity of such materials exposed to high voltage plasma discharges in long-term high repetition rate operation, specifically in the range 10-150 Hz. Due to Shapal opacity, transverse diagnostic techniques were implemented to characterize the plasma source, such as the transverse Stark broadening method for plasma density measurements, and microscopic analysis and laser spot imaging to monitor the capillary channel profile and detect any erosion effect. Additionally, a numerical analysis was carried out to study the heat transfer inside the whole plasma source during high repetition rate plasma discharge operation, and provide an estimate on the operative limits of ceramic capillaries. First, an analytical method was employed to estimate the heat power produced by a single plasma discharge through Ohmic heating, afterwards, 3D numerical simulations were performed with COMSOL Multiphysics to analyze the capillary overheating and the heat removal inside the plasma source. Experimental results and heat transfer simulations demonstrated the capability of ceramic materials to preserve the plasma properties and the capillary integrity during long-term plasma discharges operation at high repetition rate (up to 150 Hz). In addition, according to the numerical analysis, long-term operation in the kHz range can be achieved by reducing the energy deposited by a single plasma discharge, acting on the discharge duration and current intensity. In this regard, considering the operative range of 100-400 Hz foreseen by the EuPRAXIA@SPARC_LAB scientific case, the proposed design of plasma discharge capillaries made in Shapal and Macor represents a reliable solution in terms of longevity and cost-effectiveness.

In addition, Sec.6.2 included an investigation of laser-induced plasma filaments, tested and studied at SPARC_LAB facility. A complete characterization of the plasma source, based on spectroscopic techniques for plasma density and temperature measurements and other diagnostics for determining the filament dimensions and decay time, demonstrated the possibility to produce uniform plasma channels with suitable density profiles for plasma-based acceleration. In addition, the tunability of the plasma density and filament length, the jitter-free operation and the reduced energy deposition and amount of injected gas in the interaction chamber make plasma filaments particularly interesting in the context of high repetition rate plasma-based acceleration.

Finally, Ch.7 presented a preliminary design and test of the 60 cm-long capillary targeted for EuPRAXIA@SPARC_LAB project. An optimal geometrical configuration was designed by means of 3D fluid dynamics simulations, aimed at maximizing the uniformity of the gas distribution in the capillary channel. Afterwards, a first prototypical version has been realized by means of a novel approach, based on the use of modular structures to improve the mechanical processing of the device and also its cost-effectiveness. A preliminary test has proved the feasibility of the modular

capillary to produce a single 60 cm-long plasma discharge with 13 kV pulses.

Future perspectives, concerning the development of plasma sources for plasma acceleration, include studies of plasma discharges properties at high repetition rate, which may differ from those observed at 1 Hz with pulsed gas injection. In the framework of EuPRAXIA@SPARC_LAB project, the development of the 60 cm-long capillary will go on with the realization of modular ceramic devices, which will be tested for long-term operation at 100 Hz, as foreseen by the project. In addition the development of reliable simulation codes able to describe the plasma discharge formation will be a crucial step ahead in the numerical design of plasma discharge capillaries. Furthermore, studies on plasma discharges stability will provide a key step forward towards stable and efficient plasma-based accelerators.

Appendix A

Fitting optimization of Hydrogen lines with Voigt functions

As described in Ch.3, plasma density measurements are performed by means of Stark broadening method. Spectral lines of Hydrogen Balmer series are selected by a spectrometer and acquired by an ICCD camera; afterwards, the hydrogen spectral linewidth is measured to retrieve the plasma density, according to Eq.3.15.

For dense and cold plasmas, Lorenztian functions properly fit the broadened Hydrogen lines and compute the related linewidth; however, in intermediate regions (1-7 eV, 10^{15}-10^{16} cm^{-3}), Doppler and Stark effect can similarly affect the broadening of Hydrogen lines and other distribution functions are more indicated for a precise fitting. In particular, since the line profiles induced by Stark and Doppler effects are described by Lorentzian and Gaussian distribution functions respectively, an optimized fit of the spectral line can be achieved by means of a Voigt function, defined as the convolution of the Gaussian and Lorentzian functions. For instance, Fig.A.1 reports a comparison of three line profiles, Gaussian, Lorentzian and Voigt, with normalized intensity and same FWHM.

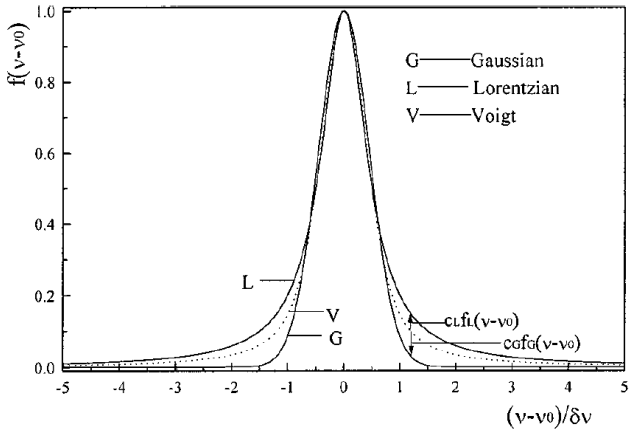

Figure A.1. Comparison between Voigt, Lorentzian and Gaussian line profiles [82].

The computation of the profile fitting algorithm, based on the use of the Voigt function, may generally become quite time consuming. Therefore, the Voigt profile can be preferably approximated by a pseudo-Voigt function, defined as a linear combination between a Gaussian and a Lorentzian function, in which the FWHM and Lorentzian weight of the pseudo-Voigt function are related to the FWHM values of the deconvoluted Gaussian and Lorentzian functions, Γ_G and Γ_L [120]:

$$f_V(x) = (1-\eta) f_G(x,\gamma_G) + \eta f_L(x,\gamma_L) \tag{A.1}$$

in which η is a parameter which mixes the two functions and $f_G(x,\gamma_G)$ and $f_L(x,\gamma_L)$ are the normalized Gaussian and Lorentzian functions:

$$f_G(x,\gamma_G) = \frac{1}{\sqrt{\pi}\gamma_G} e^{-x^2/\gamma_G^2} \tag{A.2}$$

$$f_L(x,\gamma_L) = \frac{1}{\pi\gamma_L}(1 + x^2/\gamma_L^2)^{-1} \tag{A.3}$$

with the FWHM of the two functions given by $2\sqrt{\ln 2}\gamma_G$ and $2\gamma_L$ respectively.

A further improvement in the fitting accuracy can be achieved by adding to the pseudo-Voigt two alternative functions, i.e. an irrational function and a squared hyperbolic secant function, which are intermediate between Gaussian and Lorentzian distributions [69]:

$$f_I(x,\gamma_I) = \frac{1}{2\gamma_I}[1 + (x/\gamma_I)^2]^{-3/2} \tag{A.4}$$

$$f_H(x,\gamma_H) = \frac{1}{2\gamma_H} sech^2(x/\gamma_H) = \frac{1}{2\gamma_H}\left[\frac{2}{e^{x/\gamma_H} + e^{-x/\gamma_H}}\right]^2 \tag{A.5}$$

whose FWHM are given by:

$$\Gamma_I = (2^{2/3} - 1)^{1/2}\gamma_I, \quad \Gamma_H = 2[ln(2^{1/2} + 1)]\gamma_H \tag{A.6}$$

A comparison of the two functions with Gaussian and Lorentzian distributions is reported in Fig.A.2 [69].

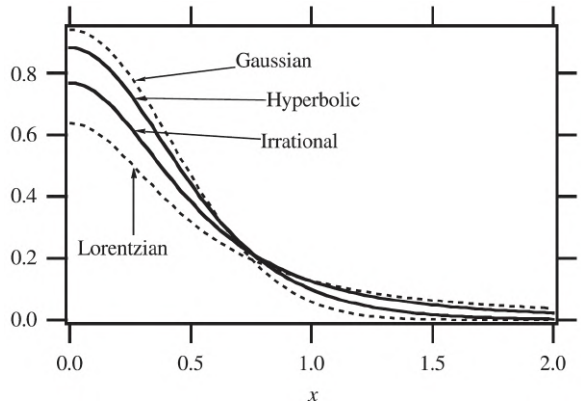

Figure A.2. Proiles of the Gaussian, Lorentzian, irrational and hyperbolic functions.

Bibliography

[1] Magnets and ids. https://www.sesame.org.jo/accelerators/technology/magnets-and-ids (2024).

[2] Ackermann, W. et al. Operation of a free-electron laser from the extreme ultraviolet to the water window. *Nat. Photon.*, **1** (2007), 336. Available from: https://doi.org/10.1038/nphoton.2007.76, doi:10.1038/nphoton.2007.76.

[3] Alejo, A., Cowley, J., Picksley, A., Walczak, R., and Hooker, S. M. Demonstration of kilohertz operation of hydrodynamic optical-field-ionized plasma channels. *Phys. Rev. Accel. Beams*, **25** (2022), 011301. Available from: https://link.aps.org/doi/10.1103/PhysRevAccelBeams.25.011301, doi:10.1103/PhysRevAccelBeams.25.011301.

[4] Alesini, D., et al. The sparc project: a high-brightness electron beam source at lnf to drive a sase-fel experiment. *Nuclear Instruments and Methods A*, **507** (2003), 345 . Available from: http://www.sciencedirect.com/science/article/pii/S0168900203009434, doi:http://dx.doi.org/10.1016/S0168-9002(03)00943-4.

[5] Allaria, E. et al. Highly coherent and stable pulses from the fermi seeded free-electron laser in the extreme ultraviolet. *Nat. Photon.*, **6** (2012), 699. Available from: https://doi.org/10.1038/nphoton.2012.233, doi:10.1038/nphoton.2012.233.

[6] Amini, K., Biegert, J., Calegari, F., et al. Symphony on strong field approximation. *Reports on Progress in Physics*, **82** (2019), 116001. Available from: https://dx.doi.org/10.1088/1361-6633/ab2bb1, doi:10.1088/1361-6633/ab2bb1.

[7] Anania, M., et al. Design of a plasma discharge circuit for particle wakefield acceleration. *Nuclear Instruments and Methods in Physics Research Section A: Accelerators, Spectrometers, Detectors and Associated Equipment*, **740** (2014), 193. Proceedings of the first European Advanced Accelerator Concepts Workshop 2013. Available from: https://www.sciencedirect.com/science/article/pii/S0168900213014344, doi:https://doi.org/10.1016/j.nima.2013.10.053.

[8] Argyropoulos, T., et al. Design, fabrication, and high-gradient testing of an x-band, traveling-wave accelerating structure milled from

copper halves. *Phys. Rev. Accel. Beams*, **21** (2018), 061001. Available from: https://link.aps.org/doi/10.1103/PhysRevAccelBeams.21.061001, doi:10.1103/PhysRevAccelBeams.21.061001.

[9] Ashkenazy, J., Kipper, R., and Caner, M. Spectroscopic measurements of electron density of capillary plasma based on stark broadening of hydrogen lines. *Phys. Rev. A*, **43** (1991), 5568. Available from: https://link.aps.org/doi/10.1103/PhysRevA.43.5568, doi:10.1103/PhysRevA.43.5568.

[10] Assmann, R. and Grebenyuk, J. N. Accelerator physics challenges towards a plasma accelerator with usable beam quality (2014). Available from: https://api.semanticscholar.org/CorpusID:55052968.

[11] Assmann, R. W., Weikum, M. K., and Akhter, T. e. a. Eupraxia conceptual design report. *Eur. Phys. J. Spec. Top.*, **229** (2020), 3675–4284. doi:https://doi.org/10.1140/epjst/e2020-000127-8.

[12] Audet, T., Lee, P., Maynard, G., Dufrénoy, S. D., Maitrallain, A., Bougeard, M., Monot, P., and Cros, B. Gas cell density characterization for laser wakefield acceleration. *Nuclear Instruments and Methods in Physics Research Section A: Accelerators, Spectrometers, Detectors and Associated Equipment*, **909** (2018), 383. 3rd European Advanced Accelerator Concepts workshop (EAAC2017). Available from: https://www.sciencedirect.com/science/article/pii/S0168900218300706, doi:https://doi.org/10.1016/j.nima.2018.01.053.

[13] Balerna, A. and Mobilio, S. Introduction to synchrotron radiation (2015). Available from: https://api.semanticscholar.org/CorpusID:52353026.

[14] Balerna, A., et al. The potential of eupraxia@sparc_lab for radiation based techniques. *Condensed Matter*, **4** (2019). Available from: https://www.mdpi.com/2410-3896/4/1/30, doi:10.3390/condmat4010030.

[15] Bambade, P., et al. The international linear collider: A global project (2019). Available from: https://arxiv.org/abs/1903.01629, arXiv:1903.01629.

[16] Biagioni, A. et al. Gas-filled capillary-discharge stabilization for plasma-based accelerators by means of a laser pulse. *Plasma Physics and Controlled Fusion*, **63** (2021), 115013. doi:10.1088/1361-6587/ac1f68.

[17] Bisesto, F., et al. The flame laser at sparc_lab. *Nuclear Instruments and Methods in Physics Research Section A: Accelerators, Spectrometers, Detectors and Associated Equipment*, **909** (2018), 452.

[18] Blumenfeld, I., Clayton, C., Decker, F., et al. Energy doubling of 42 gev electrons in a metre-scale plasma wakefield accelerator. *Nature*, **445** (2007), 741. Available from: https://doi.org/10.1038/nature05538.

[19] Bobrova, N., Esaulov, A., Sakai, J., Sasorov, P., Spence, D., Butler, A., Hooker, S., and Bulanov, S. Simulations of a hydrogen-filled capillary discharge waveguide. *Phys Rev E Stat Nonlin Soft Matter Phys*, (2002). doi:doi:10.1103/PhysRevE.65.016407.

[20] Bobrova, N. A., Sasorov, P. V., Benedetti, C., Bulanov, S. S., Geddes, C. G. R., Schroeder, C. B., Esarey, E., and Leemans, W. P. Laser-heater assisted plasma channel formation in capillary discharge waveguides. *Physics of Plasmas*, **20** (2013), 020703. Available from: https://doi.org/10.1063/1.4793447, arXiv:https://pubs.aip.org/aip/pop/article-pdf/doi/10.1063/1.4793447/16144220/020703_1_online.pdf, doi:10.1063/1.4793447.

[21] Bobrova, N. A. et al. Simulations of a hydrogen-filled capillary discharge waveguide. *Phys. Rev. E*, **65** (2001), 016407. doi:10.1103/PhysRevE.65.016407.

[22] Bourhis, J., et al. Treatment of a first patient with flash-radiotherapy. *Radiotherapy and Oncology*, **139** (2019), 18. FLASH radiotherapy International Workshop. Available from: https://www.sciencedirect.com/science/article/pii/S0167814019329597, doi:https://doi.org/10.1016/j.radonc.2019.06.019.

[23] Brinkmann, R., et al. Chirp mitigation of plasma-accelerated beams by a modulated plasma density. *Phys. Rev. Lett.*, **118** (2017), 214801. Available from: https://link.aps.org/doi/10.1103/PhysRevLett.118.214801, doi:10.1103/PhysRevLett.118.214801.

[24] Buck, A., et al. Shock-front injector for high-quality laser-plasma acceleration. *Phys. Rev. Lett.*, **110** (2013), 185006. Available from: https://link.aps.org/doi/10.1103/PhysRevLett.110.185006, doi:10.1103/PhysRevLett.110.185006.

[25] Bulanov, S., Naumova, N., Pegoraro, F., and Sakai, J. Particle injection into the wave acceleration phase due to nonlinear wake wave breaking. *Phys. Rev. E*, **58** (1998), R5257. Available from: https://link.aps.org/doi/10.1103/PhysRevE.58.R5257, doi:10.1103/PhysRevE.58.R5257.

[26] Butler, A., Spence, D. J., and Hooker, S. M. Guiding of high-intensity laser pulses with a hydrogen-filled capillary discharge waveguide. *Phys. Rev. Lett.*, **89** (2002), 185003. Available from: https://link.aps.org/doi/10.1103/PhysRevLett.89.185003, doi:10.1103/PhysRevLett.89.185003.

[27] Caldwell, A., Lotov, K., Pukhov, A., et al. Proton-driven plasma-wakefield acceleration. *Nature Phys*, **5** (2009), 363–367. Available from: https://doi.org/10.1038/nphys1248, doi:10.1038/nphys1248.

[28] Chandrasekharn, J. Plasma accelerators. *Scientific American (N. Y., USA) (via le Web)*, (2006), no pagination. Available from: https://cds.cern.ch/record/924848.

[29] Chen, F. F. *Introduction to Plasma Physics and Controlled Fusion*. Springer, 3rd edn. (2016).

[30] Chen, P., Dawson, J. M., Huff, R. W., and Katsouleas, T. Acceleration of electrons by the interaction of a bunched electron beam with a plasma. *Phys. Rev. Lett.*, **54** (1985), 693. Available from: https://link.aps.org/doi/10.1103/PhysRevLett.54.693, doi:10.1103/PhysRevLett.54.693.

[31] Chiadroni, E., Cianchi, A., Ferrario, M., Mostacci, A., Pompili, R., and Shpakov, V. A versatile thz source from high-brightness electron beams: Generation and characterization. *Condensed Matter*, **5** (2020), 40.

[32] Chiadroni, E., et al. Overview of plasma lens experiments and recent results at sparc_lab. *Nuclear Instruments and Methods in Physics Research Section A: Accelerators, Spectrometers, Detectors and Associated Equipment*, **909** (2018), 16. 3rd European Advanced Accelerator Concepts workshop (EAAC2017). Available from: https://www.sciencedirect.com/science/article/pii/S0168900218301645, doi:https://doi.org/10.1016/j.nima.2018.02.014.

[33] Cianchi, A. et al. Six-dimensional measurements of trains of high brightness electron bunches. *Physical Review Special Topics-Accelerators and Beams*, **18** (2015), 082804.

[34] Clark, T. R. and Milchberg, H. M. Time- and space-resolved density evolution of the plasma waveguide. *Physical Review Letters*, **78** (1997), 2373. Available from: https://api.semanticscholar.org/CorpusID:119690515.

[35] Clayton, C. E., Joshi, C., Darrow, C., and Umstadter, D. Relativistic plasma-wave excitation by collinear optical mixing. *Phys. Rev. Lett.*, **54** (1985), 2343. Available from: https://link.aps.org/doi/10.1103/PhysRevLett.54.2343, doi:10.1103/PhysRevLett.54.2343.

[36] Clayton, C. E., Marsh, K. A., Dyson, A., Everett, M., Lal, A., Leemans, W. P., Williams, R., and Joshi, C. Ultrahigh-gradient acceleration of injected electrons by laser-excited relativistic electron plasma waves. *Phys. Rev. Lett.*, **70** (1993), 37. Available from: https://link.aps.org/doi/10.1103/PhysRevLett.70.37, doi:10.1103/PhysRevLett.70.37.

[37] COMSOL, I. *COMSOL Multiphysics Reference Manual, version 6.1.* doi:https://www.comsol.com/.

[38] Conde, M., Yusof, Z., and Gai, W. Schottky-enabled photoemission in rf guns (2014). Available from: https://www.slideserve.com/lana/schottky-enabled-photoemission-in-rf-guns.

[39] Curcio, A. et al. Modeling and diagnostics for plasma discharge capillaries. *Phys. Rev. E*, **100** (2019), 053202. doi:10.1103/PhysRevE.100.053202.

[40] Daido, H., Nishiuchi, M., and Pirozhkov, A. S. Review of laser-driven ion sources and their applications. *Reports on Progress in Physics*, **75** (2012), 056401. Available from: https://dx.doi.org/10.1088/0034-4885/75/5/056401, doi:10.1088/0034-4885/75/5/056401.

[41] Dal Forno, M., et al. rf breakdown tests of mm-wave metallic accelerating structures. *Phys. Rev. Accel. Beams*, **19** (2016), 011301. Available from: https://link.aps.org/doi/10.1103/PhysRevAccelBeams.19.011301, doi:10.1103/PhysRevAccelBeams.19.011301.

[42] Doyle, B. L., McDaniel, F. D., and Hamm, R. W. The future of industrial accelerators and applications. *Reviews of Accelerator Science and Technology*, **10** (2019), 93. Available from: https://doi.org/10.1142/S1793626819300068, arXiv:https://doi.org/10.1142/S1793626819300068, doi:10.1142/S1793626819300068.

[43] Ehrlich, Y., Cohen, C., Zigler, A., Krall, J., Sprangle, P., and Esarey, E. Guiding of high intensity laser pulses in straight and curved plasma channel experiments. *Phys. Rev. Lett.*, **77** (1996), 4186. Available from: https://link.aps.org/doi/10.1103/PhysRevLett.77.4186, doi:10.1103/PhysRevLett.77.4186.

[44] Emma, P. et al. First lasing and operation of an angstrom-wavelength free-electron laser. *Nat. Photon.*, **4** (2010), 641. Available from: https://doi.org/10.1038/nphoton.2010.176, doi:10.1038/nphoton.2010.176.

[45] et al., A. V. Magnetic measurements for halbach-type permanent quadrupoles using a single-stretched wire system. In *Proc. 15th International Particle Accelerator Conference*, no. 15 in IPAC'24 - 15th International Particle Accelerator Conference, pp. 3864–3867. JACoW Publishing, Geneva, Switzerland (2024). ISBN 978-3-95450-247-9. Available from: https://indico.jacow.org/event/63/contributions/4908, doi:10.18429/JACoW-IPAC2024-THPS54.

[46] Faircloth, D. C. Technological aspects: High voltage (2014). Available from: http://cds.cern.ch/record/1693330, doi:10.5170/CERN-2013-007.381.

[47] Faure, J., Gustas, D., Guénot, D., Vernier, A., Böhle, F., Ouillé, M., Haessler, S., Lopez-Martens, R., and Lifschitz, A. A review of recent progress on laser-plasma acceleration at khz repetition rate. *Plasma Physics and Controlled Fusion*, **61** (2018), 014012. Available from: https://dx.doi.org/10.1088/1361-6587/aae047, doi:10.1088/1361-6587/aae047.

[48] Faure, J., Rechatin, C., Norlin, A., et al. Controlled injection and acceleration of electrons in plasma wakefields by colliding laser pulses. *Nature*, **444** (2006), 737–739. Available from: https://doi.org/10.1038/nature05393, doi:10.1038/nature05393.

[49] Ferrario, M. Injection, extraction and matching (2020). Available from: https://arxiv.org/abs/2007.04102, arXiv:2007.04102.

[50] Ferrario, M. and Assmann, R. Advanced accelerator concepts (2021). Available from: https://arxiv.org/abs/2103.10843, arXiv:2103.10843.

[51] Ferrario, M. et al. Experimental demonstration of emittance compensation with velocity bunching. *Physical review letters*, **104** (2010), 054801.

[52] Ferrario, M. et al. Eupraxia@sparc_lab design study towards a compact fel facility at lnf. *Nuclear Instruments and Methods in Physics Research Section A: Accelerators, Spectrometers, Detectors and Associated Equipment*, **909** (2018), 134. 3rd European Advanced Accelerator Concepts workshop (EAAC2017). doi:https://doi.org/10.1016/j.nima.2018.01.094.

[53] Fortov, V., Iakubov, I., and Khrapak, A. *Physics of Strongly Coupled Plasma*. Oxford University Press (2006). ISBN 9780199299805. Available from: https://doi.org/10.1093/acprof:oso/9780199299805.001.0001, doi:10.1093/acprof:oso/9780199299805.001.0001.

[54] Fridman, A. and Kennedy, L. *Plasma Physics and Engineering*. CRC Press, 3rd edn. (2021).

[55] Fritzler, S., et al. Emittance measurements of a laser-wakefield-accelerated electron beam. *Phys. Rev. Lett.*, **92** (2004), 165006. Available from: https://link.aps.org/doi/10.1103/PhysRevLett.92.165006, doi:10.1103/PhysRevLett.92.165006.

[56] Galletti, M., et al. Stable operation of a free-electron laser driven by a plasma accelerator. *Phys. Rev. Lett.*, **129** (2022), 234801. Available from: https://link.aps.org/doi/10.1103/PhysRevLett.129.234801, doi:10.1103/PhysRevLett.129.234801.

[57] Garland, M. J., Wood, J. C., Boyle, G., and Osterhoff, J. Plasma sources and diagnostics (2020). Available from: https://arxiv.org/abs/2007.08184, arXiv:2007.08184.

[58] Gibbon, P. Introduction to plasma physics (2020). Available from: https://arxiv.org/abs/2007.04783, arXiv:2007.04783.

[59] Goldston, R. J. *Introduction to Plasma Physics*. CRC Press, 1st edn. (1995). Available from: https://doi.org/10.1201/9780367806958.

[60] Gonsalves, A. J., et al. Demonstration of a high repetition rate capillary discharge waveguide. *Journal of Applied Physics*, **119** (2016), 033302. Available from: https://doi.org/10.1063/1.4940121, arXiv:https://pubs.aip.org/aip/jap/article-pdf/doi/10.1063/1.4940121/15173469/033302_1_online.pdf, doi:10.1063/1.4940121.

[61] Gonsalves, A. J., et al. Petawatt laser guiding and electron beam acceleration to 8 gev in a laser-heated capillary discharge waveguide. *Phys. Rev. Lett.*, **122** (2019), 084801. Available from: https://link.aps.org/doi/10.1103/PhysRevLett.122.084801, doi:10.1103/PhysRevLett.122.084801.

[62] Goossens, M. An introduction to plasma astrophysics and magnetohydrodynamics (2003). Available from: https://api.semanticscholar.org/CorpusID:118468858.

[63] Griem, H. R. *Spectral line broadening by plasmas*. Academic Press, University of Maryland, College Park, Maryland (1974).

[64] Griem, H. R. *Principles of Plasma Spectroscopy*. Cambridge University Press, The Edinburgh Building, Cambridge CB2 2RU, UK (1997).

[65] Grudiev, A., Calatroni, S., and Wuensch, W. New local field quantity describing the high gradient limit of accelerating structures. *Phys. Rev. ST Accel. Beams*, **12** (2009), 102001. Available from: https://link.aps.org/doi/10.1103/PhysRevSTAB.12.102001, doi:10.1103/PhysRevSTAB.12.102001.

[66] Gschwendtner, E., Turner, M., et al. Proton-driven plasma wakefield acceleration in awake. *Royal Society Publishing*, (2019). Available from: https://doi.org/10.1098/rsta.2018.0418, doi:10.1098/rsta.2018.0418.

[67] Gschwendtner, E., et al. Awake, the advanced proton driven plasma wakefield acceleration experiment at cern. *Nuclear Instruments and Methods in Physics Research Section A: Accelerators, Spectrometers, Detectors and Associated Equipment*, **829** (2016), 76–82. Available from: http://dx.doi.org/10.1016/j.nima.2016.02.026, doi:10.1016/j.nima.2016.02.026.

[68] Huba, J. D. Nrl: Plasma formulary (2004). Available from: https://api.semanticscholar.org/CorpusID:262318409.

[69] Ida, T., Ando, M., and Toraya, H. Extended pseudo-Voigt function for approximating the Voigt profile. *Journal of Applied Crystallography*, **33** (2000), 1311. Available from: https://doi.org/10.1107/S0021889800010219, doi:10.1107/S0021889800010219.

[70] Ilyin, D. Stark splitting. https://commons.wikimedia.org/w/index.php?curid=121721798 (2022).

[71] Ishikawa, T. et al. A compact x-ray free-electron laser emitting in the sub-angstrom region. *Nat. Photon.*, **6** (2012), 540. Available from: https://doi.org/10.1038/nphoton.2012.141, doi:10.1038/nphoton.2012.141.

[72] Janot, P. and Grojean, C. Fcc: the physics case. https://cerncourier.com/a/fcc-the-physics-case/ (2024).

[73] Kaganovich, D., Sasorov, P., Cohen, C., and Zigler, A. Variable profile capillary discharge for improved phase matching in a laser wakefield accelerator. *Applied Physics Letters*, **75** (1999), 772. Available from: https://doi.org/10.1063/1.124508, arXiv:https://pubs.aip.org/aip/apl/article-pdf/75/6/772/18543651/772_1_online.pdf, doi:10.1063/1.124508.

[74] Kain, V. Beam dynamics and beam losses – circular machines. *CERN Yellow Reports*, (2016), Vol 2 (2016): Proceedings of the 2014 Joint International Accelerator School: Beam Loss and Accelerator Protection. Available from: https://e-publishing.cern.ch/index.php/CYR/article/view/228, doi:10.5170/CERN-2016-002.21.

[75] Kim, J., Phung, V. L. J., Roh, K., Kim, M., Kang, K., and Suk, H. Development of a density-tapered capillary gas cell for

laser wakefield acceleration. *Review of Scientific Instruments*, **92** (2021), 023511. Available from: https://doi.org/10.1063/5.0009632, arXiv:https://pubs.aip.org/aip/rsi/article-pdf/doi/10.1063/5.0009632/15782396/023511_1_online.pdf, doi:10.1063/5.0009632.

[76] Kittel, C. *Introduction to Solid State Physics*. John Wiley and Sons Inc. (1953 1st ed.).

[77] Kuschel, S., Schwab, M. B., Yeung, M., Hollatz, D., Seidel, A., Ziegler, W., Sävert, A., Kaluza, M. C., and Zepf, M. Controlling the self-injection threshold in laser wakefield accelerators. *Phys. Rev. Lett.*, **121** (2018), 154801. Available from: https://link.aps.org/doi/10.1103/PhysRevLett.121.154801, doi:10.1103/PhysRevLett.121.154801.

[78] Labat, M. et al. Seeded free-electron laser driven by a compact laser plasma accelerator. *Nat. Photon.*, **17** (2023), 150. Available from: https://doi.org/10.1038/s41566-022-01104-w, doi:10.1038/s41566-022-01104-w.

[79] Linssen, L., Miyamoto, A., Stanitzki, M., and Weerts, H. Physics and detectors at clic: Clic conceptual design report (2012). Available from: https://arxiv.org/abs/1202.5940, arXiv:1202.5940.

[80] Litos, M., Adli, E., An, W., et al. High-efficiency acceleration of an electron beam in a plasma wakefield accelerator. *Nature*, **515** (2014), 92. Available from: https://doi.org/10.1038/nature13882.

[81] Little, P. F. *Secondary Effects*, pp. 574–662. Springer Berlin Heidelberg, Berlin, Heidelberg (1956). ISBN 978-3-642-45844-6. Available from: https://doi.org/10.1007/978-3-642-45844-6_9, doi:10.1007/978-3-642-45844-6_9.

[82] Liu, Y., Lin, J., Huang, G., Guo, Y., and Duan, C. Simple empirical analytical approximation to the voigt profile. *J. Opt. Soc. Am. B*, **18** (2001), 666. Available from: https://opg.optica.org/josab/abstract.cfm?URI=josab-18-5-666, doi:10.1364/JOSAB.18.000666.

[83] Loeb, L. B. Glow discharge structure. https://commons.wikimedia.org/wiki/File:Glow_discharge_structure_-_English.svg (2009).

[84] Lu, W., Tzoufras, M., Joshi, C., Tsung, F. S., Mori, W. B., Vieira, J., Fonseca, R. A., and Silva, L. O. Generating multi-gev electron bunches using single stage laser wakefield acceleration in a 3d nonlinear regime. *Phys. Rev. ST Accel. Beams*, **10** (2007), 061301. Available from: https://link.aps.org/doi/10.1103/PhysRevSTAB.10.061301, doi:10.1103/PhysRevSTAB.10.061301.

[85] Malka, V. Plasma wake accelerators: Introduction and historical overview. *CERN Yellow Reports*, (2016), Vol 1 (2016): Proceedings of the 2014 CAS. Available from: https://e-publishing.cern.ch/index.php/CYR/article/view/211, doi:10.5170/CERN-2016-001.1.

[86] Mehrling, T. J., Fonseca, R. A., Martinez de la Ossa, A., and Vieira, J. Mitigation of the hose instability in plasma-wakefield accelerators. *Phys. Rev. Lett.*, **118** (2017), 174801. Available from: https://link.aps.org/doi/10.1103/PhysRevLett.118.174801, doi:10.1103/PhysRevLett.118.174801.

[87] Mitchner, M. and Kruger, C. H., Jr. *Partially ionized gases*. John Wiley and Sons, Inc., New York (1973). Available from: https://www.osti.gov/biblio/4224114.

[88] Muggli, P., Hoffman, J., Marsh, K., Wang, S., Clayton, C., Katsouleas, T., and Joshi, C. Lithium plasma sources for acceleration and focusing of ultra-relativistic electron beams. In *Proceedings of the 1999 Particle Accelerator Conference (Cat. No.99CH36366)*, vol. 5, pp. 3651–3653 vol.5 (1999). doi:10.1109/PAC.1999.792400.

[89] Muggli, P., Marsh, K. A., Wang, S. M., Clayton, C. E., Lee, S. P., Katsouleas, T. C., and Joshi, C. Photo-ionized lithium source for plasma accelerator applications. *IEEE Transactions on Plasma Science*, **27** (1999), 791. Available from: https://api.semanticscholar.org/CorpusID:13146631.

[90] NIST. Nist atomic spectra database lines form. https://physics.nist.gov/PhysRefData/ASD/lines_form.html (2006).

[91] NIST. Nist libs database. https://physics.nist.gov/PhysRefData/ASD/LIBS/libs-form.html (2006).

[92] Picksley, A., et al. Meter-scale conditioned hydrodynamic optical-field-ionized plasma channels. *Physical Review E*, **102** (2020). Available from: http://dx.doi.org/10.1103/PhysRevE.102.053201, doi:10.1103/physreve.102.053201.

[93] Pinson, J. The power of attraction: Magnets in particle accelerators (2020).

[94] Poder, K., et al. Measurements of self-guiding of ultrashort laser pulses over long distances. *Plasma Physics and Controlled Fusion*, **60** (2017), 014022. Available from: https://dx.doi.org/10.1088/1361-6587/aa8f0e, doi:10.1088/1361-6587/aa8f0e.

[95] Pollock, B. B., et al. Demonstration of a narrow energy spread, ~ 0.5 GeV electron beam from a two-stage laser wakefield accelerator. *Phys. Rev. Lett.*, **107** (2011), 045001. Available from: https://link.aps.org/doi/10.1103/PhysRevLett.107.045001, doi:10.1103/PhysRevLett.107.045001.

[96] Pompili, R., Castorina, G., Ferrario, M., Marocchino, A., and Zigler, A. Guiding of charged particle beams in curved capillary-discharge waveguides. *AIP Advances*, **8** (2018), 015326. Available from: https://doi.org/10.1063/1.5011964, arXiv:https://pubs.aip.org/aip/adv/article-pdf/doi/10.1063/1.5011964/13070752/015326_1_online.pdf, doi:10.1063/1.5011964.

[97] Pompili, R. et al. Femtosecond timing-jitter between photo-cathode laser and ultra-short electron bunches by means of hybrid compression. *New Journal of Physics*, **18** (2016), 083033. Available from: http://stacks.iop.org/1367-2630/18/i=8/a=083033.

[98] Pompili, R., et al. Experimental characterization of active plasma lensing for electron beams. *Applied Physics Letters*, **110** (2017), 104101. Available from: https://doi.org/10.1063/1.4977894, arXiv:https://pubs.aip.org/aip/apl/article-pdf/doi/10.1063/1.4977894/14496944/104101_1_online.pdf, doi:10.1063/1.4977894.

[99] Pompili, R. et al. Energy spread minimization in a beam-driven plasma wakefield accelerator. *Nature Physics*, **17** (2021), 499.

[100] Pompili, R. et al. Free-electron lasing with compact beam-driven plasma wakefield accelerator. *Nature*, **605** (2022), 659–662. Available from: https://doi.org/10.1038/s41586-022-04589-1, doi:10.1038/s41586-022-04589-1.

[101] Pompili, R., et al. Acceleration and focusing of relativistic electron beams in a compact plasma device. *Phys. Rev. E*, **109** (2024), 055202. Available from: https://link.aps.org/doi/10.1103/PhysRevE.109.055202, doi:10.1103/PhysRevE.109.055202.

[102] Pompili, R., et al. Guiding of charged particle beams in curved plasma-discharge capillaries. *Phys. Rev. Lett.*, **132** (2024), 215001. Available from: https://link.aps.org/doi/10.1103/PhysRevLett.132.215001, doi:10.1103/PhysRevLett.132.215001.

[103] Pukhov, A., Meyer-ter Vehn, J., et al. Laser wake field acceleration: the highly non-linear broken-wave regime. *Appl Phys B*, **74** (2002), 355–361. Available from: https://doi.org/10.1007/s003400200795, doi:10.1007/s003400200795.

[104] Rosenzweig, J. B., Cline, D. B., Cole, B. A., Figueroa, H., Gai, W., Konecny, R. S., Norem, J., Schoessow, P. V., and Simpson, J. A. Experimental observation of plasma wake-field acceleration. *Physical review letters*, **61** (1988), 98. Available from: https://api.semanticscholar.org/CorpusID:35740820.

[105] Roth, J. R. *Industrial Plasma Engineering: Volume 1: Principles*. CRC Press, 1st edn. (1995). Available from: https://doi.org/10.1201/9780367802615.

[106] Rowlands-Rees, T. P., et al. Laser-driven acceleration of electrons in a partially ionized plasma channel. *Phys. Rev. Lett.*, **100** (2008), 105005. Available from: https://link.aps.org/doi/10.1103/PhysRevLett.100.105005, doi:10.1103/PhysRevLett.100.105005.

[107] Schmid, K., Buck, A., Sears, C. M. S., Mikhailova, J. M., Tautz, R., Herrmann, D., Geissler, M., Krausz, F., and Veisz,

L. Density-transition based electron injector for laser driven wakefield accelerators. *Phys. Rev. ST Accel. Beams*, **13** (2010), 091301. Available from: https://link.aps.org/doi/10.1103/PhysRevSTAB.13.091301, doi:10.1103/PhysRevSTAB.13.091301.

[108] Schnitzer, J. A. Glow discharge regions. https://commons.wikimedia.org/wiki/File:Glow_discharge_regions.jpg (2010).

[109] Schwoerer, H., Pfotenhauer, S., Jäckel, O., and others. Laser-plasma acceleration of quasi-monoenergetic protons from microstructured targets. *Nature*, **439** (2006), 445–448. Available from: https://doi.org/10.1038/nature04492, doi:10.1038/nature04492.

[110] Semushin, S. A. and Malka, V. High density gas jet nozzle design for laser target production. *Review of Scientific Instruments*, **72** (2001), 2961. Available from: https://api.semanticscholar.org/CorpusID:122910987.

[111] Serafini, L. and Ferrario, M. Velocity bunching in photo-injectors. In *American Institute of Physics Conference Series*, vol. 581, pp. 87–106 (2001).

[112] Shalloo, R. J., Arran, C., Corner, L., Holloway, J., Jonnerby, J., Walczak, R., Milchberg, H. M., and Hooker, S. M. Hydrodynamic optical-field-ionized plasma channels. *Phys. Rev. E*, **97** (2018), 053203. Available from: https://link.aps.org/doi/10.1103/PhysRevE.97.053203, doi:10.1103/PhysRevE.97.053203.

[113] Shalloo, R. J., et al. Low-density hydrodynamic optical-field-ionized plasma channels generated with an axicon lens. *Phys. Rev. Accel. Beams*, **22** (2019), 041302. Available from: https://link.aps.org/doi/10.1103/PhysRevAccelBeams.22.041302, doi:10.1103/PhysRevAccelBeams.22.041302.

[114] Shpakov, V., et al. Design, optimization and experimental characterization of rf injectors for high brightness electron beams and plasma acceleration. *Journal of Instrumentation*, **17** (2022), P12022.

[115] SPARC_LAB. https://sparclab.lnf.infn.it/ (2023).

[116] Spence, D. J. and Hooker, S. M. Investigation of a hydrogen plasma waveguide. *Phys. Rev. E*, **63** (2000), 015401. doi:10.1103/PhysRevE.63.015401.

[117] Spitzer, L. S. Physics of fully ionized gases (1956). Available from: https://api.semanticscholar.org/CorpusID:119377231.

[118] Strickland, D. and Mourou, G. Compression of amplified chirped optical pulses. *Optics Communications*, **56** (1985), 219. Available from: https://www.sciencedirect.com/science/article/pii/0030401885901208, doi:https://doi.org/10.1016/0030-4018(85)90120-8.

[119] Tajima, T. and Dawson, J. M. Laser electron accelerator. *Phys. Rev. Lett.*, **43** (1979), 267. doi:10.1103/PhysRevLett.43.267.

[120] Thompson, P., Cox, D. E., and Hastings, J. B. Rietveld refinement of Debye–Scherrer synchrotron X-ray data from Al_2O_3. *Journal of Applied Crystallography*, **20** (1987), 79. Available from: https://doi.org/10.1107/S0021889887087090, doi:10.1107/S0021889887087090.

[121] Tokuyama, C. *Machinable AlN ceramics SHAPAL™ Hi Msoft*. doi:https://www.tokuyama.co.jp/eng/products/advanced_materials/hi_msoft.html.

[122] Tresman, I. Electric glow discharge schematic. https://commons.wikimedia.org/wiki/File:Electric_glow_discharge_schematic.png (2009).

[123] Verra, L., et al. Experimental observation of space-charge field screening of a relativistic particle bunch in plasma. *Phys. Rev. Lett.*, **133** (2024), 035001. Available from: https://link.aps.org/doi/10.1103/PhysRevLett.133.035001, doi:10.1103/PhysRevLett.133.035001.

[124] Vieira, J., Fonseca, R. A., and Silva, L. O. Multidimensional plasma wake excitation in the non-linear blowout regime (2020). Available from: https://arxiv.org/abs/1607.03514, arXiv:1607.03514.

[125] Villa, F., Coreno, M., Ebrahimpour, Z., Giannessi, L., Marcelli, A., Opromolla, M., Petrillo, V., and Stellato, F. Aria—a vuv beamline for eupraxia@sparc_lab. *Condensed Matter*, **7** (2022). Available from: https://www.mdpi.com/2410-3896/7/1/11, doi:10.3390/condmat7010011.

[126] Wang, W. et al. Free-electron lasing at 27 nanometres based on a laser wakefield accelerator. *Nature*, **595** (2021), 516–520. Available from: https://doi.org/10.1038/s41586-021-03678-x, doi:10.1038/s41586-021-03678-x.

[127] Weller, H. G., Tabor, G., Jasak, H., and Fureby, C. A tensorial approach to computational continuum mechanics using object-oriented techniques. *Computer in Physics*, **12** (1998), 620. doi:10.1063/1.168744.

[128] Wenz, J. and Karsch, S. Physics of laser-wakefield accelerators (lwfa) (2020). Available from: https://arxiv.org/abs/2007.04622, arXiv:2007.04622.

[129] YESIL, C. Investigation of nonlinear oscillations in the gas discharge-semiconductor system: Effect of different fluid modelling approaches (2018). Available from: https://www.researchgate.net/publication/327209884.

[130] Öz, E. and Muggli, P. A novel rb vapor plasma source for plasma wakefield accelerators. *Nuclear Instruments and Methods in Physics Research Section A: Accelerators, Spectrometers, Detectors and Associated Equipment*, **740** (2014), 197. Proceedings of the first European Advanced Accelerator Concepts Workshop 2013. Available from: https://www.sciencedirect.com/science/article/pii/S0168900213015003, doi:https://doi.org/10.1016/j.nima.2013.10.093.